



National Library  
of Canada

Acquisitions and  
Bibliographic Services Branch

395 Wellington Street  
Ottawa, Ontario  
K1A 0N4

Bibliothèque nationale  
du Canada

Direction des acquisitions et  
des services bibliographiques

395, rue Wellington  
Ottawa (Ontario)  
K1A 0N4

*Your file - Votre référence*

*Our file - Notre référence*

## NOTICE

The quality of this microform is heavily dependent upon the quality of the original thesis submitted for microfilming. Every effort has been made to ensure the highest quality of reproduction possible.

If pages are missing, contact the university which granted the degree.

Some pages may have indistinct print especially if the original pages were typed with a poor typewriter ribbon or if the university sent us an inferior photocopy.

Reproduction in full or in part of this microform is governed by the Canadian Copyright Act, R.S.C. 1970, c. C-30, and subsequent amendments.

## AVIS

La qualité de cette microforme dépend grandement de la qualité de la thèse soumise au microfilmage. Nous avons tout fait pour assurer une qualité supérieure de reproduction.

S'il manque des pages, veuillez communiquer avec l'université qui a conféré le grade.

La qualité d'impression de certaines pages peut laisser à désirer, surtout si les pages originales ont été dactylographiées à l'aide d'un ruban usé ou si l'université nous a fait parvenir une photocopie de qualité inférieure.

La reproduction, même partielle, de cette microforme est soumise à la Loi canadienne sur le droit d'auteur, SRC 1970, c. C-30, et ses amendements subséquents.

UNIVERSITY OF ALBERTA

ABSOLUTE ABSORPTION INTENSITIES OF  
LIQUID METHANOL BY INFRARED SPECTROSCOPY

BY

SHULIANG ZHANG



A thesis submitted to the Faculty of Graduate Studies and Research in partial  
fulfillment of the requirement for the degree of DOCTOR OF PHILOSOPHY.

DEPARTMENT OF CHEMISTRY

Edmonton, Alberta

FALL 1994



National Library  
of Canada

Acquisitions and  
Bibliographic Services Branch

395 Wellington Street  
Ottawa, Ontario  
K1A 0N4

Bibliothèque nationale  
du Canada

Direction des acquisitions et  
des services bibliographiques

395, rue Wellington  
Ottawa (Ontario)  
K1A 0N4

*Your file    Votre référence*

*Our file    Notre référence*

**The author has granted an irrevocable non-exclusive licence allowing the National Library of Canada to reproduce, loan, distribute or sell copies of his/her thesis by any means and in any form or format, making this thesis available to interested persons.**

**L'auteur a accordé une licence irrévocable et non exclusive permettant à la Bibliothèque nationale du Canada de reproduire, prêter, distribuer ou vendre des copies de sa thèse de quelque manière et sous quelque forme que ce soit pour mettre des exemplaires de cette thèse à la disposition des personnes intéressées.**

**The author retains ownership of the copyright in his/her thesis. Neither the thesis nor substantial extracts from it may be printed or otherwise reproduced without his/her permission.**

**L'auteur conserve la propriété du droit d'auteur qui protège sa thèse. Ni la thèse ni des extraits substantiels de celle-ci ne doivent être imprimés ou autrement reproduits sans son autorisation.**

ISBN 0-315-95296-2

**Canada**

Name Shuliang Zhang

Dissertation Abstracts International is arranged by broad, general subject categories. Please select the one subject which most nearly describes the content of your dissertation. Enter the corresponding four-digit code in the spaces provided.

0494

U·M·I

SUBJECT TERM

SUBJECT CODE

## Subject Categories

### THE HUMANITIES AND SOCIAL SCIENCES

#### COMMUNICATIONS AND THE ARTS

Architecture ..... 0729  
Art History ..... 0377  
Cinema ..... 0900  
Dance ..... 0378  
Fine Arts ..... 0357  
Information Science ..... 0723  
Journalism ..... 0391  
Library Science ..... 0399  
Mass Communications ..... 0708  
Music ..... 0413  
Speech Communication ..... 0459  
Theater ..... 0465

#### EDUCATION

General ..... 0515  
Administration ..... 0514  
Adult and Continuing ..... 0516  
Agricultural ..... 0517  
Art ..... 0273  
Bilingual and Multicultural ..... 0282  
Business ..... 0688  
Community College ..... 0275  
Curriculum and Instruction ..... 0727  
Early Childhood ..... 0518  
Elementary ..... 0524  
Finance ..... 0277  
Guidance and Counseling ..... 0519  
Health ..... 0680  
Higher ..... 0745  
History of ..... 0520  
Home Economics ..... 0278  
Industrial ..... 0521  
Language and Literature ..... 0279  
Mathematics ..... 0280  
Music ..... 0522  
Philosophy of ..... 0998  
Physical ..... 0523

Psychology ..... 0525  
Reading ..... 0535  
Religious ..... 0527  
Sciences ..... 0714  
Secondary ..... 0533  
Social Sciences ..... 0534  
Sociology of ..... 0340  
Special ..... 0529  
Teacher Training ..... 0530  
Technology ..... 0710  
Tests and Measurements ..... 0288  
Vocational ..... 0747

#### LANGUAGE, LITERATURE AND LINGUISTICS

Language ..... 0679  
Ancient ..... 0289  
Linguistics ..... 0290  
Modern ..... 0291  
Literature ..... 0401  
Classical ..... 0294  
Comparative ..... 0295  
Medieval ..... 0297  
Modern ..... 0298  
African ..... 0316  
American ..... 0591  
Asian ..... 0305  
Canadian (English) ..... 0352  
Canadian (French) ..... 0355  
English ..... 0593  
Germanic ..... 0311  
Latin American ..... 0312  
Middle Eastern ..... 0315  
Romance ..... 0313  
Slavic and East European ..... 0314

#### PHILOSOPHY, RELIGION AND THEOLOGY

Philosophy ..... 0422  
Religion ..... 0318  
General ..... 0321  
Biblical Studies ..... 0319  
Clergy ..... 0320  
History of ..... 0322  
Philosophy of ..... 0469  
Theology ..... 0323

#### SOCIAL SCIENCES

American Studies ..... 0323  
Anthropology ..... 0324  
Archaeology ..... 0326  
Cultural ..... 0327  
Physical ..... 0310  
Business Administration ..... 0272  
General ..... 0770  
Accounting ..... 0454  
Banking ..... 0338  
Management ..... 0385  
Marketing ..... 0501  
Canadian Studies ..... 0503  
Economics ..... 0505  
General ..... 0508  
Agricultural ..... 0509  
Commerce-Business ..... 0510  
Finance ..... 0511  
History ..... 0358  
Labor ..... 0366  
Theory ..... 0351  
Folklore ..... 0366  
Geography ..... 0351  
Gerontology ..... 0578  
History ..... 0578  
General ..... 0578

Ancient ..... 0579  
Medieval ..... 0581  
Modern ..... 0582  
Black ..... 0328  
African ..... 0331  
Asia, Australia and Oceania ..... 0332  
Canadian ..... 0334  
European ..... 0335  
Latin American ..... 0336  
Middle Eastern ..... 0333  
United States ..... 0337  
History of Science ..... 0585  
Law ..... 0398  
Political Science ..... 0615  
General ..... 0616  
International Law and Relations ..... 0617  
Public Administration ..... 0814  
Recreation ..... 0452  
Social Work ..... 0626  
Sociology ..... 0627  
General ..... 0938  
Criminology and Penology ..... 0631  
Demography ..... 0628  
Ethnic and Racial Studies ..... 0629  
Individual and Family Studies ..... 0630  
Industrial and Labor Relations ..... 0629  
Public and Social Welfare ..... 0700  
Social Structure and Development ..... 0344  
Theory and Methods ..... 0709  
Transportation ..... 0999  
Urban and Regional Planning ..... 0453  
Women's Studies ..... 0453

### THE SCIENCES AND ENGINEERING

#### BIOLOGICAL SCIENCES

Agriculture ..... 0473  
General ..... 0285  
Agronomy ..... 0475  
Animal Culture and Nutrition ..... 0476  
Animal Pathology ..... 0359  
Food Science and Technology ..... 0478  
Forestry and Wildlife ..... 0479  
Plant Culture ..... 0480  
Plant Pathology ..... 0817  
Plant Physiology ..... 0777  
Range Management ..... 0746  
Wood Technology ..... 0306

#### Biology

General ..... 0306  
Anatomy ..... 0287  
Biostatistics ..... 0308  
Botany ..... 0309  
Cell ..... 0379  
Ecology ..... 0329  
Entomology ..... 0353  
Genetics ..... 0369  
Limnology ..... 0793  
Microbiology ..... 0410  
Molecular ..... 0307  
Neuroscience ..... 0317  
Oceanography ..... 0416  
Physiology ..... 0433  
Radiation ..... 0821  
Veterinary Science ..... 0778  
Zoology ..... 0472

#### Biophysics

General ..... 0786  
Medical ..... 0760

#### EARTH SCIENCES

Biogeochemistry ..... 0425  
Geochemistry ..... 0996

Geodesy ..... 0370  
Geology ..... 0372  
Geophysics ..... 0373  
Hydrology ..... 0388  
Mineralogy ..... 0411  
Paleobotany ..... 0345  
Paleoecology ..... 0426  
Paleontology ..... 0418  
Paleozoology ..... 0985  
Palynology ..... 0427  
Physical Geography ..... 0368  
Physical Oceanography ..... 0415

#### HEALTH AND ENVIRONMENTAL SCIENCES

Environmental Sciences ..... 0768  
Health Sciences ..... 0566  
General ..... 0300  
Audiology ..... 0992  
Chemotherapy ..... 0567  
Dentistry ..... 0350  
Education ..... 0769  
Hospital Management ..... 0758  
Human Development ..... 0982  
Immunology ..... 0564  
Medicine and Surgery ..... 0347  
Mental Health ..... 0569  
Nursing ..... 0570  
Nutrition ..... 0380  
Obstetrics and Gynecology ..... 0354  
Occupational Health and Therapy ..... 0381  
Ophthalmology ..... 0571  
Pathology ..... 0419  
Pharmacology ..... 0572  
Pharmacy ..... 0382  
Physical Therapy ..... 0573  
Public Health ..... 0574  
Radiology ..... 0575  
Recreation ..... 0575

Speech Pathology ..... 0460  
Toxicology ..... 0383  
Home Economics ..... 0386

#### PHYSICAL SCIENCES

##### Pure Sciences

Chemistry ..... 0485  
General ..... 0749  
Agricultural ..... 0486  
Analytical ..... 0487  
Biochemistry ..... 0488  
Inorganic ..... 0738  
Nuclear ..... 0490  
Organic ..... 0491  
Pharmaceutical ..... 0494  
Physical ..... 0495  
Polymer ..... 0754  
Radiation ..... 0405  
Mathematics ..... 0605  
Physics ..... 0986

##### General

Acoustics ..... 0606  
Astronomy and Astrophysics ..... 0608  
Atmospheric Science ..... 0748  
Atomic ..... 0607  
Electronics and Electricity ..... 0798  
Elementary Particles and High Energy ..... 0759  
Fluid and Plasma ..... 0609  
Molecular ..... 0610  
Nuclear ..... 0752  
Optics ..... 0756  
Radiation ..... 0611  
Solid State ..... 0463  
Statistics ..... 0346  
Applied Mechanics ..... 0984  
Computer Science ..... 0984

#### Applied Sciences

Applied Mechanics ..... 0346  
Computer Science ..... 0984

Engineering ..... 0537  
General ..... 0538  
Aerospace ..... 0539  
Agricultural ..... 0540  
Automotive ..... 0541  
Biomedical ..... 0542  
Chemical ..... 0543  
Civil ..... 0544  
Electronics and Electrical ..... 0348  
Heat and Thermodynamics ..... 0545  
Hydraulic ..... 0546  
Industrial ..... 0547  
Marine ..... 0794  
Materials Science ..... 0548  
Mechanical ..... 0743  
Metallurgy ..... 0551  
Mining ..... 0552  
Nuclear ..... 0549  
Packaging ..... 0765  
Petroleum ..... 0554  
Sanitary and Municipal ..... 0790  
System Science ..... 0428  
Geotechnology ..... 0796  
Operations Research ..... 0795  
Plastics Technology ..... 0994  
Textile Technology ..... 0621

#### PSYCHOLOGY

General ..... 0384  
Behavioral ..... 0622  
Clinical ..... 0620  
Developmental ..... 0623  
Experimental ..... 0624  
Industrial ..... 0625  
Personality ..... 0989  
Physiological ..... 0349  
Psychobiology ..... 0632  
Psychometrics ..... 0451  
Social ..... 0451





August 29, 1994

Mr. S. L. Zhang  
c/o Prof. John Bertie  
Dept. of Chemistry  
University of Alberta  
Edmonton, Alberta  
CANADA T6G 2G2

Dear Mr. Zhang:

Permission is granted by the Society for Applied Spectroscopy and the journal, *Applied Spectroscopy*, for the publication of material in the following articles to be used in your graduate thesis:

1) J. E. Bertie, S. L. Zhang and R. Manji, "Infrared Intensity of Liquids X: Accuracy of Current Methods of Obtaining Optical Constants from Multiple Attenuated Total Reflection Measurements Using the CIRCLE Cell," *Applied Spectroscopy*, 46(11), 1660-1665 (1992).

2) J. E. Bertie, S. L. Zhang, H. H. Eysel, S. Baluja and M. K. Ahmed, "Infrared Intensity of Liquids XI: Infrared Refractive Indices from 8000 cm<sup>-1</sup> to 2 cm<sup>-1</sup>, Absolute Integrated Intensities and Dipole Moment Derivatives of Methanol at 25°C," *Applied Spectroscopy*, 47(8), 1100-1114 (1993).

3) J. E. Bertie and S. L. Zhang, "Infrared Intensity of Liquids XV: Infrared Refractive Indices from 8000 cm<sup>-1</sup> to 350 cm<sup>-1</sup>, Absolute Integrated Intensities and Dipole Moment Derivatives of Methanol-d at 25°C," *Applied Spectroscopy*, 48(2), 176-189 (1994).

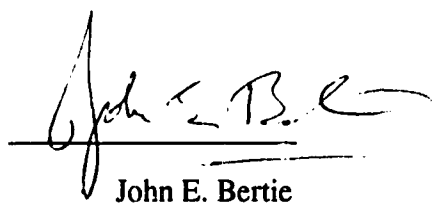
Sincerely,

James A. Holcombe  
Editor-in-Chief

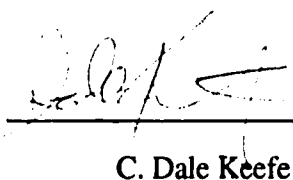
Permission is hereby granted to Shuliang Zhang to use the material contained in the following papers in his thesis.

J. E. Bertie, S. L. Zhang, and C. D. Keefe, "*Infrared Intensities of Liquids XVI: Accurate Determination of Molecular Band Intensities from Infrared Refractive Index and Dielectric Constant Spectra*" J. Mol. Struct., **324**, 157 (1994).

J. E. Bertie, S. L. Zhang, and C. D. Keefe, "*The Measurement and Use of Absolute Infrared Absorption Intensities of Neat Liquids*" Vib. Spectrosc., In press (1994).



John E. Bertie

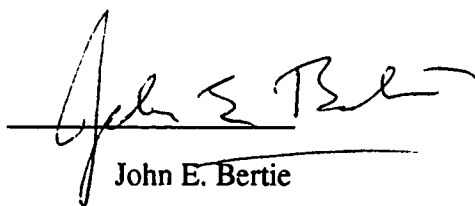


C. Dale Keefe

Permission is hereby granted to Shuliang Zhang to use the material contained in the following papers in his thesis.

J. E. Bertie and S. L. Zhang, "*Infrared Intensities of Liquids IX: The Kramers-Krönig Transform, and its Approximation by the Finite Hilbert Transform via Fast Fourier Transform*" Can. J. Chem. **70**, 520 (1994).

J. E. Bertie and S. L. Zhang, "*Infrared Intensities of Liquids XVII: Infrared Refractive Indices from 2000 to 350  $\text{cm}^{-1}$ , Absolute Integrated Intensities, Transition Moments and Dipole Moment Derivatives of Methan- $\text{d}_3$ -ol and Methanol- $\text{d}_4$ , at 25°C*" J. Chem. Phys. In press (November, 1994).



John E. Bertie

UNIVERSITY OF ALBERTA

RELEASE FORM

NAME OF AUTHOR: SHULIANG ZHANG

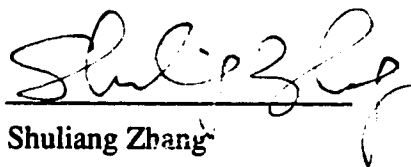
TITLE OF THESIS: ABSOLUTE ABSORPTION INTENSITIES OF LIQUID  
METHANOL BY INFRARED SPECTROSCOPY

DEGREE: Ph.D.

YEAR THIS DEGREE GRANTED: 1994

Permission is hereby granted to the University of Alberta Library to reproduce single copies of this thesis and to lend or sell such copies for private, scholarly or scientific research purposes only.

The author reserves all other publication and other rights in association with the copyright in the thesis, and except as hereinbefore provided neither the thesis nor any substantial portion thereof may be printed or otherwise reproduced in any material form whatever without the author's prior written permission.



Shuliang Zhang

Department of Chemistry  
Suzhou University  
Suzhou, 215006  
P. R. China

September 23, 1994

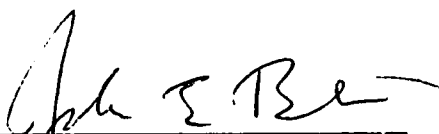
UNIVERSITY OF ALBERTA

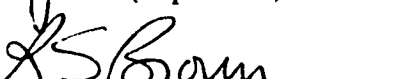
FACULTY OF GRADUATE STUDIES AND RESEARCH

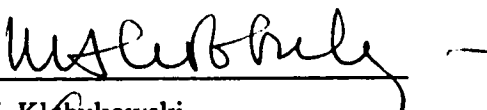
The undersigned certify that they have read, and recommend to the Faculty of Graduate Studies and Research for acceptance, a thesis entitled

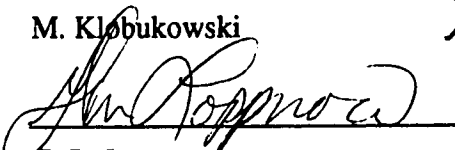
ABSOLUTE ABSORPTION INTENSITIES OF LIQUID METHANOL  
BY INFRARED SPECTROSCOPY


submitted by SHULIANG ZHANG in partial fulfillment of the requirements for the degree of DOCTOR OF PHILOSOPHY.


  
J. E. Bertie (Supervisor)

  
R. S. Brown

  
M. Klobukowski

  
G. R. Lopponow

  
F. L. Weichman

  
H. L. Strauss (External examiner)

September 23, 1994

To Shenxing and Fengye

## Abstract

This thesis describes the measurement of absolute infrared absorption intensities of liquids by attenuated total reflection (ATR) spectroscopy and transmission spectroscopy. ATR and transmission spectra have been all converted to refractive index spectra. The accuracy of the method that converts ATR spectra to refractive index spectra has been explored and significantly improved. In particular, the correct way to carry out the FFT-based Hilbert transform, an important step in the ATR method, has been found, with a consequent improvement in accuracy from 4% to 0.05%. The improved ATR method, and the transmission method of Jones *et al.*, have been used to obtain accurate intensity spectra of liquid methanol, CH<sub>3</sub>OH, and its isotopomers, CH<sub>3</sub>OD, CD<sub>3</sub>OH, and CD<sub>3</sub>OD, from ATR and transmission spectra recorded on a Bruker IFS 113 FT-IR instrument.

The refractive index spectra have been converted to the molar polarizability spectra under the Lorentz local field. It has been shown that the spectra of the molecular polarizability are the spectra that should be used to study the band shapes, and that the areas under bands in the spectrum of molar polarizability multiplied by wavenumber ( $\tilde{\nu}\alpha''_m$ ) are the most reliable source of the dipole changes of a molecule during its normal vibrations. The integrated intensities for all normal vibrations of CH<sub>3</sub>OH, CH<sub>3</sub>OD, CD<sub>3</sub>OH and CD<sub>3</sub>OD have been obtained as the areas under the  $\tilde{\nu}\alpha''_m$  bands. The separation of overlapping bands into the contributions from different normal vibrations has been done by comparing the spectra of different isotopomers. The separation has also been done by curve-fitting and the results have been compared. An accepted set of the integrated intensities was obtained by combining the two sets of data. The dipole moment derivatives with respect to symmetry coordinates have been obtained by fitting the calculated integrated intensities to the observed intensities. Dipole moment derivatives with respect to the symmetry coordinates and with respect to the internal coordinates have been obtained for all of the vibrations of methanol. This is believed to be the first time that these quantities have been determined for all vibrations of a molecule in the liquid.

## Acknowledgments

I would like to express my deepest appreciation to Dr. John Bertie for suggesting this project and for his guidance throughout the work and preparation of this thesis.

I have enjoyed working with the former and present members of Dr. Bertie's group with whom I have always had exciting and helpful discussions about science, politics, life, and everything else.

Thanks are also due to the staff of Spectral Services, Electronics, Glass-Blowing, and Machine Shops for their prompt and excellent services whenever needed.



# Table of Contents

Chapter 1	Introduction .....	1
1.1	Intensity Quantities .....	2
1.2	Methods of Obtaining Refractive Indices from ATR and Transmission Spectra .....	6
1.3	Measurements and Results for Methanol .....	10
1.4	Molecular Parameters and Discussion .....	12
1.5	References .....	14
Chapter 2	The Kramers-Krönig (KK) Transform, and its Approximation by the Finite Hilbert Transform via Fast Fourier Transforms .....	16
2.1	Introduction.....	16
2.2	General Methods.....	19
2.2.1	The Correct Spectra... ..	20
2.2.2	The Kramers-Krönig Transform.....	22
2.2.3	The Hilbert Transform .....	23
2.3	Results: Transforms from $k$ Spectrum to $n$ Spectrum for a Complete $k$ Spectrum.....	26
2.3.1	Kramers-Krönig Transforms .....	27
2.3.2	Hilbert Transforms.....	27
2.3.3	Summary .....	34
2.4	Results: Transform from $n$ Spectrum to $k$ Spectrum .....	35
2.5	Results: Transforms from $k$ Spectrum to $n$ Spectrum for a Truncated $k$ Spectrum .....	37
2.6	FFT Program Listing.....	38
2.7	References and Notes.....	42
Chapter 3	Accuracy of Current Methods of Obtaining Optical Constants from Multiple Attenuated Total Reflection (ATR) Measurements Using the CIRCLE Cell .....	45
3.1	Introduction.....	45
3.2	The Published Method .....	46
3.3	Recent Changes and the Present Method.....	48

3.3.1	General .....	48
3.3.2	Changes to the Calibration Procedure .....	49
3.3.3	Changes to Step 2, the Kramers-Krönig Transform of <i>k</i> Spectrum to <i>n</i> Spectrum.....	49
3.3.4	Changes to the Refinement Cycle.....	51
3.3.5	The Use of One Program to Permit Refinement under Computer Control.....	51
3.4	The Accuracy of the Current Programs .....	52
3.5	Reasons for Non-Convergence.....	58
3.6	Summary .....	58
3.7	References .....	59
Chapter 4	Accurate Determination of Molecular Band Intensities from Infrared Refractive Index and Dielectric Constant Spectra .....	60
4.1	Introduction.....	60
4.2	The CDHO Model for the Dielectric Constant.....	65
4.3	Methods .....	67
4.4	Results and Discussion.....	68
4.4.1	Synthetic Isolated CDHO Imaginary Polarizability Bands and Bands Calculated from Them .....	68
4.4.2	Recovery of the Intensity from Isolated Bands .....	72
4.4.3	Synthetic Double CDHO Imaginary Polarizability Bands and Bands Calculated from Them .....	76
4.4.4	Recovery of the Intensities from the Doublet Bands .....	79
4.4.5	Experimental Spectra.....	82
4.5	Conclusions .....	87
4.6	References .....	87
Chapter 5	Infrared Refractive Indices from 8000 to 2 cm <sup>-1</sup> , Absolute Integrated Intensities, and Dipole Moment Derivatives of Methanol (CH <sub>3</sub> OH) at 25°C.....	90
5.1	Introduction.....	90
5.2	Method.....	92
5.2.1	Attenuated Total Reflection Spectroscopy .....	92
5.2.2	Transmission Spectroscopy .....	94

5.3	Experimental.....	94
5.4	Results.....	97
5.5	Discussion .....	111
5.5.1	Refractive indices.....	111
5.5.2	Dipole Moment Derivatives .....	112
5.6	Appendix .....	120
5.7	References .....	123
Chapter 6	Infrared Refractive Indices from 8000 to 350 cm <sup>-1</sup> , Absolute Integrated Intensities, Transition Moments and Dipole Moment Derivatives of Methanol- <i>d</i> (CH <sub>3</sub> OD), at 25°C.....	125
6.1	Introduction.....	125
6.2	Discussion .....	139
6.4.1	The Integrated Intensities of the C-H, O-H and O-D Stretching Bands.....	140
6.4.2	The Integrated Intensities of the C-O Stretching Band.....	143
6.4.3	The Integrated Intensities of Other Bands .....	144
6.4.4	Transition Moments and Dipole Moment Derivatives.....	148
6.5	Summary .....	151
6.6	References .....	152
Chapter 7	Infrared Refractive Indices from 8000 to 350 cm <sup>-1</sup> , Absolute Integrated Absorption Intensities, Transition Moments and Dipole Moment Derivatives of Methan- <i>d</i> <sub>3</sub> -ol (CD <sub>3</sub> OH) and Methanol- <i>d</i> <sub>4</sub> (CD <sub>3</sub> OD), at 25°C.....	154
7.1	Introduction.....	154
7.2	Method and Experimental .....	155
7.3	Results.....	155
7.4	Integrated Intensities.....	172
7.4.1	The C-D, O-H and O-D Stretching Bands.....	172
7.4.2	The C-O-H in-Plane Bending Band.....	177
7.4.3	The Torsion Bands .....	178
7.4.4	The Remaining Bands .....	179
7.5	Transition Moments and Dipole Moment Derivatives .....	181

	7.6	Discussion .....	182
	7.7	References .....	185
	7.8	Note Added in Proof.....	187
Chapter 8		Integrated Absorption Intensities, Normal Coordinate Calculation, and Dipole Moment Derivatives of Molecules in Liquid Methanol .....	188
	8.1	Introduction.....	188
	8.2	Integrated Intensities.....	189
	8.2.1	Results from Isotopic Comparison .....	189
	8.2.2	Results from Curve-Fitting.....	197
	8.2.3	The Accepted Intensities .....	214
	8.3	Normal Coordinate Calculation .....	215
	8.3.1	The Geometry of the Molecules and the Definition of the Coordinates.....	215
	8.3.2	The G Matrices.....	216
	8.3.3	The Valence Force Constants.....	217
	8.3.4	The Observed and Harmonic Wavenumbers .....	222
	8.3.5	Results and Discussion.....	227
	8.4	Dipole Moment Derivatives .....	232
	8.5	Discussion .....	235
	8.6	References.....	241
Chapter 9		Conclusion .....	243

## List of Tables

Table 2.1	Parameters used for spectra calculated from the CDHO model.....	21
Table 3.1	Accuracy measures of our current program KREF for various spectra.....	53
Table 4.1	Properties of the single CDHO imaginary polarizability bands and bands calculated from them by phenomenological equations.....	69
Table 4.2	The percentage accuracy in the values of dipole moment derivatives recovered through area $C_j$ as a function of the integration range .....	73
Table 4.3	Percent error in the squared dipole moment derivatives resulting from using different values of dielectric constant.....	75
Table 4.4	Properties of the doublet CDHO imaginary polarizability bands and bands calculated from them by phenomenological equations.....	77
Table 4.5	Percent error in the recovered values of the squared dipole moment derivatives from fitting imaginary dielectric constant or absorption index spectrum for double bands.....	80
Table 4.6	Parameters of CDHO bands fitted to imaginary molar polarizability, imaginary dielectric constant and absorption index spectra of benzene, toluene and methanol, and dipole moment derivatives calculated from them .....	84
Table 5.1	Wavenumbers and refractive indices of $\text{CH}_3\text{OH}$ at the peaks in the $k$ spectrum, the associated maxima and minima in the $n$ spectrum, and regions of flat weak absorption.....	104
Table 5.2	Values of the absorption index or imaginary refractive index, between 8000 and $2\text{ cm}^{-1}$ for methanol, $\text{CH}_3\text{OH}$ , at $25^\circ\text{C}$ .....	106
Table 5.3	Values of the real refractive index, between 8000 and $2\text{ cm}^{-1}$ for methanol, $\text{CH}_3\text{OH}$ , at $25^\circ\text{C}$ .....	107
Table 5.4	The peak positions of major bands in various spectra of methanol, $\text{CH}_3\text{OH}$ .....	110
Table 5.5	Several measures of the integrated intensities of liquid methanol and the dipole moment derivatives with respect to the normal coordinates calculated from them.....	113
Table 5.6	The integrated area $C_j$ and the dipole moment derivatives calculated from it for different approximate separations of the contributions by different vibrations to the intensity .....	114
Table 5.7	Geometrical parameters of methanol.....	119

Table 6.1	The decadic linear absorption coefficients of methanol- <i>d</i> at the anchor points.....	130
Table 6.2	Wavenumbers and refractive indices of CH <sub>3</sub> OD at the peaks in the <i>k</i> spectrum, the associated maxima and minima in the <i>n</i> spectrum, and regions of flat weak absorption.....	134
Table 6.3	Values of <i>k</i> , the absorption index or imaginary refractive index, between 8000 and 350 cm <sup>-1</sup> for methanol- <i>d</i> at 25°C .....	135
Table 6.4	Values of <i>n</i> , the real refractive index, between 8000 and 350 cm <sup>-1</sup> for methanol- <i>d</i> at 25°C .....	136
Table 6.5	The peak positions of major bands in different representations of the absorption spectrum of methanol- <i>d</i> , CH <sub>3</sub> OD.....	138
Table 6.6	The integrated intensities of CH <sub>3</sub> OH and CH <sub>3</sub> OD.....	142
Table 6.7	Transition moments and dipole moment derivatives of CH <sub>3</sub> OH and CH <sub>3</sub> OD in the liquid phase.....	149
Table 7.1	The decadic linear absorption coefficients of methan- <i>d</i> <sub>3</sub> -ol and methanol- <i>d</i> <sub>4</sub> at the anchor points.....	158
Table 7.2	Wavenumbers and refractive indices of CD <sub>3</sub> OH and CD <sub>3</sub> OD at the peaks in the <i>k</i> spectrum, the associated maxima and minima in the <i>n</i> spectrum, and regions of flat weak absorption.....	165
Table 7.3	Values of the absorption index, between 8000 and 350 cm <sup>-1</sup> for methan- <i>d</i> <sub>3</sub> -ol at 25°C.....	167
Table 7.4	Values of the absorption index, between 8000 and 350 cm <sup>-1</sup> for methanol- <i>d</i> <sub>4</sub> at 25°C .....	168
Table 7.5	The peak positions and peak intensities of the major bands in different representations of the absorption spectra of CD <sub>3</sub> OH and CD <sub>3</sub> OD .....	169
Table 7.6	The integrated intensities of the C-H, C-D, O-H and O-D stretching bands of liquid methanol .....	174
Table 8.1	Integrated intensities of CH <sub>3</sub> OH .....	191
Table 8.2	Integrated intensities of CH <sub>3</sub> OD .....	192
Table 8.3	Integrated intensities of CD <sub>3</sub> OH .....	193
Table 8.4	Integrated intensities of CD <sub>3</sub> OD .....	194
Table 8.5	The parameters of the bands fitted to the α <sub>m</sub> spectrum of CH <sub>3</sub> OH.....	206
Table 8.6	The parameters of the bands fitted to the α <sub>m</sub> spectrum of CH <sub>3</sub> OD.....	207
Table 8.7	The parameters of the bands fitted to the α <sub>m</sub> spectrum of CD <sub>3</sub> OH.....	208
Table 8.8	The parameters of the bands fitted to the α <sub>m</sub> spectrum of CD <sub>3</sub> OD.....	209

Table 8.9	The definition of the internal and symmetry coordinates .....	217
Table 8.10	The values of $(G_s)_{i,j}$ for the methanol molecules .....	218
Table 8.11	The 37 initial non-zero force constants in internal coordinate space.....	220
Table 8.12	The 31 non-zero $F_{i,j}$ expressed in terms of the 37 $f_{i,j}$ of Table 8.11.....	221
Table 8.13	The non-zero $F_{i,j}$ from the $f_{i,j}$ in Table 8.11.....	222
Table 8.14	Comparison of the experimental and fitted wavenumbers .....	223
Table 8.15	The final force constants $F_{i,j}$ and $f_{i,j}$ in $\text{mdyn } \text{\AA}^{-1}$ .....	229
Table 8.16	The symmetrized eigenvectors $(l_s)_{i,j}$ .....	230
Table 8.17	Calculated and observed intensities as $ \partial\bar{\mu}/\partial Q_j ^2$ .....	232
Table 8.18	The fitted values of the x,y,z components of $\partial\bar{\mu}/\partial S_i$ .....	234
Table 8.19	The calculated values of $ \partial\bar{\mu}/\partial R $ in the x,y,z components .....	235
Table 8.20	Comparison of the values of $ \partial\bar{\mu}/\partial S_i $ obtained in this work and obtained by an ab initio calculation .....	240

## List of Figures

Figure 2.1	Refractive index spectra of single band calculated with the classical damped harmonic oscillator model.....	22
Figure 2.2	Refractive index spectra of liquid methanol calculated with the classical damped harmonic oscillator model .....	23
Figure 2.3	Refractive index spectra of liquid acetic acid calculated with the classical damped harmonic oscillator model .....	24
Figure 2.4	Schematic representation of the FFT subroutine used in this work .....	25
Figure 2.5	Percent deviations from the correct $n$ spectra calculated by KK transformation of $k$ spectra .....	26
Figure 2.6	Schematic representation of the input arrays to step 2 of the Hilbert transform algorithms.....	28
Figure 2.7	Results for our original Hilbert transform algorithm applied to a single band spectrum .....	29
Figure 2.8	Results for our original Hilbert transform algorithm compared with K-K transform applied to the simulated methanol spectrum.....	30
Figure 2.9	Results for Marshall's Hilbert transform algorithm applied to the simulated methanol spectrum .....	31
Figure 2.10	Results for new Hilbert algorithms applied to the simulated methanol spectrum .....	33
Figure 2.11	Results of Kramers-Krönig and Hilbert transforms from $n$ spectrum to $k$ spectrum.....	36
Figure 2.12	$k$ to $n$ transform of a truncated $k$ spectrum .....	38
Figure 3.1	The essential features of the CIRCLE cell.....	46
Figure 3.2	Spectra for the single Lorentzian band with FWHH = 6 cm <sup>-1</sup> and $k_{\max} = 0.1$ .....	54
Figure 3.3	Spectra for the single Lorentzian band with FWHH = 6 cm <sup>-1</sup> and $k_{\max} = 0.6$ .....	55
Figure 3.4	Spectra for simulated acetic acid.....	56
Figure 3.5	Spectra for simulated methanol.....	57
Figure 4.1	Bands SA, SB and SC of Table 4.1 plotted as different intensity quantities.....	70
Figure 4.2	Bands SE, SF and SG of Table 4.1 plotted as different intensity quantities.....	71



Figure 4.3	The percent recovery of the integrated intensity plotted against the integration range divided by FWHH.....	73
Figure 4.4	The real dielectric constant spectra for bands SA to SG .....	75
Figure 4.5	The synthetic double bands DE, DF, DA and DB of Tables 4.4 and 4.5.....	78
Figure 4.6	Comparison of the imaginary dielectric constant spectrum calculated from the synthetic doublet imaginary molar polarizability spectrum with the 'sum of singles' .....	79
Figure 4.7	Absorption and permittivity spectra of the 1500 cm <sup>-1</sup> region of the spectrum of liquid benzene .....	83
Figure 4.8	Absorption and permittivity spectra of the 700 cm <sup>-1</sup> region of the spectrum of liquid toluene.....	85
Figure 4.9	Absorption and permittivity spectra of the 1050 cm <sup>-1</sup> region of the spectrum of liquid methanol.....	86
Figure 5.1	pATR spectra of methanol recorded with KRS-5 and ZnSe ATR rods.....	96
Figure 5.2	Experimental absorbance spectra of liquid methanol in cells with CaF <sub>2</sub> windows and pathlengths 250 and 1100 μm .....	97
Figure 5.3	Eight absorption index spectra calculated from pATR spectra recorded by different workers .....	98
Figure 5.4	Three absorption index spectra of the C-O stretching band .....	99
Figure 5.5	The average absorption index spectrum from CIRCLE cell pATR measurements with a ZnSe rod above ~830 cm <sup>-1</sup> and a KRS-5 rod below 830 cm <sup>-1</sup> , and the spectrum reported by Honijk <i>et al.</i> for the region below 350 cm <sup>-1</sup> .....	100
Figure 5.6	The absorption index spectrum deduced from the pATR measurements and Honijk <i>et al.</i> 's spectrum, and two (coincident) <i>k</i> spectra from transmission spectra .....	101
Figure 5.7	The absorption index spectrum of methanol at 25°C .....	102
Figure 5.8	The real refractive index spectrum of methanol at 25°C .....	103
Figure 5.9	The molar absorption coefficient spectrum of methanol at 25°C.....	108
Figure 5.10	The molar conductivity spectrum of methanol at 25°C .....	109
Figure 5.11	The imaginary molar polarizability spectrum of methanol at 25°C .....	110
Figure 5.12	The spectrum of the imaginary polarizability multiplied by wavenumber in the O-H and C-H stretching region. The approximate methods used to separate the observed absorption into contributions from different vibrations .....	116

Figure 5.13	The O-H and C-H stretching regions of the imaginary molar polarizability spectrum. The result from curve-fitting. ....	117
Figure 6.1	pATR spectra of methanol- <i>d</i> recorded with KRS-5 and ZnSe ATR rods.....	127
Figure 6.2	Experimental absorbance spectra of liquid methanol- <i>d</i> in cells with CaF <sub>2</sub> windows and pathlengths 470 and 1200 $\mu\text{m}$ .....	128
Figure 6.3	Absorption index spectra of CH <sub>3</sub> OD calculated from cell pATR spectra.....	129
Figure 6.4	The absorption index spectrum deduced from ATR spectra, and the <i>k</i> spectrum from transmission spectra.....	131
Figure 6.5	The final absorption index spectrum of methanol- <i>d</i> at 25°C .....	132
Figure 6.6	The real refractive index spectrum of methanol- <i>d</i> at 25°C .....	133
Figure 6.7	The molar absorption coefficient spectrum of methanol- <i>d</i> at 25°C.....	138
Figure 6.8	The imaginary molar polarizability spectrum of methanol- <i>d</i> at 25°C.....	139
Figure 6.9	The spectra of imaginary polarizability multiplied by wavenumber for CH <sub>3</sub> OD and CH <sub>3</sub> OH in the regions of the O-H, C-H and O-D stretching vibrations .....	141
Figure 6.10	The spectra of imaginary polarizability multiplied by wavenumber for CH <sub>3</sub> OD and CH <sub>3</sub> OH in the regions of the C-O stretching vibration.....	143
Figure 6.11	The spectra of imaginary polarizability multiplied by wavenumber for CH <sub>3</sub> OD and CH <sub>3</sub> OH below 2000 $\text{cm}^{-1}$ .....	145
Figure 6.12	The difference spectra of imaginary polarizability multiplied by wavenumber for CH <sub>3</sub> OD and CH <sub>3</sub> OH in the regions of the C-O stretching vibration.....	147
Figure 7.1	pATR spectra of methan- <i>d</i> <sub>3</sub> -ol (top box) and methanol- <i>d</i> <sub>4</sub> (bottom box) recorded with KRS-5 (upper curves) and ZnSe (lower curves) ATR rods .....	156
Figure 7.2	Experimental absorbance spectra of liquid CD <sub>3</sub> OH and CD <sub>3</sub> OD in cells with CaF <sub>2</sub> windows.....	157
Figure 7.3A	The superimposed absorption index spectra of CD <sub>3</sub> OH, calculated from ATR spectra and from transmission spectra.....	159
Figure 7.3B	The superimposed absorption index spectra of CD <sub>3</sub> OD, calculated from ATR spectra and from transmission spectra.....	160
Figure 7.4A	The absorption index spectrum of methan- <i>d</i> <sub>3</sub> -ol at 25°C .....	162
Figure 7.4B	The absorption index spectrum of methanol- <i>d</i> <sub>4</sub> at 25°C.....	163

Figure 7.5A	The real refractive index spectrum of methan- $d_3$ -ol at 25°C .....	164
Figure 7.5B	The real refractive index spectrum of methanol- $d_4$ at 25°C.....	165
Figure 7.6A	The imaginary molar polarizability spectra of methan- $d_3$ -ol at 25°C .....	170
Figure 7.6B	The imaginary molar polarizability spectra of methanol- $d_4$ at 25°C.....	171
Figure 7.7	The spectra of the imaginary polarizability multiplied by wavenumber for $CD_3OH$ and $CD_3OD$ in the regions of the O-H, O-D and C-H stretching vibrations .....	173
Figure 7.8	The spectra of the imaginary polarizability multiplied by wavenumber for $CH_3OH$ and $CD_3OH$ (top box) and $CH_3OD$ and $CD_3OD$ (bottom box) in the O-H, O-D, C-H and C-D stretching region.....	175
Figure 7.9	The spectra of the imaginary polarizability multiplied by wavenumber for $CD_3OH$ and $CD_3OD$ in the region of the C-O-H in-plane bending band .....	177
Figure 7.10	The spectra of the imaginary polarizability multiplied by wavenumber for $CD_3OD$ and $CD_3OH$ below $1770\text{ cm}^{-1}$ .....	179
Figure 7.11	The spectra of the imaginary polarizability multiplied by wavenumber for $CH_3OH$ and $CD_3OH$ (top box) and $CH_3OD$ and $CD_3OD$ (bottom box) between $1700$ and $350\text{ cm}^{-1}$ .....	180
Figure 8.1	The $\tilde{\nu}\alpha_m''$ spectra of methanol in the OH and CH stretching regions .....	195
Figure 8.2	The $\tilde{\nu}\alpha_m''$ spectra of methanol between $1600$ and $400\text{ cm}^{-1}$ .....	196
Figure 8.3A	Curve-fitting: the spectrum of $CH_3OH$ from $3800$ to $2000\text{ cm}^{-1}$ .....	198
Figure 8.3B	Curve-fitting: the spectrum of $CH_3OH$ from $1750$ to $400\text{ cm}^{-1}$ .....	199
Figure 8.4A	Curve-fitting: the spectrum of $CH_3OD$ from $3100$ to $1750\text{ cm}^{-1}$ .....	200
Figure 8.4B	Curve-fitting: the spectrum of $CH_3OD$ from $1650$ to $375\text{ cm}^{-1}$ .....	201
Figure 8.5A	Curve-fitting: the spectrum of $CD_3OH$ from $3800$ to $1900\text{ cm}^{-1}$ .....	202
Figure 8.5B	Curve-fitting: the spectrum of $CD_3OH$ from $1750$ to $400\text{ cm}^{-1}$ .....	203
Figure 8.6A	Curve-fitting: the spectrum of $CD_3OD$ from $2800$ to $1600\text{ cm}^{-1}$ .....	204
Figure 8.6B	Curve-fitting: the spectrum of $CD_3OD$ from $1350$ to $375\text{ cm}^{-1}$ .....	205
Figure 8.7	The molecular model for $CX_3OY$ .....	215
Figure 8.8	The energy splitting of the stretching vibrations of a $C_3v\text{ CX}_3$ group .....	226

## List of Symbols

### *General*

- $\lambda$  Vacuum wavelength.
- $\tilde{\nu}$  Vacuum wavenumber; usual unit  $\text{cm}^{-1}$ .  $\tilde{\nu} = 1/\lambda$ .
- $c$  Speed of light in vacuum.
- $C$  Molar concentration; usual unit  $\text{mole L}^{-1}$ .
- $V_m$  Molar volume; usual unit  $\text{cm}^3 \text{mole}^{-1}$ .
- $\wedge$  used to indicate a complex quantity.
- $i = \sqrt{-1}$

### *Wavenumber dependent Quantities*

- $\hat{n}(\tilde{\nu})$  Complex refractive index,  $\hat{n}(\tilde{\nu}) = n(\tilde{\nu}) + i k(\tilde{\nu})$
- $n(\tilde{\nu})$  Real refractive index.
- $k(\tilde{\nu})$  Imaginary refractive index, also called the absorption index.
- $\hat{\epsilon}(\tilde{\nu})$  Complex dielectric constant,  $\hat{\epsilon}(\tilde{\nu}) = \epsilon'(\tilde{\nu}) + i \epsilon''(\tilde{\nu})$ .
- $\epsilon'(\tilde{\nu})$  Real dielectric constant, usually called the dielectric constant.
- $\epsilon''(\tilde{\nu})$  Imaginary dielectric constant, also called the dielectric loss.
- $\hat{\alpha}_m(\tilde{\nu})$  Complex molar polarizability,  $\hat{\alpha}_m(\tilde{\nu}) = \alpha'_m(\tilde{\nu}) + i \alpha''_m(\tilde{\nu})$ ;  
usual unit  $\text{cm}^3 \text{mole}^{-1}$ .
- $\alpha'_m(\tilde{\nu})$  Real molar polarizability.
- $\alpha''_m(\tilde{\nu})$  Imaginary molar polarizability.
- $E_m(\tilde{\nu})$  (Decadic) molar absorption coefficient;  
usual unit  $\text{cm}^2 \text{mole}^{-1} = 10^{-3} \text{L cm}^{-1} \text{mole}^{-1}$ .
- $K(\tilde{\nu})$  (Decadic) linear absorption coefficient; usual unit  $\text{cm}^{-1}$ .

### *Integrated Intensity Quantities*

- $A_j$  Area under band  $j$  in  $2.303E_m$  spectrum; usual unit  $\text{km mole}^{-1}$ .
- $B_j$  Area under band  $j$  in the  $V_m \tilde{\nu} \epsilon''$  spectrum divided by the Lorentz local field correction; usual unit  $\text{km mole}^{-1}$ .
- $C_j$  Area under band  $j$  in  $\tilde{\nu} \alpha_m''$  spectrum; usual unit  $\text{km mole}^{-1}$ .

### *Molecular Properties*

- $\vec{\mu}$  Dipole moment of a molecule
- $\mu_j$  Magnitude of dipole moment derivative with respect to normal coordinate  $j$ ; usual unit Debye  $\text{\AA}^{-1} \text{amu}^{-1/2}$ .
- $\vec{R}_j$  Dipole transition moment,  $\langle f | \vec{\mu} | i \rangle_j$ , of the transitions that cause band  $j$ ; usual unit Debye.

These spectra were transformed initially to spectra of the real and imaginary parts of the complex refractive index,

$$\hat{n}(\tilde{\nu}) = n(\tilde{\nu}) + i k(\tilde{\nu}) \quad (1.3)$$

where  $n(\tilde{\nu})$  is the real refractive index and  $k(\tilde{\nu})$  is the imaginary refractive index.  $n(\tilde{\nu})$  and  $k(\tilde{\nu})$  are collectively called the optical constants.  $k(\tilde{\nu})$  is also called the absorption coefficient.  $k(\tilde{\nu})$  is the major determinant of both the multiple ATR spectra and the transmission spectra measured in this work.  $n(\tilde{\nu})$  plays a secondary role in these spectra.

The intensity quantities in common use are calculated from the refractive indices. The first quantity is the complex dielectric constant,

$$\hat{\epsilon}(\tilde{\nu}) = \epsilon'(\tilde{\nu}) + i \epsilon''(\tilde{\nu}) \quad (1.4)$$

related to the refractive index, by Maxwell's relation<sup>14</sup>

$$\hat{\epsilon}(\tilde{\nu}) = \hat{n}^2(\tilde{\nu}) \quad (1.5)$$

where the real and imaginary dielectric constants are calculated by

$$\epsilon'(\tilde{\nu}) = n^2(\tilde{\nu}) - k^2(\tilde{\nu}) \quad (1.5a)$$

$$\epsilon''(\tilde{\nu}) = 2n(\tilde{\nu})k(\tilde{\nu}) \quad (1.5b)$$

The real dielectric constant is regarded by physicists as the most important physical descriptor of the vibrations of condensed phases.

Another quantity, important to chemists, is the molar absorption coefficient,  $E_m(\tilde{\nu})$  (the recommended IUPAC symbol<sup>15</sup> for this quantity,  $\epsilon(\tilde{\nu})$ , is not used in the thesis to avoid confusion with the dielectric constant.)

## 1.1 Intensity Quantities

The spectra recorded in this work were pATR spectra defined<sup>8</sup> as

$$\text{pATR}(\tilde{\nu}) = -\log_{10} \frac{I_{\text{ATR}}(\tilde{\nu})}{I_0(\tilde{\nu})} \quad (1.1)$$

and experimental absorbance spectra defined<sup>11</sup> as

$$\text{EA}(\tilde{\nu}) = -\log_{10} \frac{I_t(\tilde{\nu})}{I_0(\tilde{\nu})} \quad (1.2)$$

Here  $I_{\text{ATR}}$  is the intensity after attenuated total reflection by the sample,  $I_0$  is the incident intensity and  $I_t$  is the intensity after transmission by the cell and sample.

These spectra were transformed initially to spectra of the real and imaginary parts of the complex refractive index,

$$\hat{n}(\tilde{\nu}) = n(\tilde{\nu}) + i k(\tilde{\nu}) \quad (1.3)$$

where  $n(\tilde{\nu})$  is the real refractive index and  $k(\tilde{\nu})$  is the imaginary refractive index.  $n(\tilde{\nu})$  and  $k(\tilde{\nu})$  are collectively called the optical constants.  $k(\tilde{\nu})$  is also called the absorption index, and is the major determinant of both the multiple ATR spectra and the transmission spectra measured in this work.  $n(\tilde{\nu})$  plays a secondary role in these spectra.

Other intensity quantities in common use are calculated from the refractive indices. One such quantity is the complex dielectric constant,

$$\hat{\epsilon}(\tilde{\nu}) = \epsilon'(\tilde{\nu}) + i \epsilon''(\tilde{\nu}) \quad (1.4)$$

which is related to the refractive index, by Maxwell's relation<sup>14</sup>

$$\hat{\epsilon}(\tilde{\nu}) = \hat{n}^2(\tilde{\nu}) \quad (1.5)$$

Thus, the real and imaginary dielectric constants are calculated by

$$\epsilon'(\tilde{\nu}) = n^2(\tilde{\nu}) - k^2(\tilde{\nu}) \quad (1.5a)$$

and

$$\epsilon''(\tilde{\nu}) = 2n(\tilde{\nu})k(\tilde{\nu}) \quad (1.5b)$$

The complex dielectric constant is regarded by physicists as the most important phenomenological descriptor of the vibrations of condensed phases.

A second quantity, important to chemists, is the molar absorption coefficient,  $E_m(\tilde{\nu})$  (The accepted IUPAC symbol<sup>15</sup> for this quantity,  $\epsilon(\tilde{\nu})$ , is not used in the thesis to avoid confusion with the dielectric constant.)

$$E_m(\tilde{\nu}) = \frac{1}{Cd} A_{10}(\tilde{\nu}) = \frac{4\pi\tilde{\nu}k(\tilde{\nu})}{2.303C} \quad (1.6)$$

Here  $C$  is the molar concentration,  $d$  is the pathlength, and  $A_{10}(\tilde{\nu})$  is the absorbance. The absorbance is defined<sup>15</sup> by

$$A_{10}(\tilde{\nu}) = -\log_{10} \frac{I_t(\tilde{\nu})}{I_0(\tilde{\nu})} \quad (1.7)$$

where  $I_t$  and  $I_0$  differ solely by the absorption of radiation by the sample, and losses due to the windows and reflection effects have been removed. These window and reflection effects are the primary sources of the difference between the experimental absorbance  $EA$  in eq. (1.2) and the absorbance  $A_{10}$  in eq. (1.7).

A third intensity quantity is the linear (decadic) absorption coefficient,

$$K(\tilde{\nu}) = \frac{1}{d} A_{10}(\tilde{\nu}) = \frac{4\pi\tilde{\nu}k(\tilde{\nu})}{2.303} \quad (1.8)$$

which is related to  $E_m(\tilde{\nu})$  by

$$E_m(\tilde{\nu}) = K(\tilde{\nu})/C \quad (1.9)$$

All of the above are macroscopic properties of the liquid. Clearly they are all related, and if either  $\hat{n}(\tilde{\nu})$  or  $\hat{\epsilon}(\tilde{\nu})$  is known, all of the remaining quantities can be calculated. What is less clear is that the real and imaginary quantities are also related. The relations are the well-known Kramers-Krönig (KK) transformations. These are defined by equations

$$n(\tilde{\nu}_i) - 1 = \frac{2}{\pi} P \int_0^\infty \frac{\tilde{\nu} k(\tilde{\nu})}{\tilde{\nu}^2 - \tilde{\nu}_i^2} d\tilde{\nu} \quad (1.10a)$$

$$k(\tilde{\nu}_i) = -\frac{2\tilde{\nu}_i}{\pi} P \int_0^\infty \frac{n(\tilde{\nu}) - 1}{\tilde{\nu}^2 - \tilde{\nu}_i^2} d\tilde{\nu} \quad (1.10b)$$

and

$$\epsilon'(\tilde{\nu}_i) - 1 = \frac{2}{\pi} P \int_0^\infty \frac{\tilde{\nu} \epsilon''(\tilde{\nu})}{\tilde{\nu}^2 - \tilde{\nu}_i^2} d\tilde{\nu} \quad (1.11a)$$

$$\epsilon''(\tilde{\nu}_i) = -\frac{2\tilde{\nu}_i}{\pi} P \int_0^\infty \frac{\epsilon'(\tilde{\nu}) - 1}{\tilde{\nu}^2 - \tilde{\nu}_i^2} d\tilde{\nu} \quad (1.11b)$$

In these equations, the  $P$  indicates that the principal value of the integral should be taken. It has been shown<sup>16</sup> that there are many different approximations that can be used to find the principal value.



The result of the above equations is that if any one of  $k(\tilde{\nu})$ ,  $n(\tilde{\nu})$ ,  $\epsilon''(\tilde{\nu})$  and  $\epsilon'(\tilde{\nu})$  is known from 0 to  $\infty \text{ cm}^{-1}$ , all other macroscopic properties can be calculated from it.

The Kramers-Krönig transform defined by eq. (1.10a) is involved in the procedure that converts the recorded pATR spectra into the refractive index spectra. It requires that  $k(\tilde{\nu})$  be known over the complete wavenumber interval  $(0, \infty)$ , in order to determine  $n(\tilde{\nu})$ . In reality, a spectrum is always measured over a limited wavenumber range. Therefore, a finite integral must be taken and eq. (1.10a) is modified to

$$n(\tilde{\nu}_i) - n(\tilde{\nu}_{\max}) = \frac{2}{\pi} P \int_{\tilde{\nu}_{\min}}^{\tilde{\nu}_{\max}} \frac{\tilde{\nu} k(\tilde{\nu})}{\tilde{\nu}^2 - \tilde{\nu}_i^2} d\tilde{\nu} \quad (1.12)$$

where  $\tilde{\nu}_{\max}$  and  $\tilde{\nu}_{\min}$  are the high and low wavenumber limits of the measured spectrum.  $\tilde{\nu}_{\max}$  is taken well above the significant absorption in the infrared region and well below significant absorption in the UV and visible region. It is  $8000 \text{ cm}^{-1}$  in this work.

One of the objectives of this work was to measure absorption intensities of liquids that are accurate to a few percent. Most previous studies of liquid intensities have had lower accuracy because of the limitations of the available instruments. This has meant that the procedures used to convert the recorded spectra to optical constant spectra did not have to be very accurate, and in some cases, have proved to be insufficiently accurate for the measurements made in this work. Consequently, a good deal of time has been spent in this study to explore the accuracy of the procedures. This work is described in the first part of this thesis, Chapters 2 and 3.

The properties of liquids discussed above are macroscopic properties of the liquids. To obtain properties of the molecule, a model must be assumed for the local field,  $\mathbf{E}'$ . The local field is also called the effective field and is the field that acts on an individual molecule in the liquid. Such a model takes the form of a relation between the local field,  $\mathbf{E}'$ , and the macroscopically applied electric field,  $\mathbf{E}$ . The most simple and generally used local field is the Lorentz local field.

In this model of the local field<sup>14,17,18</sup>, a particular molecule in the liquid is imagined to be surrounded by a small sphere whose radius is nevertheless large compared with the molecular length. The effects on the central molecule produced by the matter outside and inside this sphere are considered separately. The molecular structure is neglected in determining the effect of the matter outside the sphere. It is then assumed that the polarization  $\mathbf{P}$  produced outside the sphere by the externally-applied field is constant. Inside the sphere, it can be shown for a number of important special cases, including that

of random distribution, that molecules inside the sphere do not produce a resulting field at the central molecule. Hence the molecule can be regarded as being situated in a spherical region, inside which there is vacuum and outside which there is a homogeneously polarized medium. This yields<sup>14</sup> the result that the extra field produced by other molecules on the central molecule is  $\frac{4\pi}{3} \mathbf{P}$ . Thus, the Lorentz local field is

$$\mathbf{E}' = \mathbf{E} + \frac{4\pi}{3} \mathbf{P} \quad (1.13)$$

This model is valid for strictly isotropic media. Liquids are isotropic macroscopically but not over molecular dimensions. The Lorentz local field is used in this work because of the absence of a superior simple model.

The molecular polarizability is defined by the relation

$$\mathbf{p} = \hat{\alpha} \mathbf{E}' \quad (1.14)$$

where  $\mathbf{p}$  is the dipole moment induced in the molecule by the field,  $\mathbf{E}'$ , acting on the molecule. If there are  $N$  molecules in unit volume of the liquid and  $\hat{\alpha}$  is the mean molecular polarizability, the total dipole moment  $\mathbf{P}$  induced in unit volume is

$$\mathbf{P} = N\mathbf{p} = N\hat{\alpha} \mathbf{E}' \quad (1.14a)$$

From eqs. (1.13) and (1.14a), Lorentz and Lorenz derived an equation between the mean polarizability and the dielectric constant,

$$\frac{\hat{\epsilon} - 1}{\hat{\epsilon} + 2} = \frac{4}{3} \pi N \hat{\alpha} \quad (1.15)$$

which is now called the Lorentz-Lorenz formula<sup>14</sup>. In this thesis, the complex molar polarizability,  $\hat{\alpha}_m = N_s \hat{\alpha}$ , is calculated from  $\hat{\epsilon}$  through eq. (1.15).

From the molar polarizability spectrum,  $\hat{\alpha}_m(\tilde{\nu})$ , other molecular properties can be calculated. These properties are the integrated intensities of the transition, the transition moment, and for fundamental transitions, the dipole moment derivative with respect to the normal coordinate and with respect to the internal (symmetry) coordinates.

These molecular properties have been related theoretically to the areas under bands in the spectra of  $\tilde{\nu}k$ ,  $\tilde{\nu}\epsilon''$  and  $\tilde{\nu}\alpha_m''$ , but with different levels of approximations in each case. Thus, the second objective of this work was to explore the accuracy of the methods to obtain the molecular properties through these relations. This work is described in Chapter 4.

The methods explained in Chapters 2 to 4 are used in the remainder of the thesis. The intensity spectra of methanol and its isotopomers,  $\text{CH}_3\text{OD}$ ,  $\text{CD}_3\text{OH}$  and  $\text{CD}_3\text{OD}$ , were measured and are reported in Chapters 5 to 7. The area under each spectrum was separated into contributions from different vibrations by comparing the spectra of the different isotopomers. The transition moments were calculated and the dipole moment derivatives with respect to the normal coordinates were also calculated. The dipole moment derivatives with respect to certain internal coordinates were estimated.

The overall objective of this work was to see how much molecular information can be extracted from the intensity spectra that are accurate to a few percent and how accurately this information can be obtained. To address this, the results of Chapters 5 to 7 are summarized in Chapter 8 and used in a normal coordinate and intensity calculation.

In the remaining sections of this chapter, a more detailed introduction is given to each part of the thesis. Section 1.2 covers Chapters 2 to 4 in which the methods of obtaining refractive indices and relating the integrated intensities to the dipole moment derivatives with respect normal coordinates are discussed. In Section 1.3, the measurements and results of the absorption intensities of liquid methanol and its isotopomers presented in Chapters 5 to 7 are introduced. Section 1.4 introduces Chapter 8 in which the results of separating the areas under the spectral bands are summarized, a normal coordinate calculation of all four molecules is given, and the dipole moment derivatives are obtained by fitting the calculated integrated intensities to the observed intensities.

## **1.2 Methods of Obtaining Refractive Indices from ATR and Transmission Spectra**

The multiple ATR spectra are converted to the complex refractive index spectra by an iterative procedure<sup>6-9</sup>. The transmission method, described in the literature<sup>10,11</sup>, uses a similar iterative procedure and is used to determine the intensities in weakly absorbing regions.

In the ATR method, first described<sup>8</sup> in 1985 and with further details<sup>9</sup> in 1988, one of the essential steps is the Kramers-Krönig (KK) transform of eq. (1.12) from the imaginary refractive index spectrum to the real refractive index spectrum. The numerical integral in eq. (1.12) was programmed to carry out the KK transform. McLaurin's formula was used to find the principal value of the integral. The KK transform using this formula has been

shown<sup>16</sup> to give the best accuracy, about 0.05%. This transform through eq. (1.12) is very slow on a personal computer for a typical spectrum of about 8K data points. This was particularly true at the start of this work before the recent rapid development of computation speed.

It is well-known<sup>19-24</sup> that the infinite KK transform in eq. (1.10a) is equivalent to the infinite Hilbert transform, which is equivalent to the allied Fourier integrals. The Hilbert transform can, thus, be implemented with fast Fourier transform (FFT) routines. Such implementation<sup>7</sup> is usually some 60 times faster than the KK transform for a data file containing about 8K points. Further, the time required for the FFT-based Hilbert transform is proportional to the number of data points, and that for the KK transform of eq. (1.12) is proportional almost to the *square* of the number of the data points.

Thus, the Hilbert transform implemented with FFT routines is an attractive alternative to the KK transform of eq. (1.12). In practice, several different algorithms have implemented the FFT routines in the Hilbert transform. Some algorithms in the literature<sup>25</sup> and the algorithm previously used in this laboratory were found to yield only about 4% accuracy. At about the time that the author discovered these inaccuracies empirically as discrepancies between the FFT-based Hilbert and KK transforms, Bracewell<sup>26</sup> reported that discrepancies are to be expected for the finite transforms, but gave no details of their magnitudes. Thus, the appealing very fast method of the Hilbert transform gave results that were in considerable error, while the slow KK transform gave correct answers. It was clearly worthwhile to explore whether the accuracy of the fast Hilbert transform method could be improved. In Chapter 2, the magnitudes of the discrepancies are explored and an algorithm that yields satisfactory accuracy is presented.

Different literature algorithms for the Hilbert transform are also explored in Chapter 2 to determine the important factors for accuracy. It was found for transformations between  $n(\tilde{\nu})$  and  $k(\tilde{\nu})$  that the FFT-based Hilbert transform can be much less accurate than the KK transform, or can be as accurate as the KK transform, depending on the algorithm used<sup>7,27</sup>. The satisfactory FFT-based Hilbert transform algorithm that was programmed and used in this work is called the BZ algorithm. It is presented and gives the same accuracy as the KK transform through eq. (1.12) which uses McLaurin's formula, namely about 0.05%.

It is frequently the case that the  $k$  spectrum is truncated at low wavenumber. Significant absorption exists below the lowest wavenumber in the spectrum and neither the KK nor the FFT-based Hilbert transform can give correct values of  $n(\tilde{\nu})$ . The size of the

error depends on the actual spectrum below the cutoff. A simple method is presented in Chapter 2 which improves by a factor of about 10 the accuracy at low wavenumber of the  $n$  spectrum obtained by Hilbert or KK transform of the  $k$  spectrum.

The KK and Hilbert transforms from  $n(\tilde{\nu})$  to  $k(\tilde{\nu})$  are also discussed in Chapter 2, although they are not used later in the thesis. Both were found to be less accurate than the  $k(\tilde{\nu})$  to  $n(\tilde{\nu})$  transform.

The improvements made to the original method<sup>8,9</sup> for obtaining optical constants of liquids from multiple attenuated total reflection measurements using the CIRCLE<sup>\*</sup> cell are described in Chapter 3. In this method, an experimental pATR spectrum is converted to the optical constant spectra by the following steps. First, the pATR spectrum is used to obtain an approximate  $k$  spectrum. Second, an approximate  $n$  spectrum is calculated from the approximate  $k$  spectrum by the KK or Hilbert transform. In this step,  $n(\tilde{\nu}_{\max})$  in eq. (1.12), often called  $n_{\infty}$ , is needed and is calculated<sup>9</sup> from the wavenumber dependence of the real refractive index in the visible region of the spectrum.

In the third step, a pATR spectrum is calculated from the approximate  $k(\tilde{\nu})$  and  $n(\tilde{\nu})$  by using Fresnel's equations<sup>14</sup>. This calculated pATR spectrum is then compared with the experimental spectrum and their ratio is used to adjust the approximate  $k(\tilde{\nu})$ . Steps 2 and 3 are repeated until both  $k(\tilde{\nu})$  and  $n(\tilde{\nu})$  have converged and the experimental spectrum is well fitted.

In the third step above, the number of times that light reflects at the interface of the ATR rod and the liquid must be known. This is achieved by fitting<sup>8,9</sup> the pATR spectrum of pure liquid benzene to the known refractive indices<sup>13</sup> of benzene. The number of reflections so obtained certainly includes more factors than the physical number of reflections. It is, therefore, called the effective number of reflections (NRFs) and this procedure of finding NRF is called the calibration of the CIRCLE cell.

The improvements of the ATR method described in Chapter 3 include the following. The inaccurate Hilbert transform was replaced by the KK transform with McLaurin's formula and by the FFT-based Hilbert transform with the BZ algorithm. The programs that convert the multiple ATR spectra into the complex refractive index spectra were combined into one program that allows the refinement under computer control. The calibration procedure was changed. The effective number of reflections is now determined<sup>6</sup> by using the areas under bands of benzene, instead of using the peak heights

---

\* CIRCLE is a registered trademark of Spectra-Tech Inc., Stamford, CT.

in the previous calibration procedure. This new calibration with areas is less susceptible to baseline errors than was the previous method with peak heights, and the values of NRF determined from several different spectra agreed to about 1%, which permits 1% accuracy in the obtained optical constants. Also, the overall accuracy of the computations is explored in this chapter, by analyzing multiple ATR spectra which were themselves calculated from known  $k$  spectra and the corresponding known  $n$  spectra. The optical constants were recovered from the ATR spectra and compared with the known originals.

The real and imaginary refractive spectra obtained from the multiple ATR and transmission spectra can be used<sup>1,4,5</sup> to calculate other optical properties of the liquids and, under a certain physical model, properties of the molecules in the liquids. In Chapter 4, several different absorption quantities such as the imaginary dielectric constant and the molar absorption coefficient are calculated from the refractive indices. With the assumption of the Lorentz local model, the spectra of the complex molar polarizability,  $\hat{\alpha}_m(\tilde{\nu})$ , were calculated by eq. (1.19). Similar to the spectra of  $k$ ,  $\epsilon''$ , and  $E_m$ , the imaginary part of the molar polarizability,  $\alpha_m''(\tilde{\nu})$ , also describes the absorption spectrum. The line shapes and peak positions in these different absorption spectra differ in a way that seems not to be fully recognized. Vibrational intensities of the molecules in the liquid can be calculated from any of these spectra as the magnitudes of the transition moments or the dipole moment derivatives with respect to the normal coordinates, always under an assumption about the local field but also under other approximations for the  $E_m$ ,  $k$  and  $\epsilon''$  spectra. These intensities can also be calculated, under the same approximations as for the  $\epsilon''$  spectra, from the peak wavenumbers in the  $\epsilon''$  and  $\alpha_m''$  spectra.

Also in Chapter 4, the differences between the line shapes and peak positions in the different spectra are discussed, and the accuracy of the vibrational intensities calculated from different spectra is explored. Both experimental spectra and spectra calculated from the classical damped harmonic oscillator (CDHO) model were used in the exploration. The results show that the  $\alpha_m''$  spectrum most reliably gives the molecular properties, but it does impose the Lorentz local field model on the experimental spectrum. Sometimes high accuracy may be obtained for separated bands or weak bands from the  $E_m$ ,  $k$  and  $\epsilon''$  spectra, but the anomalous dispersion in the real dielectric constant introduces an uncertainty that increases with the band strength and is difficult to assess. Therefore, only the imaginary polarizability spectra are used in the subsequent chapters for calculations of the dipole moment derivatives, except for Chapter 5 where results from  $k$  and  $\epsilon''$  spectra are included for comparison.

### 1.3 Measurements and Results for Methanol

With the methods described in Chapters 2 to 4, the absolute absorption intensities were obtained and are reported as the refractive index spectra of four liquid isotopomers, CH<sub>3</sub>OH, CH<sub>3</sub>OD, CD<sub>3</sub>OH and CD<sub>3</sub>OD, in Chapters 5 to 7. The integrated absorption intensities of different transitions were deduced as far as possible by considering the spectra of the different isotopomers, CH<sub>3</sub>OH alone in Chapter 5, CH<sub>3</sub>OH and CH<sub>3</sub>OD in Chapter 6, and CD<sub>3</sub>OH and CD<sub>3</sub>OD, CH<sub>3</sub>OH and CH<sub>3</sub>OD in Chapter 7. The dipole moment derivatives were calculated for certain vibrations of these molecules under certain approximations, the most notable of which is that the normal vibration results from a single internal coordinate. This was clearly not true for all vibrations, and Chapter 8 reports the collected data for all four isotopomers and the calculation of the dipole moment derivatives with respect to internal coordinates with the help of a normal coordinate calculation of all four molecules. This, in turn, was helped by an ab initio calculation for gaseous methanol taken from the literature<sup>28</sup>.

In Chapter 5, infrared absorption intensities of liquid methanol, CH<sub>3</sub>OH, at 25°C, are reported between 8000 and 2 cm<sup>-1</sup>. Measurements were made by attenuated total reflection spectroscopy, using CIRCLE cells of two different lengths and with several different alignments of the cell in the instrument. The pATR spectra recorded by three other workers in this laboratory between 1984 and 1991 were also included in the analysis. Steps were taken to ensure that as few parameters as possible remained unchanged throughout the series of measurements, to try to reveal systematic errors. All the ATR spectra were converted to real and imaginary refractive index spectra using the method described in Chapter 3. Measurements were also made by transmission spectroscopy in regions of weak absorption. The transmission spectra were also converted to refractive index spectra using the method described in the literature<sup>10,11</sup>. The results from the two methods agreed excellently. The ATR and transmission results were combined to give a spectrum between 7500 and 350 cm<sup>-1</sup>. This spectrum agrees excellently with the literature results<sup>29</sup> from 350 to 2 cm<sup>-1</sup>, and the two sets of measurements were combined to yield a spectrum from 7500 to 2 cm<sup>-1</sup>. The imaginary refractive index was arbitrarily set to zero between 8000 and 7500 cm<sup>-1</sup>, where it is always less than  $2 \times 10^{-6}$ , in order that the real refractive index could be calculated below 8000 cm<sup>-1</sup> by Kramers-Krönig transform. The results are reported as graphs and as tables of the real and imaginary refractive indices between 8000 and 2 cm<sup>-1</sup>. The spectrum of imaginary molar polarizability multiplied by wavenumber,  $\tilde{\nu}\alpha''_m(\tilde{\nu})$ , was

calculated under the Lorentz local field assumption, and the area under its bands was separated into contributions from different vibrations under several approximations. Much accuracy was lost in this process. The changes of the dipole moment during normal vibrations, and during O-H, C-H and C-O bond stretching and H-C-O-H torsion motion, are presented.

Chapter 6 reports infrared absorption intensities of liquid methanol-*d*, CH<sub>3</sub>OD, at 25°C, between 8000 and 350 cm<sup>-1</sup>. Similar to that in Chapter 5, ATR and transmission spectra were measured and converted to refractive index spectra. Again, the results of the two methods agreed excellently and were combined to yield an imaginary refractive index spectrum between 6187 and 350 cm<sup>-1</sup>. The imaginary refractive index spectrum was set to zero between 6187 and 8000 cm<sup>-1</sup>, where  $k$  is always less than  $2 \times 10^{-6}$ , and the real refractive index was calculated below 8000 cm<sup>-1</sup> by KK transform. The  $\tilde{\nu}\alpha''_m$  spectrum was calculated and the area under its bands was separated into contributions from different vibrations. The separation was more reliably made by combining the spectra of CH<sub>3</sub>OD and CH<sub>3</sub>OH than was possible for CH<sub>3</sub>OH alone in Chapter 5. Hence, the dipole moment derivatives of the C-H, O-H(D) and C-O stretching, and CH<sub>3</sub> deformation vibrations of the molecules were better determined in Chapter 6 than in Chapter 5, although still under the simplest approximations. The dipole moment derivatives of the C-O-H(D) in-plane bending, H-C-O-H(D) torsion, and CH<sub>3</sub> rocking vibrations were also estimated.

Chapter 7 reports absolute infrared absorption intensities of liquid methan-*d*<sub>3</sub>-ol, CD<sub>3</sub>OH, and methanol-*d*<sub>4</sub>, CD<sub>3</sub>OD, at 25°C, between 8000 and 350 cm<sup>-1</sup>. Measurements were also made by multiple ATR spectroscopy and by transmission spectroscopy. In both cases, the spectra were converted to the real and imaginary refractive index spectra. The  $k$  spectra from the two methods agreed and gave an imaginary refractive index spectrum between 7244 and 350 cm<sup>-1</sup> for CD<sub>3</sub>OH, and between 5585 and 350 cm<sup>-1</sup> for CD<sub>3</sub>OD. The imaginary refractive index spectrum was set to zero from 8000 to 7244 or 5585 cm<sup>-1</sup>, where  $k$  is always less than  $4 \times 10^{-6}$ , and the real refractive index was calculated below 8000 cm<sup>-1</sup> by KK transformation. The results are reported as graphs and tables of the refractive indices between 8000 and 350 cm<sup>-1</sup>. The  $\tilde{\nu}\alpha''_m$  spectra were calculated and the areas under their bands were separated as far as possible into the integrated intensities of different vibrations by comparing the spectra of all four isotopomers. The magnitudes of the transition moments were calculated from the integrated intensities, and the double harmonic approximation was used to calculate the



magnitudes of the dipole moment derivatives of the liquid-state molecules with respect to the normal coordinates. Dipole moment derivatives with respect to internal coordinates were also calculated under the simplest approximations, the validity of which was demonstrated by the experimental data in many cases. The consistency of the dipole moment derivatives with respect to internal coordinates obtained for different isotopomers was shown through their relative rotational corrections. Results are presented for the O–H, O–D, C–H and C–D stretching displacements, the C–O–H in-plane bending displacement, and the D–C–O–H and D–C–O–D torsion displacements. It is argued from the wavenumber and intensity data that the latter are not the torsion of the OH or OD bond against the CH<sub>3</sub> or CD<sub>3</sub> group, but are the out-of-plane bending vibration of the hydrogen atom in the O–H---O hydrogen bond.

#### 1.4 Molecular Parameters and Discussion

The behavior of molecules is properly described through quantum mechanics. Thus, the integrated intensity of a transition is related to the transition moment,  $\tilde{R}^{nm}$ , of the transition as given by

$$\tilde{R}^{nm} = \int \Psi_n \bar{\mu} \Psi_m d\tau \quad (1.16)$$

where  $\Psi_n$  and  $\Psi_m$  are the wavefunctions of the vibrational states,  $n$  and  $m$ , involved in the transition, and  $\bar{\mu}$  is the dipole moment of the molecule.

Further, if it is assumed that the potential energy is harmonic in all displacement coordinates and the dipole moment is a linear function of all displacement coordinates, the moment of a fundamental transition is related to the square of the dipole moment derivative with respect to the normal coordinate,  $|\partial \bar{\mu} / \partial Q_j|^2$ , which is denoted as  $\mu_j^2$  for brevity.

Thus, from quantum mechanics (or classical mechanics as discussed in Chapter 4), the integrated intensity of vibration  $j$  yields the value of  $|\mu_j|$ . Unfortunately,  $Q_j$  is a mass-weighted coordinate, so to make chemical use of these quantities, such as to compare the values obtained for different isotopomers, this mass weighting has to be removed.

Ab initio quantum mechanical calculations are today able to reproduce the wavenumbers of fundamental transitions accurate to a few percent and the intensities of fundamental transitions accurate to a factor of 2 or 3. And, of course, ab initio calculations are relevant to gas, not the liquid. In order to remove the mass weighting

and make initial chemical use of measured wavenumbers and intensities of liquids, it is believed best to use a well defined classical mechanical calculation, the normal coordinate calculation, and a classical model for the intensities, rather than to use a quantum mechanical calculation. In fact, both classical and quantum mechanical calculations are used in practice because the quantum mechanical calculations are helpful guides to the signs of interaction force constants and to the directions of changes in the molecular dipole moment during atomic displacements.

It is assumed that the vibrational potential energy is harmonic in the normal coordinate calculation, and the vibrational wavenumbers are functions of the force constants. In the accompanying classical model for the intensities, the integrated intensities are functions of parameters which represent the electro-optical behavior of the molecule during a vibration. One such parameter may be, for example, the change in the molecular dipole moment for unit change in a bond length of the molecule.

Traditionally, classical vibrational calculations have determined the force constants from only the wavenumber, because the intensities have not been known. The calculation can be improved if the intensities are also known, because the intensities reflect the eigenvectors of a vibration, namely the relative changes in the different internal coordinates during the vibration. Thus, the intensities place constraints on the eigenvectors which, in turn, place constraints on the values of the force constants. A calculation with both wavenumber and intensity information is likely to be more successful than a calculation with no intensity information.

While it is not difficult today to choose the parameters to use for the potential energy, there are several kinds of intensity parameters that can be used<sup>30</sup>. Among these the more widely employed are i) the changes in the total dipole moment of the molecule with internal or symmetry coordinates (the dipole moment derivatives); ii) the changes in the total dipole moment of the molecule with the Cartesian displacements of each atom (atomic polar tensors); iii) the changes of each bond moment with the vibration parameters plus equilibrium bond moments (electro-optical parameters, eops). In this work, the dipole moment derivatives were used.

In Chapter 8, the experimental information for all four isotopomers is collected. The reliability of the integrated intensities is assessed by fitting Gaussian and CDHO (near Lorentzian, see Chapter 4) bands to the spectra, calculating the integrated intensity of each band from the fitted bands, and comparing the resulting values with those deduced by

more traditional means in Chapters 5 to 7. The "accepted" values of the intensities are chosen with their estimated errors.

Finally, the wavenumbers and "accepted" intensities are fitted in a normal coordinate and intensity calculation. From this calculation are obtained the values of the dipole moment derivative with respect to the internal coordinates.

### 1.5 References

1. J. E. Bertie, S. L. Zhang, H. H. Eysel, S. Baluja, and M. K. Ahmed, *Appl. Spectrosc.* **47**, 1100 (1993).
2. J. E. Bertie and S. L. Zhang, *Applied Spectrosc.* **48**, 176 (1994).
3. J. E. Bertie and S. L. Zhang, *J. Chem. Phys.* (Accepted for publication, 1994).
4. J. E. Bertie, S. L. Zhang, and C. D. Keefe, *J. Mol. Struct.* (Accepted for publication, 1994).
5. J. E. Bertie, S. L. Zhang, and C. D. Keefe, *Vib. Spectrosc.* (Accepted for publication, 1994).
6. J. E. Bertie, S. L. Zhang, and R. Manji, *Appl. Spectrosc.* **46**, 1660 (1992).
7. J. E. Bertie and S. L. Zhang, *Can. J. Chem.* **70**, 520 (1992).
8. J. E. Bertie and H. H. Eysel, *Appl. Spectrosc.* **39**, 392 (1985).
9. J. E. Bertie, H. Harke, and M. K. Ahmed, *Croatica Chemica Acta* **61**, 391 (1988).
10. D. G. Cameron, J. P. Hawranek, P. Neelakantan, R. P. Young, and R. N. Jones, in *Computer Programs for Infrared Spectrophotometry XLII to XLVII*, National Research Council of Canada Bulletin **16**, 1977.
11. J. E. Bertie, C. D. Keefe, and R. N. Jones, *Can. J. Chem.* **69**, 1609 (1991).
12. J. E. Bertie, M. K. Ahmed, and H. H. Eysel, *J. Phys. Chem.* **93**, 2210 (1989).
13. J. E. Bertie, R. N. Jones, and C. D. Keefe, *Appl. Spectrosc.* **47**, 891 (1993).
14. M. Born and E. Wolf, *Principles of Optics*, sixth edition, Pergamon Press, 1980.
15. I. Mills, T. Cvitaš, K. Homann, N. Kallay, and K. Kuchitsu, *Quantities, Units and Symbols in Physical Chemistry*, Blackwell Scientific Publications, Oxford, 1988.
16. K. Ohta and H. Ishida, *Appl. Spectrosc.* **42**, 952 (1988).

17. H. A. Lorentz, Wiedem. Ann. **9**, 641 (1880).
18. L. Lorenz, Wiedem. Ann. **11**, 70 (1881).
19. H. Frohlich, *Theory of Dielectrics*, Oxford University Press, London, 1958. P8.
20. B. Gross, Phys. Rev. **59**, 748 (1941).
21. E. C. Titchmarsh, *Introduction to the Theory of Fourier Integrals*, Oxford University Press, London, 1962. P119.
22. M. G. Sceats and G. C. Morris, Phys. Status Solidi **A14**, 643 (1972).
23. C. W. Peterson and B. W. Knight, J. Opt. Soc. Am. **63**, 1238 (1973).
24. B. Harbecke, Appl. Phys. A: **40**, 151 (1986).
25. A. G. Marshall, in *Fourier, Hadamard and Hilbert Transforms in Chemistry*, Ed. A. G. Marshall, Plenum, New York, 1982, P108.
26. R. N. Bracewell, Science **248**, 697 (1990).
27. J. E. Bertie and S. L. Zhang, *8th International Conference on Fourier Transform Spectroscopy*, Lubeck, FRG; The Society of Photo-Optical Instrumentation Engineers, **1575**, 598-599(1991).
28. H. Torii and M. Tasumi, J. Chem. Phys. **99**, 8459 (1993).
29. D. D. Honijk, W. F. Passchier, M. Mandel, and M. N. Afsar, Infrared Physics **17**, 9 (1977).
30. *Vibrational Intensities in Infrared and Raman Spectroscopy*, Ed. W. B. Person and G. Zerbi, Elsevier, Amsterdam, 1982.

## Chapter 2    The Kramers–Krönig (KK) Transform, and its Approximation by the Finite Hilbert Transform via Fast Fourier Transforms\*

### 2.1 Introduction

Eqs. (2.1a) and (2.1b) give the Kramers-Krönig (KK) transform<sup>1,2</sup> between the optical constants<sup>3-5</sup>, which are the real and imaginary components of the complex refractive index,  $\hat{n}(\tilde{\nu}) = n(\tilde{\nu}) + i k(\tilde{\nu})$ .

$$n(\tilde{\nu}_i) - n(\infty) = \frac{2}{\pi} \text{P} \int_0^{\infty} \frac{\tilde{\nu} k(\tilde{\nu})}{\tilde{\nu}^2 - \tilde{\nu}_i^2} d\tilde{\nu} \quad (2.1a)$$

$$k(\tilde{\nu}_i) = -\frac{2\tilde{\nu}_i}{\pi} \text{P} \int_0^{\infty} \frac{n(\tilde{\nu}) - n(\infty)}{\tilde{\nu}^2 - \tilde{\nu}_i^2} d\tilde{\nu} \quad (2.1b)$$

The real and imaginary components of the complex dielectric constant<sup>6</sup>,  $\hat{\epsilon}(\tilde{\nu}) = \epsilon'(\tilde{\nu}) + i \epsilon''(\tilde{\nu})$ , are usually called the dielectric constant,  $\epsilon'(\tilde{\nu})$ , and the dielectric loss,  $\epsilon''(\tilde{\nu})$ , respectively. The KK transform between them<sup>6</sup> is obtained by replacing  $n$  and  $k$  by  $\epsilon'$  and  $\epsilon''$  in eqs. (2.1). Similarly, the KK transform between the reflectance,  $R(\tilde{\nu})$ , and the phase,  $\phi(\tilde{\nu})$ , of reflection<sup>4,7,8</sup> can be written by substitution. The complex reflection is  $\hat{r}(\tilde{\nu}) = |\hat{r}(\tilde{\nu})| e^{i\phi(\tilde{\nu})}$ , and the reflectance,  $R(\tilde{\nu})$ , is  $\hat{r}(\tilde{\nu}) \times \hat{r}^*(\tilde{\nu}) = |\hat{r}(\tilde{\nu})|^2$ . Since  $\ln \hat{r}(\tilde{\nu}) = \ln |\hat{r}(\tilde{\nu})| + i \phi(\tilde{\nu})$  and  $\ln |\hat{r}(\tilde{\nu})| = 1/2 \ln R(\tilde{\nu})$ , the KK transform is obtained by substituting  $1/2 \ln R$  for  $n$  and  $\phi$  for  $k$  in eqs. (2.1)<sup>9</sup>.

The KK transform has been used by several authors in recent years to aid the determination of the optical constants or dielectric constants from infrared transmission<sup>10,11</sup>, reflection<sup>7,12</sup>, or multiple attenuated total reflection<sup>13,14</sup> spectra.

It is well known<sup>6,15-19</sup> that the infinite KK transform is equivalent to two successive Fourier transforms, usually called the allied Fourier integrals. Stated more fully, the KK transform is equivalent to the infinite Hilbert transform, provided that the real variable is an even function of wavenumber and the imaginary variable is an odd function of wavenumber, i.e.  $n(\tilde{\nu}) = +n(-\tilde{\nu})$  and  $k(\tilde{\nu}) = -k(-\tilde{\nu})$ . Further, the Hilbert transform is equivalent to the allied Fourier integrals<sup>6,15-19</sup>. The Hilbert transform between the optical constants is shown in eqs. (2.2a) and (2.2b), and in eqs. (2.3a) and (2.3b) in its Fourier transform representation.

---

\* A version of this chapter has been published. Bertie and Zhang, *Can. J. Chem.* **70**, 520 (1992).

$$n(\tilde{\nu}_i) - n(\infty) = \frac{1}{\pi} \text{P} \int_{-\infty}^{\infty} \frac{k(\tilde{\nu})}{\tilde{\nu} - \tilde{\nu}_i} d\tilde{\nu} \quad (2.2a)$$

$$k(\tilde{\nu}_i) = -\frac{1}{\pi} \text{P} \int_{-\infty}^{\infty} \frac{n(\tilde{\nu}) - n(\infty)}{\tilde{\nu} - \tilde{\nu}_i} d\tilde{\nu} \quad (2.2b)$$

$$n(\tilde{\nu}_i) - n(\infty) = -2 \int_{-\infty}^{\infty} dt \text{Cos}(2\pi c \tilde{\nu}_i t) \int_{-\infty}^{\infty} k(\tilde{\nu}) \text{Sin}(2\pi c \tilde{\nu} t) d\tilde{\nu} \quad (2.3a)$$

$$k(\tilde{\nu}_i) = -2 \int_{-\infty}^{\infty} dt \text{Sin}(2\pi c \tilde{\nu}_i t) \int_{-\infty}^{\infty} [n(\tilde{\nu}) - n(\infty)] \text{Cos}(2\pi c \tilde{\nu} t) d\tilde{\nu} \quad (2.3b)$$

For the remainder of this chapter the term Hilbert transform will be used to mean the use of eqs. (2.3) to perform a Hilbert transform via fast Fourier transform routines. Eqs. (2.2) have not been used at all.

The KK transform is slow on most laboratory computers. For example, a fairly efficient program written in Microsoft FORTRAN version 5.0 and running under Microsoft DOS on a 16 MHz laboratory computer with an Intel 28386 cpu chip requires 13 minutes for the KK transform of a spectrum containing 8192 data points. In contrast, fast Fourier transform (FFT) routines are available which transform a data file of this length in seconds. The routines used by most FT-IR spectrometer systems to transform the interferogram into the spectrum are fast and can sometimes be used in application programs written by the user. Thus authors have described the use of FFT routines supplied by the instrument manufacturers to accomplish the Hilbert transform<sup>20,21</sup>. Other authors have described the use of FFT routines to Hilbert transform largely specular reflection data<sup>17-19</sup>.

The computer programs which run under Microsoft DOS have recently developed to permit more efficient computation of our spectral data than on the Aspect 2000 computer of our (1982) Bruker IFS 113V FT-IR spectrometer. To check the programs, the classical damped harmonic oscillator model<sup>22-24</sup> was used to synthesize real and imaginary refractive index spectra. This model calculates, for dielectric loss bands that are essentially Lorentzian in shape, the correct real refractive index spectrum to accompany the calculated imaginary refractive index spectrum.

This work began when these correct real refractive index spectra were compared with those obtained by Hilbert transformation of the imaginary refractive index spectra using our original algorithm<sup>21</sup>. Unless all of the bands are very sharp, which is frequently

not the case for liquids, the Hilbert  $n(\tilde{\nu})$ , i.e. the  $n$  spectrum obtained by Hilbert transform, deviated by several percent from the correct result.

The  $n$  spectra were also obtained by KK transformation of the imaginary refractive index spectra. The KK  $n$  spectra differed significantly from the Hilbert  $n$  spectra, but were in excellent agreement with the correct ones. Exceptions occurred if the imaginary refractive index was not near zero at the low-wavenumber limit of the spectrum.

At about the time of this empirical discovery of the discrepancies between the Hilbert and KK transforms, Bracewell<sup>25</sup> reported that discrepancies are to be expected, but he gave no details of their magnitude. Thus, the appealing very fast method of Hilbert transform gave results that are in considerable error, while the slow KK transform gave correct answers. It was clearly worthwhile to explore whether the accuracy of the fast Hilbert transform method could be improved. Most previous authors considered the accuracy of the transform qualitatively. Only Ohta and Ishida<sup>26</sup> have addressed the accuracy of the Hilbert transform at this level of accuracy.

In this chapter are presented the results of an exploration of the magnitude of the discrepancies between the correct  $n(\tilde{\nu})$ , the KK  $n(\tilde{\nu})$ , and the Hilbert  $n(\tilde{\nu})$ . Different literature algorithms for the Hilbert transform are explored to determine the important parameters for accuracy. An algorithm that yields 0.05% agreement with the correct  $n(\tilde{\nu})$  is presented. In 1988, Ohta and Ishida<sup>26</sup> reported in less detail a similar study, which has been found very helpful. The algorithm recommended from this work is similar to theirs, but uses symmetry to reduce the size of the transforms by a factor of 2 and real variables rather than complex ones to speed computation.

The Hilbert transform also converts  $n$  spectra to  $k$  spectra, although this is used less frequently. For this Hilbert transform, we give an algorithm that yields very good agreement with the correct  $k$  spectrum.

This chapter also contains a discussion of procedures to follow when the experimental data is available over most of the fingerprint region, but does not extend to the very low wavenumbers where the imaginary refractive index often returns to near zero. This situation is common, due to experimental limitations and difficulties. When the  $k$  spectrum terminates at low-wavenumber on a peak, rather than at  $k(\tilde{\nu})$  values near zero, the real refractive index spectrum calculated by either the KK transform or the Hilbert transform is seriously in error over the last several hundred wavenumbers. A method is presented that allows very good results to be obtained in those cases in which the entire  $k$

spectrum is known. In such cases the  $n$  spectrum can be calculated from the full  $k(\tilde{\nu})$  as well as from the truncated version of it, so the accuracy of the method of treating the truncated spectrum can be evaluated. This method is believe also to give the best result available when the full  $k$  spectrum is not known. But its accuracy can not be determined in such cases until the influence of the missing part of the  $k$  spectrum is known.

## 2.2 General Methods

The classical damped harmonic oscillator model<sup>22-24</sup> gives eqs. (4a) and (4b) for the real and imaginary parts of the dielectric constant in terms of the wavenumbers,  $\tilde{\nu}_j$ , the intensities,  $S_j$ , and the damping constants,  $\Gamma_j$ , of the oscillators.

$$\epsilon'(\tilde{\nu}) = \epsilon'(\infty) + \sum_j \frac{S_j(\tilde{\nu}_j^2 - \tilde{\nu}^2)}{(\tilde{\nu}_j^2 - \tilde{\nu}^2)^2 + \Gamma_j^2 \tilde{\nu}^2} \quad (2.4a)$$

$$\epsilon''(\tilde{\nu}) = \sum_j \frac{S_j \Gamma_j \tilde{\nu}}{(\tilde{\nu}_j^2 - \tilde{\nu}^2)^2 + \Gamma_j^2 \tilde{\nu}^2} \quad (2.4b)$$

The optical constants,  $n(\tilde{\nu})$  and  $k(\tilde{\nu})$  are calculated from these dielectric constants by eqs. (2.5),

$$n(\tilde{\nu}) = \left\{ \left[ (\epsilon'(\tilde{\nu}))^2 + \epsilon''(\tilde{\nu})^2 \right]^{1/2} + \epsilon'(\tilde{\nu}) \right\} / 2 \quad (2.5a)$$

$$k(\tilde{\nu}) = \left\{ \left[ (\epsilon'(\tilde{\nu}))^2 + \epsilon''(\tilde{\nu})^2 \right]^{1/2} - \epsilon'(\tilde{\nu}) \right\} / 2 \quad (2.5b)$$

In these equations, the intensity parameter  $S_j$  is related to the molecular dipole moment derivative with respect to the normal coordinate  $Q_j$ ,  $|\partial \bar{\mu} / \partial Q_j|$ , in the approximation of mechanical and electrical harmonicity, by  $S_j = (N/3\pi c^2) |\partial \bar{\mu} / \partial Q_j|^2 F_j^2$ . Here  $N$  is the number of molecules in unit volume,  $c$  is the velocity of light in vacuum, and  $F_j^2$  is the local field correction for a molecule in a liquid. In general theory,  $S_j$  is related to the sum of the squares of the molecular transition moments that contribute to the band,  $|\bar{R}_{\nu_j \nu_j}|^2$ , by

$$S_j = (8\pi^3/3hc) \sum \left[ \tilde{\nu}_j |\bar{R}_{\nu_j \nu_j}|^2 (N_{\nu_j} - N_{\nu_j}) \right]$$



where one must sum over all  $v_j''$  states that are significantly populated.

Eqs. (2.4) and (2.5) were used to calculate corresponding pairs of  $k$  and  $n$  spectra through the FORTRAN program FHARM. The program reads ASCII input and produces spectral files in Galactic Industries' SpectraCalc ".SPC" format.

In the first half of this work, the  $k$  spectrum so calculated was entered into the Hilbert transform program under consideration, with the appropriate value for  $n(\infty)$ , and the  $n_H(\tilde{\nu})$  was calculated. The spectrum was also entered into the KK transform program, and the  $n_K(\tilde{\nu})$  was calculated.

The objective of this work was to calculate  $n(\tilde{\nu})$  values from the  $k$  spectrum to suitable accuracy, where  $\sim 0.1\%$  is all that the experimental absorption data justify. Accordingly, most of the figures show for clarity the percentage deviation of the Hilbert  $n(\tilde{\nu})$  from the correct  $n(\tilde{\nu})$  at each wavenumber,  $100[n_H(\tilde{\nu})-n(\tilde{\nu})]/n(\tilde{\nu})$ . This quantity is the percent error in the  $n_H(\tilde{\nu})$  values. For the  $n(\tilde{\nu})$  values calculated by the KK transform, the percent deviation  $100[n_K(\tilde{\nu})-n(\tilde{\nu})]/n(\tilde{\nu})$  is shown to illustrate the accuracy.

For the purpose of demonstrating the actual error in the Hilbert transform routines it would be better to subtract the value of  $n(\infty)$ , and to compare  $\Delta n_H(\tilde{\nu}) = n_H(\tilde{\nu}) - n(\infty)$  or  $\Delta n_K(\tilde{\nu}) = n_K(\tilde{\nu}) - n(\infty)$  with  $\Delta n(\tilde{\nu}) = n(\tilde{\nu}) - n(\infty)$ , because the transforms calculate these differences (Eqs. (2.2) and (2.3)) which are converted to the  $n_H(\tilde{\nu})$  and  $n_K(\tilde{\nu})$  simply by adding  $n(\infty)$ . This comparison is given for the initial and final Hilbert transform algorithms.

In the second half of this chapter, the  $n$  spectra are entered into the KK or Hilbert transform after subtracting  $n(\infty)$  from each value, and the  $k_K(\tilde{\nu})$  or  $k_H(\tilde{\nu})$  are calculated. In these cases the deviation of the calculated  $k$  from the correct one is calculated as a percentage of the largest  $k$  value in the spectrum to illustrate the accuracy of the transform.

### 2.2.1 *The Correct Spectra*

Three different types of spectra have been calculated via the classical damped harmonic oscillator model for this work. The first consists of a single band at  $1600\text{ cm}^{-1}$  with a full width at half height (FWHH) ranging from  $4\text{ cm}^{-1}$  up to  $50\text{ cm}^{-1}$ . The second is a complex spectrum based on that of pure liquid methanol, and the third is a complex spectrum based on that of pure liquid acetic acid. The classical damped harmonic oscillator parameters used for these spectra are tabulated in Table 2.1. The  $k(\tilde{\nu})$  and  $n(\tilde{\nu})$  are shown in Figures (2.1) to (2.3). It should be noted that each  $k$  spectrum is complete

**Table 2.1** Parameters used for spectra <sup>a</sup> calculated from the classical damped harmonic oscillator (CDHO) model.

$j$	$\tilde{\nu}_j / \text{cm}^{-1}$	$\Gamma_j / \text{cm}^{-1}$	$S_j / \text{cm}^{-2}$
Single Band Spectrum <sup>b</sup>			
1	1600	4	14400
“Methanol” Spectrum			
1	3346	250	280000
2	2945	100	58000
3	2833	50	25000
4	1450	100	30000
5	1115	30	2500
6	1030	22	35000
7	657	200	40000
8	370	300	3000
“Acetic Acid” Spectrum			
1	3543	100	50000
2	3487	50	6000
3	3416	200	150000
4	3326	50	5000
5	3248	140	50000
6	3171	50	5000
7	3139	200	25000
8	3037	180	90000
9	2937	50	3000
10	2870	100	10000
11	2794	100	5000
12	2759	100	8000
13	2622	150	40000
14	1719	55	100000
15	1634	100	40000
16	1396	60	30000
17	1280	80	70000
18	1054	20	2000
19	1014	30	7500
20	925	250	38000
21	887	30	2000
22	723	250	50000

a) The spectra were calculated between 7800 and 50  $\text{cm}^{-1}$ , data points are 0.964  $\text{cm}^{-1}$  apart, and  $n(\infty) = 1.325$ .

b)  $\Gamma_j = 50 \text{ cm}^{-1}$  was also used with  $S_j = 180,000$ .

in the sense that the  $k$  values at the highest and lowest wavenumber points are about  $10^{-5}$  of the peak value for the single band spectra and about one thousandth of the maximum peak height for the methanol and acetic acid simulations.

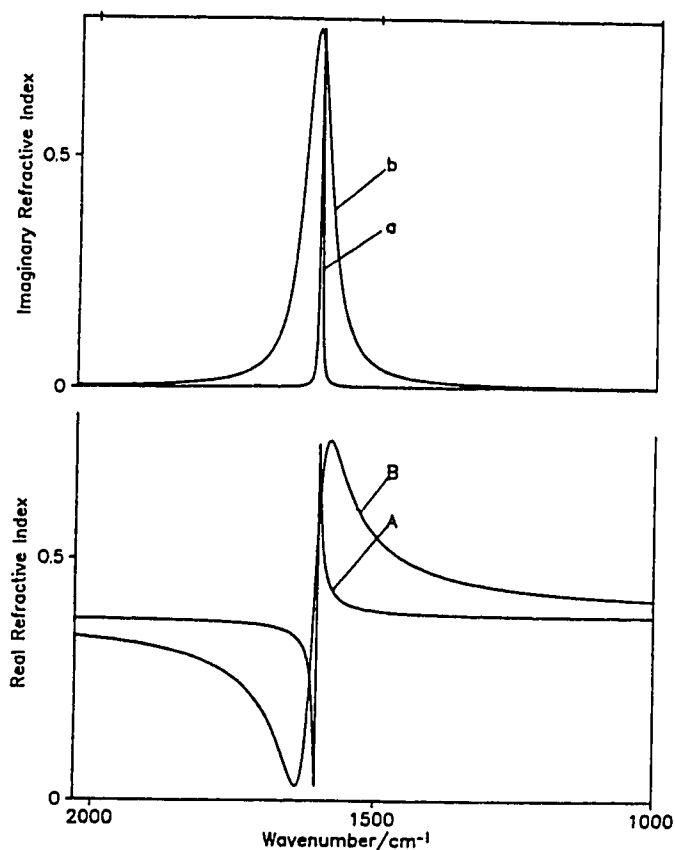


**Figure 2.1** Refractive index spectra calculated with the classical damped harmonic oscillator model. Single band spectra with FWHH = 4 cm<sup>-1</sup> and 50 cm<sup>-1</sup> (Table 2.1).

### 2.2.2 The Kramers-Krönig (KK) Transform

A FORTRAN program, KKTRANS, for this transform was based on that included in program 46 of the National Research Council of Canada's Bulletins of Computer Programs for Infrared Spectroscopy<sup>27</sup>. Several changes were made to improve the speed of the program on the laboratory computer by a factor of about 8, and a further factor of two was obtained by incorporating Ohta and Ishida's<sup>26</sup> Maclaurin formula of calculating the principal value of the integral. This latter feature also considerably improved the accuracy of the transform near the intense peaks. Program KKTRANS takes 13 minutes to transform a file containing 8192 REAL (4 byte) data points on a 16 MHz 386SX computer with a 387 math co-processor. It reads and writes files in SpectraCalc's ".SPC" format.

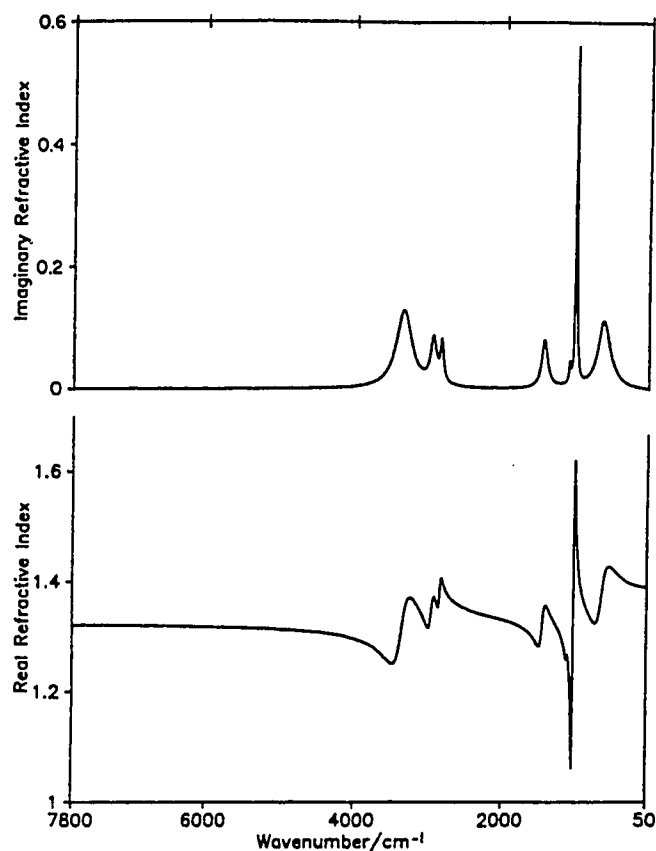


**Figure 2.2** Refractive index spectra calculated with the classical damped harmonic oscillator model. A simulated spectrum of liquid methanol (Table 2.1).

### 2.2.3 The Hilbert Transform

The Hilbert transform via two successive fast Fourier transforms (FFTs), following eqs. (2.3), consists of the following five steps:

- Step 1. Arranging the input spectral data into the appropriate form;
- Step 2. The first FFT;
- Step 3. Arranging the output of the first FFT into the appropriate form;
- Step 4. The second FFT;
- Step 5. Obtaining the desired spectrum from the output of the second FFT.

The details of the first, third, and fifth step depend on the algorithm used for the Hilbert transform, and depend on whether the transform is from  $k(\tilde{\nu})$  to  $n(\tilde{\nu})$  or vice versa. These features will be discussed in the "Results" sections. The FFT is common to

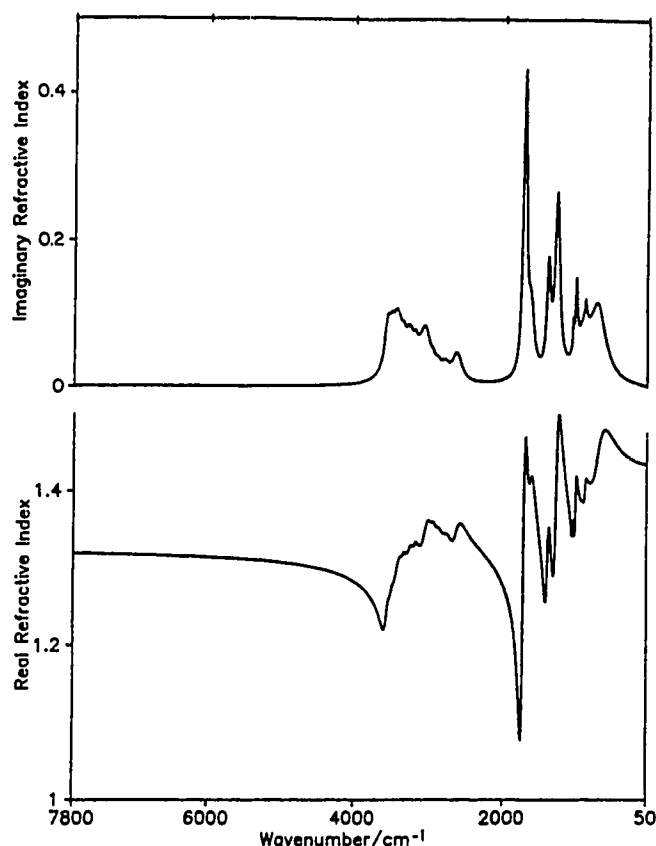


**Figure 2.3** Refractive index spectra calculated with the classical damped harmonic oscillator model. A simulated spectrum of liquid acetic acid (Table 2.1).

all algorithms, but may be used to transform real data or complex data. The output is complex in both cases, but is written into two arrays of real variables. To improve execution speed, complex variables are not used.

Four FFT subroutines were tested by ensuring that they gave the transform of a Gaussian peak of unit height correct<sup>16,28</sup> to six decimal places. All subroutines gave correct transforms, and the fastest subroutine was chosen, the FORTRAN subroutine described by Ng and Horlick<sup>29</sup>. This subroutine is based on the algorithm first suggested by Gentleman and Sande<sup>30</sup>, and its listing is in the Ph.D. thesis of Ng<sup>31</sup>. It is given in Section 2.6 of this thesis also, because there is a version of it in circulation which contains incorrect signs.

The subroutine is written with real variables to find the complex Fourier transform of a real function. It consists of three phases: a) The "Shuffle" of the real input array into

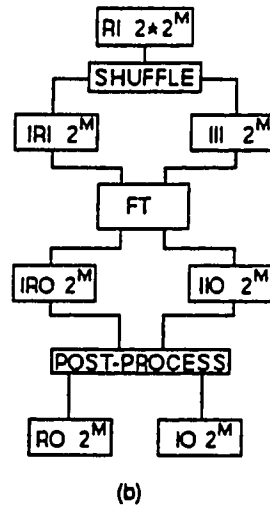
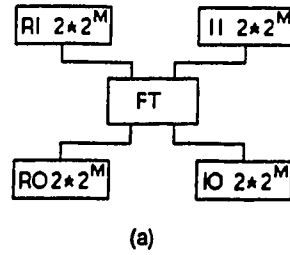


**Figure 2.4** Schematic representation of the FFT subroutine used in this work: a) The COMPLEX data mode; b) The REAL data mode.

half-sized real and imaginary input arrays to a complex FFT; b) The Complex FFT of real and imaginary input arrays to real and imaginary output arrays; c) The "Post-processing" phase to reconstruct the complex FFT of the original real input array. The "Shuffle" consists of placing the odd- and even- indexed points of the real input array into the real and imaginary, respectively, arrays input to the complex FFT. The "Post-processing" phase is that described by Zachor in an advertisement<sup>32</sup>.

As noted above, this subroutine can be used in its REAL mode, to obtain the complex transform of real data, and in its COMPLEX mode to obtain the transform of complex data. The REAL mode uses all three phases of the subroutine, while the COMPLEX mode uses only the middle phase. The diagrams shown in Figure 2.4 have been found to be helpful illustrations of these two modes. In Figure 2.4, RI, IO, etc. stand for Real Input, Imaginary Output, etc., and IRI, IIO, etc. stand for Intermediate Real Input, Intermediate Imaginary Output, etc. Figure 2.4 also notes that a Real Input array

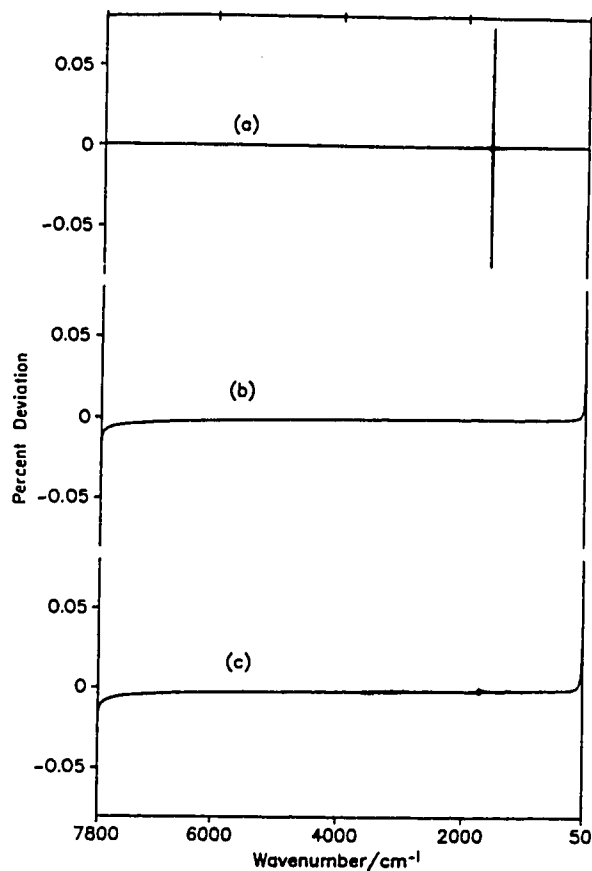


**Figure 2.5** Percent deviations from the correct  $n$  spectra calculated by KK transformation of  $k(\tilde{\nu})$ . Curve A, single band  $k(\tilde{\nu})$ , FWHH = 4  $\text{cm}^{-1}$ ; curve B, simulated methanol spectrum; curve C, simulated acetic acid spectrum.

of size  $2 \times 2^M$  in REAL mode yields all other arrays of size  $2^M$ . In COMPLEX mode all arrays have the same size.

The details of the use of this subroutine in the different Hilbert transform algorithms is given in the "Results" sections. All of the programs that use this subroutine in this subroutine read and write spectral files in SpectraCalc's ".SPC" format.

### 2.3 Results: Transforms from $k(\tilde{\nu})$ to $n(\tilde{\nu})$ for a Complete $k$ Spectrum

The results for those cases in which the  $k$  spectrum is complete are presented. Results for cases in which the  $k$  spectrum contains incomplete bands at the lowest

wavenumbers are discussed later. It should be noted that all of the spectral files start at high wavenumber and run to low wavenumber.

### 2.3.1 Kramers-Krönig Transforms

Figure 2.5 shows the percent error of the  $n_K(\tilde{\nu})$  values calculated by KKTRANS from the  $k$  spectra of Figures 2.1 to 2.3. The greatest deviation of the  $n_K(\tilde{\nu})$  values from the correct values is 0.07% for the single band of 4 cm<sup>-1</sup> FWHH, 0.004% for the single band of 50 cm<sup>-1</sup> FWHH, and 0.05% for the complex spectra. Thus, to the accuracy of current experimental data, program KKTRANS gives the correct  $n$  spectrum, provided the  $k$  spectrum is complete.

### 2.3.2 Hilbert Transforms

*The original Hilbert transform algorithm* This has been described only in general terms<sup>21</sup>. It uses the FFT subroutine in REAL mode (Figure 2.4).

Consider a  $k$  spectrum that contains NP data points. Step 1 (Section 2.2.3) of the Hilbert transform consists of three steps. First, adding zeros to the (low-wavenumber) end of the spectral data to make the number of points a power of 2,  $2^M$ , as required by the FFT subroutine. Second, adding a zero point. Third, folding the file about that zero point to create a symmetrical array centered on the added zero. In fact the array is not quite symmetrical, because the first data point in the file must be omitted from its folded position at the end of the file to keep the number of points equal to a power of 2 ( $2 \times 2^M$ ). Figure 2.6, curve (A), shows the resulting real input array schematically. This array is then input to step 2, the FFT in REAL mode.

The FFT of this symmetric real array consists of a zero imaginary transform array and a non-zero real transform array, both of size  $2^M$ . Step three of this algorithm consists of 2 steps, replacing the second half of the real transform array by zeros and adding an additional  $2^M$  zeros to restore the file to the full length,  $2 \times 2^M$ , of the real input to step 2. The resulting file is put into step 4, the FFT in REAL mode.

Step 5 of this algorithm is to obtain the NP values of  $-\Delta n_H(\tilde{\nu}) = n(\infty) - n(\tilde{\nu})$  from the first NP points in the imaginary transform array, with wavenumber decreasing with increasing point index, and to subtract them from  $n(\infty)$  to obtain the desired  $n(\tilde{\nu})$  in the same wavenumber sequence as in the original  $k(\tilde{\nu})$  array with NP points.

This algorithm programmed in FORTRAN takes 14 seconds to Hilbert transform an 8192-point  $k$  spectrum.



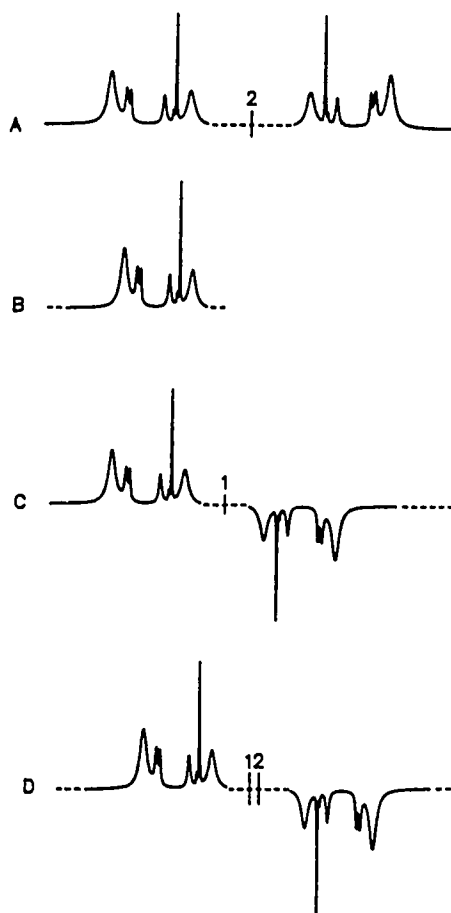


**Figure 2.6** Schematic representation of the input arrays to step 2 of the Hilbert transform algorithms. Curve A, the original algorithm; curve B, Marshall's algorithm; curve C, Ohta and Ishida's algorithm; curve D, the BZ algorithm, the preferred algorithm. 1 indicates a zero value at  $0\text{ cm}^{-1}$ ; 2 indicates an additional zero value added as a folding or inverting center; a dashed line indicates the addition of zeros.

This Hilbert transform program was checked in 1983 before it was originally used<sup>21</sup>. However, the check was made using the single band  $k$  spectrum shown in Figure 2.1, with a  $4\text{ cm}^{-1}$  FWHH, by comparing the correct and Hilbert  $n(\tilde{\nu})$ , curves (a) and (b) of Figure 2.7 (lower box). The agreement appears very good. If the percent deviation is compared, curve (B) of Figure 2.7 (upper box) the agreement appears less good. As the FWHH of the single band is increased, problems become evident, as curve (C) of Figure 2.7 (upper box) shows for a single band of FWHH  $50\text{ cm}^{-1}$ . If a more complex spectrum is used, the magnitude of the problem that initiated this work is seen.

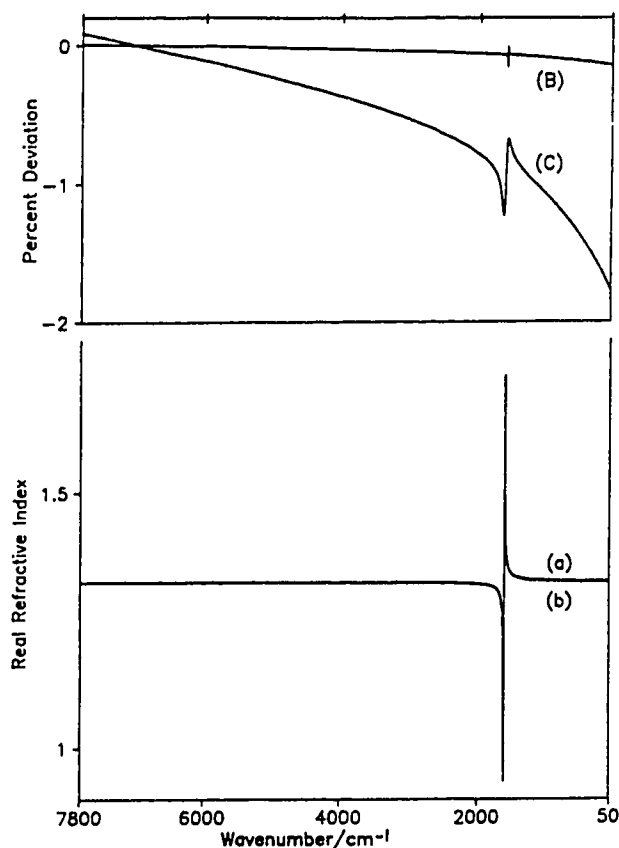


**Figure 2.7** Results for the original Hilbert transform algorithm. Lower box: curve (a), correct  $n(\tilde{\nu})$ , single band, FWHH = 4  $\text{cm}^{-1}$  (Figure 2.1 and Table 2.1); curve (b),  $n_H(\tilde{\nu})$  calculated by Hilbert transformation of the corresponding  $k(\tilde{\nu})$ . Curves (a) and (b) are indistinguishable on this scale. Upper box: percent deviation of the Hilbert transformed  $n_H(\tilde{\nu})$  from the correct  $n(\tilde{\nu})$  for: curve (B), single band spectrum, FWHH = 4  $\text{cm}^{-1}$ ; curve (C), single band spectrum, FWHH=50  $\text{cm}^{-1}$ .

Curves (a) and (b) of Figure 2.8 (lower box) show the correct  $n(\tilde{\nu})$  for the simulated methanol  $k(\tilde{\nu})$  of Figure 2.2 and that calculated from this Hilbert transform program. Curve (B) of Figure 2.8 (upper box) shows the percent error. Recall that the KK transform gave exact results for this spectrum, curve (C) of Figure 2.8 (upper box). Clearly this Hilbert transform program yields an error in  $n(\tilde{\nu})$  that increases in magnitude with decreasing wavenumber, from +0.3% to -4%. The error in the quantity actually calculated by the Hilbert transform,  $\Delta n_H(\tilde{\nu}) = n(\tilde{\nu}) - n(\infty)$ , reaches 80% at the lowest wavenumber.

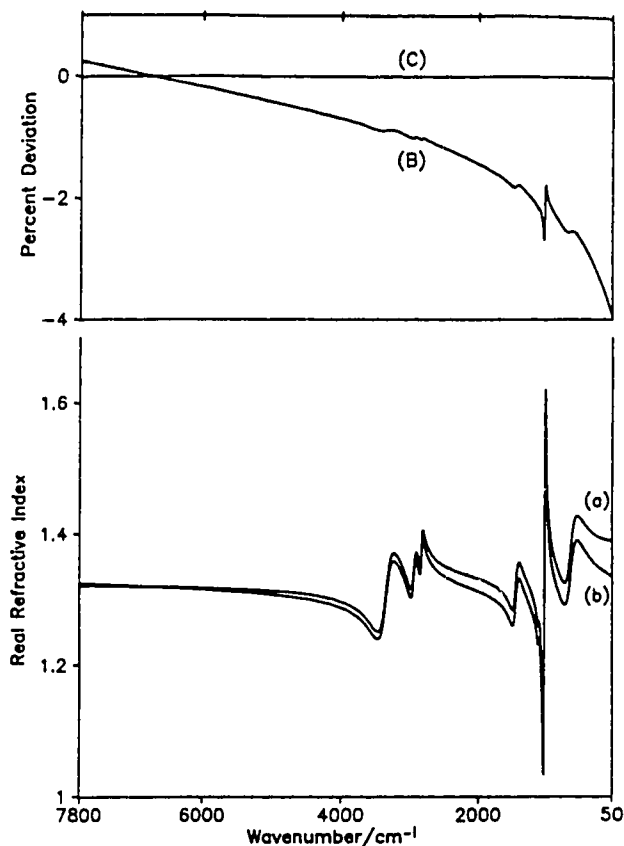


**Figure 2.8** Results for the simulated methanol spectrum. Lower box: correct  $n(\tilde{\nu})$  and our original Hilbert transformed  $n_H(\tilde{\nu})$ . Upper box: percent deviations from the correct  $n(\tilde{\nu})$  of KK transformed  $n_K(\tilde{\nu})$ , curve (C), and our original Hilbert transformed  $n_H(\tilde{\nu})$ , curve (B).

*Marshall's Hilbert transform algorithm* An algorithm presented by Marshall<sup>33,34</sup> was studied next. This was presented for the transformation of electron spin resonance absorption spectra to dispersion spectra, but the theoretical considerations are identical<sup>34</sup> to those for optical absorption and dispersion.

This algorithm uses the FFT in its COMPLEX mode. Step 1 is to add zeros to increase the number of data points to  $2^M$  from the NP  $k(\tilde{\nu})$  values. These zeros are added symmetrically, i.e. half at the beginning of the array and half at the end. The resulting array is shown schematically in Figure 2.6 curve (B). This array is input as the real array to step 2, the FFT in COMPLEX mode, and an array of zeros is input as the imaginary array. The FFT of this complex input is complex, with non-zero real and imaginary

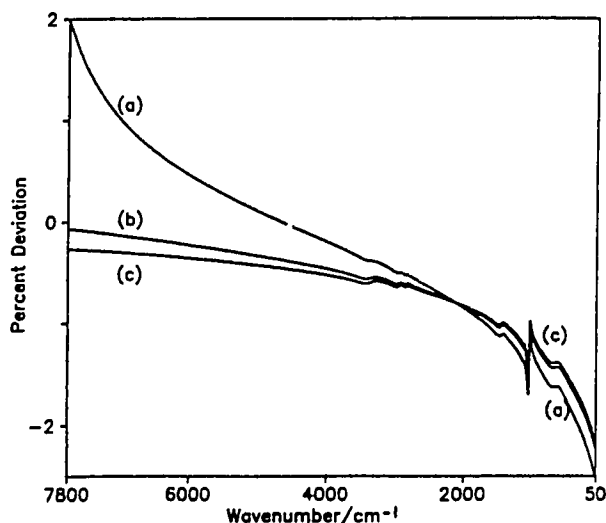


**Figure 2.9** Results for Marshall's Hilbert transform algorithm applied to the simulated methanol spectrum (Figure 2.2). Percent deviations from the correct  $n(\tilde{\nu})$  of the Hilbert  $n_H(\tilde{\nu})$  transformed with no zero-filling, curve (a), 1 level of zero-filling, curve (b), and 2 levels of zero-filling, curve (c).

transform arrays. Step three of this algorithm is to negate the second half of the real and imaginary transform arrays. These arrays are then input to the complex FFT in step 4. The  $\Delta n(\tilde{\nu})$  values are found in the imaginary transform array output from step 4. The  $\Delta n(\tilde{\nu})$  value for the highest wavenumber is at point index  $\{2^{M+Z} - 0.5(2^{M+Z} - 2^M) + 1\}$ , where Z is the level of zero-filling used (see below), and they run to lower point indices with decreasing wavenumber.

This algorithm takes about the same time as the previous one. The result for the simulated methanol spectrum (Figure 2.2) is shown as curve (a) in Figure 2.9. The percent deviations cover a 4% range, as for the previous algorithm, but range from +2% to -2%. The agreement can be improved to some extent by additional zero-filling. To use one level of zero filling you add, in step 1 of the algorithm,  $2^M$  zero points to the  $2^M$  points described above. These points were added symmetrically, half at the beginning and half at the end of the array, leaving the rest of the algorithm as described. The result for one level of zero-filling is shown as curve b of Figure 2.9. One level of zero filling considerably improves the accuracy at the high-wavenumber end of the spectrum, reducing the percent deviation to about -0.1%, but does little to improve the low-wavenumber end of the  $n(\tilde{\nu})$ . A second level of zero-filling<sup>35</sup>, curve (c) of Figure 2.9,

makes little improvement. The errors involved in both of these algorithms are too large to allow them to be used with current experimental data.

*Ohta and Ishida's Hilbert transform algorithm* At this stage of the study we became aware of the recent paper by Ohta and Ishida<sup>26</sup> who carried out a similar study. The algorithm they found to be the most accurate was programmed. They emphasized the importance of continuing the data set to 0 cm<sup>-1</sup>, and of folding the data to simulate  $k(-\tilde{\nu}) = -k(\tilde{\nu})$ . The latter is in keeping with the condition under which the Hilbert transform is equivalent to the KK transform, while the former ensures that the correct phase relationship is maintained between the data for  $\tilde{\nu}$  and that for  $-\tilde{\nu}$ .

Ohta and Ishida's algorithm uses the FFT in its COMPLEX mode. In step 1 of the algorithm, the  $k$  spectrum, which consists of NP data points extending from XSP to XEP cm<sup>-1</sup>, is extended to 0 cm<sup>-1</sup> by adding N<sub>1</sub> zeros, and is then inverted in the zero wavenumber point to yield an array of 2(NP+N<sub>1</sub>)-1 points which is antisymmetric about the 0 cm<sup>-1</sup> point. (2N<sub>2</sub>+1) zero points are then added to the end of the array to make the array contain 2x2<sup>M</sup> points. The resulting array is shown schematically as curve (C) in Figure 2.6. This array forms the real input array to the FFT of step 2, with an array of zeros as the imaginary input array.

The FFT of this complex input consists of non-zero real and imaginary transform arrays, each containing 2x2<sup>M</sup> points. In step 3 of this algorithm, the second half of each transform array is replaced with zeros. The resulting real and imaginary arrays form the real and imaginary, respectively, inputs to step 4. In step 5, the values of  $\Delta n_{II}(\tilde{\nu}) = n(\tilde{\nu}) - n(\infty)$  are obtained from the imaginary array. However, we found that they are not in the first 2<sup>M</sup> points of the imaginary output as stated in Ohta and Ishida's paper, but they start at point (2N<sub>2</sub>+3) for the highest wavenumber and proceed to increasing index for decreasing wavenumber.

This algorithm uses arrays that are twice as long as those of previous algorithms, so it takes twice as long to execute. The result for the simulated methanol spectrum is shown in Figure 2.10. The percent deviations are now -0.4% at the high wavenumber end and reduce to -0.2% at the low-wavenumber end of the spectrum. If one level of zero-filling is used, by simply adding a further 2x2<sup>M</sup> zero points to the end of the array in step 1, the agreement is improved to about 0.07%, curve (b) of Figure 2.10, but the program then takes twice as long to execute, about 70 seconds for a spectrum containing between 4096 and 8192 data points. The same result was found for the simulated acetic acid spectrum in Figure 2.3.

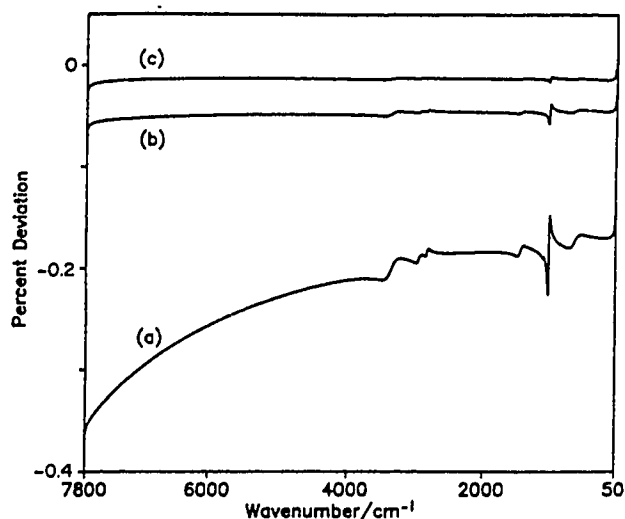


**Figure 2.10** Results for the simulated methanol spectrum (Figure 2.2). Curves (a) and (b): percent deviations from the correct  $n(\tilde{\nu})$  of Ohta & Ishida's Hilbert transformed  $n_H(\tilde{\nu})$ , calculated with no zero-filling, curve (a), and 1 level of zero-filling, curve (b). Identical results were obtained from the BZ algorithm, our preferred algorithm. Curve (c), percent deviation from the correct  $n(\tilde{\nu})$  of  $n_H(\tilde{\nu})$  calculated by the BZ algorithm with 2 levels of zero-filling.

*The BZ algorithm: the preferred algorithm* This is based on the indication from Ohta and Ishida's work that it is important to extend the data to  $0 \text{ cm}^{-1}$ , thus maintaining the correct phase difference between  $k(-\tilde{\nu})$  and  $k(\tilde{\nu})$ , and to ensure that  $k(-\tilde{\nu}) = -k(\tilde{\nu})$ . In fact, eqs. (2.2) and (2.3) suggest that the equivalence of the Hilbert and KK transforms hinges on these two points, in spite of their omission from some current algorithms.

Accordingly, step 1 of this algorithm consists of extending the  $k$  spectrum, which contains NP points between XSP and XEP  $\text{cm}^{-1}$ , to  $0 \text{ cm}^{-1}$  by adding zeros, adding an extra zero, inverting the array in this added zero point to generate an antisymmetric array, then adding  $N_2$  zero points to the beginning of the file and  $(N_2-1)$  zero points to the end of the file, to generate an antisymmetric array of length  $2 \times 2^M$ . This array is shown schematically in Figure 2.6 as curve (D).

This algorithm uses the FFT in its REAL mode, and the array is input as the real input to the FFT in step 2. The transform consists of a zero real transform array and a non-zero imaginary transform array, each of length  $2^M$ . In step 3 of the algorithm, the second half of the imaginary transform array is zeroed, and a further  $2^M$  zeros are added to the end of the array. The resulting array is the real input to the FFT in step 4. Step 5 of

the algorithm is to obtain the  $\Delta n_H(\tilde{\nu}) = n_H(\tilde{\nu}) - n(\infty)$  values from the real transform array from step 4, starting at the  $(N_2+1)$  point for the highest wavenumber and running to increasing index for decreasing wavenumber. This algorithm uses arrays half as large as those of Ohta and Ishida's method, but gives identical results to those shown in Figure 2.10. We show as curve (c) of Figure 2.10 the result with this, the preferred, algorithm, that was obtained with 2 levels of zero filling. This level of zero filling is not possible with Ohta and Ishida's algorithm under the memory limitations of Microsoft DOS, because of their double length arrays. The percent deviation with two levels of zero filling is up to 0.05%, which is the same as the percent deviation from the KK transform. The same result was found for the simulated acetic acid spectrum. For single band spectra, the maximum percent deviation using 2 levels of zero filling was 0.15% for 4  $\text{cm}^{-1}$  FWHH and 0.007% for 50  $\text{cm}^{-1}$  FWHH.

It is not immediately obvious why the BZ algorithm and that of Ohta and Ishida give identical results. In fact the identity stems from the FFT routines. To the FFT, Ohta and Ishida's input array is identical to ours except that it is phase-shifted by a constant amount for each point. Thus neither the real nor the imaginary transform arrays from step 2 of Ohta and Ishida's algorithm is zero while the real one is zero in our algorithm. Provided both of the transform arrays are used in step 4, Ohta and Ishida's method allows correctly for their asymmetrical input, but at the expense of using larger arrays.

### 2.3.3 Summary

The FFT-based Hilbert transform of  $k(\tilde{\nu})$  to  $n(\tilde{\nu})$  can be as accurate as the KK transform, provided the  $k$  spectrum is extended with zeros to 0  $\text{cm}^{-1}$ , and provided it is then inverted to yield an antisymmetric array to input to the FFT. The percent error of the calculated  $n(\tilde{\nu})$  is up to 0.05% for complex spectra.

It has been noted that this percent error is  $100[n_H(\tilde{\nu}) - n(\tilde{\nu})]/n(\tilde{\nu})$ , which overestimates the accuracy of the computation of the Hilbert transform which actually calculates  $\Delta n_H(\tilde{\nu}) = n_H(\tilde{\nu}) - n(\infty)$ . A percent deviation of 0.05% in  $n_H(\tilde{\nu})$  corresponds to a percent deviation of about 1% in  $\Delta n_H(\tilde{\nu})$ . The accuracy appears to be limited by the resolution with which the first Fourier transforms are defined. Zero-filling increases this resolution, and leads to a more accurate result for  $\Delta n_H(\tilde{\nu})$  from the second transform.

In passing it should be noted that the addition of an extra zero point after the 0  $\text{cm}^{-1}$  point in some of the algorithms is not essential. For the BZ algorithm omission of this extra zero causes the  $\Delta n_H(\tilde{\nu})$  output to start at point  $(N_2 + 2)$  instead of at  $(N_2+1)$ , and

for Ohta and Ishida's algorithm its inclusion causes the  $\Delta n_H(\tilde{\nu})$  output to start at point  $(2N_2+1)$  instead of  $(2N_2+3)$ .

The effects have been tested of relaxing the requirements to extend the data to zero and to make the  $k(\tilde{\nu})$  antisymmetric. The BZ algorithm was used, but (a) without extending the  $k(\tilde{\nu})$  to  $0 \text{ cm}^{-1}$ , and (b) extending it to  $0 \text{ cm}^{-1}$  but folding the array to make a symmetrical array instead of inverting it to make an antisymmetric array. In case (b) the accuracy of the results was as poor as that in our original method and Marshall's method. In case (a), the accuracy at high wavenumber was essentially the same as for the BZ algorithm, but deteriorated at low wavenumbers. The deterioration was to 0.4% and 1% when the lowest wavenumber in the  $k(\tilde{\nu})$  was  $50 \text{ cm}^{-1}$  and  $250 \text{ cm}^{-1}$ , respectively. Thus both requirements are necessary for results accurate to 0.05 to 0.1%.

## 2.4 Results: Transform from $n(\tilde{\nu})$ to $k(\tilde{\nu})$

An algorithm for Hilbert transformation from  $n(\tilde{\nu})$  to  $k(\tilde{\nu})$  was based on the BZ algorithm for  $k(\tilde{\nu})$  to  $n(\tilde{\nu})$ , with the necessary logical changes. First  $n$  at  $\tilde{\nu}_{\max}$  is subtracted from the  $n(\tilde{\nu})$  to give  $\Delta n(\tilde{\nu})$ . The  $\Delta n(\tilde{\nu})$  is then extended to  $0 \text{ cm}^{-1}$  by adding the value of  $\Delta n(\tilde{\nu})$  at the lowest wavenumber instead of by adding zeros. The extra point below  $0 \text{ cm}^{-1}$  is added, not as a zero but as the value of  $\Delta n(\tilde{\nu})$  at the lowest wavenumber, and the array is then folded about this point to create an array that is symmetrical.  $N_2$  zero points are then added to the beginning of the array and  $N_2-1$  are added to the end, to create a symmetric array of length  $2 \times 2^M$ .

If the  $\Delta n(\tilde{\nu})$  is extended to  $0 \text{ cm}^{-1}$  with zeros, the calculated  $k(\tilde{\nu})$  decreases steadily with decreasing wavenumber to a value  $-10\%$  of the highest peak. If the extra point is zero instead of the constant value, the discontinuity on the input to the FFT causes ripples on the transform.

This array is the real input to the FFT in REAL mode in step 2 of the Hilbert transform algorithm. The Fourier transform consists of a zero imaginary array and a non-zero real array, both of size  $2^M$ . In step 3 of the algorithm, the second half of the real transform is zeroed, and further  $2^M$  zero points are added to the end of the array. The resulting array is input to the FFT in step 4 and in step 5 the  $k(\tilde{\nu})$  is obtained from the imaginary transform array from step 4, starting at the  $N_2+1$  point for the highest wavenumber and running to increasing index with decreasing wavenumber.



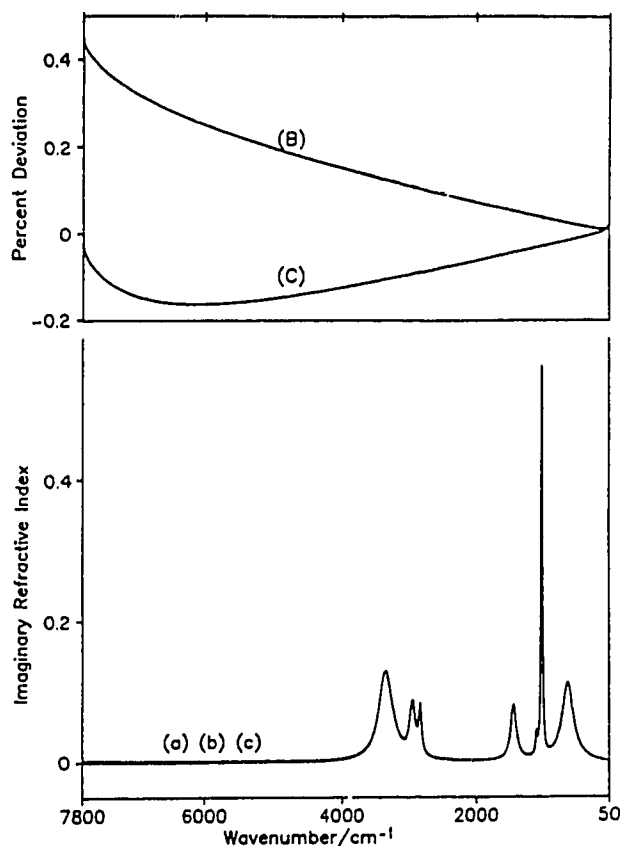


**Figure 2.11** Results of Kramers-Krönig and Hilbert transforms from  $n(\tilde{\nu})$  to  $k(\tilde{\nu})$ . Lower box, the correct  $k(\tilde{\nu})$ , curve (a), and those calculated by KK, curve (b), and Hilbert, curve (c), transformation of the simulated  $n(\tilde{\nu})$  of methanol. The three are indistinguishable on this scale. Upper box, deviations of the transformed  $k(\tilde{\nu})$  from the correct  $k(\tilde{\nu})$  as a percentage of the largest  $k$  value in the spectrum (Figure 2.2) for the KK transform, curve (B) and the BZ Hilbert transform, curve (C).

Figure 2.11 shows the results obtained for the simulated methanol spectrum of Figure 2.2. The lower box contains the correct  $k(\tilde{\nu})$ , curve (a), that calculated by KK transform, curve (b), and that calculated by this BZ Hilbert transform, curve (c). The KK transform is slightly higher than the other two at high wavenumbers. The upper box shows the deviation of the calculated and correct  $k$  values as a percentage of the largest  $k$  value in the spectrum for the KK transform, curve (B), and for the BZ Hilbert transform, curve (C). The maximum deviation is about  $-0.2\%$  of the largest  $k$  value for the Hilbert

transform and about +0.5% for the KK transform. The same result was obtained for acetic acid. For single band spectra (Figure 2.1) deviations were smaller; the greatest deviation for the BZ Hilbert transform was 0.06% for FWHH = 4 cm<sup>-1</sup> and -0.04% for FWHH=50 cm<sup>-1</sup>, and for the KK transform 0.07% for 4 cm<sup>-1</sup> FWHH and +0.1% for 50 cm<sup>-1</sup>. For 4 cm<sup>-1</sup> FWHH the deviations were on the sides of the peak while for 50 cm<sup>-1</sup> FWHH and the complex spectra they were as shown in Figure 2.11 (upper box). Zero-filling does not improve the accuracy of these  $n(\tilde{\nu})$  to  $k(\tilde{\nu})$  Hilbert transforms.

## 2.5 Results: Transforms from $k(\tilde{\nu})$ to $n(\tilde{\nu})$ for Truncated $k$ Spectra

It frequently happens that experimental  $k$  spectra are incomplete and end half-way up an absorption band rather than in the baseline. In such cases neither KK nor Hilbert transforms can be expected to give correct results, indeed the correct results are unknown. Sometimes, however, the complete spectrum is known, but it is necessary to refine a partial spectrum on its own before merging it with previously recorded spectra to cover a broader wavenumber range. Thus it is of interest to explore whether modifications can be made to a  $k$  spectrum that terminates above the baseline, in order to improve the  $n(\tilde{\nu})$  calculated from it.

A simple procedure that is similar to triangular apodization has been found usually to improve the transformed result. Figure 2.12 shows in the lower box the full  $k$  spectrum simulated for methanol, curve (a), offset from the  $k$  spectrum truncated at 700 cm<sup>-1</sup> curve (b), which in turn is offset from the  $k$  spectrum truncated at 700 cm<sup>-1</sup> and linearly extended from the last point to  $k = 0$  at 0 cm<sup>-1</sup>, curve (c). The upper box shows the correct  $n(\tilde{\nu})$ , curve A, and those obtained by KK transformation, curves BK and CK, and by BZ Hilbert transformation, curves BH and CH. The  $n$  spectra obtained by KK transformation are indistinguishable from those obtained by BZ Hilbert transformation in the figure. Comparison of curves BK and CK (or BH and CH) shows that the linear extension to low wavenumber improves the transform of the truncated file. Quantitatively, the percent deviations from the correct  $n(\tilde{\nu})$  are reduced from about 10% to about 1%.

This method of extending the  $k(\tilde{\nu})$  to zero at 0 cm<sup>-1</sup> has been applied to acetic acid, and to many other test systems with and without peaks below the truncation point. It leads to an improvement in the deviations at low wavenumbers by a factor of about 10 in all cases.

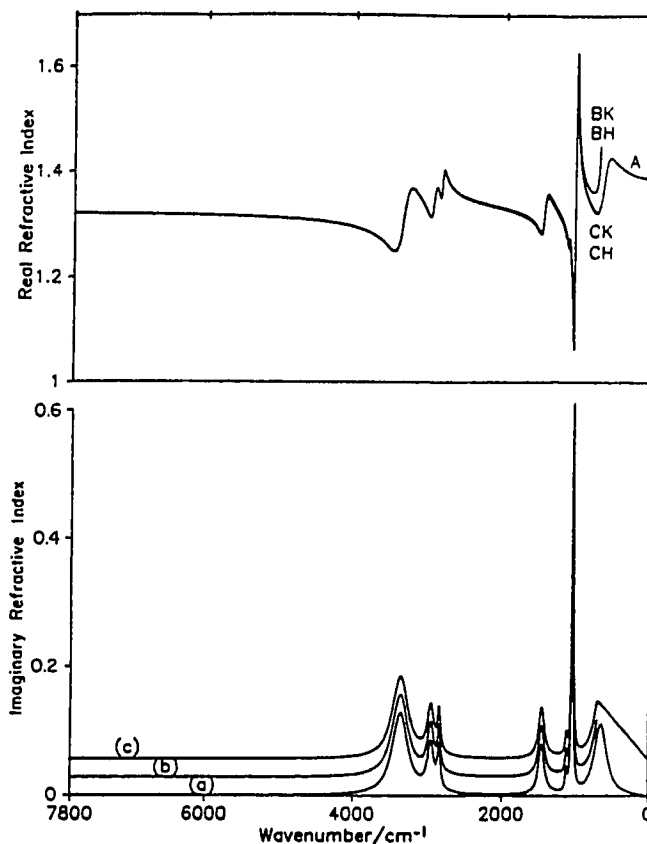


**Figure 2.12**  $k(\tilde{\nu})$  to  $n(\tilde{\nu})$  transform of a truncated  $k$  spectrum. Lower box: curve (a), the complete  $k$  spectrum; curve (b), the  $k$  spectrum truncated at  $700\text{ cm}^{-1}$ ; curve (c), curve (b) extended linearly to 0 at  $0\text{ cm}^{-1}$ ; curves (b) and (c) are offset for clarity. Upper box: curve A, the correct  $n$  spectrum; curves BK and CK,  $n_K(\tilde{\nu})$  obtained by KK transform of curves (b) and (c) of the lower box; curves BH and CH,  $n_H(\tilde{\nu})$  obtained by BZ Hilbert transform of curves (b) and (c) of the lower box.

## 2.6 FFT Program Listing

```

C      SUBROUTINE FFT(HLBT, N, N2POW, X, Y)
C      X - REAL ARRAY, Y - IMAGINARY ARRAY
C      2N- NUMBER OF POINTS IN ARRAY X ON ENTERING SUBROUTINE FOR FFT OF REAL
C      DATA.
C      N - NUMBER OF POINTS TO BE TRANSFORMED IN EACH ARRAY, X,Y; N=2N2POW
C      HLBT=0 - COMPLEX FFT, OTHERWISE, REAL FFT

```

```
SUBROUTINE FFT(HLBT, N, N2POW, X, Y)
  REAL I, I1, I2, I3, I4
  INTEGER HLBT, PASS, SEQLOC, L(15)
  DIMENSION X(1), Y(1)
  EQUIVALENCE (L13,L(1)), (L12,L(2)), (L11,L(3)), (L10,L(4)), (L9,L(5)),
+             (L8,L(6)), (L7,L(7)), (L6,L(8)), (L5,L(9)), (L4,L(10)), (L3,L(11)),
+             (L2,L(12)), (L1,L(13)), (L0,L(14)), (LA,L(15))

C    SHUFFLING DATA FOR REAL FFT
  IF(HLBT.EQ.0) GOTO 102
  DO 101 K=1,N
    K2=K*2
    X(K)=X(K2-1)
101  Y(K)=X(K2)

C    FFT; COOLEY-TUKEY ALGORITHM
102  NTHPOW=2**N2POW
     N4POW=N2POW/2
     IF(N4POW.EQ.0) GOTO 3
     DO 2 PASS=1,N4POW
       NXTLTH=2**(N2POW-2*PASS)
       LENGTH=4*NXTLTH
       SCALE=6.283185307/LENGTH
       DO 2 J=1,NXTLTH
         ARG=(J-1)*SCALE
         C1=COS(ARG)
         S1=SIN(ARG)
         C2=C1*C1-S1*S1
         S2=C1*S1*2
         C3=C1*C2-S1*S2
         S3=C2*S1+S2*C1
       DO 2 SEQLOC=LENGTH,NTHPOW,LENGTH
         J1=SEQLOC-LENGTH+J
         J2=J1+NXTLTH
         J3=J2+NXTLTH
```

```
J4=J3+NXTLTH
R1=X(J1)+X(J3)
R2=X(J1)-X(J3)
R3=X(J2)+X(J4)
R4=X(J2)-X(J4)
I1=Y(J1)+Y(J3)
I2=Y(J1)-Y(J3)
I3=Y(J2)+Y(J4)
I4=Y(J2)-Y(J4)
X(J1)=R1+R3
Y(J1)=I1+I3
IF(J.EQ.1) GOTO 1
X(J3)=C1*(R2+I4)+S1*(I2-R4)
Y(J3)=-S1*(R2+I4)+C1*(I2-R4)
X(J2)=C2*(R1-R3)+S2*(I1-I3)
Y(J2)=-S2*(R1-R3)+C2*(I1-I3)
X(J4)=C3*(R2-I4)+S3*(I2+R4)
Y(J4)=-S3*(R2-I4)+C3*(I2+R4)
GOTO 2
1  X(J3)=R2+I4
   Y(J3)=I2-R4
   X(J2)=R1-R3
   Y(J2)=I1-I3
   X(J4)=R2-I4
   Y(J4)=I2+R4
2  CONTINUE
3  IF(N2POW.EQ.2*N4POW) GOTO 5
   DO 4 J=1,NTHPOW,2
     R=X(J)+X(J+1)
     X(J+1)=X(J)-X(J+1)
     X(J)=R
     I=Y(J)+Y(J+1)
     Y(J+1)=Y(J)-Y(J+1)
4   Y(J)=I
5   DO 6 J=1,15
```

```
L(J)=1
6  IF(J.LE.N2POW) L(J)=2**(N2POW+1-J)
    IJ=1
    DO 7 JA=1,LA
    DO 7 J0=JA,L0,LA
    DO 7 J1=J0,L1,L0
    DO 7 J2=J1,L2,L1
    DO 7 J3=J2,L3,L2
    DO 7 J4=J3,L4,L3
    DO 7 J5=J4,L5,L4
    DO 7 J6=J5,L6,L5
    DO 7 J7=J6,L7,L6
    DO 7 J8=J7,L8,L7
    DO 7 J9=J8,L9,L8
    DO 7 J10=J9,L10,L9
    DO 7 J11=J10,L11,L10
    DO 7 J12=J11,L12,L11
    DO 7 JI=J12,L13,L12
    IF(IJ.GE.JI) GOTO 7
    R=X(IJ)
    X(IJ)=X(JI)
    X(JI)=R
    I=Y(IJ)
    Y(IJ)=Y(JI)
    Y(JI)=I
7  IJ=IJ+1

C  POST-PROCESSING FOR REAL FFT
    IF (HLBT.EQ.0) RETURN
    ARG=3.1415927/FLOAT(N)
    C1=COS(ARG)
    S1=-SIN(ARG)
    C1JX=1.
    S1JX=0.
    N2=N/2
```

```
N2P1=N2+1
DO 20 J=2,N2P1
NP2MJ=N+2-J
SORR1=X(J)+X(NP2MJ)
SORI1=Y(J)-Y(NP2MJ)
R=C1JX
C1JX=C1JX*C1-S1JX*S1
S1JX=R*S1+S1JX*C1
SORR2=X(J)-X(NP2MJ)
SORI2=Y(J)+Y(NP2MJ)
SORR3=C1JX*SORR2-S1JX*SORI2
SORI3=C1JX*SORI2+S1JX*SORR2
Y(J)=0.5*(SORI1-SORR3)
X(J)=0.5*(SORR1+SORI3)
IF(J.EQ.N2P1) GOTO 20
Y(NP2MJ)=-0.5*(SORI1+SORR3)
X(NP2MJ)=0.5*(SORR1-SORI3)
20  CONTINUE
X(1)=X(1)+Y(1)
Y(1)=0.
RETURN
END
```

## 2.7 References and Notes

1. R. de L. Krönig, J. Opt. Soc. Am. **12**, 547 (1926); Physica **3**, 1009 (1936).
2. H. A. Kramers, Atti Congr. Int. Fis. Como **2**, 545 (1927).
3. S. Maeda and P. N. Schatz, J. Chem. Phys. **36**, 571 (1962).
4. F. Stern, Solid State Phys. **15**, 331 (1963).
5. E. E. Bell, *Handbuch der Physik*. Edited by S. Flugge. Vol. XXV/12a, pp 28–31; Light and Matter 1a. Edited by L. Genzel. Springer-Verlag, Berlin, Heidelberg, 1967.

6. H. Frohlich, *Theory of Dielectrics*, 2nd ed. Oxford University Press, London, 1958. p8.
7. F. C. Jahoda, Phys. Rev. **107**, 1261 (1957).
8. F. W. King, J. Chem. Phys. **71**, 4726 (1979).
9. Note that this is not quite correct, because only  $\ln\{R(\omega')/R(\omega'')\}$  can be obtained by Kramers-Krönig transformation of the phase of reflection (Ref. 8).
10. T. G. Goplen, D. G. Cameron, and R. N. Jones, Appl. Spectrosc. **34**, 657 (1980).
11. J. E. Bertie, V. Behnam, and R. N. Jones, Appl. Spectrosc. **39**, 401 (1985); **40**, 427 (1986).
12. G. M. Hale, M. R. Querry, A. N. Rusk, and D. Williams, J. Opt. Soc. Am. **62**, 1103 (1972).
13. A. E. Tshmel and V. I. Vettegren, Spectrochim. Acta **29A**, 1681 (1973).
14. V. M. Zolotarev, B. A. Mikhailov, L. I. Alperovich, and S. I. Popov, Opt. Spectrosc. **27**, 430 (1969).
15. B. Gross, Phys. Rev. **59**, 748 (1941).
16. E. C. Titchmarsh, *Introduction to the Theory of Fourier Integrals*, 2nd ed. Clarendon Press, Oxford, 1948. Chapter 5; 3rd ed., Oxford University Press, London, 1962. pp119-120.
17. M. G. Sceats and G. C. Morris, Phys. Status Solidi A **14**, 643 (1972).
18. C. W. Peterson and B. W. Knight, J. Opt. Soc. Am. **63**, 1238 (1973).
19. B. Harbecke, Appl. Phys. A **40**, 151 (1986).
20. J. A. Bardwell and M. J. Dignam, Anal. Chim. Acta **172**, 101 (1985).
21. J. E. Bertie and H. H. Eysel, Appl. Spectrosc. **39**, 392 (1985).
22. G. R. Fowles, *Introduction to Modern Optics*. Holt Rinehart & Winston, New York, 1975.



23. J. A. Fahrenfort in *Infrared Spectroscopy and Molecular Structure*. Edited by M. Davies. Elsevier, New York, 1963. Chapter XI.
24. J. C. Decius and R. M. Hexter, *Molecular Vibrations in Crystals*. McGraw-Hill, New York, 1977.
25. R. N. Bracewell, *Science* **248**, 697 (1990).
26. K. Ohta and H. Ishida, *Appl. Spectrosc.* **42**, 952 (1988).
27. D. G. Cameron, J. P. Hawranek, P. Neelakantan, R. P. Young, and R. N. Jones, National Research Council of Canada Bulletin **16**. *Computer Programs for Infrared Spectrophotometry*. Program 46.
28. D. C. Champeney, *Fourier Transforms and Their Physical Applications*. Academic Press, London, 1973. p.22.
29. R. C. L. Ng and G. Horlick, *Spectrochim. Acta* **36B**, 529 (1981).
30. Bede Liu (editor), *Digital Filters and the Fast Fourier Transform*. Halsted Press, New York, 1975.
31. R. C. L. Ng, Ph. D. thesis, University of Alberta, 1981.
32. A. Zachor, *J. Opt. Soc. Am.* **56**, VI (1966).
33. A. G. Marshall, in *Fourier, Hadamard and Hilbert Transforms in Chemistry*. Edited by A. G. Marshall. Plenum, New York, 1982. p. 108.
34. F. G. Herring, A. G. Marshall, Paul S. Phillips, and D. C. Roe, *J. Mag. Res.* **37**, 292 (1980).
35. The second level of zero-filling consists of adding  $2^M$  zero points to each end of the data set used for one level of zero-filling.

## Chapter 3 Accuracy of Current Methods of Obtaining Optical Constants from Multiple Attenuated Total Reflection (ATR) Measurements Using the CIRCLE\* Cell\*\*

### 3.1 Introduction

The CIRCLE cell method for obtaining the optical constants of liquids was first described in 1985<sup>1</sup>, and refinement of the method was described with further details in 1988<sup>2</sup>. The light beam is internally reflected about 6 times in the original CIRCLE cell, which means that pATR bands that are stronger than the OH stretching band of water<sup>3</sup> absorb 99% of the incident radiation or more, and can not be measured accurately. The method was, consequently, limited to bands in the imaginary refractive index spectrum,  $k(\tilde{\nu})$ , that had  $k_{\max}$  less than about 0.3. Further, the programs to compute the optical constants from the pATR spectra were written for a 1978-vintage computer, the Aspect 2000 computer which controls our Bruker IFS 113V FTIR spectrometer. This computer is slow by today's standards, and the memory is very small, only 160 Kbytes, so the software had to be written to accommodate these limitations.

Since 1988 we have developed a short liquid holder for our CIRCLE cell, in which the radiation is internally reflected about 3 times. This allows pATR bands to be measured accurately even if the imaginary refractive index at the peak of the  $k(\tilde{\nu})$  band is about 0.6. Further, we have transferred all of our data manipulation to PC-type computers which run under Microsoft DOS or, for very large data sets, run under IBM OS/2. The programs have been completely rewritten, from the PASCAL of the Aspect 2000 computer, in Microsoft FORTRAN, and have been combined and modified extensively to give a semi-automatic refinement process.

The paper of Huang and Urban<sup>4</sup> has reminded us that these improvements to our method and programs have not been described in the literature. In this Chapter, we provide an up-to-date account of our method and computer programs and give the results of tests on simulated pATR spectra to illustrate the accuracy of the algorithms and programs. The simulated data includes the single band spectra used by Huang and Urban,

---

\* CIRCLE is a registered trade mark of Spectra-Tech Inc., Stamford, CT.

\*\* A version of this chapter has been published. Bertie, Zhang and Manji, Appl. Spectrosc. **46**, 1660 (1992).

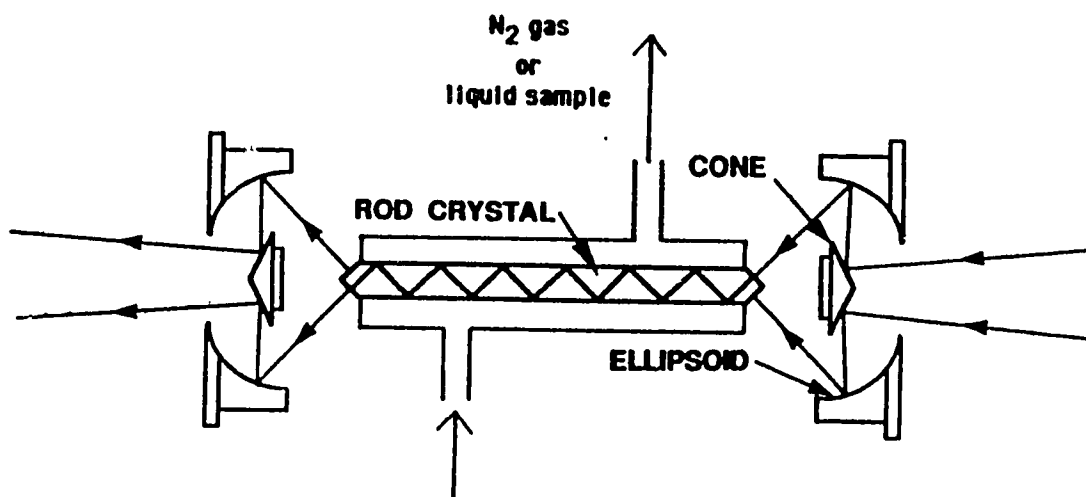


Figure 3.1 The essential features of the CIRCLE cell.

and also includes our own simulations of the spectra of pure liquid methanol and glacial acetic acid.

### 3.2 The Published Method

Our published method for obtaining optical constants from pATR spectra has been described in Refs. 1 and 2, and has been correctly summarized by Huang and Urban<sup>4</sup>. It is summarized briefly in this section for reference.

The effective number of reflections (NRF) in the CIRCLE cell, which is schematically shown in Figure 3.1, is calibrated<sup>2</sup> by measuring the pATR spectrum of benzene, for which the refractive indices are known to a few percent<sup>2,5-8</sup>, and calculating the pATR values at the peaks of about 13 bands<sup>2</sup> of benzene. The relation between the pATR and the refractive indices can be calculated through Fresnel equations. The reflectivity at the interface between a nonabsorbing medium (ATR rod) of refractive index  $n_r$  and an absorbing medium (liquid) of refractive index  $\hat{n}(\tilde{\nu}) = n(\tilde{\nu}) + i k(\tilde{\nu})$ , for light traveling in the ATR rod and polarized parallel to the interface, is<sup>1</sup>

$$R_s = \frac{n_r^2 \cos^2 \theta - 2an_r \cos \theta + Y}{n_r^2 \cos^2 \theta + 2an_r \cos \theta + Y} \quad (3.1)$$

where  $\theta$  is the angle of incidence,

$$Y = [X^2 + 4n^2k^2]^{1/2}$$

and  $a = [(X + Y)/2]^{1/2}$

where  $X = n^2 - k^2 - n_r^2 \sin^2 \theta$ .

If the angle of incidence,  $\theta$ , is  $45^\circ$  as in the CIRCLE, the reflectivity for the other polarization,  $R_p$ , is

$$R_p = R_s^2 \quad (3.2)$$

and therefore, the pATR can be calculated by

$$\text{pATR} = -\log_{10}\{0.5[R_s^{\text{NRF}} + R_s^{2\text{NRF}}]\} \quad (3.3)$$

where  $R_p^{\text{NRF}}$  has been replaced by  $R_s^{2\text{NRF}}$ . This equation is appropriate for the conditions that exist<sup>1</sup> in the CIRCLE cell, namely  $45^\circ$  incidence, equal intensities of s- and p-polarized light, and retention of polarization throughout the NRF reflections. The root-mean-squared percent deviation (RMSPD) between the measured and calculated peak pATR values is calculated for various values of NRF. The NRF value that gives the smallest RMSPD is used in the refinement.

The experimental pATR spectrum is usually extended by adding zero values from about  $6000 \text{ cm}^{-1}$  to about  $8000 \text{ cm}^{-1}$ , because the absorption is very weak in this region. The real refractive index,  $n_\infty$ , at the high wavenumber limit of the extended pATR spectrum is calculated from the wavenumber-dependence of the real refractive index in the visible region of the spectrum<sup>2</sup>. With these two pieces of data the method is the following:

**Step 1.** Calculate an approximate imaginary refractive index spectrum,  $k_a(\tilde{\nu})$ , from the experimental pATR spectrum, by assuming<sup>1</sup> that the pATR spectrum is an absorbance spectrum for a transmission cell with pathlength equal to twice the penetration depth of the evanescent wave times the number of reflections. The equation used is

$$k_a(\tilde{\nu}) = \frac{2.303}{4\pi\tilde{\nu}(\text{NRF})(2d)} \text{pATR}(\tilde{\nu}) \quad (3.4)$$

where NRF is the number of reflections in the CIRCLE cell and  $d$ , the penetration depth of the evanescent wave at each reflection, can be calculated from the distance required for the electric vector to decrease by  $e^{-1}$  in a nonabsorbing medium. This is<sup>1</sup>

$$d = \frac{\lambda}{2\pi[n_r^2 \sin^2 \theta - n^2]^{1/2}} \quad (3.4a)$$

where  $\lambda$  is the vacuum wavelength of the radiation,  $n_r$  and  $n$  are the real refractive indices of the rod and sample, respectively, and  $\theta$  is the angle of incidence, 45° in the CIRCLE cell.

Then  $k_1(\tilde{\nu}) = k_a(\tilde{\nu}) \{ 1 + \sqrt{k_a(\tilde{\nu})} \}$  is calculated and used as the initial  $k(\tilde{\nu})$ . Program CIRCLEP performs step 1.

**Step 2.** Calculate  $n(\tilde{\nu})$  from  $n_\infty$  and Kramers-Krönig (KK) transform of  $k(\tilde{\nu})$ . The transform is done by an algorithm using two successive fast Fourier transforms (FFTs), in program AHILBERT.

**Step 3.** Calculate the pATR spectrum from  $k(\tilde{\nu})$  and  $n(\tilde{\nu})$  from eqs. (3.1) and (3.3).

**Step 4.** Adjust the  $k(\tilde{\nu})$  spectrum by calculating a new  $k(\tilde{\nu})$  spectrum via the equation<sup>2</sup>

$$k_{\text{NEW}}(\tilde{\nu}) = k_{\text{OLD}}(\tilde{\nu}) \{ 1 + \text{DMP}(F(\tilde{\nu})-1) \} \quad (3.5)$$

where  $F(\tilde{\nu}) = \text{pATR}_{\text{OBS}}(\tilde{\nu}) / \text{pATR}_{\text{CALC}}(\tilde{\nu}) \quad (3.6)$

and DMP is a damping factor between 1, no damping, and 0, no change in  $k(\tilde{\nu})$ . This procedure assumes that  $k(\tilde{\nu})$  has to be increased if  $\text{pATR}_{\text{CALC}}(\tilde{\nu})$  must be increased.

Steps 3 and 4 are done by program REFLECT.

**Step 4a.** Repeat steps 3 and 4 until  $k(\tilde{\nu})$  converges at constant  $n(\tilde{\nu})$ .

**Step 5.** Repeat step 2, then repeat steps 3, 4, 4a and 2 until both  $n(\tilde{\nu})$  and  $k(\tilde{\nu})$  have converged and the pATR spectrum is well fitted. Convergence and fit were judged by

$$\text{FSUM} = \sum [\text{pATR}(\tilde{\nu})_{\text{OBS}} - \text{pATR}(\tilde{\nu})_{\text{CALC}}]^2 \quad (3.7)$$

the sum of the squared deviations over the entire spectrum. FSUM was usually near 10 initially and near  $1 \times 10^{-4}$  when successful calculations were stopped.

### 3.3 Recent Changes and the Present Method

#### 3.3.1 General

The pATR spectra are currently transferred<sup>7</sup> from the Bruker instrument to a personal computer running under the DOS operating system. They are imported into

SpectraCalc\* or GRAMS/386\* and stored in SpectraCalc's .SPC format. All of our programs read and write spectral files in this .SPC format.

The programs used on the Aspect computer were written for the PC in Turbo PASCAL and improved considerably in the process. They were then also coded in Microsoft FORTRAN, version 5.0, and the FORTRAN programs were found to execute about twice as fast as the corresponding PASCAL program. Henceforth all development was done in FORTRAN, and version 5.1 of Microsoft FORTRAN is currently used. A math co-processor is used, and the programs are now usually run on a 33MHz 486 DX computer. They also run on a 16MHz 386 SX computer with a 387 math co-processor, but about 6 times more slowly. SpectraCalc and GRAMS/386 are used for general spectral manipulation and plotting.

### 3.3.2 *Changes to the Calibration Procedure*

The effective number of reflections is now determined by calculating the areas under bands of benzene for several different values of NRF from the known optical constants of benzene<sup>8</sup>, and comparing them with the areas under the same bands in the experimental spectrum. Again the value of NRF that gives the minimum root-mean-squared percent deviation of the calculated areas from the measured ones is used in the refinement procedure. This calibration with areas is less susceptible to baseline errors than is the previous calibration with peak heights, and the values of NRF determined from several different spectra agree to about 1%, which permits a 1% accuracy in the optical constants obtained by these methods.

### 3.3.3 *Changes to Step 2, the Kramers-Krönig Transform of $k(\tilde{\nu})$ to $n(\tilde{\nu})$*

The KK transform may be done by calculating the integral in eq. (3.5) of Ref. 1. For digital data with constant spacing Ohta and Ishida<sup>9</sup> have shown that the principal value of the sum can be calculated with greatest accuracy by using McLaurin's equation. We now use<sup>10</sup> McLaurin's equation and call this procedure the KK transform.

The KK transform may also be done via two successive fast Fourier transforms with data manipulation before and between the transforms. This performs a Hilbert transform, which is equivalent to the KK transform for quantities with the properties of the optical constants. This procedure is called the Hilbert transform<sup>10</sup>. The correct algorithms for the transform have been discussed in Chapter 2.

---

\* SpectraCalc and GRAMS/386 are registered trademarks of Galactic Industries Corporation, Salem, NH.

The algorithm used in program AHILBERT, for the Hilbert transform from  $k(\tilde{\nu})$  to  $n(\tilde{\nu})$  via two successive fast Fourier transforms, has been shown to give errors of up to 4% in the calculated  $n(\tilde{\nu})$  spectrum<sup>9,10</sup>. A new procedure for the  $k(\tilde{\nu})$  to  $n(\tilde{\nu})$  Hilbert transform has been presented and shown<sup>10</sup> to give results that are accurate to better than 0.1% in  $n(\tilde{\nu})$ , only marginally poorer than the 0.05% accuracy given by the KK transform program<sup>10</sup>. For the transform from  $n(\tilde{\nu})$  to  $k(\tilde{\nu})$ , a different new procedure for the Hilbert transform yields  $k(\tilde{\nu})$  values accurate to <0.2% error of the largest  $k$  value in the spectrum – better accuracy than the <0.4% of the largest  $k$  value obtained from the KK transform program<sup>10</sup>.

It is well known that the KK and Hilbert transforms from  $k(\tilde{\nu})$  to  $n(\tilde{\nu})$  must be inaccurate if the  $k$  spectrum is incomplete. The most common form of incompleteness is that the low-wavenumber end of the spectrum occurs on the side of an absorption band, so that  $k(\tilde{\nu})$  is not near the baseline at the end of the spectrum. It has been shown<sup>10</sup> that both the KK and Hilbert transforms can be improved by a factor of 10 if the  $k$  spectrum is extended linearly from the  $k$  value at the lowest wavenumber in the spectrum to zero at 0  $\text{cm}^{-1}$ .

Consequently, our programs for processing CIRCLE cell spectra have been improved by replacing the inaccurate Hilbert transform program AHILBERT by either the new Hilbert transform program or the KK transform program.

Because the KK transform takes about 2 minutes for an 8192-point spectrum on a 33MHz 486DX computer and the Hilbert transform program takes only about 2 seconds if no zero-filling is used<sup>10</sup>, the Hilbert transform with no zero-filling is usually used until the refinement converges, and the more accurate KK transform program is then used for the small number of cycles needed to complete the refinement. In both cases the spectral data can be extended<sup>10</sup> if desired to improve the accuracy of the optical constants calculated from an incomplete pATR spectrum.

The KK transform program also includes the option of approximately tripling its execution speed, at the expense of insignificant reduction in accuracy at high wavenumbers, where the  $k(\tilde{\nu})$  values are all essentially zero, by performing the transform only at intervals of 100 or 200  $\text{cm}^{-1}$  at wavenumbers above a critical wavenumber, and then interpolating the real refractive index between the calculated points. The critical wavenumber is usually chosen near 5000  $\text{cm}^{-1}$ .

### 3.3.4 Changes to the Refinement Cycle

The much greater speed and memory size of 386 and 486-based personal computers than the Aspect 2000 enable spectra of 8192 (8K) data points, and even 16K or 32K data points under OS/2, to be processed. They also mean that step 4a of the published method can be omitted. This step was included to speed up the refinement by refining  $k(\tilde{\nu})$  several times before re-calculating  $n(\tilde{\nu})$ , because the KK transform was quite slow on the Aspect, even though it used an assembly language FFT routine. On the PCs, a new  $n(\tilde{\nu})$  is calculated after every change in the  $k(\tilde{\nu})$ , so step 5 of the refinement procedure is now:

**Step 5.** Repeat step 2, then repeat steps 3, 4 and 2 until  $n(\tilde{\nu})$  and  $k(\tilde{\nu})$  have converged and the pATR spectrum is well fitted. The convergence and fit are judged by FSUM, as before, and also by RMSPD, the root-mean-squared percent deviation of the calculated pATR spectrum from the observed one, where

$$\text{RMSPD} = \sqrt{\frac{1}{N} \sum \left[ \frac{\text{pATR}(\tilde{\nu})_{\text{OBS}} - \text{pATR}(\tilde{\nu})_{\text{CALC}}}{\text{pATR}(\tilde{\nu})_{\text{OBS}}} \right]^2} \times 100\% \quad (3.8)$$

and the sum is over the whole spectrum of N points. The contribution is set to zero for wavenumbers at which the observed pATR value is less than  $1.6 \times 10^{-5}$ .

### 3.3.5 The Use of One Program to Permit Refinement under Computer Control

The current procedures require the experimental pATR spectrum to be cleaned of negative (noise) ordinate values and, if the spectrum is one for which no approximate  $k$  spectrum is available, the pATR spectrum is first processed by CIRCLEP<sup>1,2</sup> to calculate the approximate  $k$  spectrum. The pATR spectrum and the approximate  $k$  spectrum are then processed by a single program HREF, which first calculates the  $n$  spectrum and then carries out the refinement cycle, steps 3, 4, and 2, automatically until RMSPD reaches a requested limit or until FSUM reaches a requested limit. HREF then writes the final  $k$ ,  $n$  and calculated pATR spectra to disk, and also creates a file of RMSPD and FSUM values after each cycle, to record the progress of the refinement. Facility also exists for intermediate spectra to be placed on disk during the refinement, and for the initial calculation of  $n(\tilde{\nu})$  to be omitted if a suitable  $n$  spectrum exists. For the most accurate work, the experimental pATR spectrum and the  $k$  and  $n$  spectra output by HREF are read into KREF, which is identical to HREF except that it uses the KK transform and, consequently, is much slower but more accurate.



When a strong, sharp band, such as the  $1035\text{ cm}^{-1}$  band of liquid methanol, was processed under the published refinement scheme, the calculations frequently diverged rather than converged. Such bands cause no difficulty in the new programs when a damping factor of about 0.4 is used in eq. (3.5).

### 3.4 The Accuracy of the Current Programs

Huang and Urban<sup>4</sup> tested the accuracy of the Bertie and Eysel and the Dignam and Mamiche-Afara algorithms, by synthesizing a  $k$  spectrum which consists of a single Lorentzian band and synthesizing the corresponding  $n$  spectrum, following eqs. (1) and (2) of Ref. 4. They calculated 2048-point  $k$  spectra between  $2000$  and  $1400\text{ cm}^{-1}$ , using Lorentzians centered at  $1700\text{ cm}^{-1}$  with  $6\text{ cm}^{-1}$  full width at half height and several different values of  $k_{\text{max}}$ . They then calculated the pATR spectrum for a single reflection of unpolarized light at  $45^\circ$  incidence, with  $n_r = 2.38$  for the ATR rod and  $n_\infty = 1.5$  for the sample. They then used the two algorithms to recover the  $k(\tilde{\nu})$  and  $n(\tilde{\nu})$  from the pATR spectrum. We call the recovered spectra the  $k'(\tilde{\nu})$  and  $n'(\tilde{\nu})$ .

To assess the accuracy of the algorithms they compared the  $k'(\tilde{\nu})$  and  $n'(\tilde{\nu})$  with the original  $k(\tilde{\nu})$  and  $n(\tilde{\nu})$ . To obtain a numerical measure of accuracy, they calculated the quantities  $\delta_k$  and  $\delta_n$ , where  $\delta_k$  is the root-mean-squared deviation of the recovered  $k'$  values from the original  $k$  values divided by the root-mean-squared  $k$  value and  $\delta_n$  is the root-mean-squared deviation of the recovered  $n'$  values from the original  $n$  values divided by the root-mean-squared value of  $[n(\tilde{\nu}) - n_\infty]$  by eqs. (6) and (7) of Ref. 4. The averages were taken over the region within  $15\text{ cm}^{-1}$  of the band center, i.e. between  $1715$  and  $1685\text{ cm}^{-1}$ .

Table 3.1 presents the results obtained for these tests from our current programs. The calculation of optical constants was judged successful if the refinement converged, which means, in these tests, if the quantity FSUM in eq. (3.7) reduced to  $2 \times 10^{-6}$ . This did not occur, so the calculation was not successful, for  $k_{\text{max}}$  greater than 0.60 with  $n_\infty = 1.5$ . For  $n_\infty = 1.4$  or  $1.3$  optical constants were recovered successfully for  $k_{\text{max}}$  values up to 0.70 or 0.80, respectively. These maximum  $k_{\text{max}}$  values for successful recovery of the optical constants are independent of the wavenumber at which the bands occur and are essentially independent of the bandwidth, at least up to  $20\text{ cm}^{-1}$  full width at half height.

**Table 3.1** Accuracy measures of our current program KREF <sup>a</sup> for various spectra

Quantity	$k_{\text{max}}$ for a single Lorentzian band, FWHH = 6 cm <sup>-1</sup>				CH <sub>3</sub> COOH	CH <sub>3</sub> OH
	0.1	0.3	0.4	0.6		
DMP <sup>b</sup>	1	1	1	0.1	1	0.4
RMSPD <sup>c</sup>	0.10	0.011	0.0083	0.0060	0.0047	0.0049
$\delta_k \times 100$ <sup>d</sup>	0.084	0.25	0.30	0.45	0.025	0.035
$\delta_n \times 100$ <sup>d</sup>	0.51	0.57	0.58	0.67	0.073	0.093

- a) The accuracy tests are described in the text.  $n_\infty = 1.5$  for the results in columns 2 to 5 and 1.325 for acetic acid and methanol. In all cases the program stopped when FSUM in eq. (3.7) reached  $2 \times 10^{-6}$ .
- b) The damping factor used in eq. (3.5).
- c) The root-mean-squared percent deviation of the calculated pATR spectrum from the observed one, defined by eq. (3.8).
- d)  $\delta_k$  is the root-mean-squared deviation of the recovered  $k'$  values from the original  $k$  values divided by the root-mean-squared  $k$  value.  $\delta_n$  is the root-mean-squared deviation of the recovered  $n'$  values from the original  $n$  values divided by the root-mean-squared value of  $n(\tilde{\nu}) - n_\infty$  [eqs. (6) and (7) of Ref. 4]. For the single Lorentzian band spectra (columns 2 to 5) the averages for  $\delta_k$  and  $\delta_n$  were taken only from 1715 to 1685 cm<sup>-1</sup>. For the acetic acid and methanol spectra these  $\delta_k$  and  $\delta_n$  averages were taken over the entire spectrum, as were the averages for RMSPD and FSUM for all spectra.

Table 3.1 gives the values of Huang and Urban's  $\delta_k$  and  $\delta_n$  quantities for the tests with  $n_\infty = 1.5$  and FWHH = 6 cm<sup>-1</sup>. These values can be compared with those in Huang and Urban's Tables II to IV<sup>4</sup>, where the entries in the rows labeled "McLaurin" should be used. The present  $\delta_k$  and  $\delta_n$  values are far superior to those reported<sup>4</sup> in the rows labeled "Bertie" in Tables II and III for the previously published Bertie and Eysel algorithm, and are essentially the same as those reported<sup>4</sup> in the rows labeled "Dignam" for the Dignam and Mamiche-Afara algorithm<sup>11</sup>. In Table IV of Ref. 4, the  $\delta_k$  and  $\delta_n$  values obtained from Huang and Urban's proposed algorithm are all smaller than those in Table 3.1, suggesting that their proposed algorithm is capable of recovering optical constants more accurately as well as, of course, being able to deal with the very intense absorption, with the very large values of  $k$ , that can be measured accurately in single-reflection attenuated total reflection spectroscopy.

Table 3.1 also includes the values of RMSPD, the quantity used, as well as FSUM, as a measure of the degree to which the pATR spectrum is fitted. As noted above the refinement of the optical constants was stopped when FSUM reached  $2 \times 10^{-6}$ , and RMSPD is usually near 0.01% when this occurs. RMSPD is larger than this at

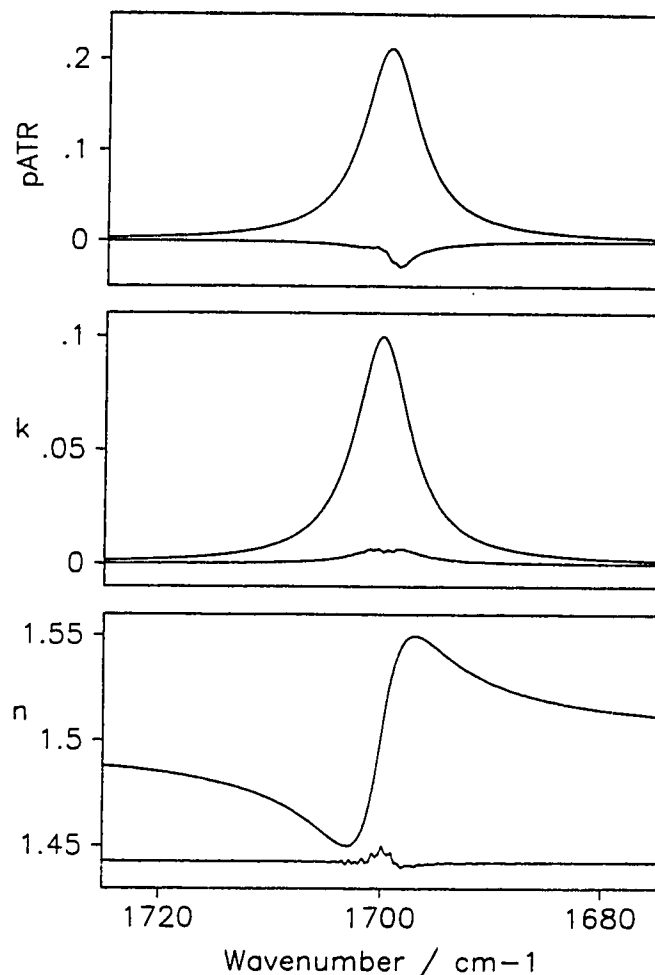


**Figure 3.2** Spectra for the single Lorentzian band with FWHH =  $6 \text{ cm}^{-1}$  and  $k_{\text{max}} = 0.1$ . Upper box: The synthesized pATR spectrum and, beneath it, 100 times the difference between it and the pATR calculated from the recovered optical constants. Middle and lower boxes: The synthesized  $k(\tilde{\nu})$  (middle) and  $n(\tilde{\nu})$  (lower) and, beneath them, 100 times the difference between them and the recovered  $k'(\tilde{\nu})$  (middle) or  $n'(\tilde{\nu})$  (lower). The  $100[n(\tilde{\nu}) - n'(\tilde{\nu})]$  is really 1.46 units lower than shown in the lower box.

convergence if the entire spectrum is rather weak, as is illustrated by the column for  $k_{\text{max}} = 0.1$  in Table 3.1.

The quality of fit represented by these numerical criteria can be illustrated by the figures. Figure 3.2 and 3.3 show the synthesized spectrum, and, underneath it, the spectrum of the deviation, multiplied by 100, of the spectrum calculated by our program KREF from the synthesized spectrum, for each of the  $\text{pATR}(\tilde{\nu})$ ,  $k(\tilde{\nu})$ , and  $n(\tilde{\nu})$ , for the cases with  $k_{\text{max}}$  equal to 0.1, Figure 3.2, and 0.6, Figure 3.3. The percent deviation is less

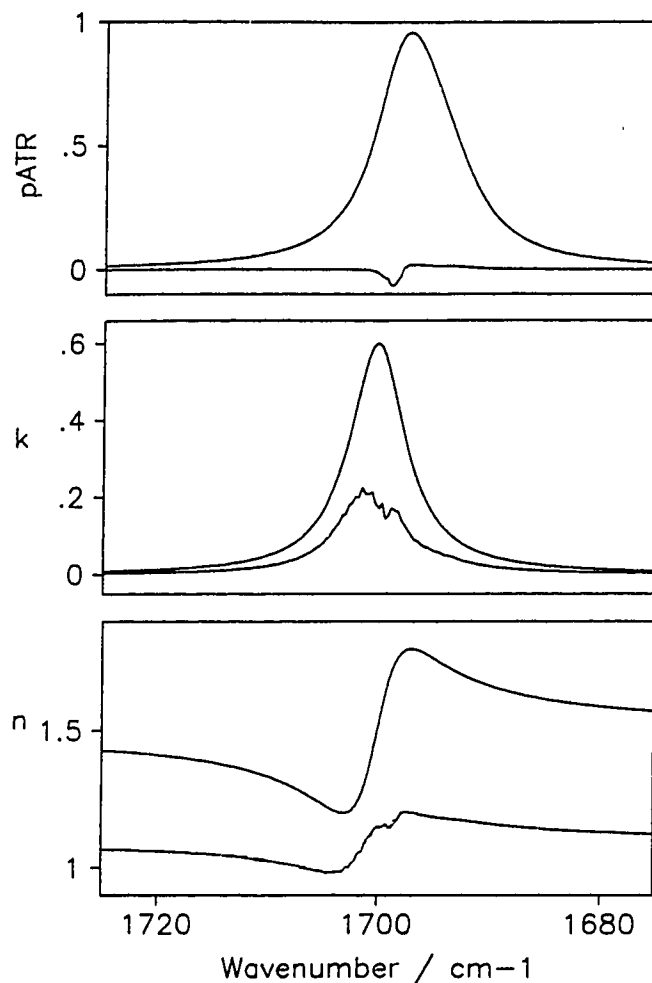


**Figure 3.3** Spectra for the single Lorentzian band with FWHH =  $5 \text{ cm}^{-1}$  and  $k_{\text{max}} = 0.6$ . Upper box: The synthesized pATR spectrum and, beneath it, 100 times the difference between it and the pATR calculated from the recovered optical constants. Middle and lower boxes: The synthesized  $k(\tilde{\nu})$  (middle) and  $n(\tilde{\nu})$  (lower) and, beneath them, 100 times the difference between them and the recovered  $k'(\tilde{\nu})$  (middle) or  $n'(\tilde{\nu})$  (lower). The  $100[n(\tilde{\nu}) - n'(\tilde{\nu})]$  is really 1.20 units lower than shown in the lower box.

than 0.2% in all cases, except that it ranges from 0.25 to 0.5% for  $k'(\tilde{\nu})$  for the Lorentzian with  $k_{\text{max}} = 0.6$ , Figure 3.3. Note that in the bottom boxes of each figure the spectrum of 100 times the deviation of  $n$  has been offset to reduce the range of  $n$  in the figure.

Our programs were also tested with the  $k$  and  $n$  spectra of acetic acid and methanol that were synthesized from the classical damped harmonic oscillator model in connection with our study of the KK and Hilbert transforms<sup>10</sup>. It should be noted that this model gives Lorentzian bands in the imaginary dielectric constant spectrum and gives slightly

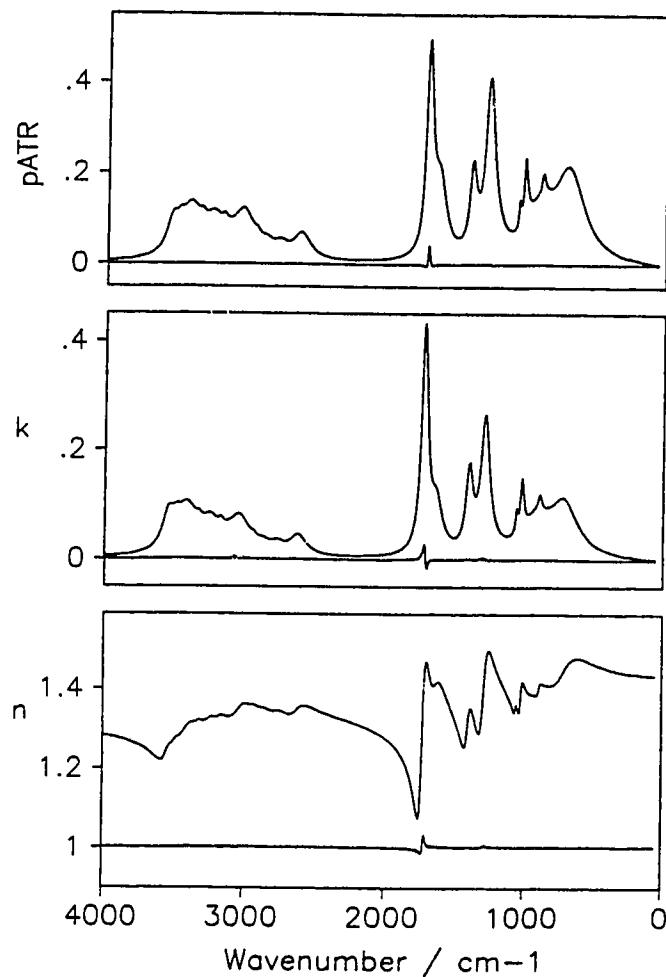


**Figure 3.4** Spectra for simulated acetic acid. Upper box: The synthesized pATR spectrum and, beneath it, 100 times the difference between it and the pATR calculated from the recovered optical constants. Middle and lower boxes: The synthesized  $k(\tilde{\nu})$  (middle),  $n(\tilde{\nu})$  (lower), and beneath them, 100 times the difference between them and the recovered  $k'(\tilde{\nu})$  (middle) or  $n'(\tilde{\nu})$  (lower). The  $100[n(\tilde{\nu}) - n'(\tilde{\nu})]$  is really 1.00 units lower than shown in the lower box.

unsymmetric bands in the  $k$  spectrum, whereas the model of Huang and Urban gives Lorentzian bands in the  $k$  spectrum. The details of the bands used to construct the acetic acid and methanol spectra are given in Table 1 of Ref. 10. The spectra contain 8039 points between 7800 and 50  $\text{cm}^{-1}$ . The pATR spectra were calculated for a single reflection of unpolarized light at  $45^\circ$  incidence with an ATR element of  $n = 2.38$ .  $n$  at 7800  $\text{cm}^{-1}$  was taken to be 1.325 for both acetic acid and methanol, which is correct for methanol and about 0.05 low for acetic acid.

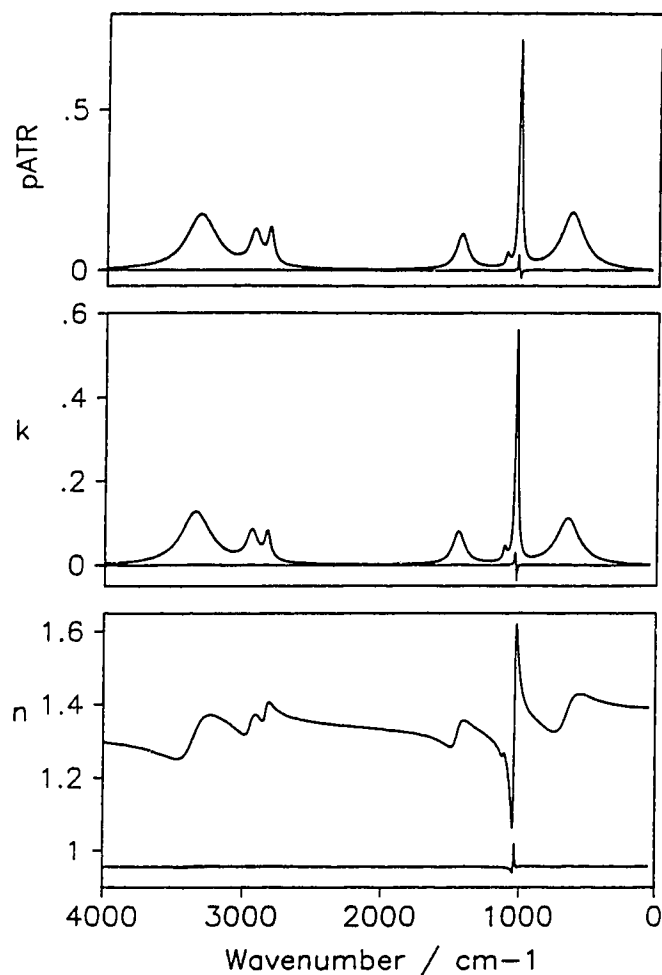


**Figure 3.5** Spectra for simulated methanol. Upper box: The synthesized pATR spectrum and, beneath it, 100 times the difference between it and the pATR calculated from the recovered optical constants. Middle and lower boxes: The synthesized  $k(\tilde{\nu})$  (middle) and  $n(\tilde{\nu})$  (lower) and, beneath them, 100 times the difference between them and the recovered  $k'(\tilde{\nu})$  (middle) or  $n'(\tilde{\nu})$  (lower). The  $100[n(\tilde{\nu}) - n'(\tilde{\nu})]$  is really 0.95 units lower than shown in the lower box.

Figure 3.4 shows the synthesized pATR,  $k$  and  $n$  spectra of acetic acid below  $4000\text{ cm}^{-1}$  and shows for each the spectrum of percent deviation between the synthesized spectrum and that calculated by KREF. Figure 3.5 shows the same for methanol. The  $\delta_k$ ,  $\delta_n$ , and RMSPD values, each calculated over the entire spectrum, are included in Table 3.1. It is clear that the pATR spectrum is fitted to better than 0.1% and the recovered  $k$  and  $n$  spectra are accurate to better than 0.1%.

### 3.5 Reasons for Non-Convergence

Figures 3.2 and 3.3 show that a peak occurs at lower wavenumber in the pATR spectrum than in the imaginary refractive index spectrum, and that the shift is larger the stronger the band. The peak in the initial estimate of the  $k$  spectrum is at the same wavenumber as in the pATR spectrum, and the refinement must shift the peak to the correct wavenumber for the  $k$  spectrum. For strong bands, the refinement sometimes diverges while it is shifting the peak, because the  $n$  spectrum gets distorted during this process. The use of a damping factor less than 1, and as small as 0.02 in extreme cases, prevents this from happening.

For bands that are slightly too strong for successful recovery, such as a single band spectrum with  $n_{\infty} = 1.5$  and  $k_{\max} = 0.65$ , the damping factor effectively stops the divergence which results from shifting the peak, but the refinement oscillates slowly instead of converging. Study of the observed and calculated pATR spectra and of the correct and calculated  $k$  spectra shows that this is due to the fact identified by Huang and Urban and shown graphically in Figure 2 of Ref. 4, namely that the refinement depends on the pATR value decreasing when the  $k$  value decreases. This factor also presumably causes the larger percent deviations of  $k(\tilde{\nu})$  noted above for the  $k_{\max} = 0.6$  case of Figure 3.3, in spite of the pATR being fitted to better than 0.1% throughout. A more sophisticated refinement algorithm, such as that suggested by Huang and Urban, may allow such spectra to be treated successfully.

It should be remembered that bands that are too strong to be treated successfully by this method are also usually too strong to be measured in the CIRCLE cell provided the real refractive index of the sample is about 1.5 or less. They are better measured by single reflection ATR, for which an algorithm like that of Digram and Mamiche-Afara or that proposed by Huang and Urban is more direct and, therefore, preferable.

### 3.6 Summary

Recent changes to our methods and programs, HREF and KREF, for the recovery of optical constants from pATR spectra obtained from the CIRCLE cell have been presented. The program has been tested on pATR spectra that were calculated from known, synthesized, optical constant spectra, both for single band spectra and for simulations of the spectra of pure acetic acid and methanol liquids. Figures 3.2 to 3.5 show some of the spectra used. They also show the deviations, multiplied by 100, of the recovered spectra

from the known spectra, and Table 3.1 contains average numerical quantities, both of which indicate the goodness of fit and the accuracy of the recovered optical constants.

The evidence presented shows that our current program KREF for the recovery of optical constants from pATR spectra gives optical constants of accuracy 0.2% or better for all except the strongest bands in the multiple attenuated total reflection spectra that are obtained with the CIRCLE cell for liquids with refractive indices of 1.5 or less. The strongest bands that can be refined successfully may give errors up to 0.5% in the recovered  $k$  spectrum, even though the pATR spectrum is fitted to 0.1% or better. The method is likely to be less successful for liquids with real refractive indices that average above 1.5 in the infrared.

When cases are encountered for which the program fails, the failure is evident from the FSUM and RMSPD values that are recorded after each cycle of refinement. Bands that are too strong to be measured in the CIRCLE cell are best measured by single-reflection ATR, for which an algorithm like that of Dignam and Mamiche-Afara<sup>11</sup>, or that proposed by Huang and Urban<sup>4</sup>, is preferable for calculating the optical constants.

### 3.7 References

1. J. E. Bertie and H.H.Eysel, *Appl. Spectrosc.* **39**, 392 (1985).
2. J. E. Bertie, H. Harke, M. K. Ahmed, and H. H. Eysel, *Croat. Chem. Acta* **61**, 391 (1988).
3. J. E. Bertie, M. K. Ahmed, and H. H. Eysel, *J. Phys. Chem.* **93**, 2210 (1989).
4. J. B. Huang and M. W. Urban, *Appl. Spectrosc.* **46**, 1666 (1992).
5. T. G. Goplen, D. G. Cameron, and R. N. Jones, *Appl. Spectrosc.* **34**, 657 (1980).
6. J. E. Bertie, R. N. Jones, and V. Behnam, *Appl. Spectrosc.* **40**, 427 (1986).
7. J. E. Bertie, C. D. Keefe, and R. N. Jones, *Can. J. Chem.* **69**, 1609 (1991).
8. J. E. Bertie, R. N. Jones, and C. D. Keefe, *Appl. Spectrosc.* **47**, 891 (1993).
9. K. Ohta and H. Ishida, *Appl. Spectrosc.* **42**, 952 (1988).
10. J. E. Bertie and S. L. Zhang, *Can. J. Chem.* **70**, 520 (1992).
11. M. J. Dignam and S. Mamiche-Afara, *Spectrochim. Acta* **44A**, 1435 (1988).



## Chapter 4    Accurate Determination of Molecular Band Intensities of liquid from Infrared Refractive Index and Dielectric Constant Spectra \*

### 4.1 Introduction

In recent years absolute infrared absorption intensities of several compounds have been measured by transmission<sup>1-8</sup> methods to an estimated accuracy of about 3%. These measurements have used the methods developed during the 1970s by R. Norman Jones and coworkers<sup>9-17</sup> at the National Research Council of Canada, recently augmented<sup>4-8</sup> by a procedure<sup>3</sup> to eliminate unpredictable variations in the position of the baseline in different transmission spectra. Absolute absorption intensities have also been measured to the same accuracy by multiple attenuated total reflection (ATR) methods<sup>7,8,18-22</sup> which use the CIRCLE cell. Other recent studies<sup>23-26</sup> have yielded intensities whose accuracy is less clear but is probably better than 10%.

The measured transmission spectra or ATR spectra are converted by an iterative procedure to spectra of the complex refractive index.

$$\hat{n}(\tilde{\nu}) = n(\tilde{\nu}) + i k(\tilde{\nu}) \quad (4.1)$$

The imaginary refractive index,  $k(\tilde{\nu})$ , is also called the absorption index, and is the major determinant of the transmission or multiple ATR spectrum in the above measurements. The real refractive index,  $n(\tilde{\nu})$ , plays a secondary role in determining the transmission or multiple ATR spectrum, and is calculated by Kramers-Krönig (KK) transformation<sup>27</sup> of the absorption index spectrum plus a value of the limiting high-wavenumber refractive index. The real refractive indices are estimated to be accurate to at least 0.5%. The real and imaginary refractive indices are collectively called the optical constants, and the results of any well-defined infrared experiment can be predicted if the optical constant spectra are known.

Thus, a number of other quantities that express the absorption and refraction of a liquid sample can be calculated from the absorption index and the real refractive index, via equations that are summarized in an appendix to a previous paper<sup>7</sup>. Among these are the linear absorption coefficient,  $K(\tilde{\nu})$ ,

---

\* A version of this chapter has been published. Bertie, Zhang, and Keefe, *J. Mol. Struct.* **324**, 157 (1994)

$$K(\tilde{\nu}) = \frac{1}{d} \log_{10} \frac{I_o(\tilde{\nu})}{I_t(\tilde{\nu})} = \frac{4\pi\tilde{\nu}k(\tilde{\nu})}{2.303} \quad (4.2)$$

and the molar absorption coefficient,  $E_m(\tilde{\nu})$ ,

$$E_m(\tilde{\nu}) = K(\tilde{\nu})/C \quad (4.3)$$

where  $d$  is the pathlength and  $C$  the molar concentration.

It is important to emphasize that the  $K$  and  $E_m$  spectra that are calculated from the  $k$  spectrum in this way are fully corrected for losses other than those due to absorption by the sample.

The area  $A_j$  that is commonly used<sup>13,26,28</sup> to describe the integrated intensity is obtained from  $E_m(\tilde{\nu})$  as

$$A_j = 2.303 \int E_m(\tilde{\nu}) d\tilde{\nu} \quad (4.4)$$

where the integral is over band  $j$ .

The complex dielectric constant

$$\hat{\epsilon}(\tilde{\nu}) = \epsilon'(\tilde{\nu}) + i\epsilon''(\tilde{\nu}) \quad (4.5)$$

can be calculated from the complex refractive index,  $\hat{n}(\tilde{\nu})$ , through the equation

$$\hat{\epsilon}(\tilde{\nu}) = \hat{n}^2(\tilde{\nu}) \quad (4.6)$$

which gives

$$\epsilon'(\tilde{\nu}) = n^2(\tilde{\nu}) - k^2(\tilde{\nu}) \quad \text{and} \quad \epsilon''(\tilde{\nu}) = 2n(\tilde{\nu})k(\tilde{\nu})$$

and the molar conductivity<sup>7</sup> equals  $V_m \hat{\nu} \epsilon''(\tilde{\nu})$ , where  $V_m$  is the molar volume. For a pure liquid,  $V_m = 1/C$ . For a binary mixture of mole fraction  $x_i$  and concentration  $C_i$  in the  $i$ th component,  $V_m$  equals  $x_i/C_i$  and is the volume of one mole of solution, not of the component.

In order to obtain molecular properties from these phenomenological quantities, a model must be assumed to relate the macroscopic electric field to the local field which acts on each molecule in the liquid. The Lorentz local field model is well defined and simple<sup>29</sup>. The model is valid for isotropic media and is used in this work, even though no liquid is isotropic at molecular distances, because of the absence of a superior simple model.

With this in mind, the quantity  $B_j$  has been defined<sup>7,19</sup> as the area under a band in the molar conductivity spectrum divided by the Lorentz local field correction  $\left(\frac{\epsilon+2}{3}\right)^2$ .

$$B_j = V_m \int \tilde{\nu} \epsilon''(\tilde{\nu}) d\tilde{\nu} + \left( \frac{\epsilon + 2}{3} \right)^2 \quad (4.7)$$

Here  $\epsilon$  is the value the dielectric constant would have at the wavenumber of the band if the band were absent from the spectrum.

As Dignam<sup>23</sup> has recently noted, the use of the Lorentz local field provides a well-known relation between the optical and dielectric constants and the polarizability,  $\alpha$ , of the molecules in the liquid. This relation is the Lorentz-Lorenz formula<sup>29</sup>

$$\frac{\epsilon - 1}{\epsilon + 2} = \frac{n^2 - 1}{n^2 + 2} = \frac{4}{3} \pi N \alpha \quad (4.8)$$

where  $N$  is the number of molecules in unit volume. This equation is frequently called the Clausius-Mossotti equation<sup>23</sup>. It is usually used at a single wavenumber at which the sample does not absorb radiation. However,  $\epsilon$ ,  $n$  and  $\alpha$  all depend on wavenumber, and absorption can be accounted for by making them complex quantities. So the generalized Lorentz-Lorenz formula is

$$\frac{\hat{\epsilon}(\tilde{\nu}) - 1}{\hat{\epsilon}(\tilde{\nu}) + 2} = \frac{\hat{n}^2(\tilde{\nu}) - 1}{\hat{n}^2(\tilde{\nu}) + 2} = \frac{4}{3} \pi N \hat{\alpha}(\tilde{\nu}) \quad (4.9)$$

where  $\hat{\alpha}(\tilde{\nu}) = \alpha'(\tilde{\nu}) + i \alpha''(\tilde{\nu})$

is the mean complex polarizability of a molecule in the liquid.

Eq. (4.9) provides a relation between  $\hat{n}$ ,  $\hat{\epsilon}$  and  $\hat{\alpha}$  at any wavenumber, whether the sample absorbs ( $k \neq 0$ ,  $\epsilon'' \neq 0$ ) or not. It yields the equations through which the real and imaginary molar polarizabilities are calculated from  $\hat{\epsilon}$ , namely

$$\alpha''_m(\tilde{\nu}) = \frac{9V_m}{4\pi} \frac{\epsilon''(\tilde{\nu})}{[\epsilon'(\tilde{\nu}) + 2]^2 + \epsilon''(\tilde{\nu})^2} \quad (4.10a)$$

$$\alpha'_m(\tilde{\nu}) = \frac{3V_m}{4\pi} \frac{[\epsilon'(\tilde{\nu}) - 1][\epsilon'(\tilde{\nu}) + 2] + \epsilon''(\tilde{\nu})^2}{[\epsilon'(\tilde{\nu}) + 2]^2 + \epsilon''(\tilde{\nu})^2} \quad (4.10b)$$

To obtain eqs. (4.10),  $\hat{\alpha}(\tilde{\nu})$  in eq. (4.9) was multiplied by Avogadro's number,  $N_a$ , to obtain the complex molar polarizability,  $\hat{\alpha}_m(\tilde{\nu})$ , i.e. the polarizability of one mole of liquid molecules, and the molar volume,  $V_m$ , was used instead of  $N_a/N$ .

The complex molar polarizability is related by  $\hat{\alpha}_m = V_m \hat{C}$  to the complex susceptibility,  $\hat{C}$ , that was defined by Clifford and Crawford<sup>30</sup> as  $1/\hat{C} = 1/\hat{\chi}_e - 4\pi/3$ , where  $\hat{\chi}_e$  is the complex electric susceptibility. The imaginary susceptibility,  $C''(\tilde{\nu})$ , is used later

in this chapter, because it is a property of unit volume and, thus, is more convenient than  $\alpha_m''(\tilde{\nu})$  for comparing the absorption observed for different liquids.

To describe the integrated intensity under band  $j$ , a third area termed  $C_j$  has been defined<sup>7</sup>, in addition to the areas  $A_j$  and  $B_j$  given above, by

$$C_j = \int \tilde{\nu} \alpha_m''(\tilde{\nu}) d\tilde{\nu} \quad (4.11)$$

The areas  $A_j$ ,  $B_j$  and  $C_j$  must be related to molecular vibrational intensities through a molecular theory. Several authors<sup>23,31,32</sup> have discussed the calculation of the complex molar polarizability of randomly oriented molecules from quantum mechanics and from the classical damped harmonic oscillator model.

The quantum mechanical treatment gives, for the dipole transition moment (dipole matrix element between the initial,  $i$ , and final,  $f$ , states)

$$C_j = \int \tilde{\nu} \alpha_m''(\tilde{\nu}) d\tilde{\nu} = \frac{N_a \pi}{3hc} g_j \tilde{\nu}_j |\vec{R}_j|^2 \quad (4.12a)$$

where  $h$  is Planck's constant,  $c$  is the velocity of light in vacuum,  $g_j$  is the degeneracy,  $\tilde{\nu}_j$  is the wavenumber and  $\vec{R}_j$  is the dipole transition moment,  $\langle f | \vec{\mu} | i \rangle_j$ , of the transitions that cause band  $j$ . Note that  $\tilde{\nu}_j |\vec{R}_j|^2$  is really the average, over all of the transitions that contribute to band  $j$ , of the product of the transition wavenumber and the square of the transition moment.

For a fundamental band, with the assumption that all of the hot bands of the fundamental contribute to the band and with the expression for the transition moment,  $\langle 1 | \vec{\mu} | 0 \rangle$ , of the fundamental transition of an electrically and mechanically harmonic oscillator<sup>33</sup>, eq. (4.12a) yields the expression for the square of the dipole moment derivative with respect to the  $j$ th normal coordinate,  $|\partial \vec{\mu} / \partial Q_j|^2$ , which is designated as  $\mu_j^2$  for brevity.

$$C_j = \int \tilde{\nu} \alpha_m''(\tilde{\nu}) d\tilde{\nu} = \frac{N_a g_j}{24 \pi c^2} \mu_j^2 \quad (4.12b)$$

The same equation is obtained from the classical damped harmonic oscillator, CDHO, model<sup>23,31,32</sup>.

The CDHO model also relates the complex molar polarizability spectrum to molecular vibrational quantities<sup>23,31,32</sup> through the equation

$$\hat{\alpha}_m(\tilde{\nu}) = \frac{\epsilon_\infty - 1}{\epsilon_\infty + 2} \frac{3 N_a}{4 \pi N} + \frac{N_a}{4 \pi^2 c^2} \sum_j \frac{(\mu_j^2 / 3)}{[\tilde{\nu}_j^2 - \tilde{\nu}^2 - i \tilde{\nu} \Gamma_j]} \quad (4.13)$$

From this equation, the real and imaginary parts of the polarizability are given by

$$\alpha_m' = \frac{\epsilon_\infty - 1}{\epsilon_\infty + 2} \frac{3 N_a}{4\pi N} + \frac{N_a}{4\pi^2 c^2} \sum_j \frac{(\mu_j^2 / 3)(\tilde{\nu}_j^2 - \tilde{\nu}^2)}{(\tilde{\nu}_j^2 - \tilde{\nu}^2)^2 + \tilde{\nu}^2 \Gamma_j^2} \quad (4.13a)$$

$$\alpha_m'' = \frac{N_a}{4\pi^2 c^2} \sum_j \frac{(\mu_j^2 / 3) \Gamma_j \tilde{\nu}}{(\tilde{\nu}_j^2 - \tilde{\nu}^2)^2 + \tilde{\nu}^2 \Gamma_j^2} \quad (4.13b)$$

In these equations,  $\epsilon_\infty$  is the real dielectric constant in the region where  $\epsilon$  and  $n$  are essentially independent of the wavelength of the radiation below the electronic absorption and above the vibrational absorption. The factor of 3 in  $(\mu_j^2 / 3)$  accounts for the random orientation of the molecules.

To the extent that the absorption bands are sufficiently far apart, expressions for the complex dielectric constant can be deduced under the CDHO model from eqs. (4.13) for the polarizability. These equations are given in the next section, and they lead to the second set of equations for obtaining  $|\vec{R}_j|^2$  and  $\mu_j^2$  from optical data, this time from the molar conductivity,  $V_m \tilde{\nu} \epsilon''$ , through eq. (4.7):

$$B_j = V_m \int \tilde{\nu} \epsilon''(\tilde{\nu}) d\tilde{\nu} + \left( \frac{\epsilon + 2}{3} \right)^2 = \frac{4\pi^2 N_a}{3hc} g_j \tilde{\nu}_j |\vec{R}_j|^2 \quad (4.14a)$$

$$= \frac{N_a}{6c^2} g_j \mu_j^2 \quad (4.14b)$$

Eqs. (4.2) to (4.4) and (4.6) show that the area  $A_j$  can be related to  $|\vec{R}_j|^2$  and  $\mu_j^2$  through eqs. (4.14) and the additional assumption that  $n(\tilde{\nu})$  can be replaced by an average value,  $\underline{n}$ , across band  $j$ . For  $\underline{n} = \sqrt{\underline{\epsilon}}$  the relations are:

$$A_j = 2.303 \int E_m(\tilde{\nu}) d\tilde{\nu} = \frac{8\pi^3 N_a}{3hc} \frac{1}{\sqrt{\underline{\epsilon}}} \left( \frac{\underline{\epsilon} + 2}{3} \right) g_j \tilde{\nu}_j |\vec{R}_j|^2 \quad (4.15a)$$

$$= \frac{\pi N_a}{3c^2} \frac{1}{\sqrt{\underline{\epsilon}}} \left( \frac{\underline{\epsilon} + 2}{3} \right)^2 g_j \mu_j^2 \quad (4.15b)$$

In eqs. (4.15),  $\underline{\epsilon}$  is frequently replaced<sup>31,32,34</sup> by  $\underline{n}^2$ .

Eqs. (4.12) relate the experimental integrated intensity to the molecular properties through the assumption of the Lorentz local field. Eqs. (4.14) and (4.15) involve additional approximations.

Unfortunately, all of these methods of obtaining molecular vibrational intensities involve the problems of integrating areas under bands whose limits are always in some doubt unless a precise fit with a standard band shape can be achieved. A possible way to avoid this difficulty is suggested by the fact that the wavenumber of a peak in the imaginary dielectric constant spectrum is lower than the wavenumber of the corresponding peak in the imaginary polarizability spectrum by an amount that depends on the intensity of the band. This suggests the attractive possibility of determining band intensities, and hence  $|\vec{R}_j|^2$  and  $\mu_j^2$ , by measuring peak wavenumbers instead of band areas. The CDHO model for the dielectric constant supplies the relation that is used, as is shown in the next section.

One purpose of this chapter is to explore the conditions under which the three sets of eqs. (4.12), (4.14) and (4.15) may be used interchangeably, and the conditions under which eqs. (4.12) must be used for accuracy.

A second purpose is to determine the extent to which the intensity can be determined from the peak wavenumbers in the  $\epsilon''$  and  $\alpha''$  spectra.

A third purpose is to draw attention to the different line shapes and peak wavenumbers in the spectra of the different absorption quantities and to emphasize that it is the polarizability that is most closely related to molecular theory.

The derivation of the dielectric constant spectrum from the polarizability spectrum under the CDHO model, the approximations that are involved in this derivation, and the relation between the peak wavenumbers in the two spectra under this model, are presented in the next section. The methods used to explore the application of these equations, the results obtained and their discussion, and the conclusions of this work, are in the following sections.

## 4.2 The CDHO Model for the Dielectric Constant

The Lorentz local field is assumed in order to calculate the complex dielectric constant from the CDHO expressions for the complex polarizability. Eq. (4.13), divided by  $N_a$ , gives  $\hat{\alpha}$ , which is substituted into the Lorentz-Lorenz equation, eq. (4.9), to yield

$$\frac{\hat{\epsilon}(\tilde{\nu}) - 1}{\hat{\epsilon}(\tilde{\nu}) + 2} = \frac{\epsilon_\infty - 1}{\epsilon_\infty + 2} + \frac{N}{3\pi c^2} \sum_j \frac{(\mu_j^2 / 3)}{[\hat{\nu}_j^2 - \tilde{\nu}^2 - i\tilde{\nu}\Gamma_j]} \quad (4.16)$$

An additional assumption is required to proceed further. It must be assumed that the oscillators in the sum in eq. (4.16) are sufficiently far apart that the dielectric constant due to all oscillators other than the one of interest, say oscillator  $j$ , is real and constant across the wavenumber region of oscillator  $j$ . If this real constant is called  $\underline{\epsilon}_j$ , eq. (4.16) becomes

$$\frac{\hat{\epsilon}(\tilde{\nu}) - 1}{\hat{\epsilon}(\tilde{\nu}) + 2} = \frac{\underline{\epsilon}_j - 1}{\underline{\epsilon}_j + 2} + \frac{N}{3\pi c^2} \frac{(\mu_j^2 / 3)}{[\tilde{\nu}_j^{*2} - \tilde{\nu}^2 - i\tilde{\nu}\Gamma_j]} \quad (4.17)$$

When  $\frac{y-1}{y+2} = b$ ,  $y-1 = \frac{3b}{1-b}$ , from which eq. (4.17) can be reduced to

$$\hat{\epsilon} = \underline{\epsilon}_j + \frac{N}{\pi c^2} \frac{(\mu_j^2 / 3)_{\text{eff}}}{[\tilde{\nu}_j^{*2} - \tilde{\nu}^2 - i\tilde{\nu}\Gamma_j]} \quad (4.18)$$

where  $(\mu_j^2 / 3)_{\text{eff}} = (\mu_j^2 / 3) \left( \frac{\underline{\epsilon}_j + 2}{3} \right)^2 \quad (4.18a)$

and  $\tilde{\nu}_j^{*2} = \tilde{\nu}_j^2 - \frac{N}{\pi c^2} \frac{(\mu_j^2 / 3)_{\text{eff}}}{(\underline{\epsilon}_j + 2)} \quad (4.18b)$

The logic that was used between eqs. (4.16) and (4.17) to combine the term in  $\epsilon_\infty$  and the sum over  $i \neq j$  into a constant term in  $\underline{\epsilon}_j$  is now used to reintroduce the sum to obtain

$$\hat{\epsilon} = \epsilon_\infty + \frac{N}{\pi c^2} \sum_j \frac{(\mu_j^2 / 3)_{\text{eff}}}{[\tilde{\nu}_j^{*2} - \tilde{\nu}^2 - i\tilde{\nu}\Gamma_j]} \quad (4.19)$$

from which

$$\epsilon' = \epsilon_\infty + \frac{N}{\pi c^2} \sum_j \frac{(\mu_j^2 / 3)_{\text{eff}} (\tilde{\nu}_j^{*2} - \tilde{\nu}^2)}{(\tilde{\nu}_j^{*2} - \tilde{\nu}^2)^2 + \tilde{\nu}^2 \Gamma_j^2} \quad (4.19a)$$

$$\epsilon'' = \frac{N}{\pi c^2} \sum_j \frac{(\mu_j^2 / 3)_{\text{eff}} \Gamma_j \tilde{\nu}}{(\tilde{\nu}_j^{*2} - \tilde{\nu}^2)^2 + \tilde{\nu}^2 \Gamma_j^2} \quad (4.19b)$$

Eqs. (4.19a) and (4.19b) were used in Chapter 2 as eqs. (2.4a) and (2.4b).

From eqs. (4.13b) and (4.19b) it can be seen that the peak wavenumbers in the  $\alpha_m''$  and  $\epsilon''$  spectra are not exactly  $\tilde{\nu}_j$  and  $\tilde{\nu}_j^*$ . However,  $\tilde{\nu}_j$  and  $\tilde{\nu}_j^*$  are exactly the peak wavenumbers in the  $\tilde{\nu}\alpha_m''$  and  $V_m\tilde{\nu}\epsilon''$  spectra, respectively. Thus,  $\tilde{\nu}_j$  and  $\tilde{\nu}_j^*$  can be

measured from the spectra and  $\mu_j^2$  can be calculated from them through the rearrangement of eqs. (4.18a) and (4.18b),

$$\mu_j^2 = \frac{27\pi c^2}{N} \frac{(\tilde{\nu}_j^2 - \tilde{\nu}_j^{*2})}{(\epsilon_j + 2)} \quad (4.20)$$

where  $N = N_A/V_m$ .

### 4.3 Methods

Synthetic and experimental spectra have been used in this work. The synthetic spectra were obtained under the CDHO model by calculating spectra of the real and imaginary molar polarizability,  $\alpha'_m(\tilde{\nu})$  and  $\alpha''_m(\tilde{\nu})$ , from selected values of  $\mu_j$ ,  $\tilde{\nu}_j$  (the resonance wavenumber), and  $\Gamma_j$  (essentially the full width at half height), through eqs. (4.13a) and (4.13b).

The real and imaginary dielectric constant spectra,  $\epsilon'(\tilde{\nu})$  and  $\epsilon''(\tilde{\nu})$ , were calculated from the polarizability through the reverse of the Lorentz-Lorenz equation, namely

$$\epsilon'(\tilde{\nu}) = \frac{\left[1 - \frac{4\pi}{3V_m} \alpha'_m(\tilde{\nu})\right] \left[1 + \frac{8\pi}{3V_m} \alpha'_m(\tilde{\nu})\right] - 2 \left[\frac{4\pi}{3V_m} \alpha''_m(\tilde{\nu})\right]^2}{\left[1 - \frac{4\pi}{3V_m} \alpha'_m(\tilde{\nu})\right]^2 + \left[\frac{4\pi}{3V_m} \alpha''_m(\tilde{\nu})\right]^2} \quad (4.21a)$$

$$\epsilon''(\tilde{\nu}) = \frac{\left[\frac{4\pi}{3V_m} \alpha''_m(\tilde{\nu})\right]}{\left[1 - \frac{4\pi}{3V_m} \alpha'_m(\tilde{\nu})\right]^2 + \left[\frac{4\pi}{3V_m} \alpha''_m(\tilde{\nu})\right]^2} \quad (4.21b)$$

The real and imaginary refractive index spectra,  $n(\tilde{\nu})$  and  $k(\tilde{\nu})$ , were calculated from  $\epsilon'(\tilde{\nu})$  and  $\epsilon''(\tilde{\nu})$  by the reverse of eqs. (4.6), namely eqs. (4.12) and (4.13) of Ref. 18, and the molar absorption coefficient spectrum,  $E_m(\tilde{\nu})$ , was calculated from  $k(\tilde{\nu})$  through eqs. (4.2) and (4.3).

It is important to emphasize that although the  $\alpha''_m$  spectra are synthetic the relation between them and the  $\tilde{\nu}\alpha''_m$ ,  $\epsilon''$ ,  $V_m\tilde{\nu}\epsilon''$ ,  $k$ , and  $E_m$  spectra is exactly what it would be for an  $\alpha''_m$  spectrum which was obtained from experiment, through the generalized Lorentz-Lorentz formula, and contains bands of the same shape. Further, in our experience, such "experimental"  $\alpha''_m$  bands are very close to the CDHO shape of eq. (4.13b), unless the atoms involved are intermolecularly hydrogen bonded.

The synthetic spectra were used to test the accuracy with which the molecular vibrational intensity can be recovered from the different spectra. This intensity can be



defined as the square of the transition moment,  $|\vec{R}_j|^2$ , or as the square of the dipole moment derivative with respect to the normal coordinate,  $\mu_j^2$ . We use  $\mu_j^2$  in this chapter. The recovered  $\mu_j^2$  values were obtained in the units  $(\text{D}\text{\AA}^{-1}\text{amu}^{-1/2})^2$  from  $A_j$ ,  $B_j$  and  $C_j$ , all in the units  $\text{km mole}^{-1}$ , through eqs. (4.15b), (4.14b) and (4.12b), in which the constant terms on the right hand sides have the magnitudes  $(0.02366)^{-1}$ ,  $(0.1487)^{-1}$ , and  $(1.8686)^{-1}$ , respectively, for these units<sup>7</sup> (Section 5.6). The  $\mu_j^2$  values were also recovered from  $[\tilde{\nu}_j^2 - \tilde{\nu}_j^{*2}]$  in  $\text{cm}^{-2}$  units through eq. (4.20); for these units, the term  $27\pi c^2/N$  equals  $2.102 \times 10^{-5} V_m$ , where  $V_m$  is in  $\text{cm}^3 \text{ mole}^{-1}$ .

#### 4.4 Results and Discussion

The results for isolated synthetic bands are presented first, to show the band symmetry and wavenumber shifts, and to determine the accuracy with which the intensity can be recovered from isolated bands. We then show results for synthetic doublets, which show the effect of neighboring bands. Finally, we present results for experimental spectra of benzene, toluene and methanol.

In order to allow the results to be directly comparable to those for liquids of different molar volumes,  $C'' = \frac{\alpha_m''}{V_m}$ ,  $\tilde{\nu}C'' = \frac{\tilde{\nu}\alpha_m''}{V_m}$  and  $\tilde{\nu}\epsilon''$  are used in this section instead of  $\alpha_m''$ ,  $\tilde{\nu}\alpha_m''$  and  $V_m\tilde{\nu}\epsilon''$ . Here  $C''$  is the (dimensionless) imaginary susceptibility<sup>30</sup>, the imaginary polarizability per unit volume.

##### 4.4.1 Synthetic Isolated CDHO $\alpha_m''$ Bands and Bands Calculated from Them

A molar volume of  $60.0 \text{ cm}^3 \text{ mole}^{-1}$  and  $\epsilon_\infty = 2.25$  were assumed. The CDHO parameters of the synthetic molar polarizability,  $\hat{\alpha}_m$ , single-band spectra are listed in Table 4.1. Included in Table 4.1 are the peak heights and peak wavenumbers in the synthetic  $C''$  and  $\tilde{\nu}C''$  spectra, and in other spectra that were calculated from the  $\alpha_m''$  and  $\alpha_m'$  spectra as described under Section 4.3.

Table 4.1 shows that the peak heights of the  $\tilde{\nu}C''$  and  $\tilde{\nu}\epsilon''$  bands are independent of wavenumber, proportional to  $\mu_j^2$  and inversely proportional to  $\Gamma_j$ . The peak heights in  $\tilde{\nu}C''$  and  $\tilde{\nu}\epsilon''$  are, thus, convenient quantities to use for comparing the intensities of bands at different wavenumbers.

The  $\tilde{\nu}C''$  peak heights of the synthesized single bands with  $\Gamma_j = 25 \text{ cm}^{-1}$  range from  $91 \text{ cm}^{-1}$  for band SA to  $568 \text{ cm}^{-1}$  for bands SE, SF & SG. Band SA is a very strong band

**Table 4.1** Properties of the CDHO imaginary polarizability bands and bands calculated from them by phenomenological equations.

Band	$\tilde{\nu}_j/\text{cm}^{-1}$	$\Gamma_j/\text{cm}^{-1}$	$\mu_j^2$ <sup>a</sup>	Peak Heights <sup>b</sup>					
				$\tilde{\nu}C''$	$\tilde{\nu}\epsilon''$	$E_m$	$C''$	$\epsilon''$	$k$
SA	1500	25	4	90.8	2.28	2.43	0.0605	1.53	0.496
SB	1500	25	9	205	5.15	5.04	0.136	3.46	1.03
SC	1500	10	9	512	12.8	9.91	0.341	8.65	2.02
SD	3000	50	25	283	7.17	7.36	0.0947	2.40	0.751
SE	3000	25	25	568	14.3	13.09	0.189	4.80	1.34
SF	1500	25	25	568	14.3	10.58	0.379	9.73	2.19
SG	750	25	25	568	14.3	7.82	0.757	20.7	3.42

Peak Wavenumber / $\text{cm}^{-1}$									
				$\tilde{\nu}C''$	$\tilde{\nu}\epsilon''$	$E_m$	$C''$	$\epsilon''$	$k$
SA	1500	25	4	1500.00	1495.50	1497.52	1499.95	1495.45	1497.46
SB	1500	25	9	1500.00	1489.86	1493.69	1499.95	1489.80	1493.61
SC	1500	10	9	1500.00	1489.86	1492.16	1499.99	1489.85	1492.14
SD	3000	50	25	3000.00	2985.93	2991.82	2999.90	2985.82	2991.68
SE	3000	25	25	3000.00	2985.90	2990.53	2999.97	2985.90	2990.48
SF	1500	25	25	1500.00	1471.65	1477.58	1499.95	1471.60	1477.45
SG	750	25	25	750.00	691.56	698.33	749.90	691.45	698.00

<sup>a</sup> Unit  $(\text{D } \text{\AA}^{-1} \text{ amu}^{-1/2})^2$

<sup>b</sup>  $V_m = 60 \text{ cm}^3 \text{ mole}^{-1}$ . Units are  $\text{cm}^{-1}$  for  $\tilde{\nu}C''$ ,  $10^3 \text{ cm}^{-1}$  for  $\tilde{\nu}\epsilon''$  and  $10^5 \text{ cm}^2 \text{ mole}^{-1}$  for  $E_m$ .

and the rest are extremely strong bands. Bands SA and SB are comparable to those observed for liquid  $\text{CH}_3\text{OH}$ <sup>7</sup> at  $1035 \text{ cm}^{-1}$  and liquid  $\text{CH}_3\text{COOH}$ <sup>35</sup> at  $1720 \text{ cm}^{-1}$ , which have FWHH = 22 and  $30 \text{ cm}^{-1}$ , respectively, and peak  $\tilde{\nu}C''$  values of 91 and  $17 \text{ cm}^{-1}$  respectively. Band SC has the same width as the  $673 \text{ cm}^{-1}$  band of liquid  $\text{C}_6\text{H}_6$  (FWHH =  $9 \text{ cm}^{-1}$ )<sup>4</sup>, but a peak  $\tilde{\nu}C''$  value 4.5 times greater.

Figure 4.1 shows the  $\tilde{\nu}\epsilon''$ ,  $\epsilon''$ ,  $\tilde{\nu}C''$ , and  $C''$  spectra in the upper boxes and the  $k$  and  $E_m$  spectra in the lower boxes for bands SA, SB and SC from Table 4.1 in the left, middle and right boxes, respectively. Band SD is not shown, and Figure 4.2 shows bands SE, SF and SG in the left, middle and right boxes respectively. In order to obtain a measure of the band symmetry that is observed visually, the first moment, FM, was calculated of each band over the limited range of one FWHH to either side of the peak<sup>36</sup>. The FM was  $0.0 \text{ cm}^{-1}$  for all of the  $\alpha_m''$  bands, and was  $0.0$  or  $\pm 0.1 \text{ cm}^{-1}$  for all of the  $\tilde{\nu}\alpha_m''$ ,  $\epsilon''$  and  $\tilde{\nu}\epsilon''$  bands as well as for the  $k$  and  $E_m$  bands of SA.

Thus for the weakest band, SA, each intensity quantity gives a symmetric band (Figure 4.1), and the peak wavenumber differences between different spectra are small, <

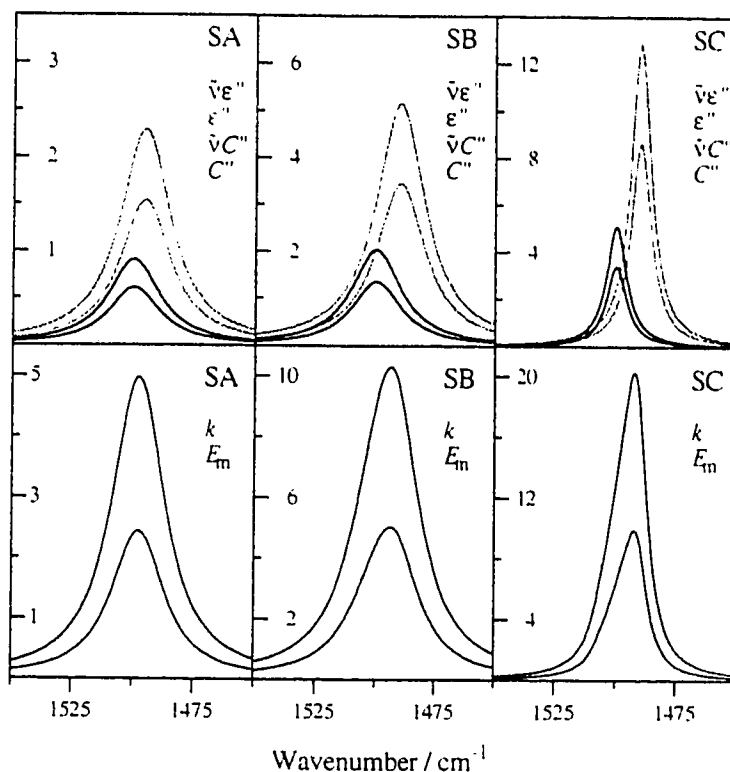


**Figure 4.1** Bands SA, SB and SC of Table 4.1 plotted as different intensity quantities (scaled). The quantities plotted are from top to bottom: upper boxes,  $\tilde{\nu}\epsilon'' / (10^3 \text{ cm}^{-1})$ ,  $\epsilon''$ ,  $\tilde{\nu}C'' / (100 \text{ cm}^{-1})$ ,  $10C''$ ; lower boxes,  $10k$  and  $E_m / (10^5 \text{ cm}^2 \text{ mole}^{-1})$ .

$4.6 \text{ cm}^{-1}$  (Table 4.1). For the next weakest band SB,  $2\frac{1}{4}$  times stronger, the  $k$  and  $E_m$  bands show asymmetry with  $\text{FM} = 0.6 \text{ cm}^{-1}$  for both, and the peak wavenumber differences reach  $11.2 \text{ cm}^{-1}$ . This asymmetry is comparable to that observed in  $k$  and  $E_m$  spectra for the  $673 \text{ cm}^{-1}$  band of benzene.

The right hand boxes in Figure 4.1 show the effect of bandwidth. Band SC has the same wavenumber,  $\tilde{\nu}_j$ , and intensity,  $\mu_j^2$ , as SB, but is  $2\frac{1}{2}$  times sharper. The wavenumber differences are almost the same as for SB (Table 4.1), but the  $k$  and  $E_m$  bands tail markedly to high wavenumber, with  $\text{FM} = 1.6 \text{ cm}^{-1}$ . The ratio of the FMs of bands SB and SC is 2.7, compared with 2.5 for the ratio of the  $\epsilon''_{\text{max}}$  values, the peak heights in the  $\epsilon''$  spectra (Table 4.1). The asymmetry depends on  $\epsilon''_{\text{max}}$  rather than the band intensity,  $\mu_j^2$ , for bands SB and SC.

The strongest bands studied, SD to SG, have the same  $\mu_j^2$ ,  $25 (\text{D } \text{\AA}^{-1} \text{ amu}^{-1/2})^2$ . SD and SE are both at  $3000 \text{ cm}^{-1}$ , but SD has  $\text{FWHH} = 50 \text{ cm}^{-1}$  while SE has  $\text{FWHH} = 25$

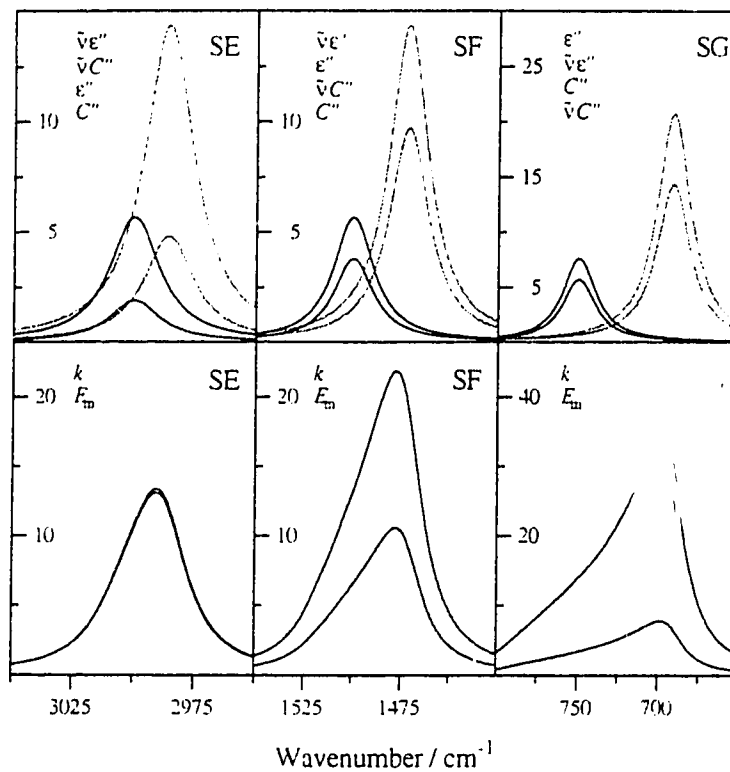


**Figure 4.2** Bands SE, SF and SG of Table 4.1 plotted as different intensity quantities (scaled). The quantities plotted are, in the sequence shown: upper boxes,  $\tilde{\nu}\epsilon'' / (10^3 \text{ cm}^{-1})$ ,  $\epsilon''$ ,  $\tilde{\nu}C'' / (100 \text{ cm}^{-1})$ ,  $10C''$ ; lower boxes,  $10k$  and  $E_m / (10^5 \text{ cm}^2 \text{ mole}^{-1})$ .

$\text{cm}^{-1}$  so the  $\tilde{\nu}C''$  peak height for SD is  $283 \text{ cm}^{-1}$ , just half of that of SE. The spectra for band SD are not shown. The wavenumber differences reach  $14.2 \text{ cm}^{-1}$ , slightly greater than for the weaker band SB at  $1500 \text{ cm}^{-1}$ . The  $k$  and  $E_m$  bands have  $\text{FM} = 0.6 \text{ cm}^{-1}$ , the same as for SB, and the  $\epsilon''_{\text{max}}$  values are 2.4 for SD and 3.5 for SB.

Bands SE, SF and SG show the effect of the peak wavenumber on bands of a given intensity and FWHH. The peak heights are the same at all wavenumbers for  $\tilde{\nu}C''$  and  $\tilde{\nu}\epsilon''$ , and that of  $E_m$  decreases by a factor just below 2 as  $\tilde{\nu}_j$  changes from  $3000$  to  $750 \text{ cm}^{-1}$ . The  $C''$ ,  $\epsilon''$  and  $k$  peak heights all increase as  $\tilde{\nu}_j$  decreases. The maximum wavenumber differences are  $14.1 \text{ cm}^{-1}$  at  $3000 \text{ cm}^{-1}$ ,  $28.4 \text{ cm}^{-1}$  at  $1500 \text{ cm}^{-1}$  and  $58.5$  at  $750 \text{ cm}^{-1}$ , approximately doubling with each factor of 2 reduction in  $\tilde{\nu}_j$ .

There are two points to note about the asymmetry of these  $k$  and  $E_m$  bands. First, it increases with decrease in wavenumber, with the FM changing from  $3 \text{ cm}^{-1}$  at  $3000 \text{ cm}^{-1}$  (SE) to  $4.8 \text{ cm}^{-1}$  at  $1500 \text{ cm}^{-1}$  (SF) to  $9.4 \text{ cm}^{-1}$  for  $k$  and  $19.7 \text{ cm}^{-1}$  for  $E_m$  at  $700 \text{ cm}^{-1}$  (SG). The  $\epsilon''_{\text{max}}$  values increase from 4.80 to 9.73 to 20.7, similar but not

proportional changes to those in FM. Second, band SF at  $1500\text{ cm}^{-1}$  has  $\epsilon''_{\text{max}} = 9.73$ , which is close to the 8.65 for the much weaker but sharper band SC, but its  $F_j^2 = 17\text{ cm}^{-1}$ , three times greater than that of SC. It appears that the asymmetry follows both the band intensity,  $\mu_j^2$ , and the peak value of  $\epsilon''$ ,  $\epsilon''_{\text{max}}$ , the latter being a measure of the anomalous dispersion of  $\epsilon'$  which undoubtedly is a major contributor to the asymmetry.

It is clear that  $k$  spectra,  $E_m$  spectra and absorbance spectra (in which the band shapes follow  $E_m$ ), should not be used for extremely strong bands if the line shape and line symmetry are of interest. Here extremely strong is defined to mean a peak  $\tilde{\nu}C''$  value over 100 and an  $\epsilon''_{\text{max}}$  value over about 2. Of particular note is the great increase in the asymmetry of  $k$  and  $E_m$  bands with decreasing wavenumber. Clearly, the  $\alpha_m''$  or  $C''$  spectrum must be used at low wavenumber if the line shape is of interest, and care should be taken when interpreting very strong asymmetric bands at low wavenumber in  $k$ ,  $E_m$  and absorbance spectra.

#### 4.4.2 Recovery of the Intensity from Isolated Bands

The value of  $\mu_j^2$  recovered from isolated bands was compared with the correct value, the  $\mu_j^2$  value used in the CDHO calculation of  $\alpha_m''$ , and is reported as a percentage of the correct value. In order to recover the intensity from  $A_j$ , it is necessary to numerically integrate the area under the band. The same procedure was adopted for the recovery from  $C_j$  and from  $B_j$ , even though these two spectra could be fitted exactly with a CDHO band and the area recovered from the parameters (see below).

The calculation of  $\mu_j^2$  from  $C_j$  gives the same percentage of the correct value for all of the bands, for the same integration range expressed as multiples of the FWHH. But the recovered value of  $\mu_j^2$  is still only 99.75% of the correct value at an integration range of 300 FWHH (i.e.  $\pm 150$  FWHH). The recovered  $\mu_j^2$  values as a percentage of the correct value are plotted in Figure 4.3 as the top curve, and are shown numerically in Table 4.2, as a function of the integration range in units of the FWHH. Integration over 3 FWHH to either side of the peak recovers 90% of the correct  $\mu_j^2$  value. In order to obtain 95% or 99% intensity accuracy the integration range must be 6.5 or 35, respectively, times the FWHH to either side of the peak.

These results suggest that if an  $\alpha_m''$  band is essentially a CDHO band the area  $C_j$ , under the corresponding  $\tilde{\nu}\alpha_m''$  band, can be obtained to high accuracy by integrating over 3 FWHH to either side of the  $\tilde{\nu}\alpha_m''$  peak and multiplying the result by 1.118. But note that if a CDHO band fits the  $\alpha_m''$  spectrum exactly, the area  $C_j$  can be obtained exactly as

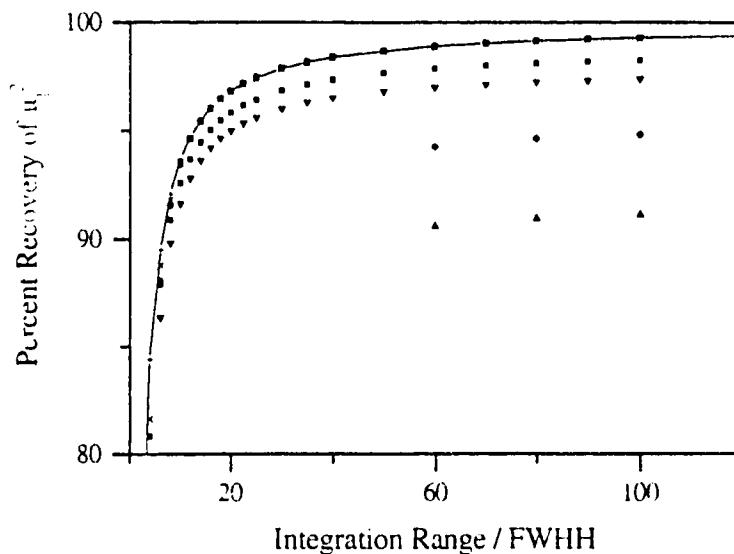


**Figure 4.3** The percent recovery of the integrated intensity, expressed as  $\mu_j^2$ , plotted against the integration range divided by FWHH. The label 20 means integration over 10 FWHH to each side of the peak. Top curve, the percent recovery is from area  $C_j$ , coincident with the percent recoveries from  $A_j$  and  $B_j$  with  $\epsilon$  equal to  $\epsilon_\infty$ . Also shown are the percent recoveries from  $A_j$  and  $B_j$  with  $\epsilon$  equal to the average of  $\epsilon'_{\max}$  and  $\epsilon'_{\min}$  for hands SF ( $A_j$  second curve,  $B_j$  third curve, from the top) and SG ( $A_j$  fourth curve from top,  $B_j$  bottom curve).

**Table 4.2** The percentage accuracy in the  $\mu_j^2$  values recovered through area  $C_j$  as a function of the integration range.

Percent accuracy of $\mu_j^2$	<u>Integration range</u> <sup>a</sup> FWHH
70	±1
90	±3
95	±6.5
98	±17
99	±35
99.5	±70
99.75	±150

<sup>a</sup> ± 6.5 with an FWHH of 10  $\text{cm}^{-1}$  and  $\tilde{\nu}_j = 1500 \text{ cm}^{-1}$  means the integration is from 1565  $\text{cm}^{-1}$  to 1435  $\text{cm}^{-1}$ .

$$C_j = \int \tilde{\nu} \alpha_m'' d\tilde{\nu} = \frac{(\tilde{\nu} \alpha_m'')_{\max} \Gamma_j \pi}{2} \quad (4.22)$$

where  $(\tilde{\nu} \alpha_m'')_{\max}$  is the peak height of the  $\tilde{\nu} \alpha_m''$  band and  $\Gamma_j$  is the width parameter of the CDHO band fitted to the  $\alpha_m''$  band. Analogous methods apply to the determination of  $A_j$  or  $B_j$  if the  $k$  or  $\epsilon''$  band is essentially a CDHO band or is fitted exactly with a CDHO band.

The values of  $\mu_j^2$  calculated from the areas  $A_j$  and  $B_j$  are identical to those from  $C_j$  if the correct value of  $\epsilon$  is used. They are included in Figure 4.3, but are indistinguishable from the  $\mu_j^2$  values from  $C_j$  (top curve). The correct value of  $\epsilon$  is the value that  $\epsilon'$  would have if the band were not present. For a single band spectrum this is the limiting high-wavenumber dielectric constant,  $\epsilon_\infty = 2.25$ , i.e. the value at which the dielectric constant levels off to high wavenumber of the band. Unfortunately, this value usually can not be found exactly for a real spectrum because of the anomalous dispersion of  $\epsilon'$  caused by the neighboring bands.

The anomalous dispersion of  $\epsilon'$  due to the single bands is shown in Figure 4.4. For isolated bands, the difference between the maximum and minimum values of  $\epsilon'$  is  $\epsilon_{\max}''$ , the peak value of  $\epsilon''$ , which is given in column 2 of Table 4.3. In order to overcome the difficulty of finding  $\epsilon$  when several bands are present,  $\epsilon$  is usually calculated as the average of the maximum and minimum values of  $\epsilon'$  in the anomalous dispersion region. Column 3 of Table 4.3 contains the values of  $\epsilon$  calculated in this way, and columns 4 and 5 contain the percent error that is introduced into the  $\mu_j^2$  values by the use of these average values in eqs. (4.14) and (4.15), instead of the correct value, 2.25. The  $\mu_j^2$  values are all lower than when  $\epsilon = 2.25$  is used. The second and third curves from the top of Figure 4.3 show the percent recovery of  $\mu_j^2$  from  $A_j$  and  $B_j$ , respectively, for band SF when the average  $\epsilon$  value was used, and the lower two curves of Figure 4.3 show the same for band SG. In both cases, better results were obtained from  $A_j$  than from  $B_j$ , but the results are not satisfactory in either case for these very strong bands.

In eqs. (4.15),  $\underline{n}$  and  $\underline{n}^2$  are frequently used instead of  $\sqrt{\epsilon}$  and  $\epsilon^{31,32,34}$ , where  $\underline{n}$  is the value that the real refractive index would have if the band were not present.  $\underline{n}^2$  can also replace  $\epsilon$  in eqs. (4.14). To explore the effect of using  $\underline{n}$  and  $\underline{n}^2$ ,  $\underline{n}$  was calculated as the average of the maximum and minimum values of  $n$  in the anomalous dispersion that is associated with the band. Column 6 of Table 4.3 includes the values of  $\underline{n}^2$  so obtained, and columns 7 and 8 show the errors in the  $\mu_j^2$  calculated from  $A_j$  and  $B_j$  when these

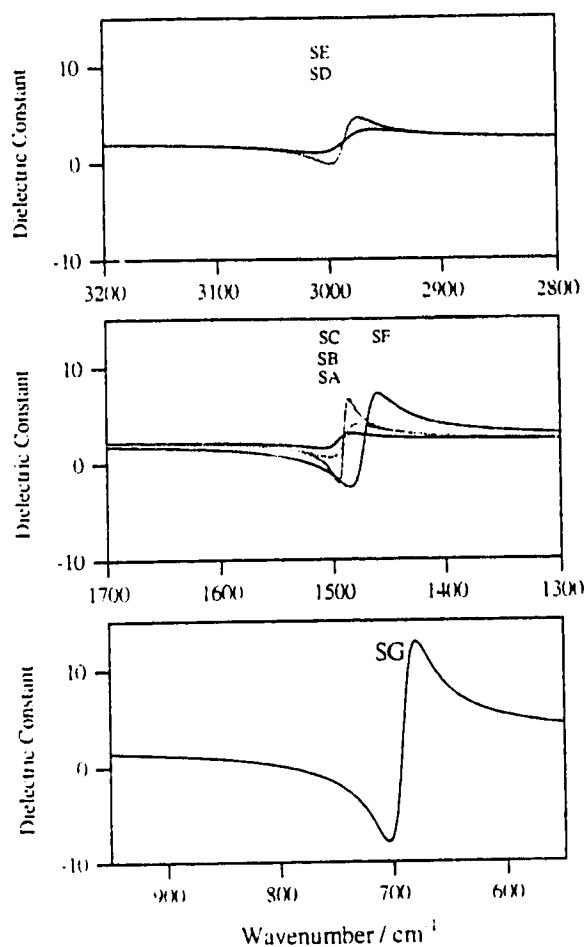


**Figure 4.4** The real dielectric constant,  $\epsilon'$ , spectra for bands SA to SG, showing the anomalous dispersion for all bands on the same ordinate scale.

**Table 4.3** Percent error in  $\mu_j^2$  resulting from using different values of  $\xi$  in eqs. (4.14) and (4.15)

Band	$\epsilon''_{\max}$	$\xi^a$	% Error in $\mu_j^2$ with $\xi$		$\bar{n}^2^c$	% Error in $\mu_j^2$ with $\bar{n}^2$	
			from $B_j^b$	from $A_j^b$		from $B_j^b$	from $A_j^b$
SA	1.53	2.256	0.3	0.2	2.258	0.4	0.2
SB	3.46	2.265	0.7	0.3	2.297	2.2	1.2
SC	8.65	2.2659	0.7	0.4	2.683	17.6	10.1
SD	2.40	2.260	0.5	0.2	2.269	0.9	0.5
SE	4.80	2.260	0.5	0.2	2.352	4.6	2.5
SF	9.73	2.291	1.9	1.0	2.823	22.4	13.0
SG	20.7	2.437	8.3	4.5	4.394	55.8	38.3

<sup>a</sup>  $\xi = (\epsilon'_{\max} + \epsilon'_{\min})/2$ .

<sup>b</sup>  $\mu_j^2$  from  $B_j$  through eq. (4.14) and from  $A_j$  through eq. (4.15).

<sup>c</sup>  $\bar{n}$  and  $\bar{n}^2$  are used in eqs. (4.14) and (4.15), instead of  $\sqrt{\xi}$  and  $\xi$ , where  $\bar{n} = (n_{\max} + n_{\min})/2$ .



values are used. The errors are larger than when  $\epsilon$  is used, so  $\mu$  was not used again in this work

It is clear from Table 4.3 that when  $\epsilon''_{\max}$  is greater than about 5, the anomalous dispersion in  $\epsilon'$  causes serious errors in the  $\mu_j^2$  values recovered from  $A_j$  and  $B_j$ , due to uncertainty in the value to use for  $\epsilon$ . In these cases the area  $C_j$ , should always be used to obtain  $\mu_j^2$ . When  $\epsilon''_{\max} \leq 2.5$ ,  $\mu_j^2$  is recovered to better than 1% from  $A_j$ ,  $B_j$  and  $C_j$ . Experimentally,  $\epsilon''_{\max}$  is usually less than 2.5.

The calculation of the  $\mu_j^2$  values from the different peak wavenumbers in the  $\tilde{\nu}\alpha''_m$  and  $\tilde{\nu}\epsilon''$  spectra through eq. (4.20) behaves identically. The result is exact if the correct value of  $\epsilon$  is known. For bands SA to SG the  $\epsilon$  values in Table 4.3 gave errors in  $\mu_j^2$  of up to 10%.

#### 4.4.3 Synthetic Double CDHO $\alpha''$ Bands and Bands Calculated from Them

A large number of synthetic double bands have been explored. The CDHO parameters which were used to calculate the  $\alpha''_m$  and  $\alpha'_m$  spectra in nine cases are shown in Table 4.4. The  $\mu_j^2$  values are on average smaller than for the isolated bands, and decrease from top to bottom in Table 4.4, in contrast to Table 4.1. The intensity ratio 4:1 was used for the two components of the doublet with the stronger band to high wavenumber, in all cases except one which has the intensity ratio 1:1. Half widths of  $20\text{ cm}^{-1}$  and, for specific purposes, 10 and  $40\text{ cm}^{-1}$ , and band separations ranging from 1.25 to 20 times the FWHH were chosen. The peak heights and wavenumbers in the  $\tilde{\nu}C''$  spectrum are included in Table 4.4, with those in the  $\tilde{\nu}\epsilon''$ ,  $E_m$  and  $\epsilon''$  spectra that were calculated from the  $\alpha''_m$  and  $\alpha'_m$  spectra, with  $V_m = 60.0\text{ cm}^3\text{ mole}^{-1}$  and  $\epsilon_\infty = 2.25$ , as described in Section 4.3.

The spectra of the imaginary susceptibility,  $C''$ , imaginary dielectric constant,  $\epsilon''$ , and imaginary refractive index,  $k$ , are shown for four cases in Figure 4.5. The spectra are scaled for convenient presentation, as noted in the caption, and the correct peak heights are in Table 4.4. Figure 4.5 shows that the relative intensities of the two components of the doublet are markedly different in the  $C''$ ,  $\epsilon''$  and  $k$  spectra, due to the effect of the real part of the polarizability on the imaginary dielectric constant,  $\epsilon''$  or imaginary refractive index,  $k$ . The imaginary susceptibility,  $C''$ , or the imaginary molar polarizability,  $\alpha''_m$ , shows the correct relative intensities.

**Table 4.4** Properties of the doublet CDHO imaginary polarizability bands and bands calculated from them by phenomenological equations.

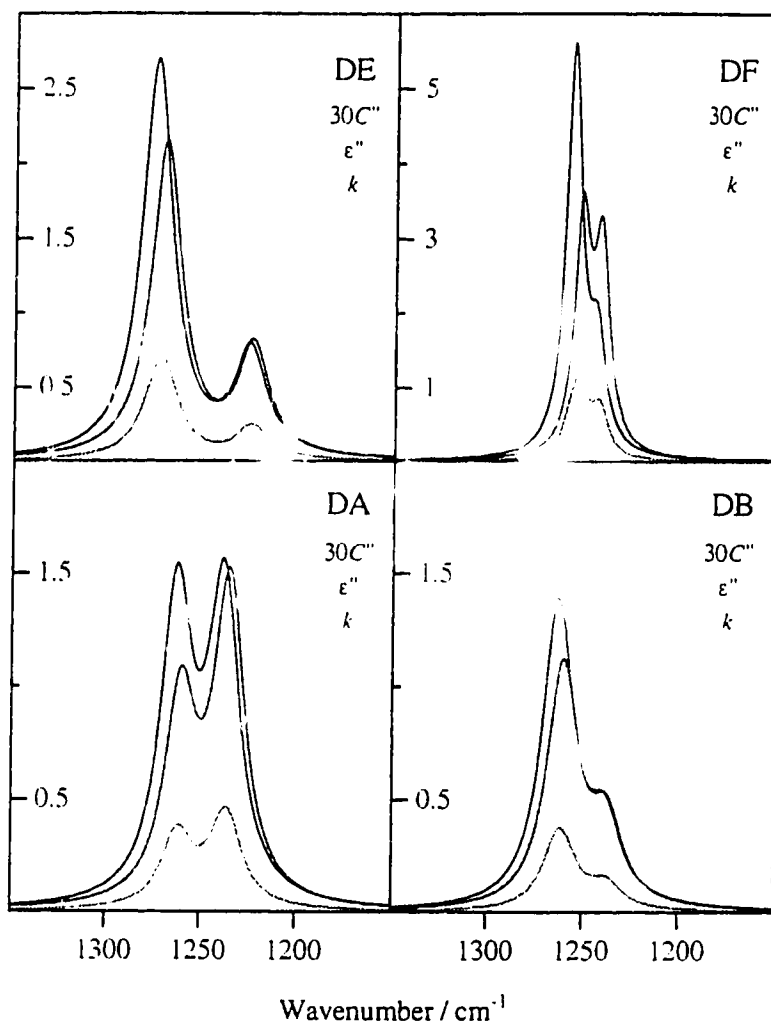
Band	$\tilde{\nu}_j/\Gamma_j$	$\Gamma_j/\text{cm}^{-1}$	$\mu_j^2$ <sup>a</sup>	Peak heights <sup>b</sup>			
				$\tilde{\nu}C''$	$\tilde{\nu}\epsilon''$	$E_m$	$\epsilon''$
DJ	2.5	20	16	458	8.10	7.52	6.44
			4	131	7.05	5.32	5.79
DH	5	20	16	455	9.95	8.17	7.75
			4	118	4.55	3.88	3.81
DG	2.5	40	16	230	5.07	5.06	3.96
			4	648	2.45	2.21	2.05
DF	1.25	10	4	235	4.53	4.88	3.62
			1	90.7	4.10	3.47	3.00
DE	2.5	20	4	115	2.73	2.91	2.15
			1	32.7	5.07	0.999	0.822
DD	1.25	20	4	118	2.67	2.91	2.13
			1	45.2	1.57	1.48	1.26
DC	1.25	10	2	118	2.67	2.91	2.13
			0.5	45.3	1.57	1.49	1.26
DB	1.25	20	2	58.8	1.42	1.56	1.12
			0.5	22.7	0.670	0.680	0.541
DA	1.25	20	2	64.8	1.37	1.61	1.09
			2	64.7	1.88	1.89	1.52

				Peak wavenumber / $\text{cm}^{-1}$			
				$\tilde{\nu}C''$	$\tilde{\nu}\epsilon''$	$E_m$	$\epsilon''$
DJ	2.5	20	16	1274.98	1256.69	1261.35	1256.65
			4	1225.30	1216.41	1219.25	1216.37
DH	5	20	16	1300.00	1280.42	1285.06	1280.38
			4	1200.04	1192.97	1195.47	1192.93
DG	2.5	40	16	1299.96	1280.33	1287.43	1280.17
			4	1200.58	1193.42	1196.26	1193.23
DF	1.25	10	4	1156.19	1251.28	1253.12	1251.27
			1	1245.43	1242.14	1243.25	1242.17
DE	2.5	20	4	1274.98	1269.83	1272.06	1269.79
			1	1225.30	1223.74	1224.42	1223.69
DD	1.25	20	4	1262.38	1257.18	1259.47	1257.14
			1	1240.73	1237.80	1238.97	1237.71
DC	1.25	10	2	1256.19	1253.58	1254.73	1253.57
			0.5	1245.43	1243.93	1244.51	1243.91
DB	1.25	20	2	1262.38	1259.71	1260.96	1259.67
			0.5	1240.73	1239.34	1239.95	1239.19
DA	1.25	20	2	1261.99	1259.36	1260.66	1259.31
			2	1238.00	1234.78	1236.17	1234.74

<sup>a</sup> Unit  $(\text{D } \text{\AA}^{-1} \text{ amu}^{-1/2})^2$ .

<sup>b</sup>  $V_m = 60 \text{ cm}^3 \text{ mole}^{-1}$ . Units are  $\text{cm}^{-1}$  for  $\tilde{\nu}C''$ ,  $10^3 \text{ cm}^{-1}$  for  $\tilde{\nu}\epsilon''$  and  $10^5 \text{ cm}^2 \text{ mole}^{-1}$  for  $E_m$ .



**Figure 4.5** The synthetic double bands DE, DF, DA and DB of Tables 4.4 and 4.5: Each box shows, from top to bottom, the  $C''$  spectrum (multiplied by 30), and the  $\epsilon''$  and  $k$  spectra calculated from the  $\alpha'_m$  and  $\alpha''_m$  through eq. (4.21b) and eq. (2.5b).

The effect of the approximations discussed in the derivation of  $\epsilon''$ , eq. (4.19), from  $\hat{\alpha}_m$ , eq. (4.13), is shown in Figure 4.6 for three doublets. Each box contains two curves. The darker curve is the correct  $\epsilon''$  spectrum, calculated through eq. (4.21b) from the doublet  $\hat{\alpha}_m$  spectra. The lighter curve is the "sum of singles", the sum of two spectra, each of which was calculated through eq. (4.21b) from the  $\hat{\alpha}_m$  spectrum of just one component,  $i$ , of the doublet. This  $\hat{\alpha}_m$  spectrum of component  $i$  was calculated by eq. (4.13), but  $\epsilon_\infty$  was replaced by the value of  $\epsilon$  at  $\tilde{\nu}_i$  due to the second component of the doublet. This is equivalent to the approximations involved in the derivation of eq. (4.19).

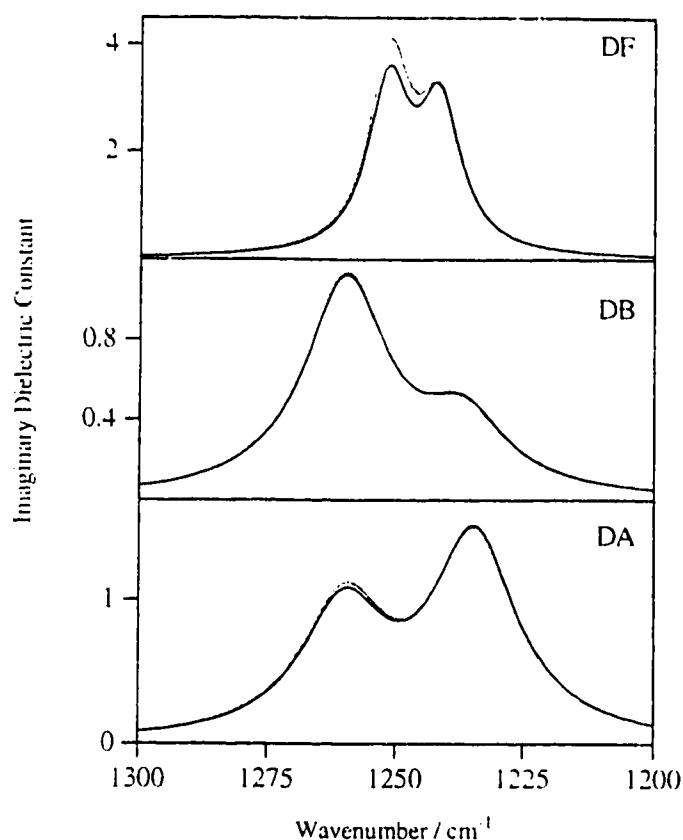


**Figure 4.6** Comparison of the  $\epsilon''$  spectrum calculated from the synthetic doublet  $\alpha_m''$  spectrum through eq. (4.21b) (darker curves) with the "sum of singles" (lighter curves), namely the sum of the  $\epsilon''$  spectra calculated through eq. (4.21b) from the individual components of the synthetic doublet, as described in the text

so the differences between the darker and lighter curves in Figure 4.6 show the error caused by these approximations. The correct  $\epsilon''$  spectrum yields a weaker high-wavenumber peak for all cases and a slightly stronger low-wavenumber peak for DA and DB.

#### 4.4.4 Recovery of the Intensities from the Doublet Bands

The doublets in the synthetic imaginary polarizability spectra can, of course, be fitted exactly with CDHO bands and the accurate intensities calculated by eq. (4.22). We note, and show later, that this also can be done for some experimental spectra.

To our surprise, it was found that in all cases the doublets in the imaginary dielectric constant,  $\epsilon''$ , spectrum could also be fitted exactly with CDHO bands, where "exactly" means with an average root-mean-squared percent deviation of less than 0.01%. The  $\epsilon''$

**Table 4.5** Percent error in the recovered values of  $\mu_j^2$  from fitting  $\epsilon''$  or  $k$  for double bands.

Band	$\Delta \tilde{\nu}_j / \Gamma_j$	$\epsilon''_{\max}$	$\epsilon^a$	% Error in $\mu_j^2$ from		
				$B_j^b$	$A_j^b$	$(\tilde{\nu}_j^2 - \tilde{\nu}_j^{*2})^b$
DJ	2.5	6.44	0.984	36	28	22
		5.79	3.774	25	1.3	18
DH	5	7.75	1.871	4.4	11	2.9
		3.81	3.180	4.0	4.3	3.0
DG	2.5	3.96	1.877	3.8	8.5	3.0
		2.05	3.160	4.8	6.0	4.8
DF	1.25	3.62	2.223	32	6.5	8
		3.30	2.223	134	4.3	144
DE	2.5	2.15	2.101	0.8	2.3	0.8
		0.822	2.708	1.0	2.4	2.0
DD	1.25	2.13	1.191	2.0	24	30
		1.26	3.025	11	0.2	82
DC	1.25	2.13	1.908	2.0	4.5	5.5
		1.26	3.022	10	0.2	88
DB	1.25	1.12	2.120	0.0	1.0	3.0
		0.541	2.652	4.0	6.0	87
DA	1.25	1.09	1.765	0.5	0.5	11
		1.52	2.577	4.5	3.0	9.5

<sup>a</sup>  $\epsilon = (\epsilon'_{\max} + \epsilon'_{\min}) / 2$ .

<sup>b</sup>  $\mu_j^2$  from  $B_j$  through eq. (4.14), from  $A_j$  through eq. (4.15) and from  $(\tilde{\nu}_j^2 - \tilde{\nu}_j^{*2})$  through eq. (4.20).

doublets were separated into individual component spectra in this way, and each component was multiplied by  $V_m \tilde{\nu}$  to produce the molar conductivity spectrum for each band. The intensity was then recovered from  $B_j$  for each component through eq. (4.14), using  $\epsilon$  as the average of the maximum and minimum values of  $\epsilon'$  for that component in the  $\epsilon'$  spectrum of the doublet. The percent error in the recovered  $\mu_j^2$  values is shown in Table 4.5.

Recovery of  $\mu_j^2$  from  $B_j$  depends on two factors,  $\epsilon''_{\max}$  and  $\Delta \tilde{\nu}_j / \Gamma_j$ , the peak-separation-to-FWHH ratio. These quantities are included in Table 4.5 for easy reference. The accuracy of recovery does not depend on  $\mu_j^2$  or on  $\Gamma_j$  *per se*, only through their effect on  $\epsilon''$  and  $\Delta \tilde{\nu}_j / \Gamma_j$ . When  $\epsilon''_{\max}$  is  $\sim 7$  (cases DJ and DH), the percent error in the  $\mu_j^2$  values is  $\sim 30\%$  when the band separation is 2.5 FWHH and  $\sim 4\%$  when the separation is 5 FWHH. The correct  $\mu_j^2$  values can not be obtained reliably for such strong bands even when they are isolated, so  $\mu_j^2$  should always be recovered from  $C_j$  for bands of this strength.

For  $\epsilon''_{\max}$  near 4 (case DG), the percent error in  $\mu_j^2$  is only 4% when the separation is 2.5 FWHH. This is far better than for bands DJ and DH in spite of the same  $\mu_j^2$  value (Table 4.4), and arises because the FWHH is  $40 \text{ cm}^{-1}$  instead of the  $20 \text{ cm}^{-1}$  of bands DJ and DH. The percent error in the recovered  $\mu_j^2$  values is less than 1% for separations  $\geq 5$  FWHH. When the separation is reduced to 1.25 FWHH for a band with the same  $\epsilon''_{\max}$  but four times weaker and four times sharper (case DF, Figure 4.5), the percent error in  $\mu_j^2$  is 30% and 130% for the stronger and weaker band, respectively. This case shows the largest difference between  $\epsilon''$  and the sum of singles in Figure 4.6.

For  $\epsilon''_{\max}$  near 2, the percent error in  $\mu_j^2$  recovered from  $B_j$  at a separation of 2.5 FWHH is only 1% (case DE, Figure 4.5) and is even better at larger separations. At 1.25 FWHH separation, the percent error in  $\mu_j^2$  is 2% for the stronger band and  $\sim 10\%$  for the weaker one (cases DD and DC). This is true whether the band has the same intensity as case DE (case DD) or is half as intense and half as broad (case DC).

For  $\epsilon''_{\max}$  near 1, very accurate  $\mu_j^2$  values are recovered from  $B_j$  at separations  $\geq 2.5$  FWHH. When the separation is 1.25 FWHH, the percent error in the recovered  $\mu_j^2$  value is  $< 1\%$  for the stronger band and about 4% for the weaker band, whether the intensity ratio of the two components of the doublet is 1:1 or 4:1 (cases DA and DB, Figures 4.5 and 4.6).

The molar absorption coefficient,  $E_m$ , equals  $\tilde{\nu}k$  apart from numerical constants [eqs. (4.2) to (4.4)]. The CDHO model is not expected to describe the  $k$  spectrum, but CDHO bands were fitted to the  $k$  bands in order to try to separate them. As expected, the fit was less good than for  $\epsilon''$  or  $\alpha_m''$  spectra and ranged from exact for bands DA and DB to very poor for bands DH and DJ. The individual bands used in the fit were converted to  $E_m$  bands through eqs. (4.2) and (4.3), and  $\mu_j^2$  was recovered from  $A_j$  through eq. (4.15). The percent errors in the  $\mu_j^2$  values recovered from  $A_j$  are included in Table 4.5. They are of the same order as those from  $B_j$ , much better in some cases and much worse in others.

The attractive possibility of recovering  $\mu_j^2$  values from wavenumber measurements instead of from area measurements, through eq. (4.20), was also explored. The percent errors in the  $\mu_j^2$  values recovered in this way are included in Table 4.5. Generally, the errors are larger than those for recovery from  $B_j$ .

These studies of double bands show that the accuracy of recovery of  $\mu_j^2$  depends on  $\epsilon''_{\max}$  and  $\Delta\tilde{\nu}_j / \Gamma_j$ . Accurate values of  $\mu_j^2$  can be obtained from  $A_j$  and  $B_j$  if the bands are

sufficiently weak and well separated. Specifically, the separation should be  $\geq 5$  FWHH if  $\epsilon''_{\max}$  is  $\sim 4$  and  $\geq 2.5$  FWHH if  $\epsilon''_{\max}$  is  $\sim 2$  or less. At smaller separations  $\mu_j^2$  from  $A_j$  and  $B_j$  may be accurate or may be in serious error. The results also show that the calculation of  $\mu_j^2$  from the peak wavenumbers in the  $\tilde{\nu}\epsilon''$  and  $\tilde{\nu}\alpha''_m$  spectra is unreliable. The only reliable way of recovering  $\mu_j^2$  with high accuracy is through the  $\alpha''_m$  spectrum and the  $C_j$ .

#### 4.4.5 Experimental Spectra

The results so far have been from spectra synthesized from the CDHO model. It is necessary to test the conclusions on real experimental spectra. The correct answers are not known for experimental spectra, but are taken to be those calculated from the molar polarizability,  $\alpha''_m(\tilde{\nu})$ , through the area  $C_j$  in eq. (4.12b). The degree to which the bands can be fitted by CDHO curves is shown, and the  $\mu_j^2$  values calculated from  $C_j$  are compared with those from  $B_j$  and  $A_j$  through eqs. (4.14b) and (4.15b). Results are presented for bands of benzene, toluene and methanol.

Figure 4.7 shows the second most intense absorption in the spectrum of liquid benzene, at  $1479\text{ cm}^{-1}$ , as the imaginary polarizability, the imaginary dielectric constant and the imaginary refractive index, with the associated real dielectric constant spectrum. This is a weaker peak than the synthetic double bands discussed above, with  $\epsilon''_{\max} = 0.45$  (Figure 4.7). The figure shows the  $\alpha''_m$ ,  $\epsilon''$  and  $k$  spectra as both the experimental spectrum and as the sum of CDHO bands fitted to it. The fitted curve is indistinguishable from the experimental curve in all three cases. The real dielectric constant spectrum is marked with horizontal lines through the curve at the values used for  $\epsilon$  for each of the bands. For the  $\alpha''_m$ ,  $\epsilon''$  and  $k$  spectra, Table 4.6 shows the wavenumbers and FWHH of the bands which fitted the spectrum, the areas under the  $\tilde{\nu}\alpha''_m$ ,  $V_m\tilde{\nu}\epsilon''$  and  $E_m$  spectra, the values of  $\epsilon$  used, and the values of  $\mu_j^2$  obtained. For the  $\epsilon''$  and  $k$  spectra, the table includes the percent deviations of  $\mu_j^2$  from the corresponding value calculated from  $C_j$ .

For the weak peak to high wavenumber (band 1) and the strong peak (band 2), the values of  $\mu_j^2$  calculated from  $B_j$  and  $A_j$  are within 0.4% of those calculated from  $C_j$ . For the weak peak to low wavenumber (band 3), which is separated from the strong band by only 1 FWHH, the deviations are 5%. Thus, even for this relatively weak group of bands which contains one strong band,  $C_j$  has to be used to obtain accurate values of  $\mu_j^2$ . The deviations of the values of  $\mu_j^2$  calculated from the peak wavenumbers (Table 4.6) through eq. (4.20) were -30%, +3.5% and +680% for bands 1 to 3 respectively. These large errors are not surprising because the wavenumber shifts between the  $\alpha''_m$  and  $\epsilon''$  spectra are very small.

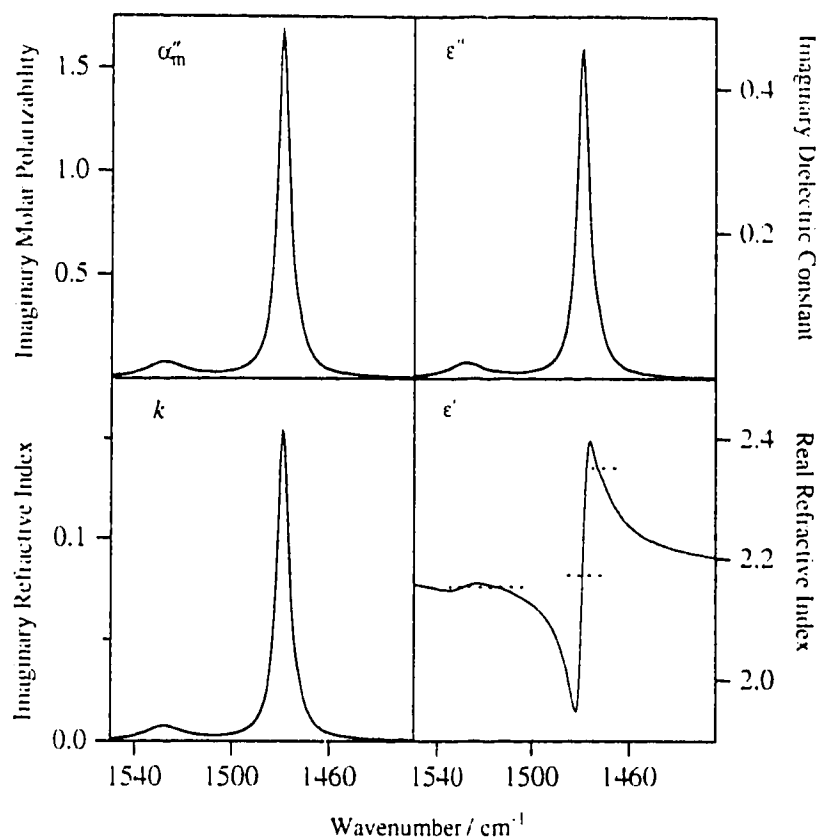


**Figure 4.7** Absorption and permittivity spectra near  $1500\text{ cm}^{-1}$  of liquid benzene,  $\text{C}_6\text{H}_6$ . The three absorption spectra are: top left,  $\alpha''_m$ ; top right,  $\epsilon''$ ; bottom left,  $k$ . The bottom right box contains the  $\epsilon'$  spectrum, with the value of  $\epsilon'$  for the different bands shown by horizontal dotted lines. The three absorption spectra are each shown as both the experimental spectrum and the sum of the three CDHO bands fitted to it. The two curves are indistinguishable in each case.

Figure 4.8 shows the  $\alpha''_m$ ,  $\epsilon''$ ,  $k$ , and  $\epsilon'$  spectra of two bands of toluene near  $700\text{ cm}^{-1}$ , in the same format as Figure 4.7. These are very strong bands with  $\epsilon''_{\text{max}} = 2.2$  and  $1.1$ . Each absorption spectrum was fitted by three CDHO bands. The fit is not as good as for benzene, with the fitted curve too high between the main bands and to high-wavenumber of the strongest band. The total area under the fitted  $\alpha''_m$  curve between  $775$  and  $650\text{ cm}^{-1}$  is  $2.7\%$  higher than that under the experimental curve. The use of nine bands in the fit reduced this error but did not eliminate it, so the simpler three-band fit was preferred. Table 4.6 contains the parameters of the fitted bands for each spectrum and the values of  $\mu_j^2$  calculated from  $C_j$ ,  $B_j$  and  $A_j$ . The deviations of the values calculated from  $B_j$  and  $A_j$  are up to  $2\%$  of the value from  $C_j$  for the two stronger bands and up to



**Table 4.6** Parameters of CDHO bands fitted to  $\alpha_m''$ ,  $\epsilon''$  and  $k$  spectra of benzene, toluene and methanol and dipole moment derivatives calculated from them.

Spectrum	Band	$\tilde{\nu}_{\text{band}}^a$	FWHH	Area <sup>b</sup>	$\epsilon^c$	$\mu_j^2$ <sup>d</sup>	% Deviation of $\mu_j^2$ <sup>c,e</sup>
$\text{C}_6\text{H}_6(\text{l})$ $\alpha_m''(\tilde{\nu})$	1	1527.89	18	0.03263		0.0610	
	2	1479.15	5.8	0.2206		0.412	
	3	1472.66	7.0	0.01319		0.0246	
$\text{C}_6\text{H}_6(\text{l})$ $\epsilon''(\tilde{\nu})$	1	1527.86	18	0.7846	2.153	0.0609	-0.2%
	2	1478.83	5.8	5.382	2.172	0.414	+0.4%
	3	1472.51	6.7	0.3303	2.350	0.0234	-5%
$\text{C}_6\text{H}_6(\text{l})$ $k(\tilde{\nu})$	1	1527.88	18	3.357	2.153	0.0608	-0.3%
	2	1478.99	5.8	22.94	2.172	0.414	+0.4%
	3	1472.57	6.8	1.369	2.350	0.0236	-4%
$\text{C}_6\text{H}_5\text{CH}_3(\text{l})$ $\alpha_m''(\tilde{\nu})$	1	729.89	6.7	0.7770		1.45	
	2	694.70	4.5	0.2202		0.411	
	3	677.50	6.9	0.008165		0.0152	
$\text{C}_6\text{H}_5\text{CH}_3(\text{l})$ $\epsilon''(\tilde{\nu})$	1	728.01	6.7	18.43	2.168	1.42	-2%
	2	694.11	4.6	6.002	2.373	0.420	+2%
	3	677.44	6.8	0.2272	2.492	0.0151	-0.7%
$\text{C}_6\text{H}_5\text{CH}_3(\text{l})$ $k(\tilde{\nu})$	1	728.89	7.1	80.61	2.168	1.45	0.0%
	2	694.38	4.6	24.19	2.373	0.415	+1%
	3	677.39	6.3	0.8193	2.492	0.0136	-11%
$\text{CH}_3\text{OH}(\text{l})$ $\alpha_m''(\tilde{\nu})$	1	1116.41	56	0.2334		0.436	
	2	1039.07	13	0.3660			
	3	1031.74	17	0.6459		2.20	
	4	1021.94	28	0.1635			
$\text{CH}_3\text{OH}(\text{l})$ $\epsilon''(\tilde{\nu})$	1	1116.63	55	4.070	1.579	0.425	-3%
	2	1036.61	13	4.432			
	3	1028.06	16	15.19	1.731	2.26	+3%
	4	1018.48	24	3.883			
$\text{CH}_3\text{OH}(\text{l})$ $k(\tilde{\nu})$	1	1116.68	55	20.26	1.579	0.424	-3%
	2	1038.39	13	28.39			
	3	1029.71	17	66.84	1.731	2.23	+1%
	4	1020.21	25	15.76			

a  $\tilde{\nu}_{\text{band}}$  is the resonance wavenumber of the fitted CDHO band. It equals  $\tilde{\nu}_j$  for the  $\alpha_m''$  spectra and  $\tilde{\nu}_j^*$  for the  $\epsilon''$  spectra.

b The full area under the band calculated from the parameters of the fitted bands. The areas presented are  $C_j$  for the  $\alpha_m''$  spectra,  $V_m \int \tilde{\nu} \epsilon'' d\tilde{\nu} = B_j \left[ \frac{\epsilon + 2}{3} \right]^2$  for the  $\epsilon''$  spectra, and  $A_j$  for the  $k$  spectra, all in the unit  $\text{km mole}^{-1}$ .

c The entries are left blank where not applicable.

d The unit is  $(\text{Debye } \text{\AA}^{-1} \text{ amu}^{-1/2})^2$ . The  $\mu_j^2$  value for  $\text{C}_6\text{H}_6$  is the sum over the two components of the degenerate vibration.

e The deviation of the  $\mu_j^2$  value from that calculated from the  $\alpha_m''$  spectrum, as a percentage of the latter.

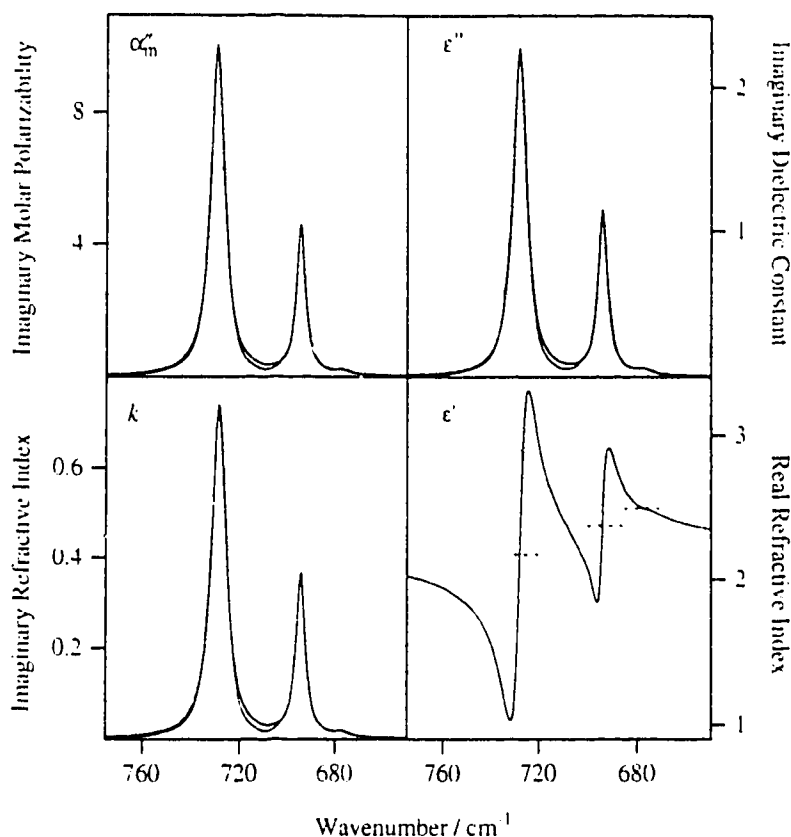


**Figure 4.8** Absorption and permittivity spectra of the  $700\text{ cm}^{-1}$  region of the spectrum of liquid toluene,  $\text{C}_6\text{H}_5\text{CH}_3$ . The three absorption spectra are: top left,  $\alpha_m''$ ; top right,  $\epsilon''$ ; bottom left,  $k$ . The bottom right box contains the  $\epsilon'$  spectrum, with the value of  $\epsilon'$  for the different bands shown by horizontal dotted lines. The three absorption spectra are each shown as both the experimental spectrum and the sum of the three CDHO bands fitted to it. The fitted curve is higher where the two curves can be distinguished.

11% for the weakest band. The percent deviations of the values calculated from the peak wavenumbers through eq. (4.20) are 2%, 0.7% and 167% for the strongest to weakest bands respectively.

Figure 4.9 shows a final experimental example that is slightly more complicated, the  $\alpha_m''$ ,  $\epsilon''$ ,  $k$ , and  $\epsilon'$  spectra of the C-O stretching band of methanol, with a weak  $\text{CH}_3$  rocking band to high wavenumber. In this case  $\epsilon_{\text{max}}''$  is 1.8. Each absorption spectrum was fitted with four bands, three of which, in a range of 1 FWHH, were needed to fit the single strong band. The fit is excellent for each spectrum, with the experimental curve slightly stronger at the peak of the strong band and at the edges of the figure. Because of the sharp rise in  $\epsilon'$  through the strong band, the same value of  $\epsilon'$  was used for the three

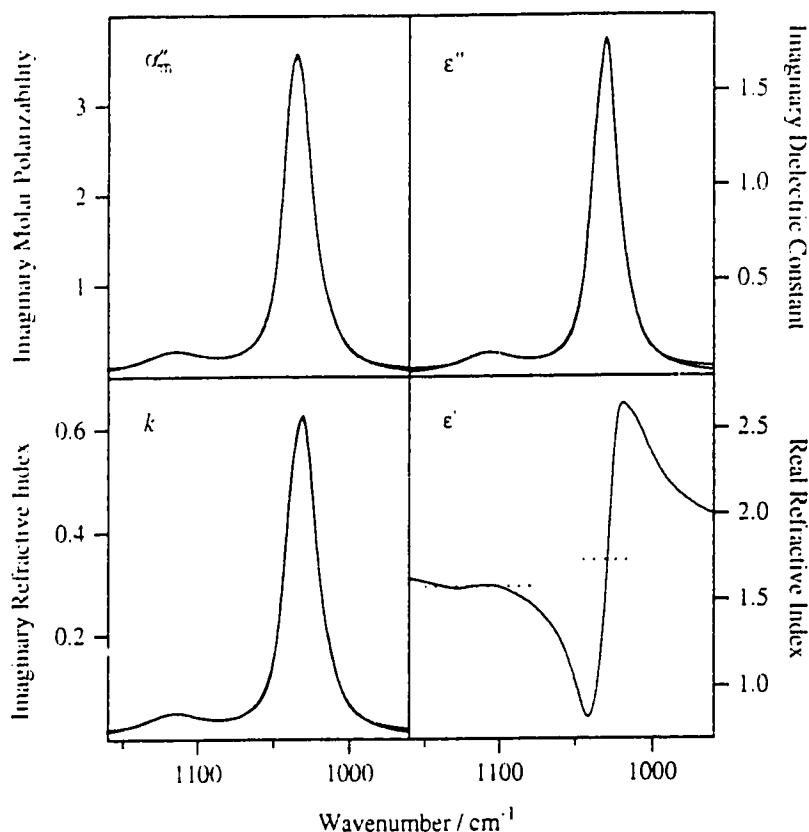


**Figure 4.9** Absorption and permittivity spectra of the  $1050\text{ cm}^{-1}$  region of the spectrum of liquid methanol,  $\text{CH}_3\text{OH}$ . The three absorption spectra are: top left,  $\alpha''_m$ ; top right,  $\epsilon''$ ; bottom left,  $k$ . The bottom right box contains the  $\epsilon'$  spectrum, with the value of  $\epsilon$  for the different bands shown by horizontal dotted lines. The three absorption spectra are each shown as both the experimental spectrum and the sum of the four CDHO bands fitted to it. The fitted curve is lower where the two curves can be distinguished.

bands fitted to it, and the areas of the three fitted bands were added together to obtain the area of the strong band. Table 4.6 contains the parameters of the fitted bands for the  $\alpha''_m$ ,  $\epsilon''$  and  $k$  spectra and the  $\mu_j^2$  values calculated from them. The values calculated from  $B_j$  and  $A_j$  deviate from those calculated from  $C_j$  by up to 3%.

It has been shown<sup>7</sup> (Section 5.5.2) for methanol spectra that were not fitted with CDHO curves that  $\mu_j^2$  calculated from  $A_j$ ,  $B_j$  and  $C_j$  are the same within 0.8% for the O-H stretching band, the unseparated C-H stretching bands and the H-C-O-H torsion band of methanol, for which  $\epsilon''_{\text{max}}$  is 0.34, 0.23 and 0.30, respectively.

#### 4.5 Conclusions

The imaginary molar polarizability,  $\alpha_m''$ , spectra yield the most reliable values of the vibrational intensities and most clearly reveal the molecular properties free from the effect of the permittivity or refraction of the liquid. However, they do subject the experimental measurements to the approximation of the Lorentz local field model.

Specifically, very strong symmetric imaginary molar polarizability or imaginary dielectric constant bands yield very asymmetric imaginary refractive index and molar absorption coefficient bands. The asymmetry increases with decreasing peak wavenumber for bands of given intensity. Clearly, the imaginary molar polarizability or the imaginary susceptibility should be used for studies in which line shape is relevant, which includes the assignment of spectral bands.

Vibrational intensities should be calculated from the imaginary molar polarizability spectrum through the area  $C_j$  if errors of 1% or greater are to be avoided. Accurate values of  $\mu_j^2$  can sometimes be obtained from the molar absorption coefficient,  $E_m$ , or the imaginary dielectric constant,  $\epsilon''$ , through the areas  $A_j$  and  $B_j$ , particularly for bands that are weak and well separated, but these methods are not generally reliable. The errors are due to the anomalous dispersion in the real dielectric constant; consequently they vary with the imaginary dielectric constant at the peak of the band and with the peak separation divided by bandwidth. The errors are increasingly serious as the peak wavenumber decreases. They are particularly serious for  $\epsilon_{\max}''$  values greater than 2, but also can be significant for much smaller  $\epsilon_{\max}''$  values. The attractive possibility of calculating intensities from wavenumber differences in the  $\tilde{\nu}\epsilon''$  and  $\tilde{\nu}\alpha_m''$  is not useful in practice.

#### 4.6 References

1. J. E. Bertie, R. N. Jones, and V. Behnam, *Appl. Spectrosc.* **39**, 401 (1985).
2. J. E. Bertie, R. N. Jones, and V. Behnam, *Appl. Spectrosc.* **40**, 427 (1986).
3. J. E. Bertie, C. D. Keefe, and R. N. Jones, *Can. J. Chem.* **69**, 1609 (1991).
4. J. E. Bertie, R. N. Jones, and C. D. Keefe, *Appl. Spectrosc.* **47**, 891 (1993).
5. J. E. Bertie, R. N. Jones, Y. Apelblat, and C. D. Keefe, *Appl. Spectrosc.* **48**, 127 (1994).
6. J. E. Bertie, R. N. Jones, and Y. Apelblat, *Appl. Spectrosc.* **48**, 144 (1994).

7. J. E. Bertie, S. L. Zhang, H. H. Eysel, S. Baluja, and M. K. Ahmed, *Appl. Spectrosc.* **47**, 1100 (1993).
8. J. E. Bertie and S. L. Zhang, *Appl. Spectrosc.* **48**, 176 (1994).
9. R. N. Jones, D. Escolar, J. P. Hawranek, P. Neelakantan, and R. P. Young, *J. Mol. Struct.* **19**, 21(1973).
10. J. P. Hawranek, P. Neelakantan, R. P. Young, and R. N. Jones, *Spectrochim. Acta* **32A**, 75 (1976).
11. J. P. Hawranek, P. Neelakantan, R. P. Young, and R. N. Jones, *Spectrochim. Acta* **32A**, 85 (1976).
12. J. P. Hawranek and R. N. Jones, *Spectrochim. Acta* **32A**, 99 (1976).
13. J. P. Hawranek and R. N. Jones, *Spectrochim. Acta* **32A**, 111 (1976).
14. R. N. Jones and R. P. Young, *Computer Programs for Infrared Spectrophotometry XVI to XXII*. National Research Council of Canada Bulletin **13** (Ottawa, 1976).
15. D. G. Cameron, J. P. Hawranek, P. Neelakantan, R. P. Young, and R. N. Jones, *Computer Programs for Infrared Spectrophotometry XLII to XLVII*. National Research Council of Canada Bulletin **16** (Ottawa, 1977).
16. T. G. Goplen, D. G. Cameron, and R. N. Jones, *Appl. Spectrosc.* **34**, 657 (1980).
17. T. G. Goplen, D. G. Cameron, and R. N. Jones, *Appl. Spectrosc.* **34**, 652 (1980).
18. J. E. Bertie and H. H. Eysel, *Appl. Spectrosc.* **39**, 392 (1985).
19. J. E. Bertie, H. Harke, M. K. Ahmed, and H. H. Eysel, *Croat. Chem. Acta* **61**, 391 (1988).
20. J. E. Bertie, M. K. Ahmed, and S. Baluja, *7th International Conference on Fourier Transform Spectroscopy*, Fairfax, Virginia; SPIE, **1145**, 518 (1989).
21. J. E. Bertie, M. K. Ahmed, and H. H. Eysel, *J. Phys. Chem.* **93**, 2210 (1989).
22. J. E. Bertie, S. L. Zhang, and R. Manji, *Appl. Spectrosc.* **46**, 1660 (1992).
23. M. J. Dignam, *Appl. Spectrosc. Rev.* **21**, 99 (1988).
24. M. A. Czarnecki and J. P. Hawranek, *J. Mol. Liq.* **46**, 151(1990).
25. M. A. Czarnecki and J. P. Hawranek, *Z. Phys. Chem.* **171**, 179 (1991).

26. M. A. Czarnecki, J. P. Hawranek, and W. Wrzeszcz, *J. Mol. Struct.* **275**, 111 (1992).
27. J. E. Bertie and S. L. Zhang, *Can. J. Chem.* **70**, 520 (1992).
28. T. Motojima, S.-I. Ikawa, and M. J. Kimura, *J. Quant. Spectrosc. Radiat. Trans.* **25**, 29 (1981).
29. M. Born and E. Wolf, *Principles of Optics: Electromagnetic Theory of Propagation, Interference and Diffraction of Light*, 808, Pergamon Press (Oxford, 1980).
30. A. A. Clifford and B. Crawford Jr., *J. Phys. Chem.* **70**, 1536 (1966).
31. J. Fahrenfort, in *Infrared Spectroscopy and Molecular Structure: An Outline of the Principles*, Ed. M. Davies, Elsevier, Amsterdam, 1963, 377.
32. J. W. Warner and M. Wolfsberg, *J. Chem. Phys.* **78**, 1722 (1983).
33. E. B. Wilson, Jr., J. C. Decius, and P. C. Cross, *Molecular Vibrations: The Theory of Infrared and Raman Vibrational Spectra*, 388, McGraw-Hill Book Company, Inc. (New York, 1955).
34. S. R. Polo and M. K. Wilson, *J. Chem. Phys.* **23**, 2376 (1955).
35. J. E. Bertie and M. K. Ahmed, Unpublished results (1992).
36. K. S. Seshadri and R. N. Jones, *Spectrochim. Acta* **19**, 1013 (1963).

## Chapter 5   Infrared Refractive Indices from 8000 to 2 cm<sup>-1</sup>, Absolute Integrated Intensities, and Dipole Moment Derivatives of Methanol (CH<sub>3</sub>OH) at 25°C \*

### 5.1 Introduction

The use of the CIRCLE cylindrical, multiple attenuated total reflection cell for the determination of the infrared refractive indices of liquids<sup>1-3</sup> has been reported. From the infrared refractive indices,  $\hat{n}(\tilde{\nu}) = n(\tilde{\nu}) + i k(\tilde{\nu})$ , can be calculated the results of any infrared spectroscopic experiment, as well as other related measures of refraction and absorption such as the complex infrared dielectric constant,  $\hat{\epsilon}(\tilde{\nu}) = \epsilon'(\tilde{\nu}) + i \epsilon''(\tilde{\nu})$ , the molar conductivity,  $V_m \tilde{\nu} \epsilon''(\tilde{\nu})$ , where  $V_m$  is the volume of one mole of pure liquid or of one mole of solution, the integrated molar conductivity under the absorption bands, the decadic molar absorption coefficient,  $E_m(\tilde{\nu}) = 4\pi \tilde{\nu} k(\tilde{\nu}) / (2.303C)$ , where  $C$  is the molar concentration of the absorbing species, the decadic linear absorption coefficient,  $K(\tilde{\nu}) = 4\pi \tilde{\nu} k(\tilde{\nu}) / 2.303$ , and the integrated absorption intensity  $A_j$  which is the integrated Napierian linear absorption coefficient. If the Lorentz model for the local field is adopted, the integrated absorption intensity  $B_j$  can be calculated. The equations that define and relate these quantities are partly given in earlier papers in this series<sup>1-3</sup> and are described in the appendix. The symbols and names recommended by IUPAC<sup>4,5</sup> have been followed in most cases.

The complex mean molecular polarizability,  $\hat{\alpha}(\tilde{\nu})$ , can also be calculated from the refractive indices if the Lorentz model for the local field is adopted, as described by Dignam<sup>6</sup>. This quantity is used in this paper, except that it is multiplied by Avogadro's number and called the (infrared) molar polarizability,  $\hat{\alpha}_m(\tilde{\nu})$ . The molar polarizability is related to Clifford and Crawford's<sup>7</sup> local susceptibility,  $\hat{C}(\tilde{\nu})$ , by  $V_m \hat{C}(\tilde{\nu}) = \hat{\alpha}_m(\tilde{\nu})$ . The molar polarizability is complex<sup>6</sup>,  $\hat{\alpha}_m(\tilde{\nu}) = \alpha'_m(\tilde{\nu}) + i \alpha''_m(\tilde{\nu})$ , and the area under band  $j$  in the  $\tilde{\nu} \alpha''_m$  spectrum is designated  $C_j$  in this work. The  $C_j$  is directly related<sup>6</sup> to the dipole moment change during a normal vibration, fully corrected for the effects described by the Lorentz local field. The area under the molar conductivity spectrum has been used previously<sup>1,2</sup> to calculate the dipole moment changes via the integrated absorption intensity  $B_j$ , but this is an approximate treatment if the spectrum contains

---

\* A version of this chapter has been published. Bertie, Zhang, Eysel, Baluja, and Ahmed, *Appl. Spectrosc.* **47**, 1100 (1993).

neighboring bands<sup>8,9</sup>. The equations needed to calculate molecular property  $\hat{\alpha}(\tilde{\nu})$  from refractive indices and to relate it to molecular dipole moment derivatives are summarized in the appendix.

Experimental results for water and heavy water have been reported<sup>10</sup> as have the effect of impurities on the absolute absorption intensity of the OH stretching band of water<sup>11</sup> and the accuracy of the calculations that yield the refractive indices from the multiple ATR spectra<sup>3</sup>.

Water was chosen for initial study because of its importance to people, because there is a considerable literature<sup>10</sup> on its infrared absorption intensities and those of its isotopomers, and because it is well known to absorb so strongly that it is difficult to measure. The primary alcohols are also of great importance. They are hydrogen bonded and absorb intensely in their broad OH stretching bands. Primary alcohols from C<sub>1</sub> to C<sub>10</sub> are liquids at room temperature, so a homologous series of considerable length can be studied. They provide data on the enhancement of the intensity of OH stretching bands on hydrogen bond formation, which is a topic of considerable interest but very limited data. The spectrum of methanol contains a sharp and very intense C–O stretching band which is difficult to measure, and deuterated forms of methanol and ethanol are available to help assignment of the intensity in cases of overlapping bands. For these reasons, methanol and the primary alcohols were chosen as important and challenging substances to study.

Preliminary results for the primary alcohols have been reported<sup>12,13</sup>, as have those for methanol-water mixtures<sup>14</sup>. In this chapter results are reported for pure liquid methanol at 25°C, between 6000 and 350 cm<sup>-1</sup>, from ATR measurements made in this laboratory by four different workers over an eight year period. These workers used CIRCLE cells of two different lengths, with two different configurations of the CIRCLE cell in the instrument. Results are also reported from transmission experiments between 7500 and 3750 cm<sup>-1</sup> and in regions of weak absorption below 3750 cm<sup>-1</sup>. These results are linked with those obtained by Honijk's et al<sup>15</sup> between 350 cm<sup>-1</sup> and 2 cm<sup>-1</sup>. The close agreement between the results obtained with this variety of factors helps to place limits on the possible systematic errors that may affect the absolute accuracy of our optical constants and integrated absorption intensities.

While the assignment of the infrared spectrum of methanol and its isotopomers is well established<sup>16</sup>, only two papers are known which have reported results of measurement of the absolute infrared absorption intensities of liquid methanol. Sethna



and Williams<sup>17</sup> studied methanol by specular reflection spectroscopy from an air-methanol interface between 6700 and 350 cm<sup>-1</sup>, as part of the extensive studies by Williams and his coworkers during the 1970s of the infrared optical constants of liquids. They unfortunately did not tabulate their quantitative intensity data, but reported in graphical form the reflectance spectrum,  $R(\tilde{\nu})$  and the real and imaginary refractive index spectra,  $n(\tilde{\nu})$  and  $k(\tilde{\nu})$ , respectively, where the complex refractive index  $\hat{n}(\tilde{\nu}) = n(\tilde{\nu}) + i k(\tilde{\nu})$ . They also reported the band intensities defined, somewhat unconventionally as discussed later, as the areas under the bands in the imaginary refractive index spectrum.

The far-infrared optical constants of methanol have been reported between 350 and 2 cm<sup>-1</sup> by Honijk, Passchier, Mandel, and Afsar<sup>15</sup>. Unfortunately, these authors also did not report their quantitative absorption spectra in tabular form, but they did show graphs on a relatively large scale. They reported the real refractive index spectrum. Instead of the imaginary refractive index spectrum they reported the linear Napierian absorption coefficient spectrum,  $\alpha(\tilde{\nu}) = -d^{-1} \log_e[I_t(\tilde{\nu})/I_o(\tilde{\nu})] = 4\pi\tilde{\nu}k(\tilde{\nu})$ , where  $d$  is the pathlength and  $I_t(\tilde{\nu})$  and  $I_o(\tilde{\nu})$  denote the intensities transmitted by and incident on the length  $d$  of liquid, after correction of the intensities for reflection losses. They called this quantity the power absorption coefficient<sup>18</sup> spectrum,  $\alpha(\tilde{\nu})$ . This meaning of  $\alpha$  is not used elsewhere in this chapter, and should not be confused with the use of  $\hat{\alpha}(\tilde{\nu})$ ,  $\hat{\alpha}_m(\tilde{\nu})$ ,  $\alpha'_m(\tilde{\nu})$ , and  $\alpha''_m(\tilde{\nu})$  to mean the complex polarizability, complex molar polarizability and its real and imaginary components.

For brevity,  $k(\tilde{\nu})$ , the imaginary refractive index is called the absorption index, its other common name, in the remainder of this chapter.  $\tilde{\nu}$  means the vacuum wavenumber of the radiation.

## 5.2 Method

### 5.2.1 Attenuated Total Reflection Spectroscopy

The method<sup>1-3</sup> used is to record multiple attenuated total reflection spectra of the empty cell and the cell full of liquid, which yield as their ratio the multiple ATR spectrum of the liquid. The negative decadic logarithm,  $-\log_{10}$ , of this multiple ATR spectrum is called the pATR spectrum, by analogy with an equilibrium constant  $K$  and  $pK$ . The pATR spectrum is converted to an approximate absorption index spectrum,  $k(\tilde{\nu})$ , via the approximate description of absorption over the penetration depth of the evanescent wave<sup>1</sup>. The absorption index spectrum is converted into the real refractive

index spectrum,  $n(\tilde{\nu})$ , via a Kramers-Krönig transform plus the value of the real refractive index at the high-wavenumber limit of the data. The real and imaginary refractive index spectra are then used, with the refractive index spectrum of the material which forms the ATR element, to calculate the pATR spectrum from Fresnel's equations, which describe the ATR process accurately if the angle of incidence is precisely known. In order to improve the fit, the refractive index values are refined as follows. The observed pATR spectrum is ratioed to the calculated one and the  $k$  value at each wavenumber is multiplied by the pATR ratio at that wavenumber, reduced by a damping factor to control the refinement if desired. The  $n$  spectrum is re-calculated, and the refinement is repeated to convergence.

In addition to the pATR spectrum, two pieces of information are required. The first is the real refractive index of the liquid at the high wavenumber limit of the observed spectrum. This is obtained from literature data as described elsewhere<sup>2</sup>. The second, a crucial parameter, is the effective number of reflections at the rod-liquid interface, NRF. This is obtained<sup>2,3</sup> by fitting the observed pATR spectrum of pure liquid benzene to the known refractive indices of benzene.

It has been noted<sup>19,20</sup> that the CIRCLE apparatus has an imprecise optical configuration, and that the method used assumes 45° incidence but the light beam is not parallel so not all of the light rays can be incident at 45°. Alternative procedures have been suggested<sup>19,20</sup> but have not been adopted because they offered no improvement over the few percent accuracy that is claimed for the absorption index values. The use of known values of the optical constants of benzene to calculate an effective number of reflections inside the ATR rod appears<sup>2,10,11</sup> to ensure that the imaginary refractive indices derived from measured pATR spectra are accurate to a few percent, even though the effective number of reflections undoubtedly includes more factors than the physical number of reflections. As is discussed later, the result obtained in this work supports this conclusion.

Important changes have been made to the methods recently and are described<sup>3,21</sup> in detail in Chapters 2 and 3. Spectral files from the Bruker instrument are imported into the Galactic Industries' program SpectraCalc, and all of the computational programs read and write files in SpectraCalc's ".SPC" format. The programs are written in FORTRAN for compilation with the Microsoft FORTRAN 5.1 compiler. PASCAL programs also exist, but the FORTRAN programs run twice as fast. An important change for this work is that the program AHILBERT, which was used to carry out the KK transform of  $k(\tilde{\nu})$

to  $n(\tilde{\nu})$  via two successive fast Fourier transforms (FFTs), has been found to be inaccurate<sup>21</sup>. It has recently been discovered experimentally<sup>21</sup> what Bracewell<sup>22</sup> has pointed out in general, that although the infinite KK and Hilbert transforms are equivalent the *finite* Hilbert transform may not be accurately done by two successive Fourier transforms if the bands are not very sharp. Consequently, the results obtained from the program AHILBERT differed from those obtained from the KK subroutine. The problem<sup>21</sup> has been corrected, and current programs give accurate results by both, the FFT and the KK algorithms. The latter is slightly more accurate, but is slower, and it is always used in the final stages of refinement. To reduce the error in the  $n(\tilde{\nu})$  caused by the incompleteness at low wavenumber of the  $k(\tilde{\nu})$  which is entered into the Hilbert or KK transformation, it is possible to add the incomplete part of the  $k(\tilde{\nu})$ , if it is known from other sources, or to extend the  $k(\tilde{\nu})$  linearly<sup>21</sup> to  $k = 0$  at  $0 \text{ cm}^{-1}$ . This addition improves the  $n(\tilde{\nu})$  which, in turn, improves the  $k(\tilde{\nu})$  that is obtained from the pATR spectrum.

### 5.2.2 Transmission Spectroscopy

Transmission spectra of methanol were measured in cells with pathlengths ranging from 140 to 1100  $\mu\text{m}$ . The experimental absorbance spectra were converted to refractive index spectra by using program RNJ46A. This program is based on the National Research Council of Canada (NRCC) program 46<sup>23</sup> which has been modified<sup>24</sup> to correct for errors in the baseline as well as making the correction<sup>23</sup> for reflection effects at the inner and outer window surfaces under certain ideal assumptions. The details of this program and its use have been described elsewhere<sup>24</sup>.

## 5.3 Experimental

Methanol and benzene were reagent grade stored over 3Å molecular sieve. Some samples of methanol were distilled under nitrogen from sodium or from Magnesium and iodine, before being stored over molecular sieve. Some samples of benzene were distilled from sodium and benzophenone before being stored over molecular sieve. The results were not sensitive to the method of purification of reagent grade materials.

Spectra were measured on a Bruker IFS 113V spectrometer at  $2 \text{ cm}^{-1}$  nominal resolution. A 10 mm aperture was used with a global source and encapsulated deuterated triglycine sulfate detectors with either KBr or polyethylene window. Ge-on-KBr, Si-on-CaF<sub>2</sub>, and 3  $\mu\text{m}$  Mylar beamsplitters were used with an optical retardation

velocity of about  $0.40 \text{ cm s}^{-1}$ . The Fourier transformation used one level of zero filling, and a trapezoidal apodization function which declined linearly from unity at 80% of maximum retardation to zero at maximum retardation.

The CIRCLE cell was kept inside the evacuated instrument and filled and emptied via Teflon tubing. The calibration spectra of benzene were recorded weekly, and the effective number of reflections did not change unless the cell or instrument was re-aligned or the cell was changed. In the middle of this work, the CIRCLE cell mount was completely re-aligned in the sample compartment, because it was found that the infrared beam passes through the compartment at a distinct angle to the physical axis of the compartment. Also while this work was in progress, a half-length liquid holder was developed for the CIRCLE cell, 30 mm long instead of the usual 60 mm. The same ATR rod, 82 mm long by 6 mm diameter with cones of  $45^\circ$  half-angle at each end, was used with both liquid holders. The short liquid holder, which was put at one end of the rod, gave the effective number of reflections, NRF, equal to  $\sim 3$  instead of the  $\sim 6$  with the full length liquid holder. Neither of these major changes caused significant differences in the refractive indices obtained.

FT-IR intensity spectra were recorded of the CIRCLE cell full of dry nitrogen gas and of the cell full of the liquid under study, and their ratio was converted to a pATR spectrum. Between samples the cell was rinsed with benzene and dried with nitrogen gas. Many pATR spectra were obtained, on different days, weeks or even years. When the ZnSe rod was used, pATR spectra were measured with Ge-on-KBr and with Si-on-CaF<sub>2</sub> beamsplitters. If the spectra with the two beamsplitters did not agree to within 3%, they were rejected. Otherwise they were averaged from 4000 to  $1600 \text{ cm}^{-1}$ , and a single pATR spectrum recorded with a ZnSe rod between 8000 and  $700 \text{ cm}^{-1}$  was obtained by merging the three spectra in the following way. The pATR values in the region from  $8000 \text{ cm}^{-1}$  to about  $6500 \text{ cm}^{-1}$  were set to zero because the absorption in that region is well below our measurement limit, the spectrum recorded with the Si-on-CaF<sub>2</sub> beamsplitter was used from  $6500$  to  $4000 \text{ cm}^{-1}$ , the average spectrum was used from 4000 to  $1600 \text{ cm}^{-1}$ , and the spectrum recorded with the Ge-on-KBr beamsplitter was used from 1600 to  $700 \text{ cm}^{-1}$ . Typically four or five such merged pATR spectra were compared and averaged to yield a "ZnSe" pATR spectrum that was converted to refractive index spectra between 8000 and  $700 \text{ cm}^{-1}$  via the method described in the previous section. Typical pATR spectra recorded with a ZnSe rod and the long and the short liquid holders are shown in Figure 5.1 (the lower two curves).

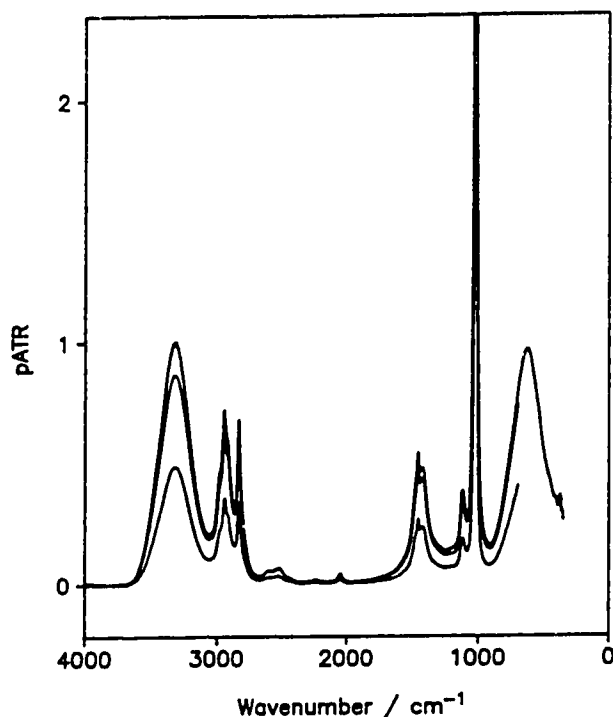


**Figure 5.1** pATR spectra of methanol recorded with KRS-5 (upper curve) and ZnSe (middle and lower curves) ATR rods. The liquid holder around the 82 mm long ATR rod was 30 mm long for the lower curve and 60 mm long for the upper two curves. The effective numbers of reflections were about 6 for the long cell and about 3 for the short cell.

Methanol does not dissolve KRS-5, i.e. Thallium bromo iodide, and CIRCLE cell rods of KRS-5 allow spectra to be recorded with Ge-on-KBr and polyethylene beamsplitters down to  $350\text{ cm}^{-1}$ . Accordingly, pATR spectra were recorded from 4000 to  $350\text{ cm}^{-1}$  with the KRS-5 ATR rods, and were transformed to refractive index spectra. The pATR spectrum recorded with the KRS-5 rod and the long liquid holder (NRF=6.2) is included in Figure 5.1 (upper curve).

Transmission spectra of liquid methanol were measured in a variable pathlength cell with  $\text{CaF}_2$  windows. A reference spectrum was first taken of the empty instrument, and a spectrum was taken of the empty cell at a certain pathlength. Then the spectrum of the cell full of methanol was taken, and the cell was rinsed with benzene, drained, and dried with nitrogen gas. In order to check for possible pathlength change when the cell was filled and emptied, the spectrum of the empty cell was repeated, and finally the spectrum of the empty instrument was repeated to check for instrument drift. The spectra of the empty cell and the spectrum of the cell full of methanol were converted to

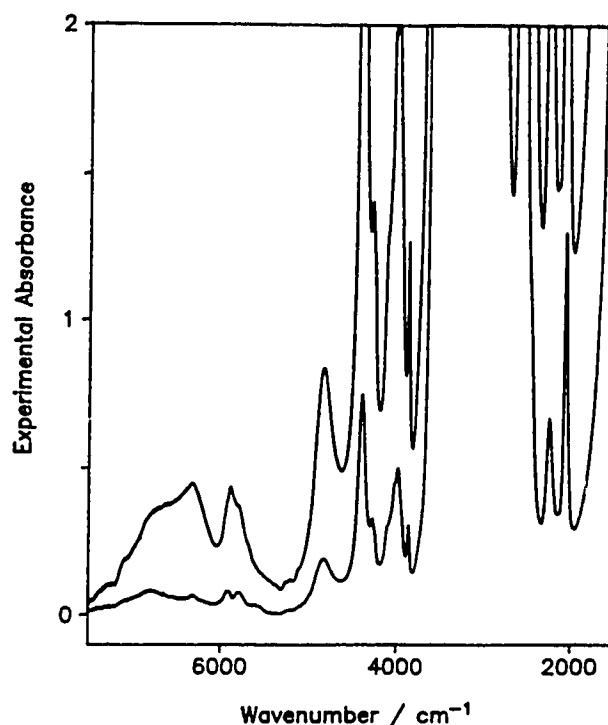


**Figure 5.2** Experimental absorbance spectra<sup>24</sup> of liquid methanol in cells with CaF<sub>2</sub> windows and pathlengths 250 and 1100  $\mu\text{m}$ .

experimental absorbance<sup>24</sup> spectra with the spectrum of the empty instrument as the reference spectrum. If the pathlengths calculated from the two empty cell spectra differed by more than 0.5%, the set of spectra was rejected. Figure 5.2 shows experimental absorbance<sup>24</sup> spectra of liquid methanol at pathlengths of 250 and 1100  $\mu\text{m}$ .

## 5.4 Results

The real refractive index of methanol at 8000  $\text{cm}^{-1}$  at 25°C was found to be  $1.325 \pm 0.001$  by fitting the values at visible wavelengths<sup>25</sup> to  $n^2 = A + B\nu^2 + C\nu^4$ , and extrapolating to 8000  $\text{cm}^{-1}$ .

Figure 5.3 shows absorption index spectra,  $k(\nu)$ , calculated from pATR spectra recorded with ZnSe (above 830  $\text{cm}^{-1}$ ) and KRS-5 (below 830  $\text{cm}^{-1}$ ) ATR rods. The figure contains 6 spectra above 830  $\text{cm}^{-1}$  and two spectra below 830  $\text{cm}^{-1}$ .

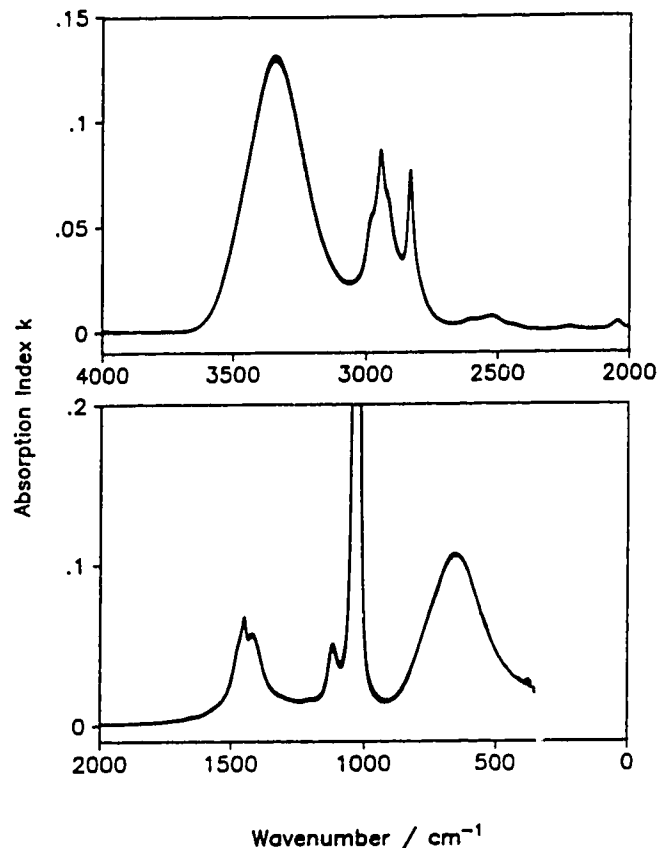


**Figure 5.3** Eight absorption index spectra,  $k(\tilde{\nu})$ , calculated from pATR spectra recorded by different workers in this laboratory between 1984 and 1991. Above 830  $\text{cm}^{-1}$ , the CIRCLE cell ATR rod was ZnSe and both long and short cells were used. Below 830  $\text{cm}^{-1}$ , the rod was KRS-5 and only the long cell was used.

Of the six spectra above 830  $\text{cm}^{-1}$ , one is the average of spectra obtained in 1984 (HHE) and 1987-8 (MKA), and two were obtained in 1989 (SB and MKA). The pATR spectra that gave these three spectra were obtained from a long CIRCLE cell, which gave about 6 reflections. They have been refined again recently with the current programs<sup>3,21</sup> so are free of the limitations of the earlier methods and programs. The detail has been given in Chapter 3. The 1033  $\text{cm}^{-1}$  C–O stretching bands in these three spectra have not been included in the final  $k$  spectrum, because they were too strong to be measured and are consequently inaccurate. The inaccuracy was shown to have negligible effect on the  $k(\tilde{\nu})$  values outside of the band.

A short CIRCLE cell which gave about 3 reflections was used for the remaining three spectra above 830  $\text{cm}^{-1}$  in Figure 5.3. One was obtained in 1990 (MKA) and has

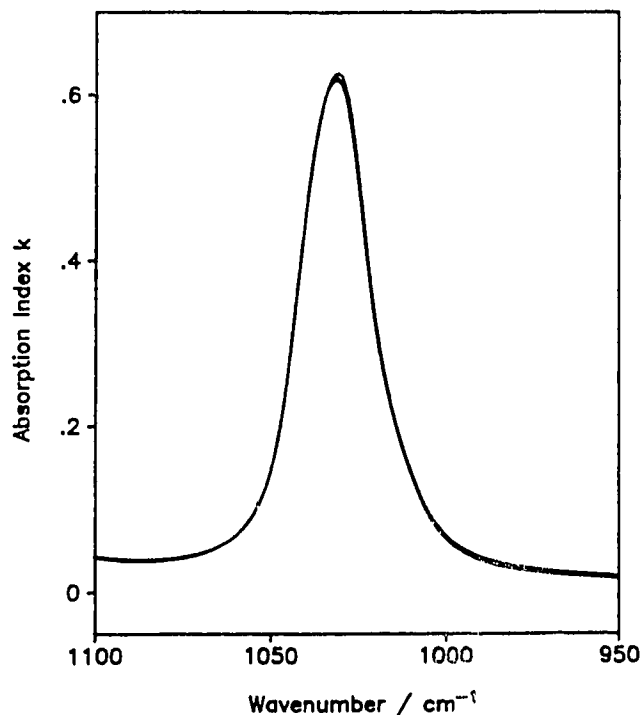


**Figure 5.4** Three absorption index spectra,  $k(\tilde{\nu})$ , of the C–O stretching band, obtained from pATR spectra recorded in the short CIRCLE cell with a ZnSe rod in 1990 and 1991.

been refined again with our current programs, and the other two were obtained in 1991 (SLZ).

The agreement between the six spectra above  $830\text{ cm}^{-1}$  is clearly excellent. Numerically it is  $\pm 1\%$  at the peak of the O–H stretching band and  $\pm 2.5\%$  elsewhere except in the baseline. The C–O stretching band at  $1033\text{ cm}^{-1}$  is off-scale in Figure 5.3. It is shown in Figure 5.4 for the three spectra recorded with the short cell. Again the agreement is excellent,  $\pm 0.75\%$  at the peak of the band.

The agreement between the imaginary refractive indices that were derived from ATR spectra measured with the full-length liquid holder around the ZnSe ATR rod and with the half length liquid holder around one end of the rod is particularly important. Any effect of the non-parallel beam we use may be expected to increase as the light proceeds down the rod. The absence of disagreement between the  $k(\tilde{\nu})$  values adds to the evidence<sup>2,3,10</sup> that the determination and use of the effective number of reflections, NRF, adequately corrects for the imperfections in the optical arrangement.



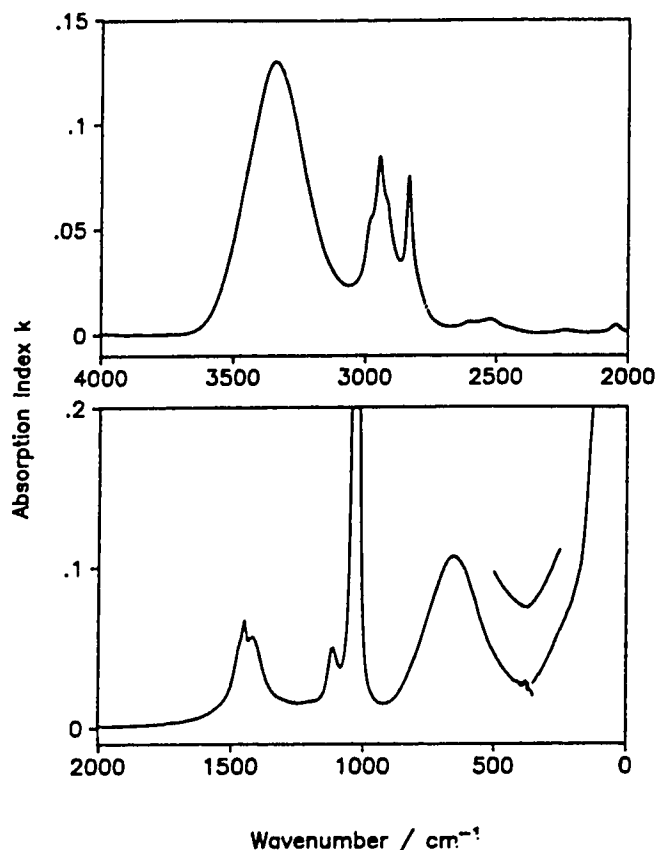


**Figure 5.5** The average absorption index spectrum from pATR measurements with a ZnSe rod above  $\sim 830 \text{ cm}^{-1}$  and a KRS-5 rod below  $830 \text{ cm}^{-1}$ , and the spectrum reported by Honijk et al<sup>15</sup> for the region below  $350 \text{ cm}^{-1}$ . The small spectrum between  $500$  and  $250 \text{ cm}^{-1}$ , offset by  $+0.05$ , shows how the two spectra were linked between  $400$  and  $300 \text{ cm}^{-1}$ .

The two spectra below  $830 \text{ cm}^{-1}$  in Figure 5.3 were obtained from long cells fitted with KRS-5 rods. One spectrum was obtained in 1987-8 (MKA) and one was obtained in 1991-2 (SLZ). Again the agreement is excellent,  $\pm 0.75\%$  at the top of the H-C-O-H torsion band.

The spectra above  $830 \text{ cm}^{-1}$  were averaged to yield a single  $k$  spectrum obtained from ZnSe rods, and this was merged with the 1991-2 spectrum from the KRS-5 rod. The 1987-8 spectrum from KRS-5 was in agreement, but it was noisier and was not used.

The final  $k$  spectrum from multiple attenuated total reflection studies is shown in Figure 5.5 from  $4000$  to  $350 \text{ cm}^{-1}$ , with the C-O stretching band off scale. Also in Figure 5.5 is the  $k$  spectrum calculated by us from readings taken from the graph of the linear absorption coefficient spectrum from  $350$  to  $2 \text{ cm}^{-1}$  reported by Honijk et al<sup>15</sup>. It

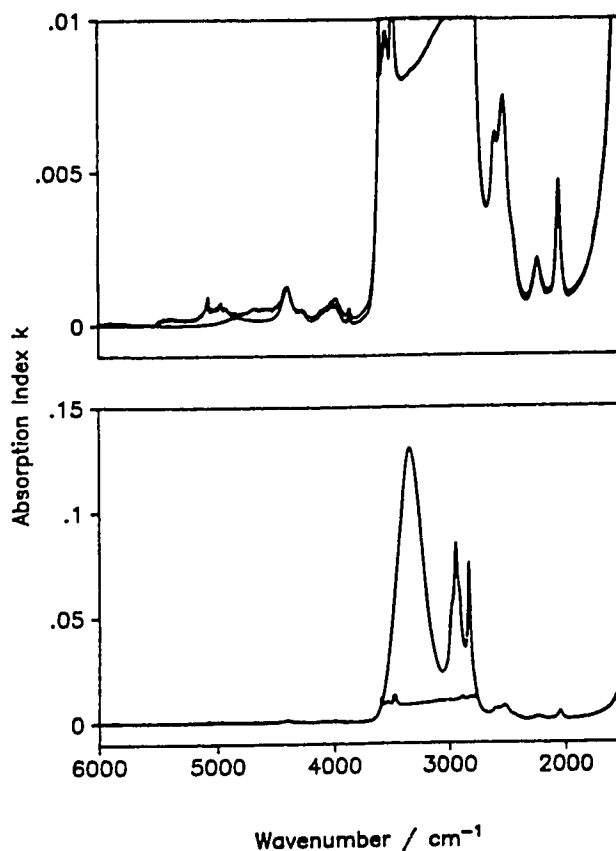


**Figure 5.6** The absorption index spectrum,  $k(\tilde{\nu})$ , deduced from the pATR measurements, and two (coincident)  $k$  spectra from transmission spectra between 6000 and 1500  $\text{cm}^{-1}$ . In the upper box the scale is greatly enlarged and the spectrum from pATR measurements is noisy above 4000  $\text{cm}^{-1}$  and higher below 2600  $\text{cm}^{-1}$ . In the lower box the line at  $k \sim 0.02$  between 3600 and 2800  $\text{cm}^{-1}$  is spurious due to complete absorption in the transmission cell.

clearly agrees very well with the spectrum from the ATR studies. Include in Figure 5.5, between 400 and 300  $\text{cm}^{-1}$  and offset by +0.05 ordinate units, is the bridge created to link the two spectra into a single spectrum from the near infrared to 2  $\text{cm}^{-1}$ . The offset in Figure 5.5 actually extends from 500 to 250  $\text{cm}^{-1}$ .

The above data gives the absorption index spectrum of methanol to good accuracy from 4000 to 2  $\text{cm}^{-1}$ . The spectrum in the weakly absorbing regions above 4000  $\text{cm}^{-1}$  is also known to some extent from the pATR spectra. To improve the accuracy above 4000  $\text{cm}^{-1}$ , and to check the absorption index values calculated from the pATR spectra in the weakly absorbing regions below 4000  $\text{cm}^{-1}$ , absorption index spectra were also determined from transmission spectra in cells with pathlengths up to 1.1 mm.

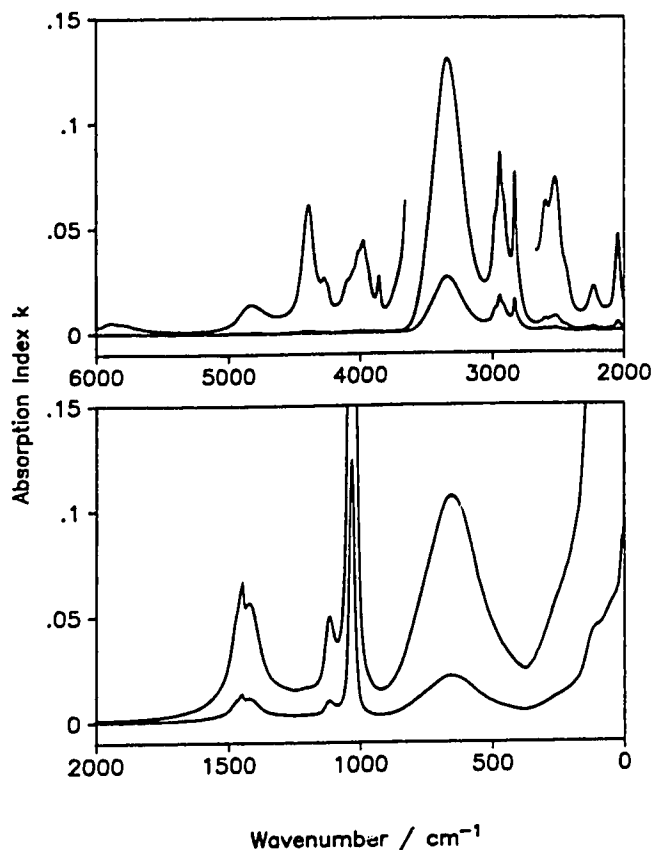


**Figure 5.7** The absorption index spectrum,  $k(\tilde{\nu})$ , of methanol at 25°C from this work. In each box the upper complete spectrum is on the  $k(\tilde{\nu})$  scale shown while the scale labels must be multiplied by 5 for the lower complete spectrum. The scale labels must be divided by 50 for the insert between 6000 and 3680  $\text{cm}^{-1}$  and by 10 for the insert between 2680 and 2000  $\text{cm}^{-1}$ . These inserts are not offset.

Twenty transmission spectra were recorded in two sets in cells with calcium fluoride windows and pathlengths from 140  $\mu\text{m}$  to 1.1 mm. Each set gave an absorption index spectrum. These are shown on a greatly expanded ordinate scale in Figure 5.6 upper, together with the final spectrum from the pATR measurements. The two  $k$  spectra from transmission measurements overlap completely in the figure, and the second curve, which is noisy above 4000  $\text{cm}^{-1}$  and higher below 2600  $\text{cm}^{-1}$ , is that from pATR measurements. The lower box of Figure 5.6 shows the same three spectra on a normal ordinate scale with the O–H stretching band from the pATR measurements near full scale. The O–H stretching band from transmission is near  $k(\tilde{\nu}) \sim 0.02$  in the lower box, hopelessly inaccurate because of total absorption in the transmission cells. The two  $k$

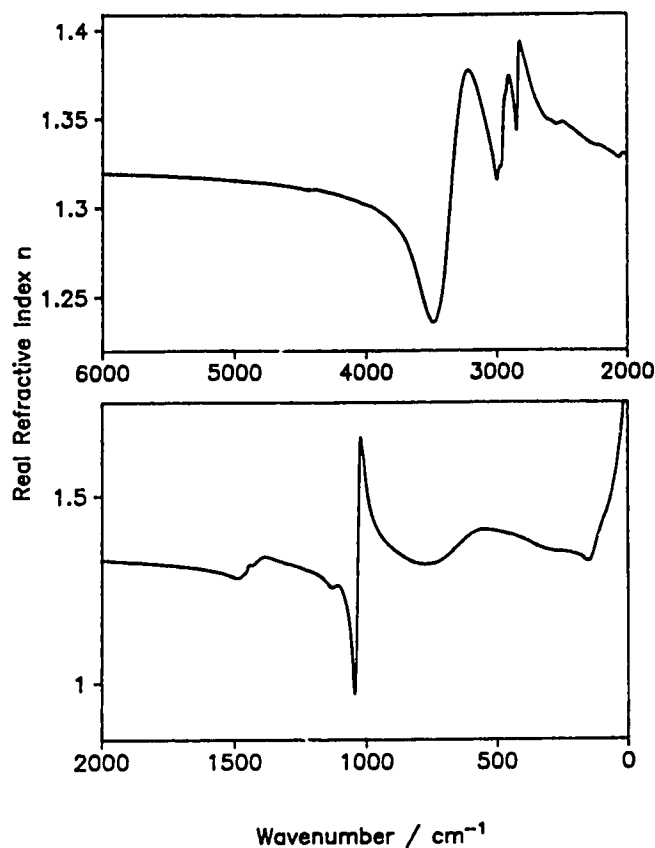


**Figure 5.8** The real refractive index spectrum of methanol at 25°C, calculated by KK transformation of the  $k$  spectrum of Figure 5.7 with  $n(8000\text{ cm}^{-1}) = 1.325$ .

spectra from transmission agree to better than 1% below  $5000\text{ cm}^{-1}$ , and agree with that from ATR to about 1% except where  $k(\nu)$  is less than 0.001 and was, consequently, not well defined by the ATR measurements.

A single absorption index spectrum from  $8000$  to  $2\text{ cm}^{-1}$  was created by merging different spectra. Specifically,  $k(\nu)$  was set to zero from  $8000\text{ cm}^{-1}$  to  $7500\text{ cm}^{-1}$ , the  $k$  spectrum from transmission measurements was used from  $7500$  to  $3750\text{ cm}^{-1}$ , the average  $k(\nu)$  from ATR measurements was used from  $3750$  to  $2400\text{ cm}^{-1}$ , the transmission result was used again from  $2400$  to  $1668\text{ cm}^{-1}$ , and the ATR average, merged with the  $k(\nu)$  obtained from Honijk *et al.*'s paper, was used below  $1668\text{ cm}^{-1}$ . This spectrum is shown in Figure 5.7. It is very well defined below  $5000\text{ cm}^{-1}$ . Above  $5000\text{ cm}^{-1}$  the spectrum is useful, but the absorption index is extremely small and is not known to better than 10%.

The  $k(\tilde{\nu})$  obtained in this way was KK transformed, using  $n(8000 \text{ cm}^{-1}) = 1.325$ , to yield the real refractive index spectrum,  $n(\tilde{\nu})$ . The final  $k$  and  $n$  spectra are in Figures 5.7 and 5.8, and their numerical values are in Tables 5.1 to 5.3.

Table 5.1 contains values of  $k(\tilde{\nu})$  and  $n(\tilde{\nu})$  at the wavenumbers of the peaks in the  $k$  spectrum and of the associated minima and maxima in the  $n$  spectrum, and in some regions of weak and flat absorption.

Tables 5.2 and 5.3 contain  $k(\tilde{\nu})$  and  $n(\tilde{\nu})$  values throughout the spectral range from 8000 to 2  $\text{cm}^{-1}$ . The separation between data points was 0.964233  $\text{cm}^{-1}$  in the original spectra. To economize on space in Tables 5.2 and 5.3, the number of points has been reduced where possible by increasing the wavenumber spacing by factors up to 16. The data presented in Tables 5.2 and 5.3 can be interpolated back to the 0.964233  $\text{cm}^{-1}$  spacing and yield the original  $k(\tilde{\nu})$  values to better than 1% below 5000  $\text{cm}^{-1}$  and generally to better than 5% above 5000  $\text{cm}^{-1}$ . The recovered  $n(\tilde{\nu})$  values agree with the original values to at least 0.1%. All other optical properties of methanol between 8000 and 2  $\text{cm}^{-1}$  can be calculated from the  $k(\tilde{\nu})$  and  $n(\tilde{\nu})$  values interpolated in this way.

Even with this reduction in data points, there are still nearly 700 values of both  $k$  and  $n$  to be reported over the spectral range of this work. To report them in a table of manageable size, the Compact Table format<sup>26</sup> has been adopted for Tables 5.2 and 5.3. The tables were prepared through program COMPTAB<sup>26</sup> and values can be recovered from them by TRECOVER<sup>26</sup>. The brief description of the format of the tables is given in the following.

In Table 5.2, the first column is labeled " $\text{cm}^{-1}$ " and in each row it contains the wavenumber,  $\tilde{\nu}(0)$ , of the first ordinate value in the row. This ordinate value is in the column labelled "0". The second column is labelled "XE" for X-exponent, and in each row contains the exponent that is used to calculate the wavenumber spacing between the ordinate values in that row. The third column is headed "YE" for Y-exponent, and in each row contains the exponent used to calculate the ordinate values in that row. The remaining column headings are 0, 1, 2, 3, ..... through 16, are the indices,  $J$ , of the ordinate values in that row. In any row, the first entry is  $\tilde{\nu}(0)$ , and the wavenumber corresponding to the ordinate value under the column heading " $J$ " is given by

$$\tilde{\nu}(J) = \tilde{\nu}(0) - \frac{15798.002}{16384} \cdot J \cdot 2^{XE}$$

and the ordinate value is that given in the table multiplied by  $10^{YE}$ . Thus, in the row which starts with 2847.38  $\text{cm}^{-1}$ , the wavenumber of the ordinate value under column

**Table 5.1\*** Wavenumbers and refractive indices at the peaks in the  $k$  spectrum, the associated maxima and minima in the  $n$  spectrum, and regions of flat weak absorption<sup>a</sup>.

Spectral feature	$\tilde{\nu}$ ( $\text{cm}^{-1}$ )	This work (25°C) $k(\tilde{\nu})$	$n(\tilde{\nu})$	Reference 17 (0°C) $k(\tilde{\nu})$	$n(\tilde{\nu})$
Peak	4823	0.000276	1.314		
Peak	4391	0.00122	1.310		
Peak	4273	0.000526	1.309		
Flat	4000	0.000790	1.302		1.306 (9)
Peak	3976	0.000873	1.301		
Peak	3859	0.000533	1.296		
$n$ minimum	3486	0.0534	1.235		1.253 (4)
$\nu\text{OH}$ peak	3345	0.130	1.306	0.125 (5)	
$n$ maximum	3213	0.0683	1.377		1.386 (7)
$n$ minimum	2995	0.0438	1.316		1.318 (6)
$\nu\text{CH}$ peak	2945	0.0849	1.343	0.070 (4)	
$n$ maximum	2903	0.0527	1.374		1.371 (6)
$n$ minimum	2843	0.0523	1.344		1.360 (6)
$\nu\text{CH}$ peak	2833	0.0757	1.365	0.053 (8)	
$n$ maximum	2817	0.0465	1.393		1.393 (4)
Peak	2595	0.00622	1.349		
$n$ minimum	2537	0.00698	1.3466		
Peak	2521	0.00732	1.3470		
$n$ maximum	2495	0.00603	1.3478		
Flat	2400	0.00173	1.343		1.348 (6)
Peak	2228	0.00213	1.335		
$n$ minimum	2060	0.00336	1.328		
Peak	2044	0.00462	1.329		
$n$ maximum	2030	0.00329	1.330		
Flat	2000	0.00144	1.329		1.336 (6)
Flat	1600	0.00766	1.302		1.310 (6)
$n$ minimum	1487	0.0377	1.279		1.285 (6)
$\delta(\text{CH}_3)$ peak	1449	0.0667	1.306	0.060 (4)	
$n$ maximum	1442	0.0584	1.316		
$n$ minimum	1435	0.0547	1.314		
$\delta(\text{OH})$ peak	1421	0.0566	1.319	unresolved	
$n$ maximum	1383	0.0380	1.337		1.344 (6)
Flat	1200	0.0164	1.295		1.286 (8)
$n$ minimum	1128	0.0406	1.254		
$\gamma(\text{CH}_3)$ peak	1115	0.0497	1.259	0.041 (6)	
$n$ maximum	1109	0.0481	1.261		
$n$ minimum	1044.2	0.295 <sup>b</sup>	0.971		1.080 (9)
$\nu\text{CO}$ peak	1031.7	0.620	1.326 <sup>c</sup>	0.570 (?)	
$n$ maximum	1020.1	0.321 <sup>d</sup>	1.6551		1.682 (9)
$n$ minimum	773	0.0596	1.315		1.312 (6)
$\tau\text{OH}$ peak	655	0.110	1.362	0.096 (3)	
$n$ maximum	550	0.0684	1.410		
Low wavenumber	400	0.0285	1.387		1.423 (6)

- a) The figures in parentheses under "Reference 17" are the estimated precisions in the last digit of the measurements taken from the graphs in Ref. 17.
- b) This value is very sensitive to wavenumber. It is 0.331 at  $1043.2 \text{ cm}^{-1}$ , where  $n = 0.973$ .
- c) This value is very sensitive to wavenumber. It is 1.370 at  $1030.7 \text{ cm}^{-1}$ , where  $k = 0.620$ .
- d) This value is very sensitive to wavenumber. It is 0.351 at  $1021.1 \text{ cm}^{-1}$ , where  $n = 1.6548$ .

**Table 5.2** Values of  $k(\tilde{\nu})$ , the absorption index or imaginary refractive index, between 8000 and 2  $\text{cm}^{-1}$  for methanol,  $\text{CH}_3\text{OH}$ , at 25°C. a,b

$\text{cm}^{-1}$	$XE$	$YE$	0	1	2	3	4	5	6	7	8	9	10	11	12	13	14	15	16
8000.24	6	-7	0	0	0	0	0	0	0	0	0	22	87	121	146	152	273	354	415
6951.15	6	-7	497	611	713	773	808	837	850	884	935	1002	1061	1003	865	696	569	551	706
5932.92	5	-7	921	1047	1088	1001	956	934	821	677	602	518	425	383	341	322	293	267	250
5408.38	5	-7	234	212	194	165	184	242	249	266	263	330	406	462	580	743	970	1315	1804
4883.84	5	-7	2289	2643	2763	2630	2355	2081	1865	1717									
4660.14	3	-7	1692	1671	1655	1641	1637	1635	1632	1645	1659	1677	1709	1741	1783	1839	1905	1979	2071
4529.00	3	-6	219	232	248	268	291	320	355	398	451	517	594	680	776	878	982	1079	1154
4397.86	3	-6	1202	1217	1187	1108	1002	891	787	697	624	568	527	499	485	486	500	517	527
4266.73	3	-7	5167	4918	4694	4460	3961	3406	3036	2825	2701	2642	2636	2644	2684	2764	2869	3007	3207
4135.59	3	-7	3462	3771	4157	4564	4869	5012	5079	5188	5363	5587	5798	5975	6201	6590	7116	7583	7762
4004.46	3	-7	7804	8014	8376	8663	8719	8292	7527	6910	6454	5926	5222	4520	3981	3607	3384	3331	3493
3873.32	3	-7	3981	4832	5316	4445	3402	2782	2477	2350	2328	2370	2468	2589	2763	2972	3227	3500	3803
3742.18	3	-6	411	445	481	520	561	604	656	719	817	945	1128	1375	1696	2102	2604	3221	3969
3611.05	3	-5	488	597	726	875	1047	1245	1466	1722	2007	2322	2665	3034	3425	3835	4267	4730	
3479.91	4	-4	572	675	777	878	979	1082	1177	1249	1292	1302	1283	1238	1176	1096	1007	910	811
3217.64	4	-5	7128	6214	5386	4669	4060	3553	3140	2810	2565	2414	2356	2397					
3044.08	2	-5	2424	2455	2495	2542	2601	2671	2760	2876	3021	3209	3447	3741	4091	4482	4871	5200	5434
2978.51	2	-5	5566	5660	5767	5961	6271	6705	7260	7873	8357	8480	8188	7685	7213	6873	6661	6533	6411
2912.94	2	-5	6213	5876	5470	5093	4768	4498	4263	4064	3903	3771	3664	3584	3537	3532	3573	3675	3875
2847.38	2	-5	4264	4986	6075	7188	7558	6991	6059	5192	4494	3955	3538	3210	2937	2698	2486	2293	2115
2777.95	3	-5	1787	1501	1258	1058	896	763	662	585	525	480	445	419	401	389	384	384	391
2646.82	3	-6	4035	4239	4537	4955	5467	5903	6154	6218	6106	5971	5949	6068	6288	6582	6905	7179	7318
2515.68	3	-6	7254	6949	6429	5772	5094	4492	4018	3688	3464	3288	3108	2878	2596	2290	1993	1733	1519
2384.54	3	-6	1353	1225	1130	1060	1006	969	950	927	921	931	960	1010	1079	1169	1283	1417	1572
2253.41	3	-6	1744	1916	2058	2129	2103	1984	1810	1632	1489	1383	1291	1202	1137	1104	1098	1106	1115
2122.27	3	-6	1120	1134	1176	1264	1425	1698	2105	2655	3360	4174	4624	4205	3286	2495	1994	1663	1414
1991.14	3	-6	1236	1125	1064	1035	1024	1026	1036	1051	1071	1094	1122	1152	1182	1217	1255	1294	1337
1860.00	3	-6	1385	1434	1486	1544	1604	1667	1738	1813	1888	1971	2060	2151	2251	2361	2479	2604	2733
1723.87	3	-6	2868	3012	3170	3344	3532	3748	3991	4242	4460	4734	5007	5280	5564	5895	6284	6695	7217
1597.73	3	-5	780	846	920	1000	1090	1189	1296	1407	1531	1692	1885	2129	2457				
1501.31	2	-5	2664	2910	3192	3509	3857	4229	4588	4900	5156	5395	5651	5947	6310	6631	6562	5988	5554
1435.74	2	-5	5464	5519	5596	5646	5658	5630	5556	5437	5271	5055	4804	4534	4261	3991	3733	3492	3274
1370.17	2	-5	3078	2903	2750	2617	2499	2396	2305	2225	2153	2091	2037	1986	1944	1906	1872	1841	1813
1304.60	2	-5	1784	1758	1730	1704	1680	1657	1636	1616	1598	1583	1565	1549	1537	1526	1528	1524	1525
1239.03	2	-5	1527	1534	1542	1552	1563	1579	1595	1608	1621	1633	1641	1642	1646	1650	1659	1674	1697
1173.47	2	-5	1727	1764	1811	1871	1943	2033	2154	2317	2536	2835	3226	3695	4182	4597	4871	4967	4915
1107.90	2	-4	476	451	425	402	386	379	379	387	403	430	473	536	631	778	1021	1463	2310
1042.33	2	-4	3688	5054	5947	6202	5578	4187	2944	2155	1601	1161	846	641	510	424	363	319	286
976.76	2	-5	2608	2407	2241	2105	1990	1893	1807	1734	1677	1630	1592	1563	1542	1532	1527	1530	1538
911.20	2	-5	1551	1565	1586	1617	1650	1689	1742	1793	1852	1925	2000	2081	2174	2266	2370	2479	
837.91	4	-4	298	358	425	500	580	661	741	825	905	981	1045	1084	1089	1077	1043	991	914
575.64	4	-5	8298	7423	6617	5901	5296	4822	4349	3931	3623	3332	3091	2891	2746	2607	2648	2872	3285
313.37	4	-4	372	423	478	545	601	654	720	784	875	991	1207	1594	1991	2188	2268	2366	2567
64.60	1	-4	2588	2626	2649	2684	2720	2728	2758	2783	2804	2831	2850	2870	2901	2933	2940	2952	2981
31.81	1	-4	3021	3043	3082	3136	3200	3278	3395	3548	3699	3862	4020	4253	4352	4359	4344	4560	7379

- a) The column headed  $\text{cm}^{-1}$  contains the wavenumber of the first  $k(\tilde{\nu})$  value in the row. The columns headed  $XE$  and  $YE$  contain the X-exponent and the Y-exponent, respectively, for the row. The columns headed 0,1,2,...16, contain the ordinate values, and the headings give the indices of the ordinate values in the row. In a row which starts with  $\tilde{\nu}(0)$ , the wavenumber corresponding to the ordinate indexed  $J$  is  $\tilde{\nu}(J) = \tilde{\nu}(0) - \frac{15798.002}{16384} \cdot J \cdot 2^{XE}$ . The  $k(\tilde{\nu})$  values in that row are the ordinate value shown times  $10^{YE}$ . Thus, the entry indexed 16 in the first row of the table shows that  $k = 415 \times 10^{-7} = 4.15 \times 10^{-5}$  at  $\tilde{\nu} = 8000.24 - \frac{15798.002}{16384} \cdot 16 \cdot 2^6 = 7012.86 \text{ cm}^{-1}$ .
- b) The  $k(\tilde{\nu})$  values in the table can be interpolated to the original wavenumber spacing,  $0.96423 \text{ cm}^{-1}$ , and yield the original  $k(\tilde{\nu})$  values accurate to 1% below  $5000 \text{ cm}^{-1}$  and 5% above  $5000 \text{ cm}^{-1}$ , by program TRECOVER<sup>20</sup>.

**Table 5.3** Values of  $n(\tilde{\nu})$ , the real refractive index, between 8000 and 2  $\text{cm}^{-1}$  for methanol,  $\text{CH}_3\text{OH}$ , at 25  $^\circ\text{C}$ .<sup>a,b</sup>

$\text{cm}^{-1}$	$XE$	0	1	2	3	4	5	6	7	8	9	10	11	12	13	14	15	16
8000.24	6	13222	13222	13221	13221	13220	13219	13219	13218	13218	13217	13216	13216	13215	13214	13213	13213	13212
6951.15	6	13211	13210	13209	13209	13208	13207	13206	13205	13204	13203	13202	13201	13200	13198	13197	13195	13194
5932.92	5	13193	13192	13192	13191	13190	13189	13188	13188	13187	13186	13185	13183	13182	13181	13180	13179	13178
5408.38	5	13176	13175	13174	13172	13171	13170	13168	13166	13165	13163	13161	13160	13158	13156	13154	13152	13150
4883.84	5	13148	13146	13144	13142	13140	13138	13135	13132									
4660.14	3	13131	13130	13130	13129	13128	13127	13126	13125	13125	13124	13123	13122	13121	13120	13119	13118	13117
4529.00	3	13116	13115	13114	13113	13111	13110	13109	13108	13107	13106	13104	13103	13103	13102	13102	13101	13102
4397.86	3	13102	13102	13103	13103	13103	13102	13101	13100	13099	13097	13096	13094	13093	13091	13090	13088	13087
4266.73	3	13086	13085	13084	13082	13081	13080	13078	13076	13074	13072	13070	13068	13066	13065	13063	13061	13059
4135.59	3	13057	13055	13053	13051	13049	13047	13045	13043	13041	13039	13037	13035	13033	13030	13028	13026	13024
4004.46	3	13022	13020	13017	13015	13013	13012	13009	13006	13004	13001	12998	12994	12990	12986	12982	12978	12974
3873.32	3	12969	12965	12962	12959	12954	12949	12944	12938	12933	12927	12921	12915	12909	12902	12896	12889	12881
3742.18	3	12874	12866	12857	12848	12839	12829	12819	12807	12795	12782	12768	12753	12737	12720	12702	12684	12664
3611.05	3	12643	12621	12599	12576	12553	12530	12506	12483	12461	12440	12421	12404	12389	12377	12367	12359	
3479.91	4	12354	12367	12397	12439	12493	12569	12674	12803	12947	13094	13237	13367	13483	13578	13657	13714	13753
3217.64	4	13770	13771	13756	13731	13699	13661	13620	13575	13528	13478	13426	13372					
3044.08	2	13358	13344	13330	13314	13298	13282	13264	13245	13225	13205	13186	13170	13158	13155	13163	13180	13201
2978.51	2	13219	13230	13232	13228	13225	13227	13244	13286	13360	13455	13540	13593	13619	13630	13638	13651	13672
2912.94	2	13701	13726	13738	13739	13733	13723	13711	13698	13682	13666	13649	13631	13610	13588	13563	13535	13503
2847.38	2	13466	13437	13448	13537	13693	13829	13902	13928	13931	13922	13909	13896	13884	13873	13862	13851	13841
2777.95	3	13820	13799	13776	13753	13731	13708	13687	13668	13650	13633	13617	13602	13588	13575	13563	13551	13540
2646.82	3	13529	13520	13510	13502	13496	13493	13492	13490	13488	13484	13479	13474	13470	13467	13466	13466	13469
2515.68	3	13472	13475	13477	13477	13475	13471	13467	13461	13457	13453	13449	13446	13443	13439	13435	13430	13425
2384.54	3	13420	13415	13410	13406	13401	13396	13392	13388	13384	13380	13375	13371	13367	13364	13360	13357	13354
2253.41	3	13351	13349	13348	13348	13347	13347	13347	13345	13343	13340	13337	13334	13330	13327	13323	13319	13312
2122.27	3	13309	13305	13301	13296	13291	13287	13282	13279	13278	13281	13290	13299	13303	13300	13296	13291	13287
1991.14	3	13282	13277	13273	13269	13264	13260	13257	13253	13249	13245	13242	13238	13234	13231	13227	13223	13219
1860.00	3	13215	13211	13207	13203	13199	13195	13191	13186	13182	13178	13173	13168	13163	13159	13154	13148	13143
1728.87	3	13138	13132	13126	13120	13114	13108	13102	13095	13089	13082	13075	13067	13059	13050	13041	13032	13021
1597.73	3	13011	13000	12989	12978	12966	12954	12942	12928	12912	12894	12875	12853	12830				
1501.31	2	12818	12808	12800	12795	12795	12801	12816	12836	12858	12878	12899	12923	12957	13018	13102	13153	13150
1435.74	2	13140	13143	13156	13176	13199	13225	13252	13279	13304	13327	13345	13359	13367	13372	13372	13369	13364
1370.17	2	13357	13348	13339	13329	13319	13309	13299	13289	13280	13270	13261	13252	13243	13234	13226	13217	13210
1304.60	2	13202	13194	13186	13179	13171	13163	13154	13146	13138	13129	13120	13111	13102	13092	13082	13073	13063
1239.03	2	13052	13042	13032	13022	13011	13000	12990	12979	12968	12957	12946	12933	12920	12905	12889	12872	12854
1173.47	2	12835	12814	12792	12769	12744	12716	12687	12655	12622	12589	12560	12542	12538	12549	12570	12591	12605
1107.90	2	12608	12598	12568	12523	12463	12391	12309	12214	12104	11974	11821	11637	11411	11126	10759	10296	09825
1042.33	2	09797	10617	11991	13703	15454	16428	16518	16323	16109	15864	15589	15329	15106	14921	14767	14637	14526
976.76	2	14431	14347	14274	14208	14149	14095	14045	13999	13956	13916	13879	13843	13809	13777	13747	13718	13690
911.20	2	13664	13638	13613	13588	13565	13542	13519	13497	13476	13455	13435	13415	13397	13378	13360	13343	
837.91	4	13281	13228	13190	13165	13152	13157	13174	13204	13252	13321	13413	13521	13637	13744	13845	13941	14015
575.64	4	14066	14100	14101	14100	14082	14063	14043	14016	13987	13956	13923	13885	13845	13796	13736	13677	13633
313.37	4	13591	13560	13536	13521	13520	13510	13494	13467	13432	13382	13329	13285	13257	13245	13241	13241	13241
64.60	1	14992	15047	15110	15170	15256	15323	15387	15470	15546	15627	15716	15794	15881	15983	16093	16180	16265
31.81	1	16370	16491	16598	16707	16860	16942	17130	17324	17584	17883	18323	18872	19558	20386	21224	22594	27103

- a) The column headed  $\text{cm}^{-1}$  contains the wavenumber of the first  $n(\tilde{\nu})$  value in the row. The column headed  $XE$  contains the X-exponent for the row. The columns headed 0, 1, 2, ..., 16, contain the  $n(\tilde{\nu})$  values with the decimal point implicitly after the first digit in each value, and the headings give the indices of the  $n(\tilde{\nu})$  values in the row. In a row which starts with  $\tilde{\nu}(0)$ , the wavenumber corresponding to the ordinate indexed  $J$  is  $\tilde{\nu}(J) = \tilde{\nu}(0) - \frac{15798.002}{16384} \cdot J \cdot 2^{XE}$ . Thus the entry indexed 16 in the first row of the table shows that  $n = 1.3212$  at  $\tilde{\nu} = 8000.24 - \frac{15798.002}{16384} \cdot 16 \cdot 2^6 = 7012.86 \text{ cm}^{-1}$ , and the entry indexed 16 in the row which starts with  $1107.90 \text{ cm}^{-1}$  shows that  $n = 0.9825$  at  $\tilde{\nu} = 1046.19 \text{ cm}^{-1}$ .
- b) The  $n(\tilde{\nu})$  values in the table can be interpolated to the original wavenumber spacing,  $0.96423 \text{ cm}^{-1}$ , and yield the original  $n(\tilde{\nu})$  values accurate to 0.1%, by program TRECOVER<sup>25</sup>.



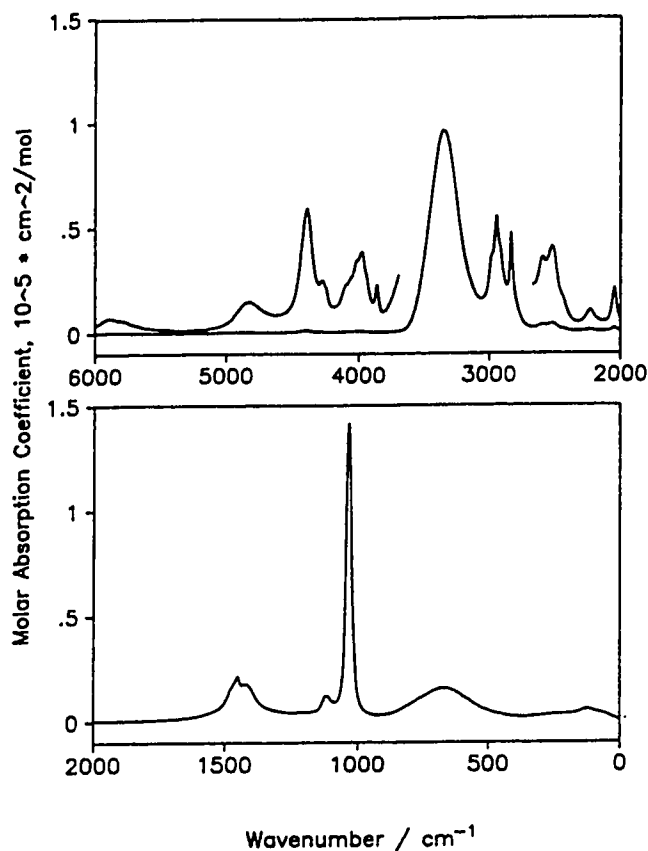


**Figure 5.9** The molar absorption coefficient spectrum,  $E_m(\tilde{\nu})$ , of methanol at 25°C, calculated from the absorption index spectrum in Figure 5.7. The scale shown applies to the complete spectrum. The scale labels must be divided by 50 for the insert between 6000 and 3680  $\text{cm}^{-1}$  and by 10 for the insert between 2680 and 2000  $\text{cm}^{-1}$ . These inserts are not offset.

heading "12" is  $(2847.38 - 0.964233 \times 12 \times 2^2) = 2801.10 \text{ cm}^{-1}$  and the  $k$  value at this wavenumber is  $2937 \times 10^{-5} = 0.0294$ , believed accurate to about 2%. The first wavenumber on the next row is  $2777.95 \text{ cm}^{-1}$  at which  $k(\tilde{\nu})$  is  $1787 \times 10^{-5} = 0.0179$ , from the columns headed "0" and "YE". Note that the spacing on this next row is  $0.964233 \times 2^3$ , not the  $0.964233 \times 2^2$  of the previous row, and that this is also the spacing between the first point on this row and the last point on the previous row.

The format of Table 5.3 is the same as that of Table 5.2 with two exceptions. The wavenumbers in the  $n(\tilde{\nu})$  table are the same as in the  $k(\tilde{\nu})$  table. The values of  $n(\tilde{\nu})$  are consistent in size so, first, no Y-exponent is needed and, second, the decimal point is omitted to save space because it always lies after the first digit in the ordinate values. Thus the entry under heading "12" in the row which starts at  $2847.38 \text{ cm}^{-1}$  is 13884,

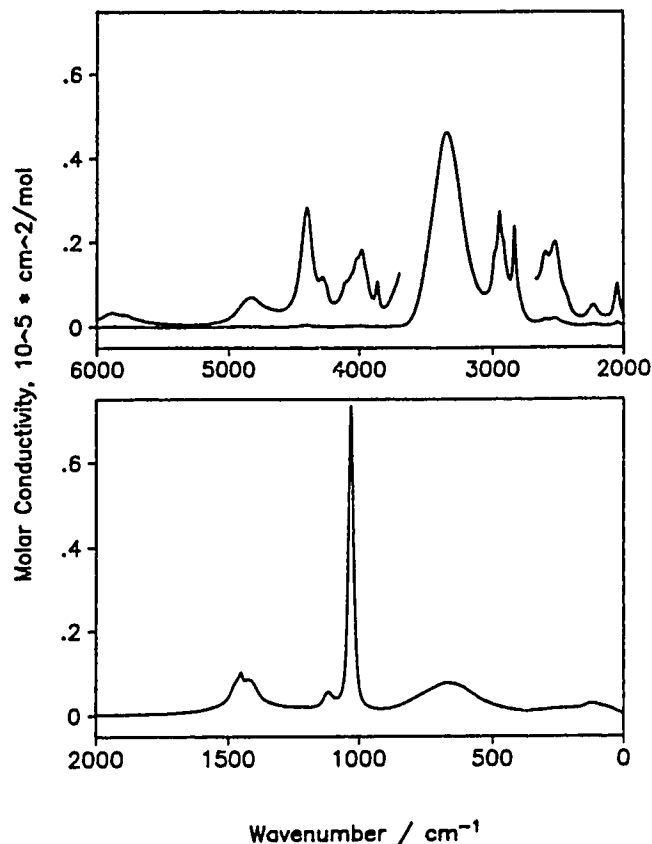


**Figure 5.10** The molar conductivity spectrum,  $V_m \tilde{\nu} \epsilon''(\tilde{\nu})$ , of methanol at 25°C calculated from the refractive index spectra in Figures 5.7 and 5.8. The scale shown applies to the complete spectrum in each box. The scale labels must be divided by 50 for the insert between 6000 and 3680  $\text{cm}^{-1}$  and by 10 for the insert between 2680 and 2000  $\text{cm}^{-1}$ . These inserts are not offset.

meaning that  $n = 1.3884$  at 2801.10  $\text{cm}^{-1}$ . The first ordinate entry in the row starting at 1042.33  $\text{cm}^{-1}$  is 09797 (under heading "0"), indicating that  $n = 0.9797$  at 1042.33  $\text{cm}^{-1}$ .

Figures 5.9 to 5.11 show the molar absorption coefficient spectrum,  $E_m(\tilde{\nu})$ , the molar conductivity spectrum,  $V_m \tilde{\nu} \epsilon''(\tilde{\nu})$ , and the imaginary molar polarizability spectrum under the Lorentz local field assumption,  $\alpha_m''(\tilde{\nu})$ , respectively. The molar concentration  $C = 24.69 \text{ mol L}^{-1}$  or molar volume  $V_m = 40.50 \text{ ml mol}^{-1}$  for methanol was used.

It should be noted that the peak position of the same band is different in different spectra. The peak positions of the major bands in the methanol spectra are summarized in Table 5.4. The difference increases with the intensity of the band.

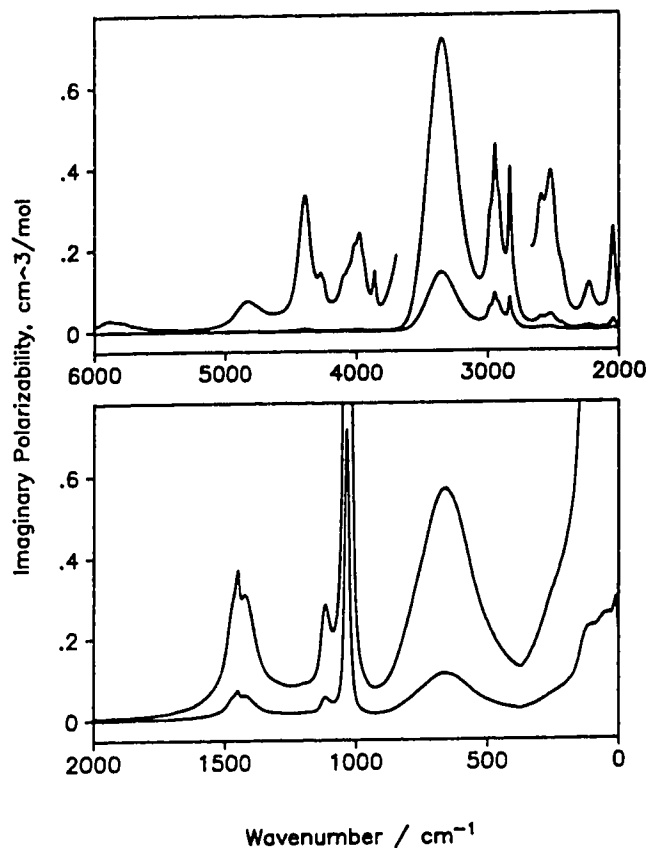


**Figure 5.11** The imaginary molar polarizability spectrum,  $\alpha_m''(\tilde{\nu})$ , of methanol at 25°C, calculated from the refractive index spectra in Figures 5.7 and 5.8 under the assumption of the Lorentz local field. The scale shown applies to the upper complete spectrum in each box and the scale labels must be multiplied by 5 for the lower complete spectrum. The scale labels must be divided by 50 for the insert between 6000 and 3680  $\text{cm}^{-1}$  and by 10 for the insert between 2680 and 2000  $\text{cm}^{-1}$ . These inserts are not offset.

**Table 5.4** The peak positions of major bands in various spectra of methanol,  $\text{CH}_3\text{OH}$ .

Vibration	Type of spectrum						
	pATR	$k$	$E_m$	$\epsilon''$	$V_m \tilde{\nu} \epsilon''$	$\alpha_m''$	$\tilde{\nu} \alpha_m''$
$\nu(\text{O-H})$	3322.4	3342.3	3347.5	3337.3	3337.6	3350.9	3354.0
$\nu(\text{C-H})$	2942.9	2944.7	2944.8	2944.2	2944.3	2945.2	2945.3
$\nu(\text{C-H})$	2831.4	2832.6	2832.6	2832.2	2832.3	2832.8	2832.9
$\delta(\text{CH}_3)$	1448.7	1449.6	1449.7	1449.3	1449.4	1449.8	1450.0
$\delta(\text{O-H})$	1416.8	1421.1	1422.3	1420.0	1421.5	1421.9	1423.2
$\gamma(\text{CH}_3)$	1114.6	1115.2	1115.8	1115.0	1115.5	1115.4	1116.0
$\nu(\text{C-O})$	1022.8	1031.3	1031.4	1028.5	1028.6	1034.8	1034.9
$\tau(\text{O-H})$	627.9	656.3	668.5	651.1	665.2	660.6	672.7

## 5.5 Discussion

### 5.5.1 *Refractive indices*

The refractive index values can be compared with the only literature values, those of Sethna and Williams<sup>17</sup> which were obtained by specular reflection from an air-methanol surface for a sample at 0°C, rather than by ATR and transmission spectroscopy of a sample at 25°C. Table 5.1 includes the  $k$  and  $n$  values obtained by Sethna and Williams. These values had to be measured by a ruler from enlarged versions of the figures in Ref. 17, because the  $k(\nu)$  and  $n(\nu)$  values were not tabulated. The numbers in parentheses in Table 5.1 give the precision in the last digit of the measurements taken from the figures in Ref. 17.

Based on the accuracy found for water<sup>10</sup>, and the excellent agreement reported above between absorption index values,  $k(\nu)$ , from pATR spectra and from transmission spectra, our  $k$  values are estimated to be accurate to about  $\pm 3\%$  below 5000  $\text{cm}^{-1}$  and  $\pm 10\%$  above 5000  $\text{cm}^{-1}$  where the absorption is very weak. Sethna and Williams did not estimate the error in their  $k$  values. They did estimate the uncertainty in the areas under bands in the  $k$  spectrum to be about 10 to 15%, but it is unclear what uncertainty in  $k(\nu)$  this implies.

The two absorption index values (Table 5.1) at the peak of the O–H stretching band agree to 4%. The agreement is about 10% for the C–O stretching band at 1032  $\text{cm}^{-1}$  and the CH<sub>3</sub> deformation band at 1449  $\text{cm}^{-1}$ , 18% for the C–H stretching band at 2945  $\text{cm}^{-1}$  and the CH<sub>3</sub> rock band at 1115  $\text{cm}^{-1}$ , and 30% for the lower-wavenumber C–H stretching band at 2833  $\text{cm}^{-1}$ . In all cases our  $k$  values are greater and our spectra show better resolution than those in Ref. 17, as is to be expected from the better instrumentation available today. Our values are believed to be the more reliable, partly because of superior instrumentation, and partly because the pATR and transmission measurements depend on  $k(\nu)$  more than on  $n(\nu)$  while Sethna and Williams' specular reflection measurements<sup>17</sup> from air at near normal incidence depend on  $n(\nu)$  more than on  $k(\nu)$ .

Given equal instrumentation, Sethna and Williams' measurements should be better than ours for the  $n$  spectrum which describes the refraction, while ours should be more reliable for the  $k$  spectrum which describes the absorption. In fact, the two sets of real refractive index values agree to 0.3% at 4000  $\text{cm}^{-1}$ , and agree to better than 0.7% at most other wavenumbers. The few agreements worse than 0.7% are mostly associated with the minima in  $n(\nu)$  to high-wavenumber of the absorption bands. Thus, at 3486, 2843

and  $1044\text{ cm}^{-1}$  the agreement is 1.4%, 1.2% and, the only major disagreement, 10%. The only other agreement worse than 0.7% is 1.6% at  $1020\text{ cm}^{-1}$ , the maximum in  $n(\bar{\nu})$  to low wavenumber of the C–O stretching band. Sethna and Williams did not trust their data below  $600\text{ cm}^{-1}$ , so the 2.5% agreement at  $400\text{ cm}^{-1}$  is not significant.

A qualitative disagreement exists in that Sethna and Williams reported anomalous dispersion in  $n(\bar{\nu})$  between  $1660$  and  $1600\text{ cm}^{-1}$ , even though they saw no absorption peak in the  $k$  spectrum in that region. No absorption and no anomalous dispersion was found in this work at these wavenumbers.

Sethna and Williams reported the areas under the O–H, C–H and C–O stretching bands in their  $k$  spectrum to be  $29.92$ ,  $11.38$  and  $20.01\text{ cm}^{-1}$ , respectively, with an estimated error of 10 to 15%. Unfortunately, they did not cite their integration ranges, but their description suggests  $3800$  to  $3060\text{ cm}^{-1}$ ,  $3060$  to  $2670\text{ cm}^{-1}$ , and  $1240$  to  $920\text{ cm}^{-1}$  as probable ranges. Over these ranges, the areas under our  $k$  spectrum are  $36.8$ ,  $13.8$ , and  $24.6\text{ cm}^{-1}$ , respectively, about 21 to 23% greater than those of Sethna and Williams.

### 5.5.2 Dipole Moment Derivatives

The optical constant spectra can be used to calculate the changes in molecular dipole moment during normal vibrations, using the equations discussed in the appendix. In this section, the information given by the present results is discussed. It is concluded that the treatment presented here is at least the equal of any in the literature on liquids, but considerably more work is needed before the accuracy in the optical constant spectra can be carried over into the molecular properties. There is considerable uncertainty associated with resolving the observed spectrum into contributions from the different vibrations, and this reduces the accuracy of the derived molecular properties.

The areas under the  $k$  spectrum were compared above with those found by Sethna and Williams. These areas are related to the integrated intensity  $A_j$  by appendix (Section 5.6) eqs. (A5.8) and (A5.9) with  $\bar{\nu}$  set equal to the peak wavenumber in eq. (A5.8).  $A_j$  is approximately related to the dipole moment derivative by eq. (A5.11).

In preliminary reports of this work<sup>2,12,13</sup>, values of  $B_j$  in eq. (4.7) or eq. (A5.13) were reported for the O–H, C–H and C–O stretching modes, and the dipole moment derivatives of the O–H stretching modes of hydrogen-bonded and non-hydrogen bonded methanol, were calculated from  $B_j$  via eq. (A5.14).

**Table 5.5** Several measures of the integrated intensities of liquid methanol at 25°C and the dipole moment derivatives with respect to the normal coordinates calculated from them.

Vibration	cm <sup>-1</sup> range	$A_j$ <sup>a</sup>	$ \partial\bar{\mu}/\partial Q_j ^2$ <sup>b</sup>	$B_j$ <sup>a</sup>	$ \partial\bar{\mu}/\partial Q_j ^2$ <sup>b</sup>	$C_j$ <sup>a</sup>	$ \partial\bar{\mu}/\partial Q_j ^2$ <sup>b</sup>
$\nu(\text{OH})$	3813 – 3059	624	12.6	85.2	12.7	6.75	12.6
$\nu(\text{CH})$	3059 – 2660	204	3.99	26.8	3.98	2.14	4.00
$\nu(\text{CO})$	1191 – 915	127	2.56	17.3	2.58	1.36	2.54
$\tau(\text{OH})$	915 – 365	105	2.05	13.7	2.04	1.10	2.05

- a) The integrated areas  $A_j$ ,  $B_j$ , and  $C_j$  are in the units km mole<sup>-1</sup>.
- b)  $|\partial\bar{\mu}/\partial Q_j|^2$  is the square of dipole moment derivative with respect to the normal coordinate in the units (Debye Å<sup>-1</sup> amu<sup>-1/2</sup>)<sup>2</sup>. The values in this column were calculated from the integrated areas in the neighboring column to the left. The values of  $\bar{n}$  are 1.306, 1.357, 1.313 and 1.363 for the O–H, C–H, C–O and H–C–O–H torsion, respectively. For the C–H stretching mode, the quantity tabulated is the sum of  $|\partial\bar{\mu}/\partial Q_j|^2$  over all three C–H stretching modes of methanol.

In Table 5.5 are presented the current values of the integrated intensity  $A_j$  in eq. (A5.9), the integrated intensity  $B_j$  in eq. (A5.13), and the integrated intensity  $C_j$  in eqs. (A5.16) and (A5.18). Table 5.5 includes  $g_j|\partial\bar{\mu}/\partial Q_j|^2$ , the degeneracy of the vibration,  $g_j$ , times the square of the dipole moment derivative with respect to the normal coordinate. Each of the three columns of this quantity was calculated from the integrated intensity immediately to its left, via the relevant equation in Section 5.6 with the appropriate numerical factor. The calculations involving  $A_j$  and  $B_j$  need values of  $\bar{n}$  (Chapter 4 and Section 5.6). These were calculated from the maximum and minimum values of  $n$  in Table 5.1, and are shown in footnote "b" of Table 5.5.

It is noted in the introduction and the appendix that the equations for  $A_j$  and  $B_j$  contain approximations (Chapter 4). The agreement in Table 5.5 between the  $g_j|\partial\bar{\mu}/\partial Q_j|^2$  values calculated from  $A_j$ ,  $B_j$ , and  $C_j$  makes it clear that the approximations are good approximations for liquid methanol. Only for the C–O stretching band do the  $g_j|\partial\bar{\mu}/\partial Q_j|^2$  values differ by more than 1%. In the following discussion only the integrated intensity  $C_j$  is considered.

In order to obtain the results in Table 5.5, assumptions were made about how to separate the overlapping bands into contributions from the different vibrations. In fact the most simple possible assumptions were made, namely that the O–H stretching vibration causes all of the intensity between 3813 and 3059 cm<sup>-1</sup>, the C–H stretching

**Table 5.6** The integrated area  $C_j$  and the dipole moment derivatives calculated from it for different approximate separations of the contributions by different vibrations to the intensity.

Vibration	cm <sup>-1</sup> range	Case 1	Case 2	Case 3	Average		
		$C_j$	$C_j$	$C_j$	$C_j$	$ \partial\bar{\mu}/\partial Q_j ^2$ <sup>a</sup>	$ \partial\bar{\mu}/\partial R ^2$ <sup>b</sup>
$\nu(\text{OH})$	3813 – 3059	6.75	6.89	7.58	7.1	13.3	3.5
$\nu(\text{CH})$	3059 – 2660	2.14	2.01	1.31	1.8	3.4	1.0
$\nu(\text{CO})$	1191 – 915	1.36	1.23	1.32	1.3	2.4	4.1
$\tau(\text{OH})$	915 – 365	1.10	0.755	0.959	0.94	1.8	0.88

- a) The integrated area  $C_j$  is in the units km mole<sup>-1</sup>.
- b)  $|\partial\bar{\mu}/\partial Q_j|^2$  is the dipole moment derivative with respect to the normal coordinate, in the units (Debye Å<sup>-1</sup> amu<sup>-1/2</sup>)<sup>2</sup>. For the C–H stretching modes, the quantity tabulated is the sum of  $|\partial\bar{\mu}/\partial Q_j|^2$  over the three C–H stretching modes of methanol.
- c)  $|\partial\bar{\mu}/\partial R|^2$  is the magnitude of the change in dipole moment with unit change in internal coordinate. For O–H, C–H and C–O bond stretching coordinates the dipole moment was assumed to be along the bond; for H–C–O–H torsion it was assumed to be perpendicular to the COH plane.

vibrations cause the intensity between 3059 and 2660 cm<sup>-1</sup>, the C–O stretching band causes all of the intensity between 1191 and 915 cm<sup>-1</sup>, and the H–C–O–H torsion, which can be called the O–H···O out-of-plane bending vibration in this hydrogen bonded phase of methanol, causes all of the intensity between 915.1 and 365.4 cm<sup>-1</sup>.

These assumptions are clearly questionable but the physical origins of the observed absorption spectrum are not sufficiently understood to know how to separate it correctly into the contributions from the different vibrations. Accordingly the effects of other approximations that can reasonably be made to achieve this separation are examined, and directions for future work to resolve this limitation on the use of accurate absorption spectra are indicated. The results from the other approximations are summarized in Table 5.6.

As noted above, the first separation method used was to assume that all absorption between particular wavenumbers is due to one vibration. This is trivial to compute, and convenient for comparing spectra of mixtures, but is theoretically unsound because spectral band shapes are approximately Lorentzian or Gaussian or some mixture of the two, and the envelopes of different bands undoubtedly overlap. The results of this method are repeated in Table 5.6 as Case 1.

For the O–H and C–H stretching bands two other approximate separation methods were tried. First, a straight line was drawn from the curve at  $3117.0\text{ cm}^{-1}$  to  $\tilde{\nu}\alpha''_m = 0.0$  at  $2962.1\text{ cm}^{-1}$ , as is shown in Figure 5.12 (top), to approximately extrapolate the O–H stretching band under the CH absorption. The exact positioning of this line is clearly somewhat arbitrary. The area between  $3812.6\text{ cm}^{-1}$  and this line was assigned to O–H stretch and that from the line to  $2660.3\text{ cm}^{-1}$  was assigned to the C–H stretching modes. The areas,  $C_j$ , from this method are in Table 5.6 as Case 2. Second, a straight line was drawn under the C–H stretching peaks, between the points on the spectrum at  $3058.6$  and  $2700.8\text{ cm}^{-1}$ , as is shown in Figure 5.12 (top). The area above this line was attributed to the C–H stretching modes, and all of the remaining area above the wavenumber axis between  $3812.6$  and  $2660.3\text{ cm}^{-1}$  was assigned to the O–H stretch. The areas,  $C_j$ , from this method are in Table 5.6 as Case 3.

For the C–O stretching mode, the first method, repeated as Case 1 in Table 5.6, clearly assigns the area of the weak peak at  $1115\text{ cm}^{-1}$  to the C–O stretch as well as the area of the strong peak at  $1035\text{ cm}^{-1}$ . Two approximate separation methods were applied to remedy this. First, Case 2 in Table 5.6, an attempt was made to extrapolate the strong band under the weak one by drawing a straight line from the curve at  $1082.8\text{ cm}^{-1}$  to  $\tilde{\nu}\alpha''_m = 0.0007$  at  $1133.9\text{ cm}^{-1}$ , where  $0.0007$  is the  $\tilde{\nu}\alpha''_m$  value at the lower integration limit,  $915.1\text{ cm}^{-1}$ . The area between this line and  $915.1\text{ cm}^{-1}$  was assigned to the C–O stretch. Second, Case 3 in Table 5.6, a straight line was drawn between the points on the curve at  $1162.8$  and  $1082.8\text{ cm}^{-1}$ , as shown in Figure 5.12 (middle). The area above this line was assigned to the  $1115\text{ cm}^{-1}$  peak and the remaining area between  $1190.8$  and  $915.1\text{ cm}^{-1}$  was assigned to the C–O stretch.

For the H–C–O–H torsion band, two separation methods were again tried, to consider the possibility that much of the underlying absorption in this region is due to the tail of the low-wavenumber absorption by intermolecular vibrations of the liquid lattice. The first, Case 2 in Table 5.6, consisted of assigning to the vibration the area above a straight line drawn between the curve points at  $915.1$  and  $365.4\text{ cm}^{-1}$ . In the second, Case 3 in Table 5.6, the area above a straight line drawn between  $\tilde{\nu}\alpha''_m = 0.0$  at  $915.1\text{ cm}^{-1}$  and the curve at  $365.4\text{ cm}^{-1}$  was assigned to the vibration, as shown in Fig. 5.12 (bottom).

From Table 5.6, the  $C_j$  areas, and hence the squares of the dipole moment derivatives,  $|\partial\bar{\mu}/\partial Q_j|^2$ , vary with the separation method by about  $\pm 6\%$  for the O–H and



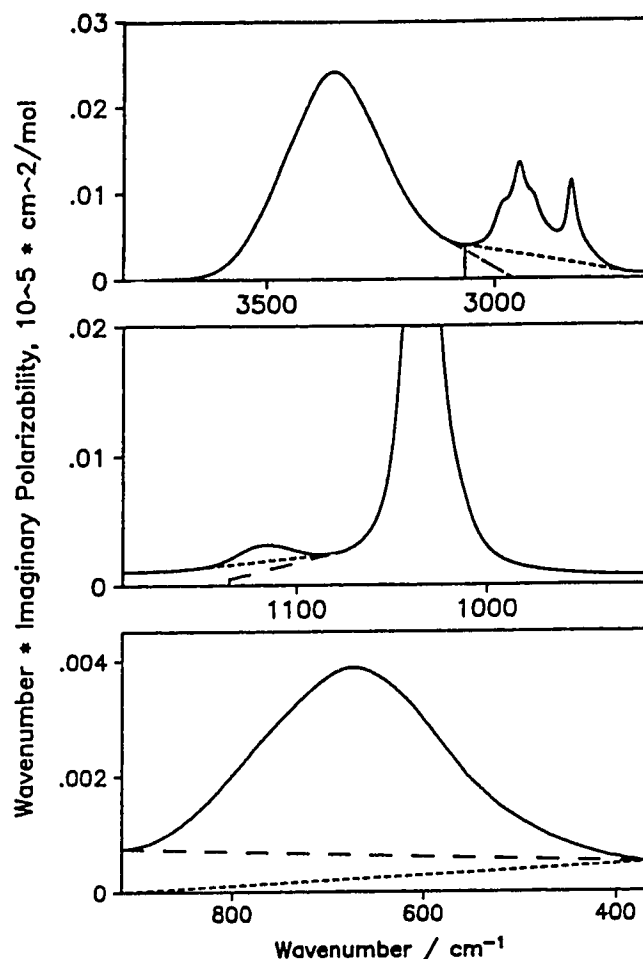


**Figure 5.12** The approximate methods used to separate the observed absorption into contributions from different vibrations: Top box, O-H and C-H stretches; Middle box, C-O stretch and  $\text{CH}_3$  rock; Bottom box, H-C-O-H torsion. In each box the long-dashed line illustrates Case 2 of Table 5.6 and the short-dashed line illustrates Case 3.

C-O stretching modes and by  $\pm 22\%$  for the C-H stretching and H-C-O-H torsion vibrations.

The usefulness of curve-fitting to indicate the correct separation method has been explored. Most of the bands in the  $\alpha_m''$  spectrum have been fitted with classical damped harmonic oscillator (CDHO) bands, which are nearly Lorentzian and are described<sup>6,8</sup> (Chapter 4) by the terms in the sum in eq. (A5.20) of the appendix. Gaussian curves were used to fit bands due to the H-bonded hydrogen atom.

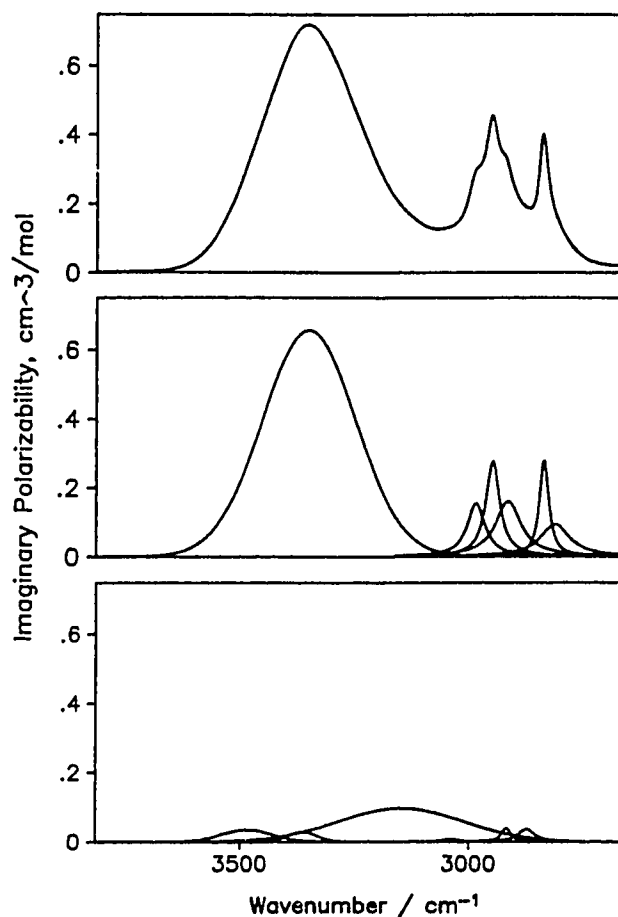


**Figure 5.13** The O–H and C–H stretching regions of the imaginary molar polarizability spectrum: Top box, the experimental spectrum and the curve resulting from curve fitting; the two appear as one; Middle box, the bands used to fit the obvious features in the spectrum; Bottom box, the additional, unsuspected bands needed to obtain a satisfactory fit.

The O–H and C–H stretching regions of the  $\alpha''_m$  spectrum are shown in the upper box of Figure 5.13, with the resultant curve of our fitting attempt. Only one curve can be seen, indicating that the fit was excellent. The middle box of Figure 5.13 shows the bands that fitted the obvious features of the spectrum. The bottom box shows the additional bands that were necessary to obtain a good fit even though their presence is unsuspected from the spectrum. It remains a valid question whether they indicate actual transitions or simply indicate that the obvious bands are not CDHO or Gaussian in shape. It also remains a valid question which, if any, of the area in these bands should be assigned to the O–H and C–H stretching vibrations.

If it is assumed that all of the intensity in this region originates in the O–H and C–H stretching fundamentals, the assignment of the intensity in these unsuspected features is clear, with the exception of the broad band at  $3147\text{ cm}^{-1}$ . If the area of the  $3147\text{ cm}^{-1}$  band is all assigned to the O–H vibration, the curve fit yields the area  $6.9\text{ km mole}^{-1}$  for the OH and  $2.06\text{ km mole}^{-1}$  for the C–H vibration. If only 60% of the area of this band is assigned to OH, the areas are  $6.48$  and  $2.48\text{ km mole}^{-1}$  for the O–H and C–H stretching vibrations, respectively. Following CDHO theory, it is the  $\alpha_m''$  spectrum that was fitted (Figure 5.13), but the component peaks were multiplied by  $\nabla$  before measuring the areas quoted, which are, thus, areas under the  $\nabla\alpha_m''$  spectrum and compare directly with those in Tables 5.5 and 5.6.

The curve fit, thus, gave essentially the same information as the cruder techniques used in Cases 1 to 3. A similar result was obtained for the lower-wavenumber regions, in which it was more difficult to obtain a good fit. Essentially no new information was obtained about the correct area of the H–C–O–H torsion vibration, but the curve fitting suggested that the area under the C–O stretching band may be as low as  $1.15\text{ km mole}^{-1}$ .

All of these results indicate that the areas  $C_j$  have the approximate values  $7.1$ ,  $1.8$ ,  $1.3$  and  $0.94\text{ km mole}^{-1}$  shown in Table 5.6 for the O–H, C–H, C–O stretching and H–C–O–H torsion vibrations, respectively. These values can not be regarded as accurate to any better than about  $\pm 6\%$  for the O–H and C–O vibrations and to  $\pm 22\%$  for the C–H and H–C–O–H torsion vibrations. Thus, the 3% accuracy in the optical constant spectra is reduced to 6% and 22% for the molecular property.

From these values, the molecular property  $|\partial\bar{\mu}/\partial Q_j|^2$  was calculated to be  $13.3$ ,  $3.4$ ,  $2.43$  and  $1.8\text{ (Debye } \text{\AA}^{-1}\text{ amu}^{-1/2})^2$  for the O–H, C–H, C–O stretching and H–C–O–H torsion vibrations respectively. Again, for the C–H stretching vibrations, this value is the sum of  $|\partial\bar{\mu}/\partial Q_j|^2$  over all three C–H stretching vibrations. The  $|\partial\bar{\mu}/\partial Q_j|^2$  values were converted to the  $|\partial\bar{\mu}/\partial R|$  values listed in Table 5.6, where  $R$  is an internal valence displacement coordinate and  $|\partial\bar{\mu}/\partial R|$  was assumed to lie in the direction of the internal coordinate, i.e. along the OH, CO and CH bonds and perpendicular to the COH plane. The following procedures and assumptions were used for this conversion.

The fundamental relation is

$$\frac{\partial\bar{\mu}}{\partial Q_j} = \sum_i \frac{\partial\bar{\mu}}{\partial R_i} \frac{\partial R_i}{\partial Q_j} = \sum_i \frac{\partial\bar{\mu}}{\partial R_i} l_{ij}$$

**Table 5.7** Geometry of methanol. <sup>a</sup>

Parameter	Value
$r_{\text{OH}}$	0.945 Å
$r_{\text{CO}}$	1.425 Å
$r_{\text{CH}}$	1.094 Å
$\angle\text{HCH}$	108.63°
$\angle\text{HCO}$	110.30°
$\angle\text{HOC}$	108.50°

a) After Ref. 27. The 3.3° tilt of the methyl group reported in Ref. 27 was ignored. The HCO angles were calculated by ignoring the tilt angle of the methyl group.

where the  $l_{ij}$  are the eigenvectors given by a normal coordinate calculation for coordinate  $i$  in normal coordinate  $j$  and give the displacement of internal coordinate  $i$  during unit displacement of normal coordinate  $j$ . The sum is a vector sum. To calculate the eigenvectors, the molecule was assumed to have  $C_s$  symmetry, with the OH bond trans to a CH bond in the HCOH plane. The geometry<sup>27</sup> used is given in Table 5.7, and the carbon-12 scale of atomic masses was used. The internal coordinates,  $R_i$ , were taken to be the changes in the OH, CH, and CO bond lengths and, for the H–C–O–H torsion,  $R_\tau$  was defined as 1 Å times the change in the dihedral angle between the HOC plane and the OCH plane of the trans CH bond. The O–H and C–H stretching vibrations were treated as diatomic oscillators, i.e. as uncoupled oscillators in methanol, at 3350 and 1035  $\text{cm}^{-1}$ , respectively. The symmetric  $\text{CH}_3$  stretching vibration, ( $A'$  under  $C_s$ ) was assigned at 2833  $\text{cm}^{-1}$ , and the antisymmetric  $\text{CH}_3$  stretching vibrations were assigned at 2980  $\text{cm}^{-1}$  ( $A'$  under  $C_s$ ) and 2945  $\text{cm}^{-1}$  ( $A''$  under  $C_s$ ), following the work of Günthard and coworkers<sup>16</sup>. The in-plane and out-of-plane CH stretching force constants were calculated from these wavenumbers to be 4.4190 and 4.8105  $\text{mdyne } \text{\AA}^{-1}$ , and the two  $f_{\text{CH,CH}'}$  interaction constants were assumed equal and were calculated to be +0.1736  $\text{mdyne } \text{\AA}^{-1}$ . The two non-equivalent  $|\partial\bar{\mu}/\partial R_{\text{CH}}|$  values were assumed equal and the relation  $|\partial\bar{\mu}/\partial Q_j|^2 = 3.29 |\partial\bar{\mu}/\partial R_{\text{CH}}|^2$  was calculated. For the H–C–O–H torsion, assumed uncoupled to other vibrations, the relation was calculated to be  $|\partial\bar{\mu}/\partial Q_j|^2 = 2.336 |\partial\bar{\mu}/\partial R_\tau|^2$ .

In the later chapters, attempts are made to improve our knowledge of the separation of the intensity into contributions from the different vibrations by comparing the spectra of  $\text{CH}_3\text{OH}$ ,  $\text{CH}_3\text{OD}$ ,  $\text{CD}_3\text{OH}$  and  $\text{CD}_3\text{OD}$ .

## 5.6 Appendix

The electromagnetic quantities used in this work are the complex refractive index  $\hat{n}(\nu)$ , the complex dielectric constants,  $\hat{\epsilon}$ , and the complex molar polarizability  $\hat{\alpha}_m(\tilde{\nu})$ .

They are defined in eqs. (A5.1) to (A5.3)

$$\hat{n}(\nu) = n(\nu) + i k(\nu) \quad (\text{A5.1})$$

$$\hat{\epsilon}(\nu) = \epsilon''(\nu) + i \epsilon'(\nu) \quad (\text{A5.2})$$

$$\hat{\alpha}_m(\tilde{\nu}) = \alpha'_m(\tilde{\nu}) + i \alpha''_m(\tilde{\nu}) \quad (\text{A5.3})$$

The complex refractive index is related to complex dielectric constant by

$$\hat{\epsilon} = \hat{n}^2 \quad \text{i. e.} \quad \epsilon' = n^2 - k^2 \quad \text{and} \quad \epsilon'' = 2nk \quad (\text{A5.4})$$

The (decadic) molar absorption coefficient,

$$E_m(\nu) = \frac{1}{Cd} \log_{10} \frac{I_o(\tilde{\nu})}{I_t(\tilde{\nu})} \quad (\text{A5.5})$$

where  $d$  is pathlength in cm,  $C$  is the molar concentration, and  $I_o$  and  $I_t$  are incident and transmitted intensities corrected for reflection losses, is related to  $k(\nu)$ , the imaginary refractive index, usually called the absorption index, by

$$E_m(\nu) = 4\pi\nu k(\nu)/(2.303C) \quad (\text{A5.6})$$

The (decadic) linear absorption coefficient,

$$K(\nu) = \frac{1}{d} \log_{10} \frac{I_o(\tilde{\nu})}{I_t(\tilde{\nu})} \quad (\text{A5.7})$$

is related to the absorption index  $k(\nu)$  by

$$K(\nu) = 4\pi\nu k(\nu)/2.303 \quad (\text{A5.8})$$

A widely used measure of infrared integrated intensity for band  $j$  is  $A_j$ , defined by

$$A_j = \frac{2.303}{C} \int K(\tilde{\nu}) d\tilde{\nu} = 2.303 \int E_m(\tilde{\nu}) d\tilde{\nu} \quad (\text{A5.9})$$

For a gas,  $A_j$  is related<sup>28</sup> to the molecular property  $\partial\bar{\mu}/\partial Q_j$ , where  $\bar{\mu}$  is the molecular dipole moment and  $Q_j$  is a mass-weighted normal coordinate, by

$$A_j = \frac{\pi N_a}{3c^2} g_j \left| \frac{\partial\bar{\mu}}{\partial Q_j} \right|^2 \quad (\text{A5.10})$$

where  $g_j$  is the degeneracy of vibration  $j$ .

For a liquid, the corresponding equation is<sup>29</sup>

$$A_j = \frac{\pi N_a}{3c^2 \underline{n}} g_j \left| \frac{\partial \bar{\mu}}{\partial Q_j} \right|_{\text{eff}}^2 \quad (\text{A5.11})$$

where

$$\left| \frac{\partial \bar{\mu}}{\partial Q_j} \right|_{\text{eff}} = \left( \frac{\underline{n}^2 + 2}{3} \right) \left| \frac{\partial \bar{\mu}}{\partial Q_j} \right| \quad (\text{A5.12})$$

where the Lorentz local field has been assumed.  $\underline{n}$  is the value the real refractive index would have at the position of the absorption band if the band were not present. This expression for  $A_j$  of a liquid is approximate, because  $1/\underline{n}$  is not a constant.

In previous studies, we have used the quantity  $B_j$  as a measure of integrated intensity of bands, where

$$B_j = \left( \frac{3}{\underline{n}^2 + 2} \right)^2 V_m \int \tilde{\nu} \epsilon'' d\tilde{\nu} \quad (\text{A5.13})$$

where  $V_m \tilde{\nu} \epsilon''$  is the molar conductivity at  $\tilde{\nu}$ .  $V_m$  is the volume of one mole of liquid or solution. For pure liquids,  $V_m = 1/C$  where  $C$  is the molar concentration, and for solutions,  $V_m = x_A/C_A$  where  $x_A$  and  $C_A$  are the mole fraction and molar concentration, respectively, of component A in the solution. Under an approximate development<sup>8,9</sup> of the CDHO model that is only exact for isolated bands,  $B_j$  is related to the molecular property  $|\partial \bar{\mu} / \partial Q_j|$  by

$$B_j = \frac{N_a}{6c^2} g_j \left| \frac{\partial \bar{\mu}}{\partial Q_j} \right|^2 \quad (\text{A5.14})$$

For pure liquids,  $B_j$  is related to  $A_j$  by the approximate relation

$$A_j = B_j \frac{2\pi}{\underline{n}} \left( \frac{\underline{n}^2 + 2}{3} \right)^2 \quad (\text{A5.15})$$

For solutions, the approximate relation is

$$A_j = B_j \frac{2\pi}{\underline{n} x_A} \left( \frac{\underline{n}^2 + 2}{3} \right)^2 \quad (\text{A5.15a})$$

where  $x_A$  is the mole fraction of the component whose concentration was used to calculate  $E_m$  in eq. (A5.5) or (A5.6).

Another quantity,  $C_j$ , is also used as a measure of integrated intensity. Following Dignam<sup>6</sup> we define  $C_j$  by

$$C_j = \int \tilde{\nu} \alpha_m'' d\tilde{\nu} \quad (\text{A5.16})$$

where  $\alpha_m''$  is the imaginary molar polarizability. Under the Lorentz local field model,

$$\hat{\alpha}_m(\tilde{\nu}) = \frac{3V_m}{4\pi} \frac{\hat{\epsilon}(\tilde{\nu}) - 1}{\hat{\epsilon}(\tilde{\nu}) + 2} \quad (\text{A5.17})$$

so  $\alpha_m''$  can be calculated<sup>6</sup> from the dielectric constants, and hence from the refractive indices, by

$$\alpha_m'' = \frac{9V_m}{4\pi} \frac{\epsilon''}{(\epsilon' + 2)^2 + \epsilon''^2} \quad (\text{A5.18})$$

The local susceptibility,  $\hat{C}(\tilde{\nu})$ , used by Clifford and Crawford<sup>7</sup> is related to  $\alpha_m''(\tilde{\nu})$  via

$$V_m \hat{C}(\tilde{\nu}) = \alpha_m''(\tilde{\nu}) \quad (\text{A5.19})$$

Under the CDHO model for randomly oriented molecules, the imaginary molar polarizability is given by

$$\hat{\alpha}_m(\tilde{\nu}) = \frac{N_a}{12\pi^2 c^2} \sum_j g_j \left| \frac{\partial \bar{\mu}}{\partial Q_j} \right|^2 \frac{\Gamma_j \tilde{\nu}}{(\tilde{\nu}_j^2 - \tilde{\nu}^2)^2 + \Gamma_j^2 \tilde{\nu}^2} \quad (\text{A5.20})$$

where  $\tilde{\nu}_j$  is the oscillator wavenumber and  $\Gamma_j$  is the damping constant, both in  $\text{cm}^{-1}$ .  $\Gamma_j$  is essentially the full width at half height (FWHH) of the band

From eqs. (A5.16) and (A5.20), the integrated intensity  $C_j$  is related<sup>6</sup> to the molecular property  $\left| \partial \bar{\mu} / \partial Q_j \right|$  by

$$C_j = \frac{N_a}{24\pi c^2} \sum_j g_j \left| \frac{\partial \bar{\mu}}{\partial Q_j} \right|^2 \quad (\text{A5.21})$$

The integrated intensities  $C_j$ ,  $A_j$  and  $B_j$  are, thus, related by the approximate eqs.

$$A_j = C_j \frac{8\pi^2}{\underline{n}} \left( \frac{\underline{n}^2 + 2}{3} \right)^2 \quad (\text{A5.22})$$

and

$$B_j = 4\pi C_j \quad (\text{A5.23})$$

These approximate relations assume that  $(\epsilon'')^2$  is negligible compared with  $(\epsilon' + 2)^2$  and the relation to  $A_j$  also assumes that  $\underline{n}$  is constant.

Simple numerical factors relate the experimental quantities and the molecular properties in eqs. (A5.11), (A5.14) and (A5.21). In eq. (A5.11), if  $A_j$  is in  $\text{km mol}^{-1}$ , multiplying  $A_j$  by  $23.66 \times 10^{-3} \underline{n}$  or by  $15.85 \times 10^{-15} \underline{n}$  yields  $g_j \left| \partial \bar{\mu} / \partial Q_j \right|_{\text{eff}}^2$  in  $(\text{Debye } \text{\AA}^{-1} \text{amu}^{-1/2})^2$  or  $\text{C}^2 \text{ kg}^{-1}$ , respectively. In eq. (A5.14), if  $B_j$  is in  $\text{km mol}^{-1}$ , multiplying  $B_j$  by 0.1487 or by  $9.96 \times 10^{-14}$  yields  $g_j \left| \partial \bar{\mu} / \partial Q_j \right|^2$  in  $(\text{Debye } \text{\AA}^{-1} \text{amu}^{-1/2})^2$  or  $\text{C}^2 \text{ kg}^{-1}$ , respectively. In eq. (A5.21), if  $C_j$  is in  $\text{km mol}^{-1}$ , multiplying  $C_j$  by 1.8686 or by  $1.252 \times 10^{-12}$  gives  $g_j \left| \partial \bar{\mu} / \partial Q_j \right|^2$  in  $(\text{Debye } \text{\AA}^{-1} \text{amu}^{-1/2})^2$  or  $\text{C}^2 \text{ kg}^{-1}$ , respectively.

## 5.7 References

1. J. E. Bertie and H. H. Eysel, *Appl. Spectrosc.* **39**, 392 (1985).
2. J. E. Bertie, H. Harke, M. K. Ahmed, and H. H. Eysel, *Croatica Chim. Acta* **61**, 391 (1988).
3. J. E. Bertie, S. L. Zhang, and R. Manji, *Appl. Spectrosc.* **46**, 1660 (1992).
4. N. Sheppard, H. A. Willis, and J. C. Rigg, *Spectrochim. Acta* **43A**, 1(1987).
5. I. Mills, T. Cvitaš, K. Homann, N. Kallay, and K. Kuchitsu, *Quantities, Units and Symbols in Physical Chemistry*. Blackwell Scientific Publications, Oxford, 1988.
6. M. J. Dignam, *Appl. Spectrosc. Rev.* **24**, 99 (1988).
7. A. A. Clifford and B. Crawford, Jr., *J. Phys. Chem.* **70**, 1536 (1966).
8. J. Fahrenfort, in *Infrared Spectroscopy and Molecular Structure*. Edited by Mansel Davies. Elsevier, Amsterdam, 1963. Chapter XI.
9. J. W. Warner and M. Wolfsberg, *J. Chem. Phys.* **78**, 1722 (1983).
10. J. E. Bertie, M. K. Ahmed, and H. H. Eysel, *J. Phys. Chem.* **93**, 2210 (1989).
11. J. E. Bertie, M. K. Ahmed, and S. Baluja, *J. Phys. Chem.* **93**, 6660 (1989).
12. H. H. Eysel and J. E. Bertie, *Proceedings of the 5th International Conference on Fourier Transform Spectroscopy*. Society of Photo-Optical Instrumentation Engineers, SPIE **553**, 230 (1985).
13. H. H. Eysel and J. E. Bertie, *J. Mol. Struct.* **142**, 227 (1986).



14. J. E. Bertie, M. K. Ahmed, and S. Baluja, *Proceedings of the 7th International Conference on Fourier Transform Spectroscopy*. Society of Photo-Optical Instrumentation Engineers, SPIE **1145**, 518 (1989).
15. D. D. Honijk, W. F. Passchier, M. Mandel, and M. N. Afsar, *Infrared Phys.* **17**, 9 (1977).
16. A. Serrallach, R. Meyer, and Hs. H. Günthard, *J. Mol. Spectrosc.* **52**, 94 (1974) and citations therein.
17. P. Sethna and D. Williams, *J. Phys. Chem.* **83**, 405 (1979).
18. J. Chamberlain, *The Principles of Interferometric Spectroscopy*, John Wiley & Sons, London, 1979.
19. R. P. Sperline, S. Muralidharan and H. Freiser, *Appl. Spectrosc.* **40**, 1019 (1986)
20. Y. Marechal. Personal Communication 1990.
21. J. E. Bertie and S. L. Zhang. *Can. J. Chem.* **70**, 520 (1992).
22. R. N. Bracewell. *Science* **248**, 697 (1990).
23. D. G. Cameron, J. P. Hawranek, P. Neelakantan, R. P. Young, and R. N. Jones, "Computer Programs for Infrared Spectrophotometry XLII to XLVII" in *National Research Council of Canada Bulletin* 16, 1977.
24. J. E. Bertie, C. D. Keefe and R. N. Jones, *Can. J. Chem.* **69**, 1609 (1991).
25. *International Critical Tables of Numerical Data, Physics, Chemistry and Technology* **7**. McGraw-Hill, New York, 1930. P34.
26. J. E. Bertie, R. N. Jones, and Y. Apelblet, *Appl. Spectrosc.* **47**, 1989 (1993).
27. R. M. Lees and J. G. Baker, *J. Chem. Phys.* **48**, 5299 (1968).
28. E. B. Wilson, J. C. Decius, and P. C. Cross, *Molecular Vibrations*. McGraw-Hill, New York, 1954.
29. S. R. Polo and M. K. Wilson, *J. Chem. Phys.* **23**, 2376 (1953).

## Chapter 6 Infrared Refractive Indices from 8000 to 350 cm<sup>-1</sup>, Absolute Integrated Intensities, Transition Moments and Dipole Moment Derivatives of Methanol-*d*, at 25°C \*

### 6.1 Introduction

In an earlier paper<sup>1</sup> in this series<sup>1-4</sup>, we reported the absolute infrared absorption intensities of liquid methanol determined by a combination of the CIRCLE cylindrical multiple attenuated total reflection (ATR) and transmission methods. The intensity quantities initially determined by these methods are the complex refractive index spectra,  $\hat{n}(\tilde{\nu}) = n(\tilde{\nu}) + i k(\tilde{\nu})$ , where  $n(\tilde{\nu})$  is the real refractive index and  $k(\tilde{\nu})$  is the imaginary refractive index at wavenumber  $\tilde{\nu}$ . The imaginary refractive index  $k(\tilde{\nu})$  is also called absorption index<sup>5,6</sup>, and  $n(\tilde{\nu})$  and  $k(\tilde{\nu})$  are collectively called the optical constants. The accuracy of the measurements was estimated to be  $\pm 0.5\%$  for  $n(\tilde{\nu})$  values,  $\pm 3\%$  for  $k(\tilde{\nu})$  values below 5000 cm<sup>-1</sup> and  $\pm 10\%$  for  $k(\tilde{\nu})$  values above 5000 cm<sup>-1</sup>.

Equations that were summarized previously<sup>7</sup> (Section 5.6) allow other optical properties to be calculated from the refractive indices. In particular, one can calculate the spectra of the decadic molar absorption coefficient,  $E_m(\tilde{\nu})$ , the molar conductivity,  $V_m \tilde{\nu} \epsilon''(\tilde{\nu})$ , where  $V_m$  is the volume of one mole of pure liquid or of one mole of solution and  $\epsilon''(\tilde{\nu})$  is the imaginary dielectric constant or dielectric loss, and the imaginary molar polarizability  $\alpha_m''(\tilde{\nu})$ . The calculation of  $\alpha_m''(\tilde{\nu})$  requires the assumption of the Lorentz local field. The integrated areas  $A_j$ ,  $B_j$ , and  $C_j$  can be calculated<sup>7</sup> (Chapter 4) from the areas under bands in these spectra, but the magnitudes of the dipole moment changes during the normal vibrations of the molecule in the liquid,  $\mu_j = |\partial \bar{\mu} / \partial Q_j|$ , are best calculated from the areas  $C_j$ , under the harmonic approximation. This was discussed in Chapter 4.

The most general molecular property that can be calculated from the integrated intensity of the  $j$ th vibration,  $C_j$ , is the square of the transition moment<sup>8</sup> or dipole moment matrix element<sup>9</sup>,  $|\bar{R}^{nm}|^2$ , where  $\bar{R}^{nm} = \int \Psi_n \bar{\mu} \Psi_m d\tau$ , and  $\bar{\mu}$  is the dipole moment. The fundamental bands involve only the lowest two vibrational states of the motion,  $n = 1$  and  $m = 0$ , and the symbol  $|\bar{R}^{10}|$  can be written as  $|R_j^f|$ . The required relation<sup>10</sup> is then

---

\* A version of this chapter has been published. Bertie and Zhang, Appl. Spectrosc. 48, 176 (1994).

$$C_j = \frac{N_a \pi}{3hc} g_j \tilde{\nu}_j |R_j^f|^2 \quad (6.1)$$

where  $N_a$  is Avogadro's number,  $h$  is Planck's constant,  $c$  is the velocity of light in vacuum, and  $g_j$  is the degeneracy of the vibration. Numerically the relation is  $|R_j^f|^2 = 31.50 C_j / \tilde{\nu}_j$ , where  $|R_j^f|$  is in Debye if  $C_j$  is in  $\text{km mol}^{-1}$  and  $\tilde{\nu}_j$  is in  $\text{cm}^{-1}$ . The value of  $|R_j^f|^2$  obtained from this treatment is such that  $\tilde{\nu}_j |R_j^f|^2$  is the mean of the  $\tilde{\nu}_i |R_i^f|^2$  values of all the transitions  $i$  that contribute to band  $j$ <sup>10</sup>. Unlike the calculation of the dipole moment derivatives, the calculation of the transition moment does not depend on mechanical and electrical harmonicity of the vibration<sup>10</sup>.

It was noted<sup>1</sup> in the study of liquid  $\text{CH}_3\text{OH}$  that much of the accuracy of the optical constants is lost when areas of overlapping bands are separated into the integrated intensities of different vibrations in order to calculate  $\mu_j$ . In this chapter, infrared absorption intensities of liquid methanol- $d$ ,  $\text{CH}_3\text{OD}$ , at  $25^\circ\text{C}$ , are reported, from ATR measurements between  $4500$  and  $350 \text{ cm}^{-1}$  and from transmission measurements between  $6187$  and  $3057 \text{ cm}^{-1}$  and in regions of weak absorption below  $2100 \text{ cm}^{-1}$ . The spectra of methanol- $d$  and methanol are compared to seek improvement in the separation of overlapping bands and, hence, in the reliability of the molecular properties calculated from the integrated intensities  $C_j$  for both  $\text{CH}_3\text{OH}$  and  $\text{CH}_3\text{OD}$ .

While the assignment<sup>11</sup> of the infrared spectrum of methanol and its isotopomers is well established, no report of measurements of absolute infrared absorption intensities of liquid methanol- $d$  is known.

## 6.2 Method

The methods used to obtain the complex refractive indices from multiple attenuated total reflection spectra and from transmission spectra have been fully described<sup>1-4,12-14</sup>. The spectra were recorded at  $2 \text{ cm}^{-1}$  nominal resolution and digitized at  $0.964233 \text{ cm}^{-1}$  intervals. The experimental methods and instrumentation, as well as the operating conditions and procedures, were identical to those reported<sup>1</sup> for normal methanol,  $\text{CH}_3\text{OH}$ , with the following exceptions.

The methanol- $d$ ,  $\text{CH}_3\text{OD}$ , was from two sources. Aldrich methyl alcohol- $d$  99.5 + atom % D, GOLD LABEL, gave no evidence of impurity by either infrared spectroscopy or gas chromatography. GC-IR study of the lower grade Aldrich methyl alcohol- $d$ , 99.5

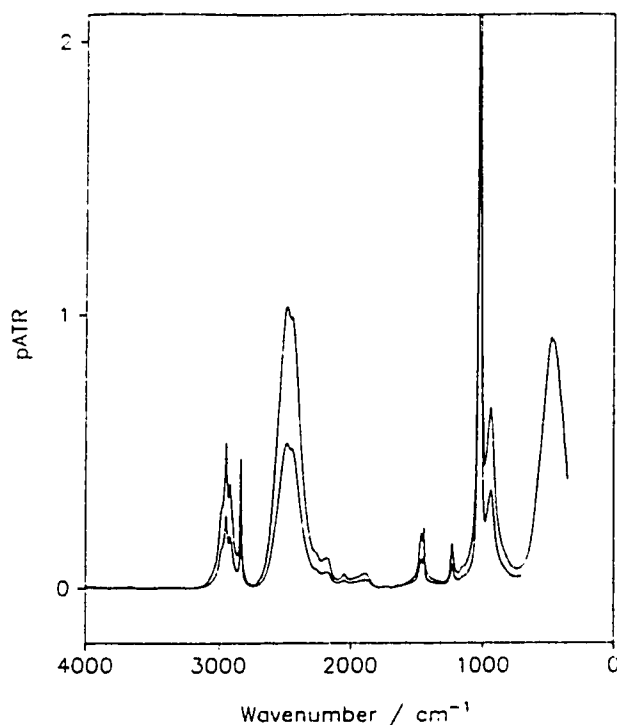


**Figure 6.1** pATR spectra of methanol-*d* recorded with KRS-5 (upper curve) and ZnSe (lower curve) ATR rods. The liquid holder around the 82 mm long ATR rod was 30 mm long for the lower curve and 60 mm long for the upper curve. The effective number of reflections was about 6 for the upper curve and about 3 for the lower curve.

+ atom % D revealed 1% of an impurity that is probably methyl formate. The infrared spectrum, including intensities, of this sample, was identical to that of the Aldrich GOLD LABEL sample, except for a very weak doublet at 1730/1715  $\text{cm}^{-1}$  that is clearly due to the impurity. The material was used as supplied.

The ZnSe CIRCLE cell ATR rod was used only with the short liquid holder which gave ~ 3 reflections. The long liquid holder (~ 6 reflections) was used only with the KRS-5 ATR rod for low wavenumbers.

### 6.3 Results

The pATR spectra of  $\text{CH}_3\text{OD}$  obtained with the long KRS-5 cell and the short ZnSe cell are shown as the upper and lower curves in Figure 6.1. Experimental absorbance spectra of  $\text{CH}_3\text{OD}$  in cells with 470 and 1200  $\mu\text{m}$  pathlengths are shown in Figure 6.2.

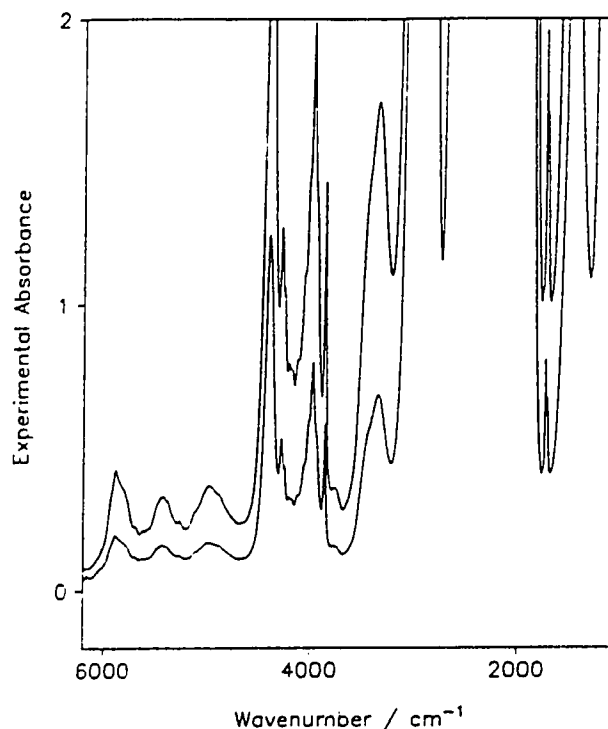


**Figure 6.2** Experimental absorbance spectra of liquid methanol-*d* in cells with CaF<sub>2</sub> windows and pathlengths 470 and 1200 μm. The very weak doublet at 1730/1715 cm<sup>-1</sup> is due to impurity.

The real refractive index of methanol at 8000 cm<sup>-1</sup> at 25°C was found<sup>1</sup> to be  $1.325 \pm 0.001$  by fitting the values at visible wavelengths<sup>15</sup> to  $n^2 = A + B\nu^2 + C\nu^4$ , and extrapolating to 8000 cm<sup>-1</sup>. The only value we have found<sup>16</sup> for methanol-*d* is at the Sodium-D line,  $n_D = 1.3270$ , where that of CH<sub>3</sub>OH is 1.3290. Therefore we estimate the real refractive index of methanol-*d* at 8000 cm<sup>-1</sup> to be  $1.323 \pm 0.001$ .

Figure 6.3 shows absorption index spectra,  $k(\nu)$ , calculated from pATR spectra recorded with ZnSe (above 700 cm<sup>-1</sup>, curves A and C) and KRS-5 (750–350 cm<sup>-1</sup>, curve B) ATR rods. The  $k(\nu)$  values calculated from pATR spectra depend on the  $n(\nu)$  values<sup>1</sup>. The  $n(\nu)$  values are calculated from the  $k(\nu)$  values by Kramers-Krönig transformation<sup>1</sup>, and are sensitive to the significant absorption below 350 cm<sup>-1</sup>. Honijk *et al.*<sup>17</sup> have measured this absorption for liquid methanol. Their  $k(\nu)$  values are tabulated in Table 2 of Ref. 1 and shown in Figure 7 of Ref. 1 (also Figure 5.7). The absorption is due to rotational and translational motion of the molecules in the liquid, and is undoubtedly very similar for methanol and methanol-*d*. Accordingly, during the

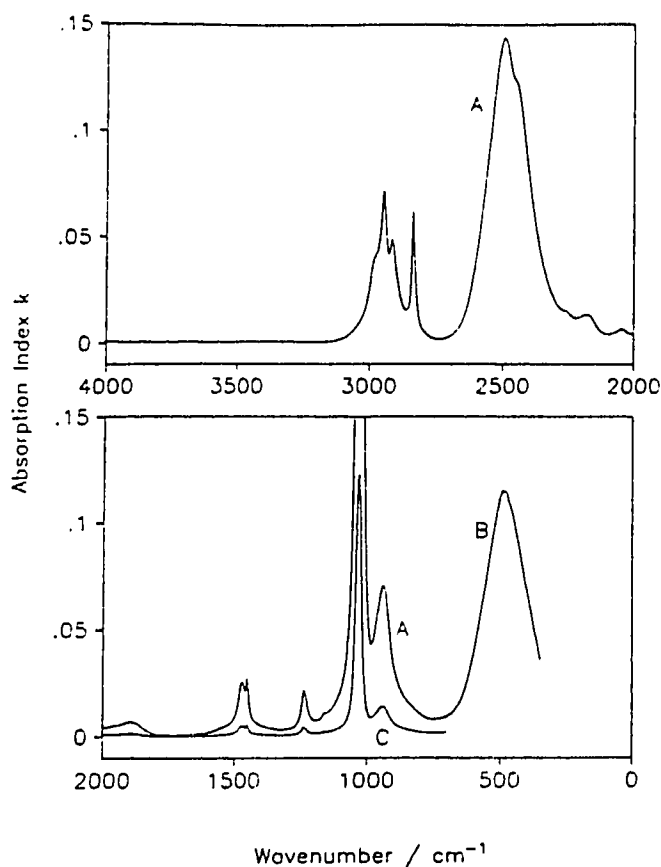


**Figure 6.3** Absorption index spectra,  $k(\tilde{\nu})$ , of  $\text{CH}_3\text{OD}$  calculated from CIRCLE cell pATR spectra. Above  $700\text{ cm}^{-1}$  (curves A and C), the ZnSe ATR rod and the short cell were used. Below  $750\text{ cm}^{-1}$  (curve B), the KRS-5 rod and the long cell were used. In the bottom box, the ordinate scale is correct for curves A and B. The ordinate labels must be multiplied by 5 for curve C which is the same spectrum as curve A.

calculation of  $k(\tilde{\nu})$  and  $n(\tilde{\nu})$  from the pATR spectra obtained with the KRS-5 rod, Honijk *et al.*'s  $k(\tilde{\nu})$  values for methanol between  $350$  and  $2\text{ cm}^{-1}$  were appended to the  $k(\tilde{\nu})$  values of methanol-*d* during the Kramers-Krönig transformation<sup>1</sup>, in order to improve the  $n(\tilde{\nu})$  and  $k(\tilde{\nu})$  values obtained. Similarly, during the calculation of  $k(\tilde{\nu})$  and  $n(\tilde{\nu})$  from the pATR spectra obtained with the ZnSe rod, the  $k(\tilde{\nu})$  values obtained from the KRS-5 cell and those of Honijk *et al.* were appended between  $700$  and  $350\text{ cm}^{-1}$  and between  $350$  and  $2\text{ cm}^{-1}$ , respectively, to the  $k(\tilde{\nu})$  values from the ZnSe cell (above  $700\text{ cm}^{-1}$ ) during the Kramers-Krönig transformation. A single absorption index spectrum of methanol-*d* was obtained by merging at  $740\text{ cm}^{-1}$  the two resulting  $k$  spectra, shown in Figure 6.3, curves A and B. This single  $k$  spectrum is known to good accuracy from

**Table 6.1** The decadic linear absorption coefficients,  $K(\tilde{\nu})$ , of methanol-*d* at the anchor points.

Wavenumber ( $\text{cm}^{-1}$ )	$K(\tilde{\nu})$ ( $\text{cm}^{-1}$ )	95% confidence limit of $K^a$
6186.5	0.00 <sup>b</sup>	
4670.7	1.594	4.8%
4151.9	5.831	1.1%
3681.4	2.103	0.8%
2730.7	24.07	1.3%
2092.3	45.25	1.2%
1997.8	44.33	1.4%
1768.4	8.233	0.4%
1685.4	8.257	0.4%
1315.2	22.94	1.4%

a) As a percentage of the  $K(\tilde{\nu})$ .

b) Set to zero, because the absorption was too weak to measure in 1.2 mm path.

3100 to 350  $\text{cm}^{-1}$ . The spectrum in the weakly absorbing region from 3100  $\text{cm}^{-1}$  to 6000  $\text{cm}^{-1}$  is also known to some extent from these pATR spectra.

To improve the accuracy above 3100  $\text{cm}^{-1}$ , and to check the absorption index values calculated from the pATR spectra in the weakly absorbing regions below 3100  $\text{cm}^{-1}$ , absorption index spectra were determined from transmission spectra in cells with pathlengths up to 1.2 mm. Twenty one absorbance spectra were recorded in cells with calcium fluoride windows and pathlengths from 80  $\mu\text{m}$  to 1.2 mm. In a procedure<sup>14</sup> to correct unpredictable variations in the baselines of the absorbance spectra, the decadic linear absorption coefficient<sup>1,5,6</sup>,  $K(\tilde{\nu})$ , was determined at *anchor point* wavenumbers<sup>14</sup> in the baseline from spectra in which the absorption at the anchor points is very strong. The values of  $K(\tilde{\nu})$  at the anchor points are given in Table 6.1, with their 95% confidence limits.

After the baselines were corrected<sup>14</sup>, the absorbance spectra were converted to absorption index spectra. Each absorption index spectrum was used in those regions in which the absorbance was between 0.2 and 1.5 with the cell pathlength that was used. Accordingly, the many absorption index spectra were averaged and merged in appropriate spectral regions to yield a single  $k$  spectrum from transmission spectroscopy. It is shown in Figure 6.4 in the regions for which it is useful, namely 6187 to 3049  $\text{cm}^{-1}$ , 2812 to 2652  $\text{cm}^{-1}$ , and 2318 to 1500  $\text{cm}^{-1}$ .

The  $k$  spectrum from pATR measurements is included in Figure 6.4, in which the same spectra are shown over the same wavenumber range in both boxes, but on a greatly

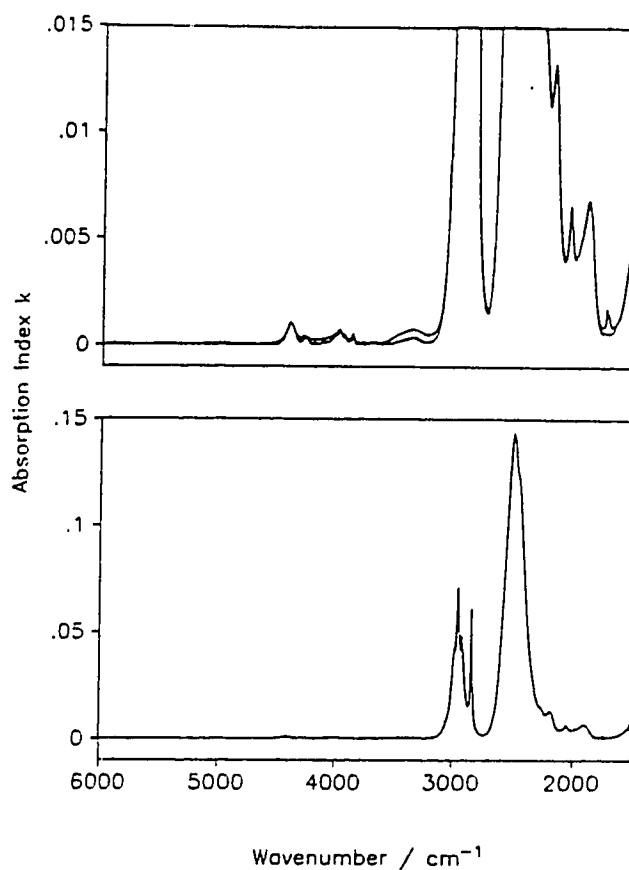


**Figure 6.4** The absorption index spectrum,  $k(\tilde{\nu})$ , deduced from ATR spectra, and the  $k$  spectrum from transmission spectra between 6000 and 1500  $\text{cm}^{-1}$ . The  $k$  spectrum from the transmission measurement is shown for three separate regions in both boxes: 6000–3049, 2812–2652 and 2318–1500  $\text{cm}^{-1}$ . In the top box the ordinate scale is greatly enlarged and the spectrum from the ATR measurement is noisy above 3000  $\text{cm}^{-1}$  and lower below 2000  $\text{cm}^{-1}$ . In the bottom box the same two spectra are shown on a normal ordinate scale with the O–D stretching band near full scale. The weak doublet at 1730/1715  $\text{cm}^{-1}$  is due to impurity.

expanded ordinate scale in the top box. The agreement can be seen in the top box. Above 3050  $\text{cm}^{-1}$ , the  $k$  spectrum from transmission measurements is much smoother and much more reliable. Between 2812 and 2652  $\text{cm}^{-1}$ , the two  $k$  spectra overlap. Between 2318 and 1500  $\text{cm}^{-1}$  two  $k$  spectra overlap except that the spectrum from transmission shows the small impurity peaks at 1730/1715  $\text{cm}^{-1}$ , and is higher to either side of these peaks. The impurity peaks were extremely weak, and were replaced by a straight line between 1767.4 and 1689.3  $\text{cm}^{-1}$  in the final  $k$  spectrum. The broad weak band near 3400  $\text{cm}^{-1}$  (Figure 6.4, top box) may be partly due to the small amount of



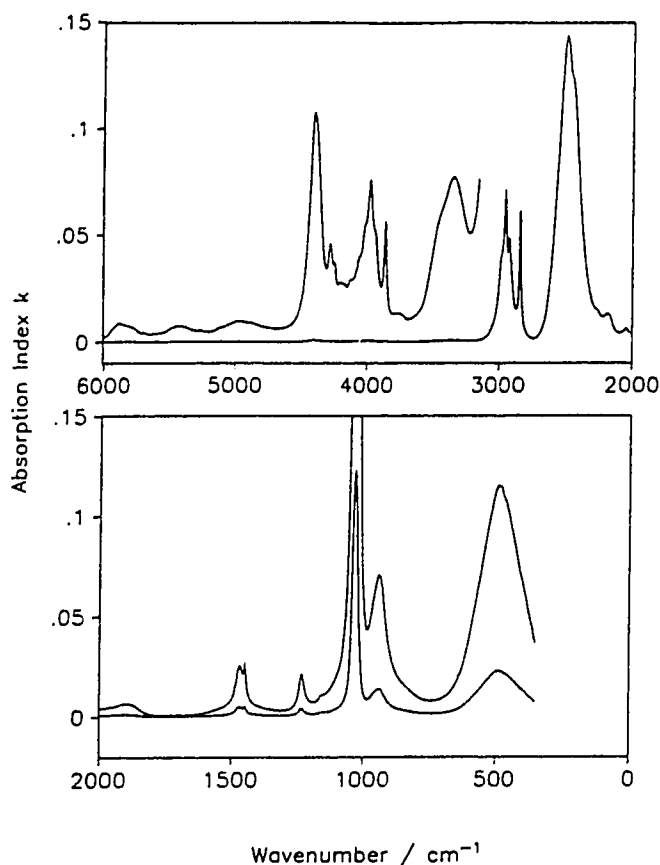


**Figure 6.5** The final absorption index spectrum of methanol-*d* at 25 °C from this work. In the top box, the ordinate labels apply to the complete spectrum (lower curve) and scale labels must be divided by 100 for the insert (upper curve) between 6000 and 3150  $\text{cm}^{-1}$ . In the bottom box, the ordinate labels apply to the upper curve and the scale labels must be multiplied by 5 for the lower curve.

$\text{CH}_3\text{OH}$  in the  $\text{CH}_3\text{OD}$ . The bottom box of Figure 6.4 shows the same spectra on a normal ordinate scale with the O–D stretching band from the ATR measurement near full scale. The extreme weakness of the impurity bands is evident in this box. The  $k$  spectrum from ATR measurement agrees with that from transmission to better than 2% below 4500  $\text{cm}^{-1}$  except where  $k(\nu)$  is less than 0.001 and was, consequently, not well defined by the ATR measurement.

A single absorption index spectrum from 8000 to 350  $\text{cm}^{-1}$  was created by merging the two  $k$  spectra. Specifically,  $k(\nu)$  was set to zero from 8000  $\text{cm}^{-1}$  to 6187  $\text{cm}^{-1}$ , the  $k(\nu)$  from transmission was used from 6187 to 3057  $\text{cm}^{-1}$ , the  $k(\nu)$  from ATR was used from 3057 to 2100  $\text{cm}^{-1}$ , the transmission result was used again from 2100 to 1570  $\text{cm}^{-1}$ ,

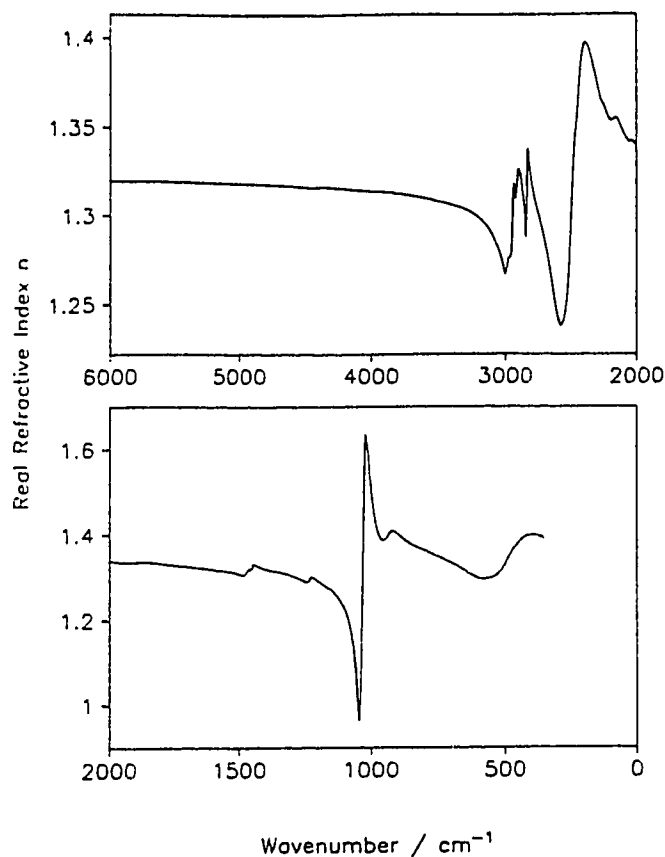


**Figure 6.6** The real refractive index spectrum of methanol-*d* at 25°C, calculated by KK transformation of the *k* spectrum of Figure 6.5 with  $n(8000\text{ cm}^{-1}) = 1.323$  and Honijk *et al.*'s *k* spectrum appended between 350 and  $2\text{ cm}^{-1}$ .

and the  $k(\nu)$  from ATR was used below  $1570\text{ cm}^{-1}$ . This spectrum is in Figure 6.5. It is very well defined below  $5900\text{ cm}^{-1}$ . Above  $5900\text{ cm}^{-1}$  it is useful, but  $k(\nu)$  is extremely small and is not known to better than 10%.

The *k* spectrum of liquid  $\text{CH}_3\text{OD}$  in Figure 6.5 was Kramers-Krönig transformed, with  $n(8000\text{ cm}^{-1}) = 1.323$ , and with Honijk *et al.*'s *k* spectrum<sup>17</sup> of  $\text{CH}_3\text{OH}$  below  $350\text{ cm}^{-1}$  included in the transform. The resulting *n* spectrum is shown in Figure 6.6. Table 6.2 contains values of  $k(\nu)$  and  $n(\nu)$  at the wavenumbers of the peaks in the *k* spectrum and of the associated minima and maxima in the *n* spectrum, and in some regions of weak and flat absorption. The numerical values of  $k(\nu)$  and  $n(\nu)$  throughout the spectrum are given in the Compact Table format<sup>18</sup> in Tables 6.3 and 6.4.

**Table 6.2** Wavenumbers and refractive indices at the peaks in the  $k$  spectrum, the associated maxima and minima in the  $n$  spectrum, and regions of flat weak absorption.

Spectral feature	$\tilde{\nu}$ / $\text{cm}^{-1}$	$k(\tilde{\nu})$	$n(\tilde{\nu})$
flat	7000	$<2 \times 10^{-6}$	1.321
flat	6000	0.000019	1.320
flat	5000	0.000095	1.318
peak	4404	0.001078	1.316
peak	3974	0.000760	1.314
peak	3860	0.000562	1.313
$n$ minimum	2995	0.02894	1.267
$\nu(\text{CH})$ peak(shoulder)	2981	0.03979	1.273
$n$ maximum	2971	0.04219	1.276
$n$ minimum	2963	0.04693	1.276
$\nu(\text{CH})$ peak	2946	0.07120	1.298
$n$ maximum	2936	0.05098	1.318
$n$ minimum	2922	0.04372	1.309
peak	2914	0.04840	1.316
$n$ maximum	2901	0.03527	1.326
$n$ minimum	2843	0.03679	1.288
$\nu(\text{CH})$ peak	2836	0.06133	1.316
$n$ maximum	2828	0.03312	1.338
$n$ minimum	2576	0.06080	1.238
$\nu(\text{OD})$ peak	2493	0.1437	1.307
$n$ maximum	2390	0.06970	1.398
peak	2178	0.01329	1.354
peak	2044	0.00641	1.342
peak	1891	0.00669	1.335
flat	2000	0.004065	1.339
$n$ minimum	1481	0.01683	1.304
$\delta(\text{CH}_3)$ peak	1467	0.02559	1.313
$n$ maximum	1457	0.02198	1.319
$n$ minimum	1451	0.02269	1.317
$\delta(\text{CH}_3)$ peak	1446	0.02736	1.324
$n$ maximum	1442	0.01938	1.331
$n$ minimum	1241	0.01527	1.286
$\gamma(\text{CH}_3)$ peak	1232	0.02161	1.293
$n$ maximum	1222	0.01500	1.299
$n$ minimum	1044.2	0.2875 <sup>a</sup>	0.9622
$\nu(\text{CO})$ peak	1030.7	0.6140	1.334 <sup>b</sup>
$n$ maximum	1020.1	0.3326 <sup>c</sup>	1.635
$n$ minimum	954	0.06420	1.386
$\delta(\text{COD})$ peak	939	0.07090	1.394
$n$ maximum	920	0.05307	1.408
$n$ minimum	579	0.05320	1.294
$\tau(\text{HCO})$ peak	485	0.1151	1.347
$n$ maximum	394	0.0650	1.398
low wavenumber	350	0.0370	1.386

a) This value is very sensitive to wavenumber. It is 0.321 at  $1043.2 \text{ cm}^{-1}$ , where  $n = 0.9628$ .

b) This value is very sensitive to wavenumber. It is 1.290 at  $1031.7 \text{ cm}^{-1}$ , where  $k = 0.609$ .

c) This value is very sensitive to wavenumber. It is 0.304 at  $1019.1 \text{ cm}^{-1}$ , where  $n = 1.634$ .

**Table 6.3** Values of  $k(\tilde{\nu})$ , the absorption index or imaginary refractive index, between 8000 and 350  $\text{cm}^{-1}$  for methanol-*d* at 25°C.a,b

$\text{cm}^{-1}$	X	E	Y	0	1	2	3	4	5	6	7	8	9	10	11	12	13	14	15	16
8000.25	7	-7	0	0	0	0	0	0	0	0	0	0	0	0	0	0	0	0	17	
6133.49	4	-7	22	28	31	41	58	80	105	135	168	211	271	367	499	624	707	820	895	
5871.22	4	-7	865	818	795	769	748	728	680	639	555	473	418	415	412	382	351	354	386	
5608.95	4	-7	385	383	408	417	432	470	524	594	652	688	721	744	759	752	725	716	671	
5346.68	4	-7	620	584	557	533	519	530	542	508	485	474	478	494	523	566	624	669	688	
5084.40	4	-7	715	754	804	849	891	932	971	982	979	973	949	926	911	901	889	852	812	
4822.13	4	-7	780	750	723	700	683	667	649	632	621	620	627	632	648	670	708	756	827	
4559.86	4	-6	93	107	127	156	199	262	360	506	685	915	1076	1039						
4382.44	3	-7	9869	9026	7988	6952	5970	5080	4370	3867	3570	3449	3500	3747	4170	4537	4544	4150	3729	
4251.31	3	-7	3680	3661	3071	2735	2685	2766	2816	2784	2741	2737	2741	2675	2584	2577	2668	2796	2897	
4120.17	3	-7	2932	2938	2952	3037	3189	3349	3568	3829	4000	4049	4140	4422	4880	5318	5509	5619	5964	
3989.03	3	-7	6585	7276	7599	7068	6026	5447	5258	5006	4408	3703	3163	2802	2603	2590	2830	3482	4778	
3861.76	2	-7	5474	5532	4754	3781	2996	2457	2101	1860	1684	1564	1473	1418	1372	1344	1322	1310	1299	
3796.19	2	-7	1302	1299	1311	1318	1329	1336	1346	1343	1348	1339	1337	1328	1322	1311	1307	1287	1277	
3726.76	3	-7	1231	1183	1138	1097	1067	1052	1049	1054	1077	1113	1145	1175	1211	1257	1312	1374	1443	
3587.91	4	-7	1596	1845	2206	2697	3253	3807	4384	4994	5487	5873	6160	6433	6747	7025	7423	7655	7732	
3325.64	4	-6	761	729	684	634	586	545	516	506	517	550	611	712	873	1126	1546	2212	3274	
3076.87	1	-6	3441	3616	3800	3993	4199	4415	4640	4879	5130	5392	5666	5992	6220	6491	6782	7098	7423	
3045.05	0	-5	760	780	796	816	832	845	860	882	910	929	941	963	982	1000	1028	1041	1066	
3028.66	0	-5	1094	1106	1139	1163	1180	1224	1257	1273	1305	1334	1362	1400	1440	1484	1515	1551	1601	
3011.30	1	-5	1696	1788	1898	2039	2137	2291	2443	2616	2814	2987	3192	3358	3535	3691	3802	3927	3984	
2978.52	1	-5	4020	4068	4120	4168	4219	4299	4409	4528	4693	4864	5101	5373	5682	6035	6438	6816	7059	
2945.73	1	-5	7119	6920	6525	6034	5525	5098	4726	4448	4269	4191	4179	4253	4372	4508	4650	4771	4839	
2912.95	1	-5	4809	4687	4481	4236	3983	3743	3527	3329	3135	2959	2794	2632	2480	2342	2207	2091	1992	
2880.17	1	-5	1906	1828	1747	1685	1632	1582	1554	1537	1527	1526	1527	1540	1575	1611	1655	1751	1932	
2847.38	1	-5	2198	2650	3295	4134	5075	5880	6133	5654	4788	3957	3312	2815	2411	2060	1772	1525	1334	
2814.60	1	-5	1173	1045	939	856	786	723	668	626	584	551	522	497	473	450	427	398	376	
2782.78	0	-6	3668	3543	3461	3359	3267	3199	3085	2998	2947	2866	2798	2736	2659	2594	2521	2491	2461	
2766.39	0	-6	2392	2379	2334	2261	2260	2192	2158	2147	2085	2099	2050	1997	1959	1908	1846	1846	1846	
2749.99	0	-6	1792	1727	1738	1729	1659	1625	1656	1631	1611	1607	1577	1587	1578	1533	1549	1561	1539	
2733.60	0	-6	1551	1529	1529	1579	1546	1525	1540	1538	1579	1585	1555	1575	1575	1562	1625	1623	1709	
2717.21	0	-6	1892	1843	1823	1896	1899	1954	2018	2047	2116	2180	2230	2294	2344	2431	2526	2583	2636	
2699.85	1	-6	2762	2924	3122	3252	3420	3587	3717	3940	4122	4357	4579	4807	5123	5354	5591	5925	6235	
2667.07	1	-5	655	689	723	764	805	844	890	937	990	1039	1098	1158	1223	1292	1364	1441	1522	
2634.29	1	-5	1603	1693	1789	1890	1995	2103	2216	2333	2456	2582	2711	2846	2982	3127	3269	3421	3569	
2601.50	1	-5	3729	3890	4056	4219	4387	4564	4738	4916	5095	5287	5476	5671	5879	6080	6292	6508	6719	
2562.93	3	-4	758	843	927	1016	1109	1204	1294	1367	1416	1437	1425	1384	1327	1275	1244	1228	1197	
2431.80	3	-4	1139	1062	977	890	806	726	652	583	521	465	415	372	333	299	269	243	218	
2300.66	3	-5	1967	1798	1670	1586	1540	1516	1474	1386	1283	1206	1162	1159	1186	1228	1275	1312	1328	
2169.53	3	-5	1303	1212	1055	876	718	603	521	467	430	402	396	405	429	467	521	587	639	
2038.39	3	-6	6163	5371	4677	4295	4122	4066	4099	4211	4380	4576	4758	4922	5097	5319	5585	5877	6168	
1907.26	3	-6	6424	6612	6692	6639	6413	5974	5322	4542	3746	3028	2434	1968	1616	1353	1163	1025	932	
1776.12	3	-6	874	853	857	862	866	870	874	878	883	887	891	895	900	912	938	978	1032	
1648.84	2	-6	1068	1104	1146	1192	1246	1304	1368	1438	1514	1597	1686	1782	1889	2006	2123	2241	2367	
1583.27	2	-6	2501	2641	2782	2929	3105	3249	3422	3601	3763	3966	4116	4281	4478	4662	4872	5135	5410	
1517.70	2	-5	575	616	662	712	779	868	974	1121	1301	1538	1849	2180	2439	2555	2516	2346	2163	
1454.07	1	-5	2142	2194	2373	2612	2736	2548	2141	1767	1498	1316	1181	1074	990	921	867	825	787	
1421.28	1	-6	7562	7266	7004	6767	6610	6403	6211	6076	5961	5826	5743	5610	5470	5340	5230	5098	4980	
1388.50	1	-6	4959	4845	4805	4696	4641	4594	4504	4466	4425	4421	4308	4236	4148	4084	4021	3987	3944	
1355.71	1	-6	3926	3854	3802	3799	3723	3715	3617	3525	3518	3439	3378	3362	3335	3303	3233	3223	3199	
1322.93	1	-6	3197	3260	3183	3177	3172	3107	3148	3167	3159	3139	3196	3216	3205	3212	3254	3291	3320	
1291.11	0	-6	3318	3344	3385	3430	3448	3445	3477	3517	3564	3600	3628	3684	3740	3782	3825	3880	3939	
1274.72	0	-6	4024	4108	4183	4263	4322	4455	4552	4576	4715	4844	4946	5107	5260	5383	5558	5759	5917	
1257.36	1	-5	636	684	743	815	900	995	1117	1262	1430	1623	1813	1989	2111	2161	2129	2032	1893	
1224.58	1	-5	1734	1576	1426	1302	1198	1107	1034	977	927	883	848	819	795	773	760	748	743	
1191.79	1	-5	736	731	733	734	736	743	752	764	779	801	824	854	888	921	966	1004	1043	
1159.01	1	-5	1068	1086	1090	1099	1099	1111	1120	1125	1139	1164	1173	1201	1222	1248	1276	1298	1329	
1126.23	1	-5	1357	1399	1433	1469	1513	1563	1613	1659	1711	1768	1818	1880	1941	2012	2076	2148	2224	
1093.44	1	-5	2308	2397	2490	2599	2716	2844	2992	3150	3332	3538	3772	4033	4334	4679	5078	5552	6091	
1061.62	0	-4	641	675	712	753	800	853	910	974	1050	1136	1234	1349	1483	1641	1825	2038	2285	
1045.23	0	-4	2564	2875	3209	3556	3924	4274	4585	4884	5153	5408	5628	5877	6048	6034	6092	6140	6105	
1028.84	0	-4	6038	5875	5650	5376	5053	4691	4328	3949	3611	3326	3044	2798	2570	2374	2198	2032	1879	
1012.45	0	-4	1737	1603	1479	1363	1256	1160	1072	994	924	861	806	756	713	674	640	609		
994.13	2	-5	5206	4684	4389	4316	4401	4612	4908	5247	5599	5947	6267	6564	6820	7005	7089	7029	6804	
928.56	2	-5	6417	5941	5435	4941	4491	4080	3717	3413	3148	2927	2735	2567	2422	2287	2165	2061	1987	
862.99	2	-5	1895	1815	1754	1693	1642	1588	1535	1489	1444	1394	1347	1295	1247	1199	1159	1112	1072	
797.42	2	-5	1038	1000	960	933	908	885	858	853	832	824	801	804	804	800				

**Table 6.4** Values of  $n(\tilde{\nu})$ , the real refractive index, between 8000 and 350  $\text{cm}^{-1}$  for methanol-*d* at 25°C.<sup>a,b</sup>

$\text{cm}^{-1}$	$X_F$	0	1	2	3	4	5	6	7	8	9	10	11	12	13	14	15	16
8000.25	7	13213	13213	13212	13212	13211	13210	13209	13209	13208	13207	13206	13205	13204	13203	13201	13200	
6133.49	4	13200	13200	13199	13199	13199	13199	13198	13198	13198	13198	13198	13197	13197	13197	13197	13197	13197
5871.22	4	13197	13196	13196	13196	13196	13196	13196	13196	13195	13195	13195	13195	13194	13194	13194	13194	13193
5608.95	4	13193	13193	13192	13192	13192	13192	13191	13191	13191	13191	13190	13190	13190	13190	13189	13189	13189
5346.68	4	13189	13188	13188	13188	13187	13187	13187	13186	13186	13186	13185	13185	13185	13184	13184	13184	13183
5084.40	4	13183	13182	13182	13182	13181	13181	13181	13180	13180	13180	13179	13179	13178	13178	13178	13177	13177
4822.13	4	13176	13176	13175	13175	13174	13174	13173	13172	13172	13171	13171	13170	13169	13169	13168	13167	13166
4559.86	4	13166	13165	13164	13163	13161	13160	13159	13158	13158	13158	13160	13162					
4382.44	3	13163	13164	13164	13164	13164	13163	13163	13162	13161	13160	13159	13159	13158	13158	13158	13158	13158
4251.31	3	13157	13157	13157	13156	13155	13155	13154	13154	13153	13153	13152	13152	13151	13150	13150	13149	13149
4120.17	3	13148	13148	13147	13147	13146	13145	13145	13144	13144	13143	13143	13142	13142	13141	13141	13141	13140
3989.03	3	13140	13140	13140	13141	13141	13140	13140	13140	13139	13139	13138	13137	13136	13134	13133	13132	13132
3861.76	2	13132	13133	13134	13134	13133	13133	13132	13131	13131	13130	13130	13129	13129	13128	13128	13127	13127
3796.19	2	13126	13126	13125	13125	13124	13124	13123	13123	13123	13122	13122	13121	13121	13120	13120	13119	13119
3726.76	3	13118	13117	13116	13115	13114	13113	13112	13111	13110	13109	13108	13106	13105	13104	13103	13102	13100
3587.91	4	13098	13095	13092	13090	13087	13084	13081	13079	13076	13073	13070	13067	13064	13062	13057	13053	13049
3325.64	4	13045	13041	13036	13031	13025	13018	13010	13002	12993	12983	12972	12959	12945	12928	12909	12887	12861
3076.87	1	12858	12855	12851	12848	12844	12840	12837	12833	12829	12826	12822	12818	12815	12811	12807	12803	12799
3045.05	0	12796	12795	12793	12791	12789	12787	12784	12782	12780	12778	12776	12773	12771	12769	12766	12764	12761
3028.66	0	12759	12756	12753	12751	12747	12744	12743	12740	12737	12734	12731	12727	12724	12721	12719	12715	12711
3011.30	1	12704	12700	12693	12687	12682	12676	12673	12668	12669	12669	12675	12681	12689	12700	12712	12721	12738
2978.52	1	12746	12753	12757	12762	12763	12761	12764	12763	12761	12762	12762	12771	12777	12795	12823	12867	12928
2945.73	1	12998	13067	13125	13158	13175	13179	13172	13158	13141	13124	13107	13096	13093	13095	13106	13123	13149
2912.95	1	13179	13207	13230	13247	13257	13262	13265	13264	13262	13259	13255	13251	13244	13236	13228	13217	13208
2880.17	1	13198	13187	13177	13166	13154	13141	13129	13116	13104	13091	13077	13063	13048	13030	13011	12987	12958
2847.38	1	12928	12898	12880	12882	12925	13019	13154	13279	13351	13377	13379	13372	13363	13350	13336	13320	13303
2814.60	1	13286	13271	13256	13243	13230	13218	13207	13196	13186	13177	13168	13160	13152	13145	13138	13131	13124
2782.78	0	13120	13117	13113	13110	13106	13103	13100	13096	13093	13090	13087	13084	13080	13077	13074	13071	13068
2766.39	0	13065	13061	13059	13055	13052	13050	13046	13044	13041	13038	13035	13032	13029	13027	13024	13021	13018
2749.99	0	13016	13012	13009	13007	13004	13000	12997	12995	12992	12989	12986	12983	12980	12977	12974	12971	12968
2733.60	0	12965	12963	12959	12956	12954	12950	12947	12944	12941	12939	12935	12932	12929	12925	12922	12919	12915
2717.21	0	12912	12910	12906	12903	12900	12897	12894	12890	12887	12884	12881	12877	12874	12870	12867	12864	12861
2699.85	1	12855	12848	12841	12835	12828	12821	12814	12807	12800	12792	12785	12778	12770	12762	12755	12747	12738
2667.07	1	12730	12722	12714	12705	12696	12688	12679	12670	12660	12651	12641	12632	12622	12612	12602	12593	12582
2634.29	1	12573	12563	12553	12543	12534	12524	12515	12506	12497	12489	12480	12472	12464	12457	12450	12442	12436
2601.50	1	12429	12423	12418	12412	12407	12403	12399	12395	12391	12387	12385	12382	12381	12378	12379	12379	12380
2562.93	3	12393	12415	12443	12479	12528	12597	12688	12802	12934	13072	13208	13329	13420	13483	13535	13604	13693
2431.80	3	13782	13854	13908	13944	13966	13977	13978	13971	13958	13941	13921	13898	13875	13851	13827	13803	13779
2300.66	3	13754	13729	13704	13680	13660	13644	13634	13625	13611	13595	13579	13563	13550	13541	13536	13534	13537
2169.53	3	13542	13549	13552	13547	13536	13523	13510	13496	13483	13470	13458	13446	13435	13426	13419	13415	13417
2038.39	3	13422	13422	13415	13407	13400	13392	13385	13379	13373	13368	13364	13360	13357	13353	13350	13348	13347
1907.26	3	13348	13349	13351	13354	13358	13361	13363	13363	13360	13355	13349	13343	13336	13329	13323	13316	13310
1776.12	3	13304	13298	13293	13288	13283	13278	13273	13268	13263	13259	13254	13249	13244	13239	13233	13228	13222
1648.84	2	13219	13217	13214	13211	13208	13205	13202	13199	13196	13193	13190	13186	13183	13180	13177	13174	13171
1583.27	2	13168	13165	13162	13158	13155	13152	13149	13145	13142	13139	13136	13132	13128	13123	13119	13114	13109
1517.70	2	13103	13097	13091	13083	13075	13067	13058	13049	13041	13036	13038	13035	13032	13028	13023	13019	13014
1454.07	1	13181	13175	13176	13174	13174	13174	13174	13174	13174	13174	13174	13174	13174	13174	13174	13174	13174
1421.28	1	13233	13228	13223	13218	13214	13211	13207	13203	13199	13196	13193	13190	13187	13184	13181	13177	13174
1388.50	1	13171	13168	13166	13163	13160	13157	13154	13152	13149	13146	13144	13142	13139	13136	13133	13131	13128
1355.71	1	13125	13123	13120	13117	13114	13112	13110	13106	13103	13101	13097	13094	13090	13088	13084	13081	13078
1322.93	1	13074	13071	13068	13065	13061	13058	13054	13050	13047	13043	13039	13035	13032	13027	13023	13019	13015
1291.11	0	13013	13010	13008	13006	13004	13002	12999	12997	12994	12992	12989	12987	12984	12982	12979	12977	12974
1274.72	0	12971	12968	12966	12963	12960	12957	12955	12951	12948	12945	12942	12938	12935	12932	12928	12925	12922
1257.36	1	12915	12907	12899	12892	12884	12877	12871	12866	12862	12855	12852	12846	12840	12834	12827	12821	12814
1224.58	1	12988	12991	12990	12986	12979	12972	12965	12957	12949	12941	12933	12924	12917	12907	12899	12891	12882
1191.79	1	12874	12865	12857	12848	12839	12831	12821	12812	12802	12793	12784	12775	12765	12757	12748	12741	12734
1159.01	1	12728	12722	12715	12706	12697	12688	12678	12667	12656	12644	12632	12620	12607	12594	12581	12567	12553
1126.23	1	12538	12523	12506	12491	12473	12456	12438	12419	12400	12380	12359	12336	12313	12289	12263	12236	12208
1093.44	1	12177	12146	12111	12074	12035	11993	11948	11900	11848	11791	11731	11665	11594	11516	11430	11336	11232
1061.62	0	11174	11115	11052	10984	10911	10836	10755	10668	10575	10477	10373	10264	10152	10037	9925	9820	9728
1045.23	0	09659	09622	09628	09677	09778	09956	10164	10403	10674	10972	11292	11643	12040	12568	13294	13343	13775
1028.84	0	14227	14679	15084	15449	15767	16011	16189	16304	16330	16349	16344	16312	16269	16211	16160	16105	16047
1012.45	0	15986	15923	15857	15787	15714	15640	15565	15489	15414	15341	15269	1					

The accuracy of the refractive index spectra obtained in this work is expected to be the same as for CH<sub>3</sub>OH<sup>1</sup>, except that better spectra were obtained above 4500 cm<sup>-1</sup> for CH<sub>3</sub>OD. Thus, the accuracy of  $k(\tilde{\nu})$  is estimated to be  $\pm 3\%$  below 5900 cm<sup>-1</sup> and  $\pm 10\%$  above 5900 cm<sup>-1</sup> and the accuracy of  $n(\tilde{\nu})$  to be  $\pm 0.5\%$ .

The intensity spectrum of greatest familiarity to analytical chemists is the molar (decadic) absorption coefficient spectrum,  $E_m(\tilde{\nu})$ . This may be calculated<sup>7</sup> from the  $k$  spectrum (Table 6.3 and Figure 6.5) and the molar concentration  $C = 24.45 \text{ mol L}^{-1}$  at 25°C through the equation  $E_m(\tilde{\nu}) = 4\pi\tilde{\nu}k(\tilde{\nu})/(2.303C)$ . It is shown in Figure 6.7 in the units 10<sup>5</sup> cm<sup>2</sup> mol<sup>-1</sup>, which are the same as 10<sup>2</sup> L mol<sup>-1</sup> cm<sup>-1</sup>.

The intensity spectrum that is the most directly related to theory, albeit through the approximation of the Lorentz local field, is the imaginary molar polarizability spectrum<sup>7</sup>,  $\alpha_m''(\tilde{\nu})$ . This was calculated<sup>7</sup> from the refractive index spectra in Figures 6.5 and 6.6 and the molar volume at 25°C, 40.90 mL mol<sup>-1</sup>. It is shown in Figure 6.8 in the unit cm<sup>3</sup> mol<sup>-1</sup>.

The density of CH<sub>3</sub>OD is 0.8127 g mL<sup>-1</sup> at 20°C<sup>19</sup>. That of CH<sub>3</sub>OH is 0.79134 g mL<sup>-1</sup> at 20 °C and 0.78660 g mL<sup>-1</sup> at 25 °C<sup>20</sup>. The density of CH<sub>3</sub>OD was taken to be 0.8080 g mL<sup>-1</sup> at 25°C on the assumption that the temperature dependence is the same for CH<sub>3</sub>OH and CH<sub>3</sub>OD. The molar concentration and volume at 25°C are, thus, 24.45 mol L<sup>-1</sup> and 40.90 cm<sup>3</sup> mol<sup>-1</sup>.

The peak wavenumbers of the major bands in different representations of the absorption spectrum of methanol-*d* are listed in Table 6.5.

#### Footnotes to Tables 6.3 and 6.4:

- a) The column headed cm<sup>-1</sup> contains the wavenumber of the first  $k(\tilde{\nu})$  value in the row. The columns headed *XE* and *YE* contain the X-Exponent and the Y-Exponent, respectively, for the row. The columns headed 0,1,2,...16, contain the ordinate values, and the headings give the indices of the ordinate values in the row. In a row which starts with  $\tilde{\nu}(0)$ , the wavenumber corresponding to the ordinate indexed *J* is  $\tilde{\nu}(J) = \tilde{\nu}(0) - \frac{15798.002}{16384} \cdot J \cdot 2^{XE}$ . In Table 6.3, the  $k(\tilde{\nu})$  values in that row are the ordinate value shown times 10<sup>YE</sup>. In Table 6.4, the  $n(\tilde{\nu})$  values are given directly with the decimal point implicitly after the first digit. Thus the entry indexed 16 in the third row of Tables 6.3 and 6.4 shows that at  $\tilde{\nu} = 5871.22 - \frac{15798.002}{16384} \cdot 16 \cdot 2^4 = 5624.38 \text{ cm}^{-1}$  the ordinate values are  $k = 386 \times 10^{-7} = 3.86 \times 10^{-5}$  and  $n = 1.3193$ .
- b) The 4-point spline interpolation program TRECOVER<sup>18</sup>, interpolated the  $k(\tilde{\nu})$  values in Table 6.3 to the original wavenumber spacing, 0.96423 cm<sup>-1</sup>, and yielded the original  $k(\tilde{\nu})$  values accurate to 6% above 5900 cm<sup>-1</sup>, 2% between 5900 and 3850 cm<sup>-1</sup>, and 1% below 3850 cm<sup>-1</sup> except for 2% at about 10 points between 1350 and 1310 cm<sup>-1</sup>. The original  $n(\tilde{\nu})$  values were similarly recovered accurate to 0.02%, except for 0.04% at a few points below 500 cm<sup>-1</sup>.

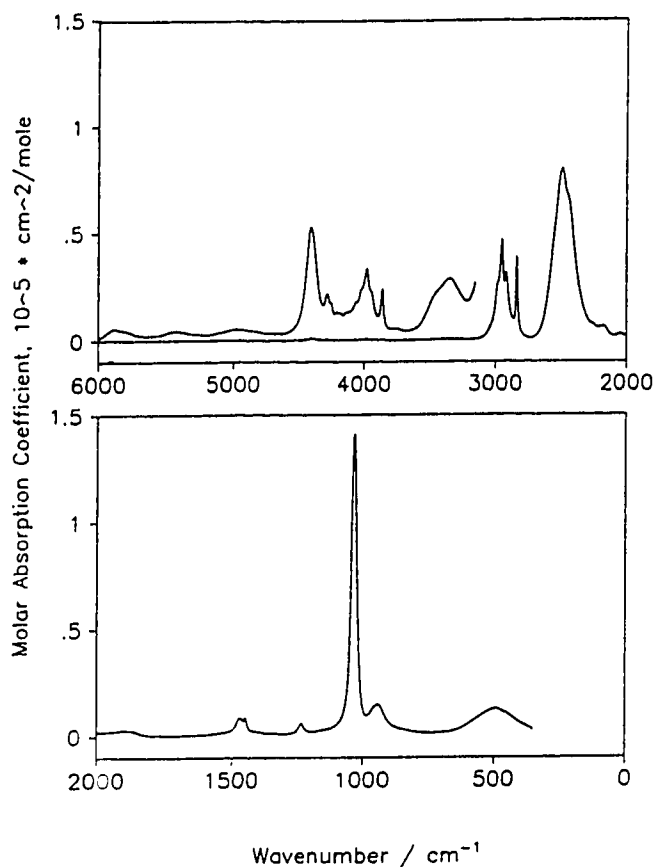


**Figure 6.7** The molar absorption coefficient spectrum of methanol-*d* at 25°C calculated from the absorption index spectrum in Figure 6.5. The units of  $E_m(\tilde{\nu})$  are  $10^5 \text{ cm}^2 \text{ mol}^{-1}$ , i.e.  $10^2 \text{ L cm}^{-1} \text{ mol}^{-1}$ . In the top box, the scale shown applies to the complete spectrum (lower curve) and the scale labels must be divided by 50 for the insert (upper curve) above  $3150 \text{ cm}^{-1}$ .

**Table 6.5** The peak positions of major bands in different spectra of methanol-*d*,  $\text{CH}_3\text{OD}$ .

Band	Type of Spectrum						
	pATR	$k$	$E_m$	$\epsilon''$	$V_m \tilde{\nu} \epsilon''$	$\alpha''_m$	$\tilde{\nu} \alpha''_m$
$\nu(\text{C-H})$	2945.3	2946.2	2946.3	2945.9	2946.0	2946.5	2946.5
$\nu(\text{C-H})$	2835.6	2836.1	2836.1	2836.0	2836.0	2836.3	2836.3
$\nu(\text{O-D})$	2480 <sup>a</sup>	2493	2494	2489	2490	2496	2497
$\delta(\text{CH}_3)$	1466.3	1466.7	1466.9	1466.6	1466.7	1466.9	1467.0
$\delta(\text{CH}_3)$	1446.3	1446.5	1446.5	1446.4	1446.4	1446.5	1446.6
$\gamma(\text{CH}_3)$	1231.8	1232.1	1232.2	1232.0	1232.1	1232.2	1232.3
$\nu(\text{C-O})$	1022.6	1031.1	1031.2	1028.1	1028.2	1034.4	1034.4
$\delta(\text{COD})$	937.5	939.6	940.3	939.0	939.8	940.0	940.8
$\tau(\text{HCOD})$	475	485	494	482	492	491	496

a) The high-wavenumber component of the doublet at  $2480/2442 \text{ cm}^{-1}$  (Figure 6.1).

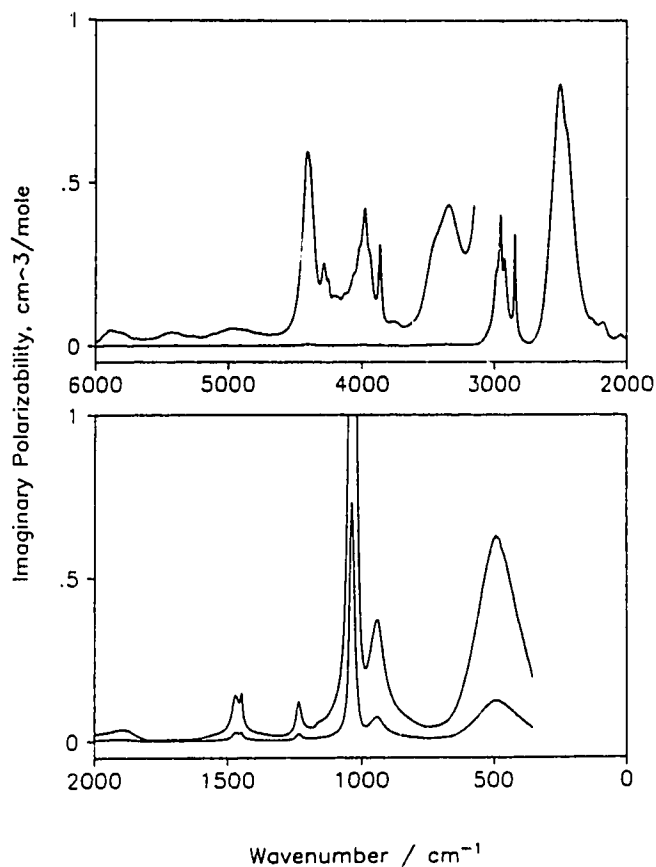


**Figure 6.8** The imaginary molar polarizability spectrum of methanol-*d* at 25°C, calculated from the refractive index spectra in Figures 6.5 and 6.6 under the assumption of the Lorentz local field. The units are  $\text{cm}^3 \text{mol}^{-1}$ . In the top box, the scale shown applies to the complete spectrum and the scale labels must be divided by 100 for the insert above  $3150 \text{ cm}^{-1}$ . In the bottom box, the scale shown applies to the upper curve and the scale labels must be multiplied by 5 for the lower curve.

## 6.4 Discussion

It was noted<sup>1</sup> that the separation of the area under the absorption spectrum into intensities of different vibrations could not be carried out with confidence. Different approximations, all of which are reasonable, led to differences in  $\mu_j^2$  which ranged from 6% to 22% even though the optical constants are known to 3% or better. This section describes the improvement in the accuracy of this separation of the area into integrated intensities of different vibrations that is obtained when the spectra of both  $\text{CH}_3\text{OH}^1$  and



CH<sub>3</sub>OD are available. In particular, the contribution from the O–H, O–D and C–H stretching vibrations can be determined with confidence, as can those from the CH<sub>3</sub> deformation and C–O stretching vibrations. The magnitudes of the transition moments are calculated and values of the dipole moment derivatives with respect to both the normal coordinates and the valence internal coordinates are improved, including some that could not be obtained from the spectrum of CH<sub>3</sub>OH alone.

#### 6.4.1 *The Integrated Intensities of the C–H, O–H and O–D Stretching Bands*

The C–H, O–H and O–D stretching regions of the  $\nabla\alpha''_m$  spectra of CH<sub>3</sub>OH and CH<sub>3</sub>OD are shown as curves H and D, respectively, in the top box of Figure 6.9. For CH<sub>3</sub>OD the C–H and O–D stretching bands are completely separated. The areas were measured above zero ordinate. That due to the C–H stretching vibrations is  $C_j = 1.314$  km mol<sup>-1</sup>, taken between 3215.7 and 2732.6 cm<sup>-1</sup>, and that due to the O–D stretch is  $C_j = 4.01$  km mol<sup>-1</sup>, taken between 2732.6 and 1730.8 cm<sup>-1</sup>. The integration limits 2732.6 cm<sup>-1</sup> and 1730.8 cm<sup>-1</sup> are minima in the spectrum (Figures 6.5 and 6.8, also Figure 6.4 with the impurity doublet at 1730/1715 cm<sup>-1</sup> omitted). The OD area was measured below the dashed lines shown in the middle box of Figure 6.9 between 2274.6 and 2237.0 cm<sup>-1</sup>, 2219.7 and 2119.4 cm<sup>-1</sup>, and 2093.4 and 1780.9 cm<sup>-1</sup>. The O–D stretching band is, thus, seen to have a tail which extends from ~ 2250 cm<sup>-1</sup> to 1730 cm<sup>-1</sup>.

The areas of the weak features omitted from the O–D stretching band are 0.002 km mol<sup>-1</sup> for  $2\gamma(\text{CH}_3)$ , the overtone of the CH<sub>3</sub> rock, between 2274.6 and 2237.0 cm<sup>-1</sup>, 0.027 km mol<sup>-1</sup> for  $\nu(\text{C–O}) + \gamma(\text{CH}_3)$ , the C–O stretch and CH<sub>3</sub> rock combination, between 2219.7 and 2119.4 cm<sup>-1</sup>, and 0.066 km mol<sup>-1</sup> for the overlapping bands  $2\nu(\text{C–O})$  and  $2\delta(\text{C–O–D})$ , the overtones of the C–O stretch and the C–O–D in-plane bend, between 2093.4 and 1780.9 cm<sup>-1</sup>. In each case it is assumed that this intensity is intrinsic to the overtone or combination transition. This assumption may not be correct, but the total intensity assigned to these transitions is only 0.095 km mol<sup>-1</sup>, i.e. 2.4% of the O–D stretching intensity. These areas are summarized in Table 6.6.

For CH<sub>3</sub>OH, Figure 6.9 (bottom) and curve H in Figure 6.9 (top), the assumptions are made that the integrated intensity of the C–H stretching vibrations is the same in CH<sub>3</sub>OH as in CH<sub>3</sub>OD, and that all of the  $C_j = 9.00$  km mol<sup>-1</sup> intensity for CH<sub>3</sub>OH between 3813.5 and 2324.8 cm<sup>-1</sup> is due to the O–H and C–H stretching vibrations. The value  $C_j = 7.69$  km mol<sup>-1</sup> is obtained for the O–H stretching vibration. The integration limits are, again, at absorption minima [Figure 5.2 and Figure 6.9 (bottom)], and the integration omits the weak peaks near 2500 cm<sup>-1</sup>, as is shown by the dashed line from

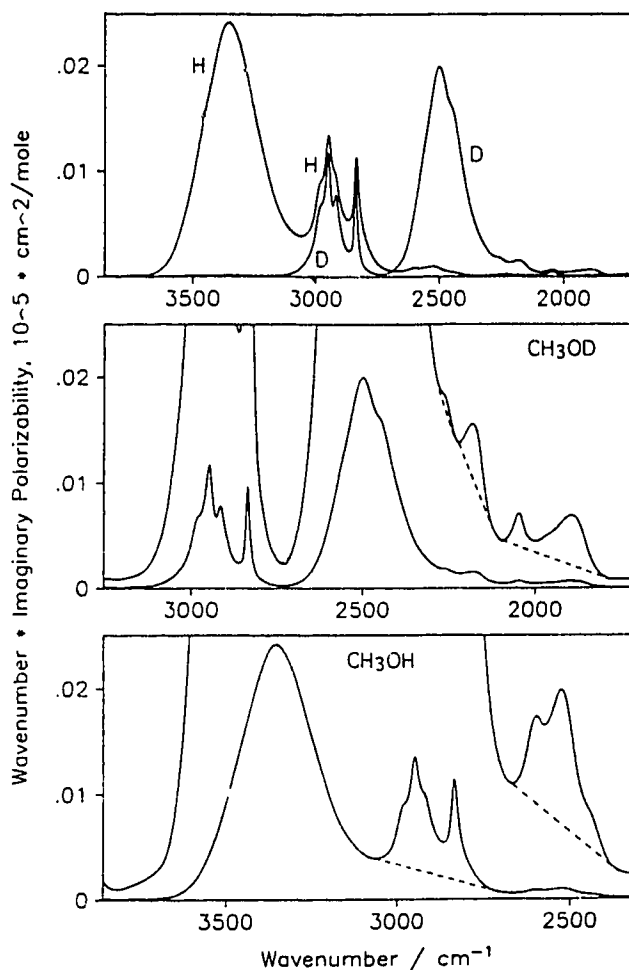


**Figure 6.9** The  $\tilde{\nu}\alpha_m''$  spectra of  $\text{CH}_3\text{OD}$  and  $\text{CH}_3\text{OH}$  in the regions of the O-H, C-H and O-D stretching vibrations. Top box:  $\text{CH}_3\text{OD}$  (curve D) and  $\text{CH}_3\text{OH}$  (curve H); Middle box:  $\text{CH}_3\text{OD}$ ; Bottom box:  $\text{CH}_3\text{OH}$ . The dashed lines separate integration regions.

2660.3 to 2369.1  $\text{cm}^{-1}$  in the upper, expanded, curve in Figure 6.9 (bottom). The area above this dashed line is 0.088  $\text{km mol}^{-1}$  and is tentatively assigned to the sum of the intensities intrinsic to the combination transitions,  $\delta(\text{CH}_3) + \gamma(\text{CH}_3)$ ,  $\delta(\text{C-O-H}) + \gamma(\text{CH}_3)$ , and  $\delta(\text{C-O-H}) + \nu(\text{C-O})$ , i. e.  $\text{CH}_3$  deformation +  $\text{CH}_3$  rock, C-O-H in-plane bend +  $\text{CH}_3$  rock, and C-O-H in-plane bend + C-O stretch. These contributions to the intensity are also summarized in Table 6.6.

**Table 6.6** The integrated intensities of methanol <sup>a</sup>.

Band	$\tilde{\nu}_{\max}$ (cm <sup>-1</sup> )	Integration Range <sup>b</sup> (cm <sup>-1</sup> )	$C_j$ (km mol <sup>-1</sup> )	
			From Original Spectrum	From Difference Spectrum
<b>CH<sub>3</sub>OD <sup>c</sup></b>				
$\nu(\text{C-H})$	2981/2947/2836	3216–2733	1.314	d
$\nu(\text{O-D})$	2497	2733–1731	4.01	d
$2\gamma(\text{CH}_3)$	~ 2260	2275–2237	0.002	d
$\nu(\text{C-O})+\gamma(\text{CH}_3)$	2178	2220–2119	0.027	d
$2\nu(\text{C-O})$	2044	} 2093–1781	0.066	d
$2\delta(\text{C-O-D})$	1892			
$\delta(\text{CH}_3)$	1467/1447	1731–1296	0.198	0.186 *
$\gamma(\text{CH}_3)$	1232	1296–1180	} 0.030	0.058 *
$\gamma(\text{CH}_3)$	~ 1160	1180–1080		0.031 *
$\nu(\text{C-O})$	1034	$\infty - 0$	1.27	d
$\delta(\text{C-O-D})$	941	1011–734	0.086	0.26±0.02 *
$\tau(\text{H-C-O-D})$	496	734–332	0.5±0.1	0.5±0.1
<b>CH<sub>3</sub>OH <sup>c</sup></b>				
$\nu(\text{C-H})$	2980/2945/2833		1.314 <sup>e</sup>	d
$\nu(\text{O-H})$	3354	3813–2325	7.69	d
$\delta(\text{CH}_3)+\gamma(\text{CH}_3)$	2596	} 2660–2369	0.088	d
$\delta(\text{C-O-H})+\gamma(\text{CH}_3)$	2522			
$\delta(\text{C-O-H})+\nu(\text{C-O})$	2439			
$2\gamma(\text{CH}_3)$	2229	2325–2117	0.035	d
$2\nu(\text{C-O})$	2045	2117–1951	0.038	d
$\delta(\text{CH}_3)$	1450		0.198 <sup>e</sup>	0.186 <sup>e</sup>
$\delta(\text{C-O-H})$	1423	1951–1180	0.71	0.73
$\gamma(\text{CH}_3)$	–	} 1180–1080	0.038	0.147 *
$\gamma(\text{CH}_3)$	1116			
$\nu(\text{C-O})$	1035	$\infty - 0$	1.24	d
$\tau(\text{H-C-O-H})$	673	980–365	0.95±0.2	1.02±0.08 *

- a) The  $\tilde{\nu}_{\max}$  are peak wavenumbers in the  $\tilde{\nu}\alpha_m''$  spectrum and the areas  $C_j$  are under the  $\tilde{\nu}\alpha_m''$  spectrum<sup>7</sup>. Where two areas are given, the values marked with an asterisk are preferred.
- b) The integration range is for the area from the original spectrum except when an area is reported from a difference spectrum.
- c) Assignments follow from Ref. 11.  $\gamma$  means rock,  $\delta$  means a valence angle deformation, and  $\tau$  means torsion.
- d) The difference spectrum was not used for this band.
- e) Assumed equal to the corresponding value for CH<sub>3</sub>OD.

This separation of C–H and O–H stretching vibrations is almost identical to that termed Case 3 in Table VI and Figure 12 of Ref. 1. It is illustrated in Figure 6.9 (bottom, lower curve) by the straight dashed line drawn under the C–H bands between

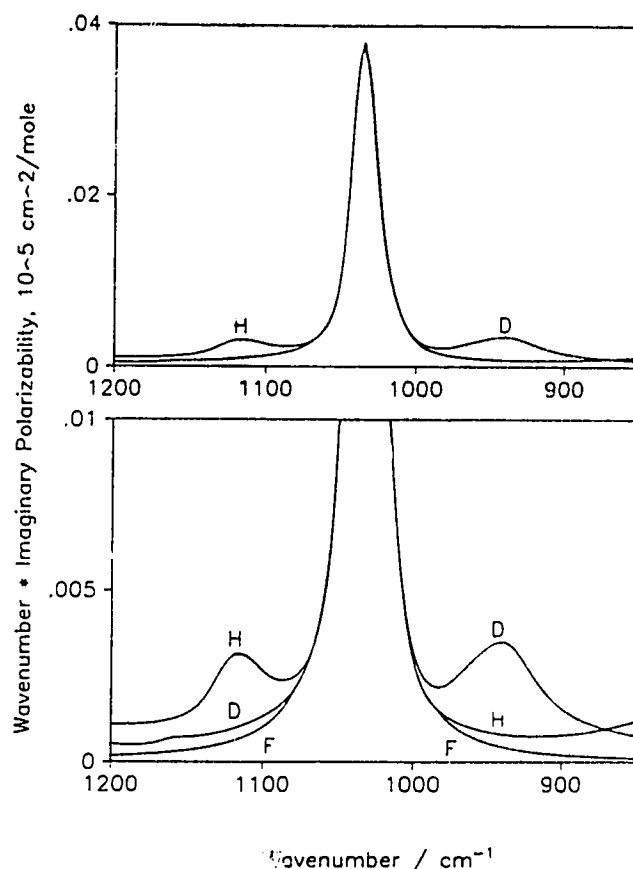


**Figure 6.10** The  $\tilde{\nu}\alpha''_m$  spectra of  $\text{CH}_3\text{OH}$  (curves H) and  $\text{CH}_3\text{OD}$  (curves D) in the region of the C–O stretching band. The lowest curve, labeled F, in the bottom box shows the fitted wings joined to the experimental band at 1078 and 984  $\text{cm}^{-1}$ .

the spectral points at 3058.6 and 2700.8  $\text{cm}^{-1}$ . It assigns all of the intensity below the dashed line to the O–H stretching band, and means that the O–H band has a tail which extends from  $\sim 3050$   $\text{cm}^{-1}$  to 2325  $\text{cm}^{-1}$ . An analogous tail runs from  $\sim 2250$  to 1730  $\text{cm}^{-1}$  in the O–D stretching band of  $\text{CH}_3\text{OD}$  in Figure 6.9 (middle). It is probable that most of the intensity in this tail originates with the O–H (or O–D) stretching vibration, though some of it may arise from intensity intrinsic to overtone or combination transitions.

#### 6.4.2 The Integrated Intensities of the C–O Stretching Band

The C–O stretching band is at 1034 and 1035  $\text{cm}^{-1}$  in the  $\tilde{\nu}\alpha''_m$  spectrum of  $\text{CH}_3\text{OD}$  and  $\text{CH}_3\text{OH}$  respectively. It overlaps the  $\text{CH}_3$  rocking band at 1116  $\text{cm}^{-1}$  in the  $\text{CH}_3\text{OH}$  spectrum (curves H in Figure 6.10) and the C–O–D in-plane bending band at 941  $\text{cm}^{-1}$  in

the CH<sub>3</sub>OD spectrum (curves D in Figure 6.10). The CH<sub>3</sub> rocking band is shifted to above 1200 cm<sup>-1</sup> in CH<sub>3</sub>OD<sup>11</sup>. The C–O stretching bands in the two spectra overlap almost completely.

This fact was used to determine the integrated intensity of the C–O stretching band. The high-wavenumber side of the band from the CH<sub>3</sub>OD spectrum between 1195 and 1065 cm<sup>-1</sup> was merged with the peak and low-wavenumber side of the band from the CH<sub>3</sub>OH spectrum between 1065 and 910 cm<sup>-1</sup> to obtain a CO band with no overlapping peaks (Figure 6.10). The area above zero ordinate was  $C_j = 1.238 \text{ km mol}^{-1}$  between 1192 and 915 cm<sup>-1</sup>. The central part of the CO band is not identical in the spectra of CH<sub>3</sub>OH and CH<sub>3</sub>OD, so we also obtained a CO band with no overlapping bands by merging the high-wavenumber side and peak of the CH<sub>3</sub>OD spectrum between 1195 and 1010 cm<sup>-1</sup> with the low-wavenumber side of the CH<sub>3</sub>OH spectrum between 1010 and 910 cm<sup>-1</sup>. We obtained  $C_j = 1.259 \text{ km mol}^{-1}$  between 1192 and 915 cm<sup>-1</sup>.

In order to ensure that the intensity in the wings of the C–O stretching band was properly considered, we also fitted the C–O stretching band. Bands in the  $\alpha''_m$  spectrum have a well-defined shape in the classical damped harmonic oscillator (CDHO) model (Ref. 1 and citations therein). Thus the CO band with no overlapping peaks in the  $\nabla\alpha''_m$  spectrum (See above and Figure 6.10) was converted to an  $\alpha''_m$  band and was fitted between 1195 and 910 cm<sup>-1</sup> to a CDHO band. The central part of the experimental band was then merged (at 1078 and 984 cm<sup>-1</sup>) with the wings of the fitted CDHO band, and the result was multiplied by  $\nabla$  to generate the  $\nabla\alpha''_m$  band shown as curve F in Figure 10 (bottom). This was done for each of the two non-overlapping CO bands described above, with nearly identical results in the wings. The area under this band between infinity and 0 cm<sup>-1</sup> was 1.243 km mol<sup>-1</sup> when the central part of the CH<sub>3</sub>OH peak was used and 1.269 km mol<sup>-1</sup> when the central part of CH<sub>3</sub>OD was used. The simpler method of the previous paragraph gave essentially the same result. We conclude that the area  $C_j$  for the C–O stretching band is 1.24 km mol<sup>-1</sup> for CH<sub>3</sub>OH and 1.27 km mol<sup>-1</sup> for CH<sub>3</sub>OD, both probably accurate to about 3%. The value for CH<sub>3</sub>OH agrees with the value  $1.30 \pm 0.07 \text{ km mol}^{-1}$  reported previously<sup>1</sup> for CH<sub>3</sub>OH, and is believed to be more reliable.

#### 6.4.3 The Integrated Intensities of Other Bands

The areas of the remaining bands below the 1730.8 cm<sup>-1</sup> minimum for CH<sub>3</sub>OD and the 1950.6 cm<sup>-1</sup> minimum for CH<sub>3</sub>OH were also assessed in two ways. First, the easy

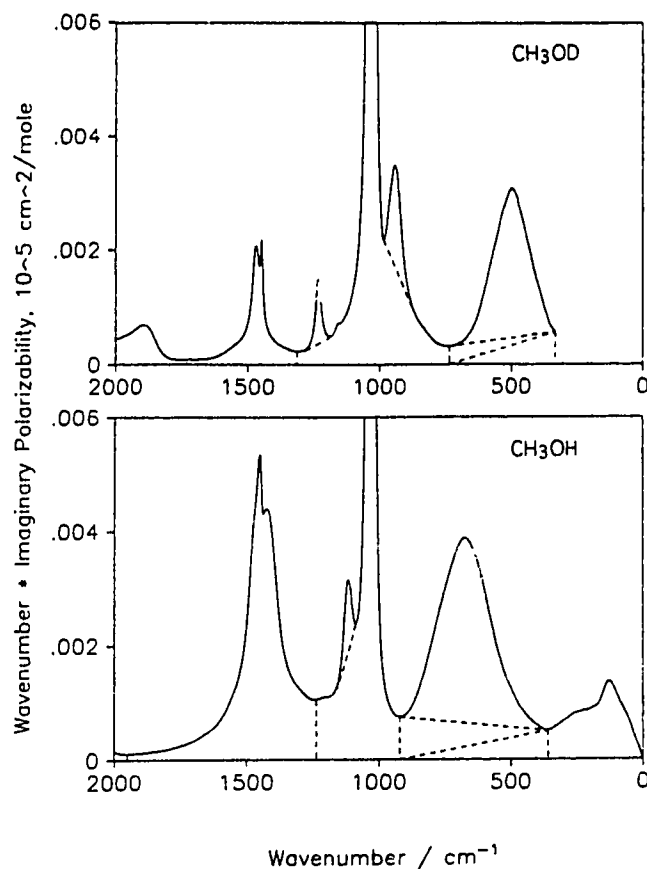


**Figure 6.11** The  $\tilde{\nu}\alpha''_m$  spectra of  $\text{CH}_3\text{OD}$  (top box) and  $\text{CH}_3\text{OH}$  (bottom box) below 2000  $\text{cm}^{-1}$ . The dashed lines separate integration regions.

method, by neglecting the wings of the CO band and, second, by subtracting the CO band with its wings from the spectrum.

The first approach is illustrated in Figure 6.11. The  $\text{CH}_3$  deformation bands near  $1450 \text{ cm}^{-1}$  are overlapped with the C–O–H in-plane bending band<sup>11</sup> in the spectrum of  $\text{CH}_3\text{OH}$  (Figure 6.11, bottom). The C–O–D vibration is at lower wavenumber in the  $\text{CH}_3\text{OD}$  spectrum (Figure 6.11, top) and only the deformation bands are left near  $1500 \text{ cm}^{-1}$ , with the  $\text{CH}_3$  rocking band well separated at  $1232 \text{ cm}^{-1}$ . For  $\text{CH}_3\text{OH}$  and  $\text{CH}_3\text{OD}$ , the integration limits were taken at the nearest minima in the  $\tilde{\nu}\alpha''_m$  spectrum to either side of the band. They were  $1950.6$  to  $1230.4 \text{ cm}^{-1}$  for  $\text{CH}_3\text{OH}$  and  $1730.8$  to  $1305.6 \text{ cm}^{-1}$  for  $\text{CH}_3\text{OD}$ . The areas, measured above zero ordinate, are  $C_j = 0.908 \text{ km mol}^{-1}$  for  $\text{CH}_3\text{OH}$  and (Table 6.6)  $0.198 \text{ km mol}^{-1}$  for  $\text{CH}_3\text{OD}$ . The intensity contributed by the

deformation bands in CH<sub>3</sub>OH is assumed to be the same as the 0.198 km mol<sup>-1</sup> in CH<sub>3</sub>OD, and the intensity for the C–O–H in-plane bending vibration of CH<sub>3</sub>OH is obtained as  $C_j = 0.710 \text{ km mol}^{-1}$  (Table 6.6).

It is natural to take the integrated intensity of the C–O–D in-plane bend as the area above the dashed line drawn between the spectral points at 983.5 and 869.7 cm<sup>-1</sup> in Figure 6.11 (top). This area is 0.086 km mol<sup>-1</sup>. Similarly, the intensity of the CH<sub>3</sub> rocking vibration can be estimated as the area above the dashed line between the spectral points at 1281.5 and 1191.8 cm<sup>-1</sup> for CH<sub>3</sub>OD (Figure 6.11, top), and at 1157.1 and 1086.7 cm<sup>-1</sup> for CH<sub>3</sub>OH (Figure 6.11, bottom). These areas are  $C_j = 0.030 \text{ km mol}^{-1}$  for CH<sub>3</sub>OD and 0.038 km mol<sup>-1</sup> for CH<sub>3</sub>OH.

The integrated intensities of the H–C–O–H and H–C–O–D torsion vibrations are difficult to assess. The bands combine at low wavenumber with the absorption by intermolecular motion in the liquid, and there is no reliable way to separate them. For CH<sub>3</sub>OH, estimates of  $C_j$  have been obtained<sup>1</sup> in the three ways shown in Figure 6.11, bottom: Case 1, all of the area under the band between 915.1 cm<sup>-1</sup> and 365.4 cm<sup>-1</sup>; Case 2, the area above the dashed line through the spectral points at 915.1 and 365.4 cm<sup>-1</sup>; Case 3, the area above the dashed line through zero at 915.1 and the spectral point at 365.4 cm<sup>-1</sup>. The values obtained were 1.10, 0.755 and 0.959 km mol<sup>-1</sup>, respectively. For CH<sub>3</sub>OD, taking the integration range 733.8 to 331.7 cm<sup>-1</sup>, these three cases give (Figure 6.11, top) 0.609, 0.429 and 0.495 km mol<sup>-1</sup>.

In a second approach, designed to assess the reliability of the above values, the C–O stretching band, with its fitted wings, was subtracted from the  $\nabla\alpha''_m$  spectrum. The resulting difference spectra are shown in Figure 6.12, in which CH<sub>3</sub>OD is shown in the top box and CH<sub>3</sub>OH in the bottom box. The original  $\nabla\alpha''_m$  spectra are included in Figure 6.12 for reference. The integration limits were taken at the minima in the difference spectra. The  $C_j$  values obtained by this approach should be more reliable than those from the easy method.

For CH<sub>3</sub>OD, Figure 6.12 (top), the integrated intensity of the CH<sub>3</sub> deformation bands was taken as the total area under the difference spectrum between 1730.8 and 1295.9 cm<sup>-1</sup>,  $C_j = 0.186 \text{ km mol}^{-1}$ . The CH<sub>3</sub> rocking intensity is the total area between 1295.9 and 1180.2 cm<sup>-1</sup>,  $C_j = 0.058 \text{ km mol}^{-1}$ . The small area above zero ordinate between 1180.2 and 1080 cm<sup>-1</sup>,  $C_j = 0.031 \text{ km mol}^{-1}$ , could be partly due to this vibration, but is assigned to the second CH<sub>3</sub> rocking band, which is visible at ~ 1160 cm<sup>-1</sup>. To low-wavenumber of the CO band lie the C–O–D in-plane bend and the

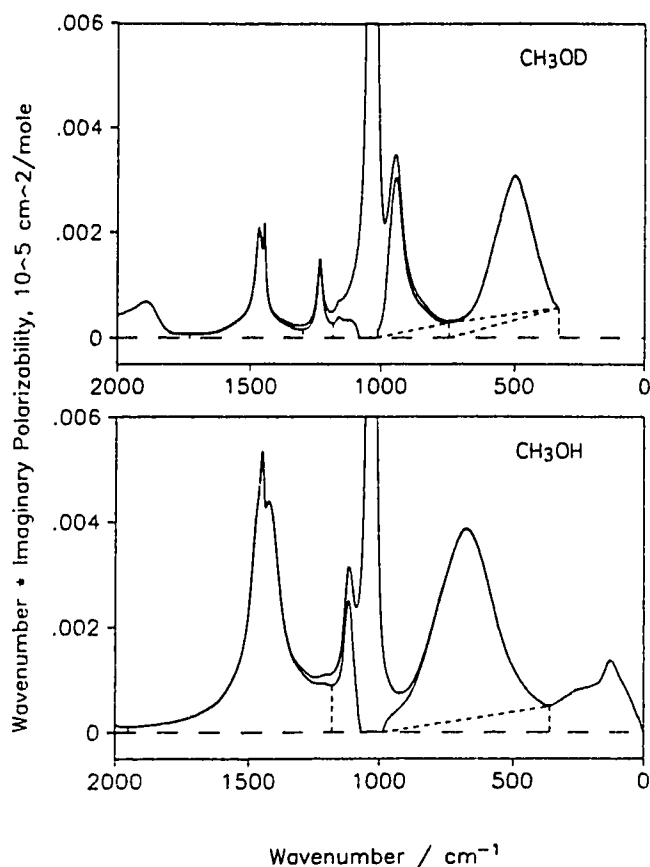


**Figure 6.12** The  $\tilde{\nu}\alpha_m''$  spectra of methanol and methanol-*d* below 2000  $\text{cm}^{-1}$  and the difference spectra which results when the C–O stretching band, including its CDHO wings, is subtracted from it. Top box:  $\text{CH}_3\text{OD}$ , bottom box:  $\text{CH}_3\text{OH}$ . The dashed lines separate integration regions.

H–C–O–D torsion. For both bands the baseline presents an unresolved uncertainty, and for each band, different cases were calculated. For the C–O–D in-plane bend the values  $C_j = 0.280$  and  $0.240 \text{ km mol}^{-1}$  were found for (1) the total area between 1011.5 and 733.8  $\text{cm}^{-1}$  and (2) the area above a straight line between zero at 1011.5  $\text{cm}^{-1}$  and the spectral point at 733.8  $\text{cm}^{-1}$ .  $C_j = 0.26 \pm 0.02 \text{ km mol}^{-1}$  is taken as the best value for the C–O–D in-plane bend.

For the H–C–O–D torsion the  $C_j$  values are 0.605, 0.431 and 0.491 for the three cases described above and illustrated by dashed lines in Figure 6.12 (top). These are essentially the values given by the easy method and the average value and the deviation,  $C_j = 0.5 \pm 0.1 \text{ km mol}^{-1}$  are taken as the best values obtainable for the H–C–O–D torsion with our current knowledge.



For CH<sub>3</sub>OH, Figure 6.12 (bottom), the combined integrated intensities of the CH<sub>3</sub> deformation and C–O–H in-plane bending vibrations were taken to be the total area under the difference spectrum between 1950.6 and 1180.2 cm<sup>-1</sup>,  $C_j = 0.914 \text{ km mol}^{-1}$ . The CH<sub>3</sub> deformation intensity was assumed to be the same as in CH<sub>3</sub>OD, 0.186 km mol<sup>-1</sup>, from which  $C_j = 0.728 \text{ km mol}^{-1}$  was obtained for the C–O–H in-plane bend. The total area between 1180.2 and 1067.4 cm<sup>-1</sup>,  $C_j = 0.147 \text{ km mol}^{-1}$  was assigned to the CH<sub>3</sub> rock. Below the C–O stretching band is the H–C–O–H torsion. The total area between 980 and 365.4 cm<sup>-1</sup> is 1.097 km mol<sup>-1</sup> and that above the dashed line between 0 at 980 cm<sup>-1</sup> and the spectral point at 365.4 cm<sup>-1</sup> is 0.943 km mol<sup>-1</sup>. The average value and deviation,  $C_j = 1.02 \pm 0.08 \text{ km mol}^{-1}$ , were taken as the best values available for the H–C–O–H torsion.

All of these areas are summarized in Table 6.6. The values from the difference spectra are preferred, because they have been largely corrected for the wings of the C–O stretching band that dominates the region. The easy method seriously underestimates the intensity of the CH<sub>3</sub> rocks in both molecules and the intensity of the C–O–D in-plane deformation in CH<sub>3</sub>OD.

#### 6.4.4 Transition Moments and Dipole Moment Derivatives

The magnitude of the effective transition moment,  $|R_j^f|$ , of vibration  $j$  can be calculated from the integrated intensity  $C_j$  by eq. (6.1). If it is assumed that the oscillator is mechanically and electrically harmonic, the change in the molecular dipole moment during the vibration,  $\mu_j$ , can also be calculated from the integrated intensity,  $C_j$ . With further assumptions, about the coupling between displacements, the changes in dipole moment, when a bond is stretching or an angle is increased, can be found. These calculations are presented in this section.

The  $C_j$  values in km mol<sup>-1</sup> (Table 6.6 and column 3 of Table 6.7) were converted to  $|R_j^f|^2$  values in Debye<sup>2</sup> by multiplying them by 31.50 and dividing them by the peak wavenumber of the band, or by the average of the peak wavenumbers for the CH<sub>3</sub> stretching and CH<sub>3</sub> deformation vibrations. The  $|R_j^f|$  values obtained are in column 4 of Table 6.7. The value reported for the CH<sub>3</sub> stretching and the deformation vibrations is the square root of the sum of the  $|R_j^f|^2$  values for the three stretching or deformation vibrations.

**Table 6.7** Transition moments and dipole moment derivatives of CH<sub>3</sub>OH and CH<sub>3</sub>OD in the liquid phase

Band	$\tilde{\nu}_{\max}$ in $\tilde{\nu}\alpha''_m(\tilde{\nu})$ (cm <sup>-1</sup> )	$C_j$ (km mol <sup>-1</sup> )	$ R_j^f $ (D)	$\mu_j^2$ (D <sup>2</sup> Å <sup>-2</sup> amu <sup>-1</sup> )	Conversion Factor	$\mu_R^2$ (D <sup>2</sup> Å <sup>-2</sup> )	$\mu_R^a$ (D Å <sup>-1</sup> )
<b>CH<sub>3</sub>OD</b>							
v(C-H)	2981/2947/2836	1.31	0.119 <sup>b</sup>	2.45 <sup>c</sup>	0.3051	0.747	0.864
v(O-D)	2497	4.01	0.225	7.49	1.7888	13.40	3.66
δ(CH <sub>3</sub> )	1467/1447	0.186	0.063 <sup>b</sup>	0.348 <sup>c</sup>	0.1832	0.0637	0.252
v(C-O)	1034	1.27	0.197	2.37	6.854	16.27	4.03
δ(C-O-D)	941	0.26±0.02	0.093	0.49±0.04	1.375	0.67	0.82
τ(H-C-O-D)	496	0.5±0.1	0.178	0.93	0.9510	0.89	0.94
<b>CH<sub>3</sub>OH</b>							
v(C-H)	2980/2945/2833	1.31	0.119 <sup>b</sup>	2.45 <sup>c</sup>	0.3051	0.747	0.864
v(O-H)	3354	7.69	0.269	14.4	0.9482	13.63	3.69
δ(CH <sub>3</sub> )	1477/1450	0.186	0.063 <sup>b</sup>	0.348 <sup>c</sup>	0.1832	0.0637	0.252
δ(C-O-H)	1423	0.73	0.127	1.36	0.7800	1.06	1.03
v(C-O)	1035	1.24	0.194	2.32	6.854	15.9	3.99
τ(H-C-O-H)	673	1.02±0.08	0.218	1.91±0.15	0.5992	1.14	1.07

a)  $\mu_R$  is the magnitude of the change of dipole moment for unit change in the internal coordinate. It is assumed to lie along the CH bond for the C-H stretching coordinate and along the bisector of the HCH angle for the HCH deformation coordinate.

b) This value is the square root of the sum of  $|R_j^f|^2$  over all three CH<sub>3</sub> stretching or deformation vibrations. The averaged wavenumber was used in the calculation.

c) This value is  $\sum_j \mu_j^2$  over all CH<sub>3</sub> stretches or deformations.

The  $C_j$  values in km mol<sup>-1</sup> were also converted to  $\mu_j^2$  values, in the units (Debye Å<sup>-1</sup>)<sup>2</sup> amu<sup>-1</sup>, by multiplying them by the numerical factor<sup>7</sup> 1.8686. The  $C_j$  values and the resulting  $\mu_j^2$  values are in Table 6.7. For the C-H stretching and CH<sub>3</sub> deformation vibrations, the  $\mu_j^2$  value in the table is the sum of  $\mu_j^2$  over the three C-H stretching or deformation vibrations.

The significance of the  $\mu_j^2$  values is not easy to appreciate because  $\mu_j^2$  is influenced by the effective mass of the oscillator  $j$ . To remove this influence of the effective mass, the simplest possible treatment was used to calculate values of  $\mu_R = |\partial \bar{\mu} / \partial R|$ , where  $R$  is a valence internal displacement coordinate. In order to obtain all  $\mu_R$  quantities in the units Debye Å<sup>-1</sup>, the angular internal coordinates were defined as the change in angle multiplied by 1 Å. The direction of  $\bar{\mu}_R$  is not known, but it is not important for the calculations presented below except for the CH stretch, for which  $\bar{\mu}_{CH}$  is assumed to be parallel to the C-H bond, and for the CH<sub>3</sub> deformation, for which  $\bar{\mu}_{HCH}$  is assumed to lie

along the HCH bisector. A more complete treatment, which takes account of the interactions between the different internal coordinates, will be presented when the experimental results for CD<sub>3</sub>OD and CD<sub>3</sub>OH are available.

The following procedures and assumptions were used to convert  $\mu_j^2$  values to the  $\mu_R$  values presented in Table 6.7. The fundamental relation is

$$\frac{\partial \bar{\mu}}{\partial Q_j} = \sum_i \frac{\partial \bar{\mu}}{\partial R_i} \frac{\partial R_i}{\partial Q_j} = \sum_i \frac{\partial \bar{\mu}}{\partial R_i} l_{ij}$$

where the  $l_{ij}$  are the eigenvectors that describe the displacement of internal coordinate  $i$  during unit displacement of normal coordinate  $j$ . The sum is a vector sum. In order to calculate the eigenvectors, the molecule was assumed to have C<sub>s</sub> symmetry with the O–D bond trans to a C–H bond in the HCOD plane. The geometry<sup>21</sup> used is summarized in Table VII of Ref. 1, and the carbon-12 scale of atomic masses was used. The internal coordinates,  $R_i$ , were taken to be the increases in the O–D, C–H, and C–O bond lengths for the stretching motion. The HCH deformation and the C–O–H in-plane bending coordinates,  $R_\theta$  and  $R_\phi$  respectively, were defined as 1 Å times the increase in the angle.

The O–H, O–D and C–O stretching vibrations were treated as diatomic oscillators, namely as uncoupled oscillators at 3354 cm<sup>-1</sup> in CH<sub>3</sub>OH and at 2497 and 1034 cm<sup>-1</sup> respectively in CH<sub>3</sub>OD. Thus, this gave  $\mu_{OH}^2 = 0.9482\mu_j^2$  for the O–H stretching vibration,  $\mu_{OD}^2 = 1.7888\mu_j^2$  for the O–D stretching vibration, and  $\mu_{CO}^2 = 6.854\mu_j^2$  for the C–O stretching vibration. The unit of these conversion factors is amu. The C–H stretching vibrations were treated as the coupled C–H stretching vibrations of an isolated CH<sub>3</sub> group of C<sub>s</sub> symmetry. The symmetric CH<sub>3</sub> stretch (A' under C<sub>s</sub>) was assigned at 2836 cm<sup>-1</sup>, and the antisymmetric CH<sub>3</sub> stretches were assigned at 2981 cm<sup>-1</sup> (A' under C<sub>s</sub>) and 2947 cm<sup>-1</sup> (A'' under C<sub>s</sub>), following the work of Günthard and coworkers<sup>11</sup>. The force constants, assumptions and treatment have been described previously<sup>1</sup> and yielded the relation  $\mu_j^2 = 3.277\mu_{CH}^2$ , i.e.  $\mu_{CH}^2 = 0.3051\mu_j^2$ . The C–O–H and C–O–D in-plane bending vibrations were treated as uncoupled oscillators, and the relations were found to be  $\mu_{COH}^2 = 0.7800\mu_j^2$  and  $\mu_{COD}^2 = 1.375\mu_j^2$ , respectively.

The CH<sub>3</sub> deformation vibrations were treated as the coupled CH<sub>3</sub> deformation vibrations of an isolated CH<sub>3</sub> group of C<sub>3v</sub> symmetry. The symmetric deformation (A<sub>1</sub> under C<sub>3v</sub>) was assigned at 1447 cm<sup>-1</sup>, and the antisymmetric deformations (E under C<sub>3v</sub>) were assigned together at 1467 cm<sup>-1</sup>, following the work of Günthard and coworkers<sup>11</sup>. The deformation force constant and the interaction force constant were calculated from these wavenumbers to be 0.7619 and 0.1925 m dyn Å<sup>-1</sup>. The relation

$\mu_{\text{HCH}}^2 = 0.1832\mu_j^2$  was calculated (this relation is independent of the values of the force constants under this approximation). The conversion factor 0.1832 is listed with the other conversion factors in Table 6.7.

The availability of the spectrum of  $\text{CH}_3\text{OD}$  has yielded values of  $C_j$  and  $\mu_R$  for the O–H and C–H stretching vibrations of  $\text{CH}_3\text{OH}$  that are much more reliable than those in Ref. 1 (Chapter 5). For the C–O stretching vibration the new value of  $C_j$  agrees with that reported previously within its error limits but is more precise and is about 5% smaller. For the C–H, O–H, O–D and C–O stretching bands, the reliability of the  $C_j$  values is close to that of the refractive index values,  $\pm 3\%$ , and the new  $\mu_R$  values are believed accurate to about 2% subject to the approximations made in their calculation from  $C_j$ .

For the torsion vibration of  $\text{CH}_3\text{OH}$ ,  $C_j = 0.94 \text{ km mol}^{-1}$  was reported in Table VI of Ref. 1 (i.e. Table 5.6). This corresponds to  $\mu_j^2 = 1.8 \text{ D}^2 \text{ \AA}^{-2} \text{ amu}^{-1}$ . The torsion coordinate was defined as  $1 \text{ \AA}$  times the change in the dihedral angle between the COH plane and the OCH plane of the trans C–H bond. The  $\mu_\tau$  for the torsion in  $\text{CH}_3\text{OH}$  was calculated to be  $0.88 \text{ D \AA}^{-1}$  under this definition of the internal coordinate. It is more appropriate to define<sup>22</sup> the torsion coordinate as  $1 \text{ \AA}$  times the average change in the three dihedral angles between the COH plane and the OCH planes of the three C–H bonds. With this definition, the relation between  $\mu_\tau^2$  and  $\mu_j^2$  was found to be  $\mu_\tau^2 = 0.9510\mu_j^2$  for  $\text{CH}_3\text{OD}$  and  $\mu_\tau^2 = 0.5992\mu_j^2$  for  $\text{CH}_3\text{OH}$ . Had this definition been used in the previous paper with the value  $\mu_j^2 = 1.8 \text{ D}^2 \text{ \AA}^{-2} \text{ amu}^{-1}$ , it would have yielded the value  $\mu_\tau = 1.04 \text{ D \AA}^{-1}$  instead of  $0.88 \text{ D \AA}^{-1}$  previously reported. In the present work, the subtraction of the wings of the C–O stretching band (Figure 6.12) has indicated that  $C_j$  and  $\mu_j^2$  are about 7% greater than in Ref. 1 (Chapter 5) and that  $\mu_\tau = 1.07 \text{ D \AA}^{-1}$ .

The agreement between the  $\mu_R$  values of  $\text{CH}_3\text{OH}$  and  $\text{CH}_3\text{OD}$  suggests that the intensities included in Table 6.7 are reliable except for those of the C–O–H and C–O–D in-plane bending vibrations and, to a lesser extent, the torsion.

## 6.5 Summary

The absorption index, real refractive index, and molar absorption coefficient spectra of  $\text{CH}_3\text{OD}$  have been presented between  $8000$  and  $350 \text{ cm}^{-1}$ . The accuracy of the absorption indices and absorption coefficients is believed to be  $\pm 3\%$  below and  $\pm 10\%$

above  $5900\text{ cm}^{-1}$ . Integrated absorption intensities have been measured as  $C_j$ , the area under the spectrum of the imaginary molar polarizability multiplied by wavenumber,  $\nabla\alpha_m''(\tilde{\nu})$ . The availability of the spectra of both  $\text{CH}_3\text{OH}$  and  $\text{CH}_3\text{OD}$  has enabled the integrated intensities to be determined to a few percent with confidence for the O–H, O–D, C–H, and C–O stretching, and  $\text{CH}_3$  deformation motions. From the intensities, we have calculated the transition moments and, under the approximation of mechanical and electrical harmonicity, the dipole moment derivatives with respect to the normal coordinates,  $Q_j$ . We have also calculated the dipole moment derivatives with respect to changes in the internal coordinates under the simplest approximations. Studies of  $\text{CD}_3\text{OH}$  and  $\text{CD}_3\text{OD}$  may help to improve our confidence in our knowledge of the intensities of the C–O–H and C–O–D in-plane bending, H–C–O–H and H–C–O–D torsion, and  $\text{CH}_3$  rocking motions.

## 6.6 References

1. J. E. Bertie, S. L. Zhang, H. H. Eysel, S. Baluja, and M. K. Ahmed, *Appl. Spectrosc.* **47**, 1100 (1993).
2. J. E. Bertie and H. H. Eysel, *Appl. Spectrosc.* **39**, 392 (1985).
3. J. E. Bertie, H. Harke, M. K. Ahmed, and H. H. Eysel, *Croatica Chim. Acta* **61**, 391 (1988).
4. J. E. Bertie, S. L. Zhang, and R. Manji, *Appl. Spectrosc.* **46**, 1660 (1992).
5. I. Mills, T. Cvitaš, K. Homman, N. Kallay, and K. Kuchitsu, *Quantities, Units and Symbols in Physical Chemistry*. Blackwell Scientific Publications, Oxford, 1988.
6. N. Sheppard, H. A. Willis, and J. C. Rigg, *Spectrochim Acta* **43A**, 1 (1987).
7. The appendix in Ref. 1, i.e. Section 5.6 of this thesis.
8. G. Herzberg, *Molecular Spectra and Molecular Structure II. Infrared and Raman Spectra of Polyatomic Molecules*. Van Nostrand, Princeton, 1945.
9. E. B. Wilson, J. C. Decius, and P. C. Cross, *Molecular Vibrations*. McGraw-Hill, New York, 1955.
10. M. J. Dignam, *Appl. Spectrosc. Rev.* **24**, 99 (1988).
11. A. Serrallach, R. Meyer, and H. H. Günthard, *J. Mol. Spectrosc.* **52**, 94 (1974).

12. J. E. Bertie and S. L. Zhang, *Can. J. Chem.* **70**, 520 (1992).
13. D. G. Cameron, J. P. Hawranek, P. Neelakantan, R. P. Young, and R. N. Jones, "*Computer Programs for Infrared Spectrophotometry XLII to XLVII*" in *National Research Council of Canada Bulletin* 16, 1977.
14. J. E. Bertie, C. D. Keefe, and R. N. Jones, *Can. J. Chem.* **69**, 1609 (1991).
15. *International Critical Tables of Numerical Data, Physics, Chemistry and Technology*, **7**. McGraw-Hill, New York, 1930. P34.
16. Aldrich Chemical Company, Inc., *Catalog, Handbook of Fine Chemicals*. Milwaukee, 1992.
17. D. D. Honijk, W. F. Passchier, M. Mandel, and M. N. Afsar, *Infrared Physics* **17**, 9 (1977).
18. J. E. Bertie, Y. Apelblat, and R. N. Jones, *Appl. Spectrosc.* **47**, 1989 (1993).
19. *CRC Handbook of Chemistry and Physics*, 64th edition, CRC Press, Inc., Boca Raton, 1983.
20. *International Critical Tables of Numerical Data, Physics, Chemistry and Technology*, **3**. McGraw-Hill, New York, 1928. P27.
21. R. M. Lees and J. G. Baker, *J. Chem. Phys.* **48**, 5299 (1968).
22. Y. Morino and T. Shimanouchi, *Pure & Appl. Chem.* **50**, 1707 (1978).

## Chapter 7 Infrared Refractive Indices from 8000 to 350 $\text{cm}^{-1}$ , Absolute Integrated Absorption Intensities, Transition Moments and Dipole Moment Derivatives of Methan- $d_3$ -ol and Methanol- $d_4$ , at 25°C \*

### 7.1 Introduction

In previous studies<sup>1,2</sup> of the absolute infrared absorption intensities of liquid methanol isotopomers, the results for liquid  $\text{CH}_3\text{OH}$  and  $\text{CH}_3\text{OD}$  determined by a combination of the CIRCLE cylindrical multiple attenuated total reflection (ATR) and transmission methods have been reported. The intensity quantities initially determined by these methods are the complex refractive index spectra,  $\hat{n}(\nu) = n(\nu) + i k(\nu)$ , where  $n(\nu)$  is the real refractive index and  $k(\nu)$  is the imaginary refractive index at wavenumber  $\nu$ . The imaginary refractive index  $k(\nu)$  is also called the absorption index<sup>3,4</sup>, and  $n(\nu)$  and  $k(\nu)$  are collectively called the optical constants.

Equations that were summarized previously<sup>5</sup> in Section 5.6 allow other optical properties and the properties of the molecules in the liquid to be calculated from the refractive indices.

It was noted<sup>1</sup> in the study of liquid  $\text{CH}_3\text{OH}$  that much of the accuracy of the optical constants is lost when areas of overlapping bands are separated into the integrated intensities of different vibrations. It was also noted<sup>2</sup> that the availability of both  $\text{CH}_3\text{OH}$  and  $\text{CH}_3\text{OD}$  improved this situation and allowed confidence that the integrated intensities of the O–H, O–D, C–H, and C–O stretching, and  $\text{CH}_3$  deformation, vibrations were determined with an accuracy of about 5%, i.e. that the values determined are within 5% of the correct value. In this chapter infrared absorption intensities of liquid methan- $d_3$ -ol,  $\text{CD}_3\text{OH}$ , and methanol- $d_4$ ,  $\text{CD}_3\text{OD}$ , at 25°C, are reported. ATR measurements were made between 4500 and 350  $\text{cm}^{-1}$  for both liquids, and transmission measurements were made between 7244 and 3637  $\text{cm}^{-1}$  for  $\text{CD}_3\text{OH}$ , between 5585 and 2713  $\text{cm}^{-1}$  for  $\text{CD}_3\text{OD}$ , and in regions of weak absorption below the O–H or O–D stretching band. The spectra of methan- $d_3$ -ol and methanol- $d_4$  are considered in combination with those<sup>1,2</sup> of  $\text{CH}_3\text{OH}$  and  $\text{CH}_3\text{OD}$ , to seek improvement in the separation of overlapping bands and, hence, in the reliability of the molecular properties calculated from the integrated intensities  $C_j$  for these molecules.

---

\* A version of this chapter has been accepted for publication. Bertie and Zhang, J. Chem. Phys.(1994)

The assignment of the infrared spectrum of methanol and its isotopomers is well established<sup>6</sup>. In contrast, we have found no report of the measurement of absolute infrared absorption intensities of liquids methan-*d*<sub>3</sub>-ol and methanol-*d*<sub>4</sub>.

## 7.2 Method and Experimental

The methods used to obtain the complex refractive indices from multiple attenuated total reflection spectra and from transmission spectra have been fully described<sup>1,7-12</sup>. The spectra were recorded at 2 cm<sup>-1</sup> nominal resolution and digitized at 0.964233 cm<sup>-1</sup> intervals. The experimental methods and instrumentation, as well as the operating conditions and procedures, were identical to those reported<sup>1</sup> for normal methanol, CH<sub>3</sub>OH, with the following exceptions.

The fully deuterated methanol, CD<sub>3</sub>OD, was reagent grade with 99.8% atom D. GC-IR study of this sample showed no evidence of impurity. It was used as supplied. The CD<sub>3</sub>OH sample was prepared from the CD<sub>3</sub>OD in the following way. Equal volumes of CD<sub>3</sub>OD and distilled H<sub>2</sub>O were mixed and distilled. The distillate contained some CD<sub>3</sub>OD and more CD<sub>3</sub>OH. It was then added to an equal volume of H<sub>2</sub>O and distilled again. This process was repeated at least four times. If the water-methanol exchange was complete each time, the atom percent H in the hydroxyl group of the final product should exceed 99.9%. A mass spectrometric study of this sample showed no more than 0.2 atom% D in the hydroxyl group. GC-IR study of the sample revealed no impurity. Water analysis showed that the sample contained about 0.2% of water and IR spectra showed only extremely weak OD absorption in the sample of CD<sub>3</sub>OH.

The ZnSe ATR rod was used in the CIRCLE cell only with the short liquid holder which gave ~3 reflections. The KRS-5 ATR rod was used for low wavenumbers, only with the long liquid holder which gave ~ 6 reflections.

## 7.3 Results

Over ten pATR spectra of CD<sub>3</sub>OH and CD<sub>3</sub>OD were obtained with the long KRS-5 cell and over twenty spectra of each compound were obtained with the short ZnSe cell. Sample pATR spectra with KRS-5 and ZnSe cells are shown as the upper and lower curves in the top (CD<sub>3</sub>OH) and bottom (CD<sub>3</sub>OD) boxes of Figure 7.1, respectively. Figure 7.2 shows experimental absorbance spectra<sup>12</sup> from transmission cells with 3000



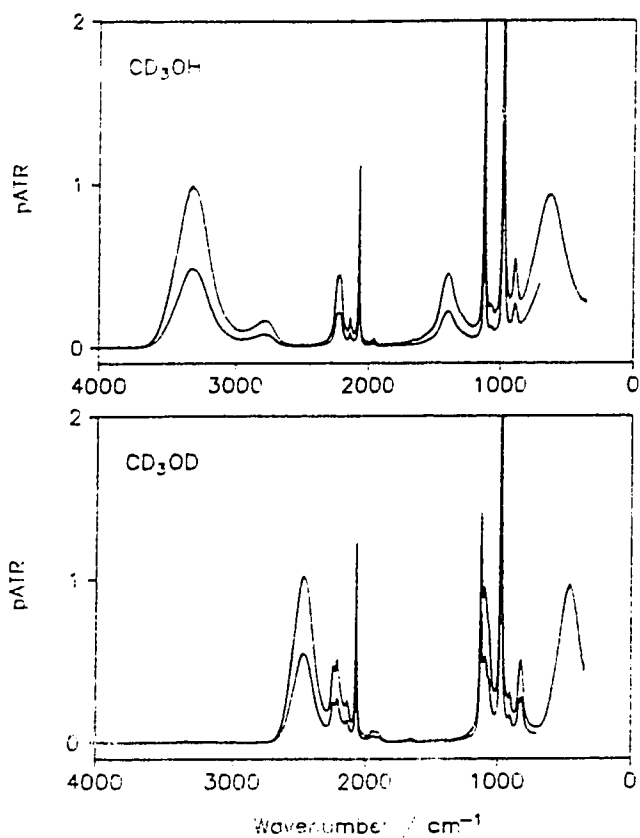


**Figure 7.1** pATR spectra of methan- $d_3$ -ol (top box) and methanol- $d_4$  (bottom box) recorded with KRS-5 (upper curves) and ZnSe (lower curves) ATR rods. The liquid holder around the 82 mm long ATR rod was 60 mm long for the upper curves and 30 mm long for the lower curves. The effective number of reflections was  $\sim 6$  for the upper curves and  $\sim 3$  for the lower curves.

and 40  $\mu\text{m}$  pathlengths for  $\text{CD}_3\text{OH}$  (top box) and with 3000 and 150  $\mu\text{m}$  pathlengths for  $\text{CD}_3\text{OD}$  (bottom box).

The real refractive index of methanol at  $8000\text{ cm}^{-1}$  at  $25^\circ\text{C}$  was found<sup>1</sup> to be  $1.325 \pm 0.001$  by fitting the values at visible wavelengths<sup>13</sup> to  $n^2 = A + B\nu^2 + C\nu^4$ , and extrapolating to  $8000\text{ cm}^{-1}$ . The only value we have found<sup>14</sup> for methan- $d_3$ -ol and methanol- $d_4$  is at the Sodium-D line,  $n_D = 1.3270$  and  $1.3262$ , respectively, where that of  $\text{CH}_3\text{OH}$  is  $1.3290$ . Therefore we estimate the real refractive index of methan- $d_3$ -ol at  $8000\text{ cm}^{-1}$  to be  $1.323 \pm 0.001$  and that of methanol- $d_4$  at  $8000\text{ cm}^{-1}$  to be  $1.322 \pm 0.001$ .

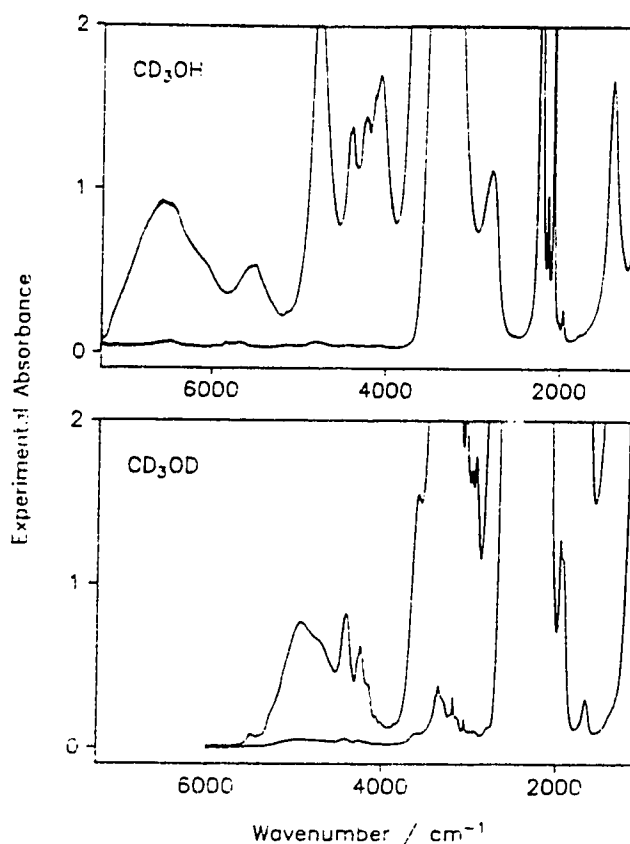


**Figure 7.2** Experimental absorbance spectra<sup>12</sup> in cells with calcium fluoride windows. Top box: liquid methan-*d*<sub>3</sub>-ol at pathlengths 3000 and 40  $\mu\text{m}$ ; Bottom box: liquid methanol-*d*<sub>4</sub> at pathlengths 3000 and 150  $\mu\text{m}$ .

The  $k(\tilde{\nu})$  values calculated from pATR spectra depend on the  $n(\tilde{\nu})$  values<sup>1</sup>. The  $n(\tilde{\nu})$  values are calculated from the  $k(\tilde{\nu})$  values by Kramers-Krönig transformation<sup>10</sup> as discussed in Chapter 2, and are sensitive to the significant absorption below 350  $\text{cm}^{-1}$ . Honijk *et al.*<sup>15</sup> have measured this absorption for liquid  $\text{CH}_3\text{OH}$ . Their  $k(\tilde{\nu})$  values are tabulated in Table II of Ref. 1 (Table 5.2) and shown in Figure 7 of Ref. 1 (Figure 5.7). The absorption is due to intermolecular vibrations arising from rotational and translational motions of the molecules in the liquid<sup>16</sup>, and is undoubtedly similar for methanol and methan-*d*<sub>3</sub>-ol or methanol-*d*<sub>4</sub>. Accordingly, during the calculation of  $k(\tilde{\nu})$  and  $n(\tilde{\nu})$  from the pATR spectra obtained with the KRS-5 rod, the  $k(\tilde{\nu})$  values<sup>15</sup> for  $\text{CH}_3\text{OH}$  between 350 and 2  $\text{cm}^{-1}$  were appended to the  $k(\tilde{\nu})$  values of  $\text{CD}_3\text{OH}$  or  $\text{CD}_3\text{OD}$  during the Kramers-Krönig transformation<sup>1</sup>, in order to obtain the best  $n(\tilde{\nu})$  and  $k(\tilde{\nu})$  values. Similarly, during the calculation of  $k(\tilde{\nu})$  and  $n(\tilde{\nu})$  from the pATR spectra

**Table 7.1** The decadic linear absorption coefficients,  $K(\tilde{\nu})$ , of CD<sub>3</sub>OH and CD<sub>3</sub>OD at the anchor points.

CD <sub>3</sub> OH			CD <sub>3</sub> OD		
Wavenumber (cm <sup>-1</sup> )	$K(\tilde{\nu})$ (cm <sup>-1</sup> )	95% confidence limit of $K^a$	Wavenumber (cm <sup>-1</sup> )	$K(\tilde{\nu})$ (cm <sup>-1</sup> )	95% confidence limit of $K^a$
7244.2	0.156	23% <sup>b</sup>	5584.8	0.00 <sup>c</sup>	
5815.2	1.088	0.6%	4531.9	1.457	1.6%
4541.5	2.513	1.0%	3912.8	0.315	2.5%
3880.0	2.540	1.0%	3550.0	4.639	1.9%
2944.7	178.7	0.3%	3072.0	5.886	1.1%
2454.9	19.34	0.5%	2859.9	3.727	0.7%
2156.0	123.7	0.3%	1768.4	6.663	0.6%
2107.8	106.6	0.5%	1542.7	4.867	0.5%
1862.9	15.54	0.6%			
1249.6	134.7	4.0%			

a As a percentage of  $K(\tilde{\nu})$ .

b The absorption is too weak to be measured accurately in 4 mm path. The confidence limit, 0.0365 cm<sup>-1</sup>, is equivalent to an uncertainty in  $k$  of  $9 \times 10^{-7}$  at this wavenumber.

c Set to zero, because the absorption at this wavenumber is too weak to be measured in 3 mm path.

obtained with the ZnSe rod, the  $k(\tilde{\nu})$  values obtained from the KRS-5 cell and those of Honijk *et al.* were appended between 700 and 350 cm<sup>-1</sup> and between 350 and 2 cm<sup>-1</sup>, respectively, to the  $k(\tilde{\nu})$  values from the ZnSe cell during the Kramers-Krönig transformation.

A single absorption index spectrum for each compound was created from the pATR measurements using the ZnSe and KRS-5 rods in the following way. The  $k$  spectra of CD<sub>3</sub>OH from pATR spectra recorded with the KRS-5 cell agreed to better than 1% and were averaged. The  $k$  spectra from the ZnSe cell agreed to better than 1.5% and were also averaged. The averaged  $k(\tilde{\nu})$  from the KRS-5 cell is higher than that from the ZnSe cell by about 2% between 804 and 748 cm<sup>-1</sup>. They were merged over this region to give a single  $k$  spectrum for CD<sub>3</sub>OH. For CD<sub>3</sub>OD the  $k$  spectra from the ZnSe cell agreed to better than 1%, except for 1.5% at the CO peak, and were averaged. The  $k$  spectra from the KRS-5 cell agreed to about 1% and were also averaged. These two averaged  $k$  spectra agreed to better than 1% and were merged at 710.6 cm<sup>-1</sup> to obtain a single  $k$  spectrum for CD<sub>3</sub>OD.

The  $k$  spectra from pATR measurements are known to good accuracy from 3600 to 350 cm<sup>-1</sup> and from 2700 to 350 cm<sup>-1</sup> for CD<sub>3</sub>OH and CD<sub>3</sub>OD, respectively. The spectra in the weakly absorbing regions above and below the O–H and O–D stretching bands are also known to some extent from these pATR spectra. In order to improve the accuracy

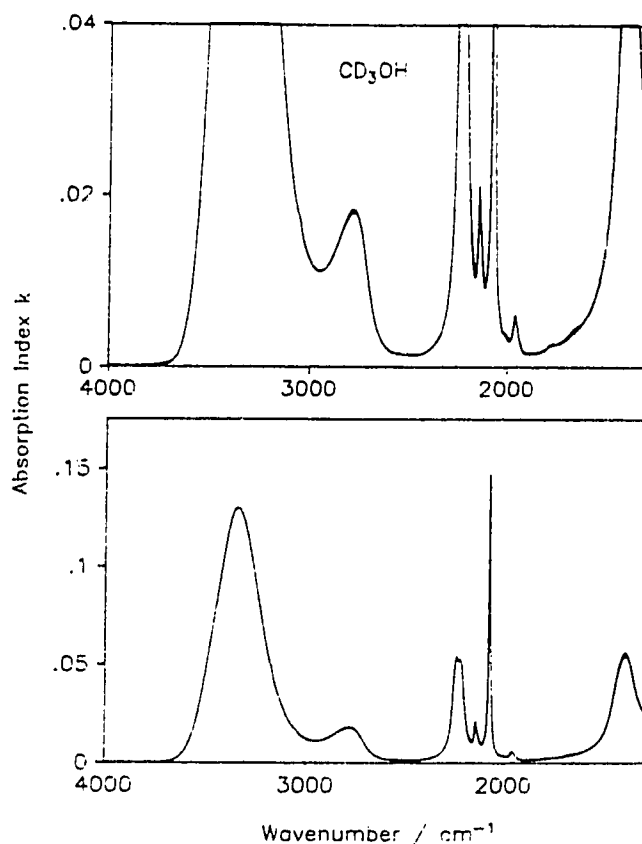


**Figure 7.3A** The superimposed absorption index spectra of  $\text{CD}_3\text{OH}$ , calculated from ATR spectra and from transmission spectra. In the top box the ordinate scale is greatly enlarged. The bottom box shows the same two spectra on a normal ordinate scale with the O-H stretching band near full scale. The  $k$  spectrum from transmission is shown for four separate regions in both boxes: 4000-3637, 3036-2327, 2181-2082 and 2023-1300  $\text{cm}^{-1}$ .

of the  $k$  spectra in these weakly absorbing regions, the  $k$  spectra were also determined from transmission spectra in cells with calcium fluoride windows and pathlengths up to 4 mm for  $\text{CD}_3\text{OH}$  and 3 mm for  $\text{CD}_3\text{OD}$ . Seventeen spectra of  $\text{CD}_3\text{OH}$  were recorded with pathlengths from 40  $\mu\text{m}$  to 4 mm. Twenty four spectra of  $\text{CD}_3\text{OD}$  were recorded with pathlengths from 110  $\mu\text{m}$  to 3 mm.

In order to correct unpredictable variations in the baselines of the transmission spectra, the decadic linear absorption coefficient<sup>1,3,4</sup>,  $K(\nu)$ , was determined at *anchor point* wavenumbers<sup>12</sup> in the baseline, from spectra in which the absorption at the anchor points is very strong. The values of  $K(\nu)$  at the anchor points are given in Table 7.1, with their 95% confidence limits. After their baselines were corrected<sup>12</sup>, the spectra were converted to  $k$  spectra. Each  $k$  spectrum is useful in those regions in which the

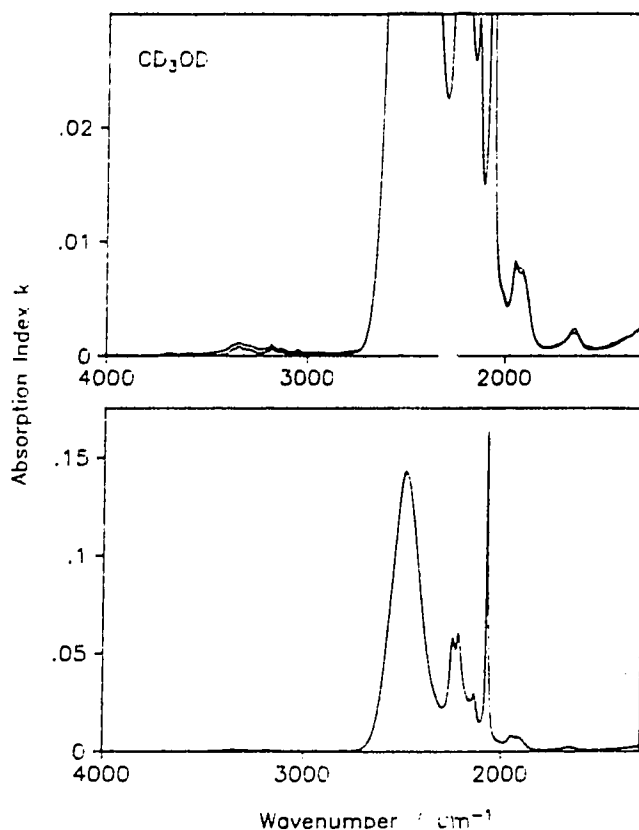


**Figure 7.3B** The superimposed absorption index spectra of  $\text{CD}_3\text{OD}$ , calculated from ATR spectra and from transmission spectra. In the top box the ordinate scale is greatly enlarged. The bottom box shows the same two spectra on a normal ordinate scale with the O–D stretching band near full scale. The  $k$  spectrum from transmission is shown for two separate regions in both boxes: 4000–2713 and 2044–1300  $\text{cm}^{-1}$ . The  $k$  spectrum from ATR is noisier, lower above 2800  $\text{cm}^{-1}$  and higher below 2000  $\text{cm}^{-1}$ .

absorbance was between 0.2 and 2.0 with the cell pathlength that was used.

Accordingly, the many absorption index spectra were averaged and merged to give  $k$  spectra in the regions 4044 to 3637  $\text{cm}^{-1}$ , 3036 to 2327  $\text{cm}^{-1}$ , 2181 to 2082  $\text{cm}^{-1}$ , and 2023 to 1300  $\text{cm}^{-1}$  for  $\text{CD}_3\text{OH}$  and the regions 5585 to 2713  $\text{cm}^{-1}$  and 2044 to 1258  $\text{cm}^{-1}$  for  $\text{CD}_3\text{OD}$ .

Figures 7.3A and 7.3B show for  $\text{CD}_3\text{OH}$  and  $\text{CD}_3\text{OD}$  respectively, the  $k$  spectra from transmission and from pATR measurements between 4000 and 1300  $\text{cm}^{-1}$ . In each figure, the same spectra are shown in both boxes, but on a greatly expanded ordinate scale in the top box. For  $\text{CD}_3\text{OH}$  the agreement can be seen in the top box of Figure 7.3A to be generally 2% with small regions up to 3%.

A single spectrum for CD<sub>3</sub>OH between 8000 and 350 cm<sup>-1</sup> was created by merging the two  $k$  spectra. Specifically,  $k(\nu)$  was set to zero from 8000 to 7244 cm<sup>-1</sup>. Above ~ 3700 cm<sup>-1</sup>, the absorption is too weak to be measured well by ATR and only the  $k$  spectrum from transmission was used between 7244 and 3037 cm<sup>-1</sup>. Between 3036 and 2327 cm<sup>-1</sup>, the agreement between the two  $k$  spectra is within 1% (except for about 3% between 2590 and 2420 cm<sup>-1</sup> where  $k < 0.001$ ), the spectrum from absorbance is higher, and the average of the two  $k(\nu)$  was used. Between the symmetric and asymmetric C–D stretching bands, i.e. between 2181 and 2082 cm<sup>-1</sup>, the two  $k$  spectra agree to about 3% with a minimum  $k$  value of ~ 0.01. The average of the two  $k$  spectra was used in this small region. Between 2023 and 1600 cm<sup>-1</sup>, the  $k$  values are small and a very weak shoulder due to the bending vibration of H<sub>2</sub>O is visible in the  $k$  spectrum from ATR on the greatly expanded ordinate scale in the top box of Figure 7.3A. Accordingly, only the  $k(\nu)$  from transmission was used in this region. From 1600 to 1300 cm<sup>-1</sup>, the two  $k$  spectra agree within 2% and were averaged. The  $k$  spectrum from ATR was used in the regions 2327 to 2181 cm<sup>-1</sup>, 2082 to 2023 cm<sup>-1</sup>, and below 1300 cm<sup>-1</sup>. The resulting  $k$  spectrum of CD<sub>3</sub>OH is shown in Figure 7.4A. It is well defined where  $k \geq 4 \times 10^{-5}$ . In the regions where  $k < 4 \times 10^{-5}$  (all above 5000 cm<sup>-1</sup>),  $k(\nu)$  is not known to better than 10%.

For CD<sub>3</sub>OD the agreement between the  $k$  spectra from transmission and pATR measurements can be seen in the top box of Figure 7.3B. Above ~ 2800 cm<sup>-1</sup>, the  $k$  spectrum from ATR is noisier and lower, and the agreement is poor because the absorption is too weak to be determined accurately by ATR. In the very weak regions which lie between ~ 2700 and ~ 1250 cm<sup>-1</sup>, the  $k(\nu)$  from ATR is higher and, again, noisier. The two  $k$  spectra in this region generally agree to about 3% except where the  $k$  value is smaller than 0.002.

A single absorption index  $k$  spectrum for CD<sub>3</sub>OD was created by merging the two  $k$  spectra. Specifically,  $k(\nu)$  was set to zero in the region from 8000 to 5585 cm<sup>-1</sup> where the  $k(\nu)$  values are less than 10<sup>-6</sup>; The  $k(\nu)$  from transmission was used from 5585 to 2713 cm<sup>-1</sup>; The  $k(\nu)$  from ATR was used from 2713 to 2044 cm<sup>-1</sup>; The  $k(\nu)$  from transmission was used again from 2044 to 1258 cm<sup>-1</sup>; The  $k(\nu)$  from ATR was used below 1258 cm<sup>-1</sup>. The  $k$  spectrum of CD<sub>3</sub>OD so created is shown in Figure 7.4B. It is well defined where  $k \geq 4 \times 10^{-5}$ . In the regions where  $k < 4 \times 10^{-5}$  (all are above 3740 cm<sup>-1</sup>),  $k(\nu)$  is not known to better than 10%.

The  $k$  spectrum of liquid CD<sub>3</sub>OH in Figure 7.4A and that of liquid CD<sub>3</sub>OD in Figure 7.4B were Kramers-Krönig transformed with  $n(8000 \text{ cm}^{-1}) = 1.323$  for CD<sub>3</sub>OH or

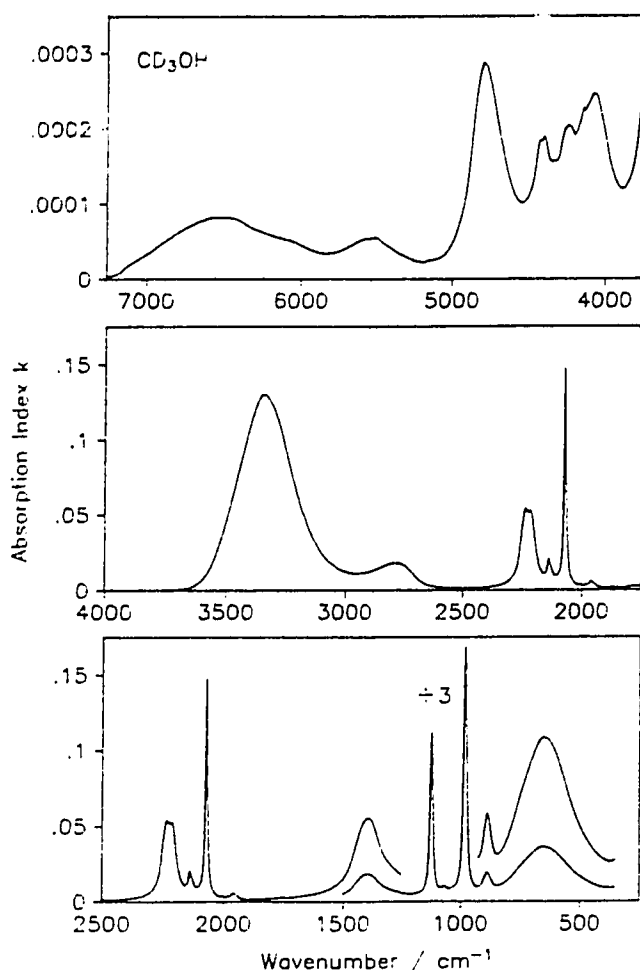


**Figure 7.4A** The absorption index spectrum of  $\text{CD}_3\text{OH}$  at  $25^\circ\text{C}$ . In the top box, the ordinate has been expanded 500 times. In the bottom box, the ordinate labels are for the upper curves and must be multiplied by 3 for the lower curve which extends from 1500 to 350  $\text{cm}^{-1}$ .

1.322 for  $\text{CD}_3\text{OD}$ , and with the  $k$  spectrum<sup>15</sup> of  $\text{CH}_3\text{OH}$  below 350  $\text{cm}^{-1}$  included in the transform. The resulting  $n$  spectrum is shown in Figure 7.5A for  $\text{CD}_3\text{OH}$  and in Figure 7.5B for  $\text{CD}_3\text{OD}$ .

Table 7.2 contains values of  $k(\tilde{\nu})$  and  $n(\tilde{\nu})$  for both liquids at the wavenumbers of the peaks in the  $k$  spectrum and of the associated minima and maxima in the  $n$  spectrum, and in some regions of weak and flat absorption. The numerical values of  $k$  throughout the spectrum are given in the Compact Table format<sup>17</sup> in Table 7.3 for  $\text{CD}_3\text{OH}$  and in Table 7.4 for  $\text{CD}_3\text{OD}$ .  $k(\tilde{\nu})$  values at the original spacing can be obtained without loss

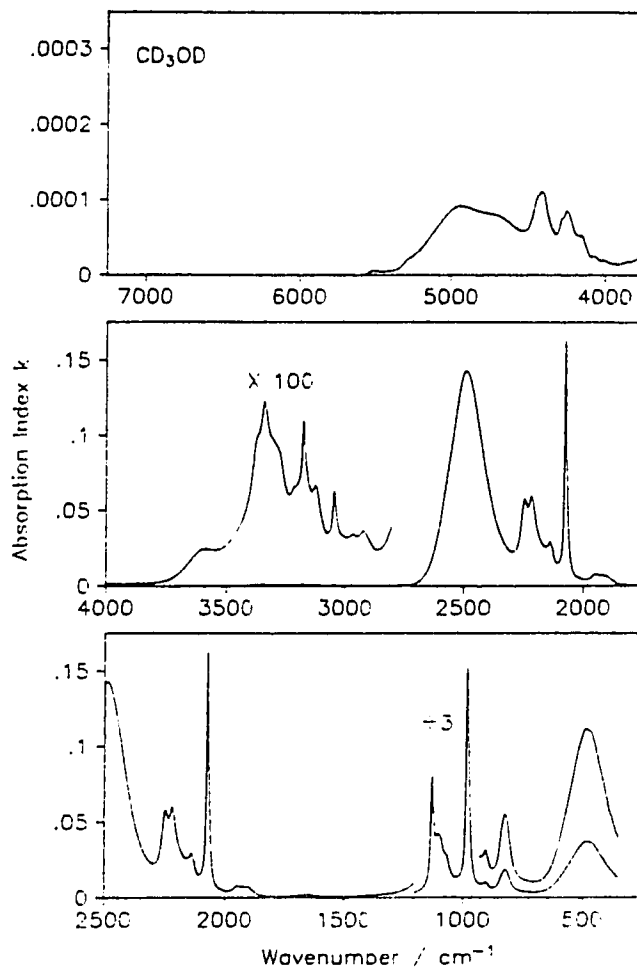


**Figure 7.4B** The absorption index spectrum of  $\text{CD}_3\text{OD}$  at  $25^\circ\text{C}$ . In the top box, the ordinate has been expanded 500 times. In the middle box, the ordinate labels must be divided by 100 for the upper curve. In the bottom box, the ordinate labels are for the upper curves and must be multiplied by 3 for the lower curve which extends from 1200 to 350  $\text{cm}^{-1}$ .

of accuracy by interpolation<sup>17</sup> and the  $n(\tilde{\nu})$  values can be obtained<sup>17</sup> without loss of accuracy from the  $k(\tilde{\nu})$  values by Kramers-Krönig transformation<sup>10</sup> with the value of  $n$  at 8000  $\text{cm}^{-1}$  given above.

The accuracy of the refractive index spectra obtained in this work is expected to be the same as for  $\text{CH}_3\text{OH}$ <sup>1</sup> and for  $\text{CH}_3\text{OD}$ <sup>2</sup>. Thus,  $k(\tilde{\nu})$  is estimated to be accurate to  $\pm 3\%$  except for  $\pm 10\%$  where  $k < 4 \times 10^{-5}$ . The estimated accuracy of  $n(\tilde{\nu})$  is  $\pm 0.5\%$ .



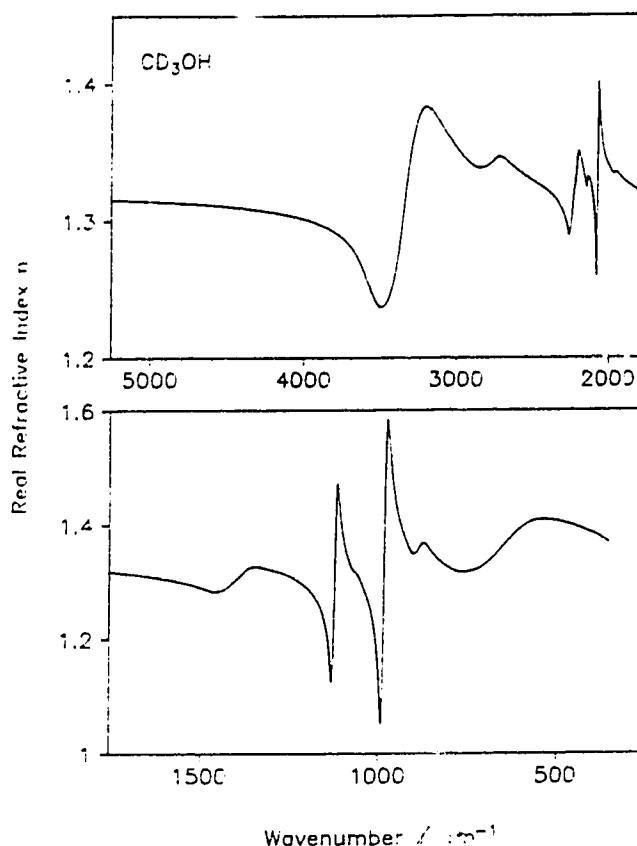


**Figure 7.5A** The real refractive index spectrum of methan- $d_3$ -ol at 25°C, obtained by Kramers-Krönig transformation of the  $k$  spectrum of Figure 7.4A with  $n(8000 \text{ cm}^{-1}) = 1.323$  and the  $k$  spectrum<sup>15</sup> of  $\text{CH}_3\text{OH}$  appended between 350 and 2  $\text{cm}^{-1}$ .

The spectra of other intensity quantities can be calculated from the refractive index spectra<sup>5</sup> and the molar concentration  $C=24.49 \text{ mol L}^{-1}$  for  $\text{CD}_3\text{OD}$  or  $C=24.59 \text{ mol L}^{-1}$  for  $\text{CD}_3\text{OH}$ , or their reciprocal, the molar volume. The peak wavenumbers of the major bands differ in the spectra of different intensity quantities as shown in Table 7.5. The table includes the peak values of the molar absorption coefficient and the imaginary dielectric constant. The real and imaginary dielectric constant spectra are of particular interest to physicists. They are not shown, partly to save space, partly because they are qualitatively the same as the real and imaginary refractive index spectra in Figures 7.4 and 7.5, and partly because they can be calculated<sup>5,17</sup> easily from the data in Tables 7.3 and 7.4.

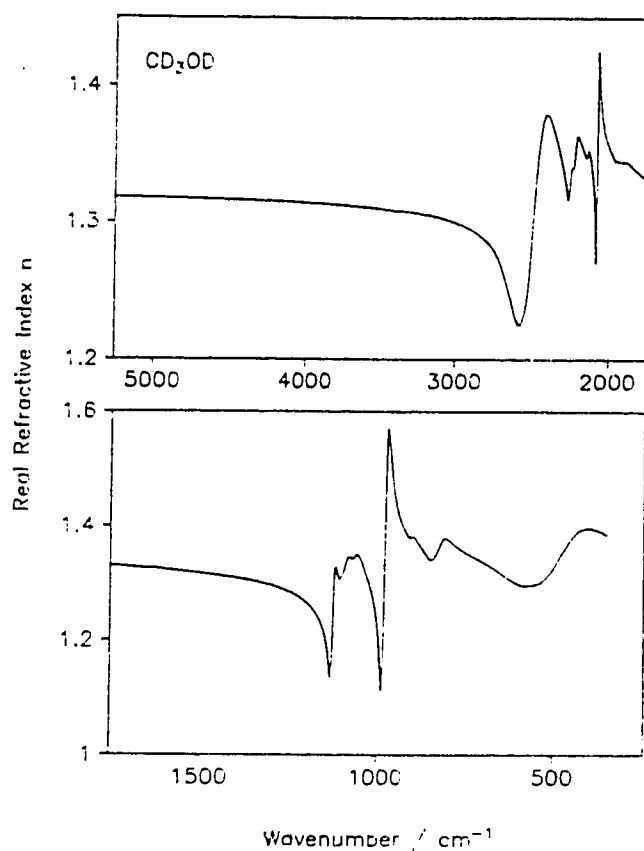


**Figure 7.5B** The real refractive index spectrum of methanol- $d_4$  at 25°C, obtained by Kramers-Krönig transformation of the  $k$  spectrum of Figure 7.4B with  $n(8000\text{ cm}^{-1}) = 1.322$  and the  $k$  spectrum<sup>15</sup> of  $\text{CH}_3\text{OH}$  appended between 350 and  $2\text{ cm}^{-1}$ .

**Table 7.2** Wavenumbers and refractive indices at the peaks in the  $k$  spectrum, the associated maxima and minima in the  $n$  spectrum, and regions of flat weak absorption.

CD <sub>3</sub> OH				CD <sub>3</sub> OD			
Spectral feature	$\tilde{\nu}/\text{cm}^{-1}$	$k(\tilde{\nu})$	$n(\tilde{\nu})$	Spectral feature	$\tilde{\nu}/\text{cm}^{-1}$	$k(\tilde{\nu})$	$n(\tilde{\nu})$
flat	8000	0 <sup>a</sup>	1.3204	flat	8000	0 <sup>a</sup>	1.3205
flat	7500	0 <sup>a</sup>	1.3200	flat	7000	0 <sup>a</sup>	1.3200
peak	6532	0.000082	1.3188	flat	6000	0 <sup>a</sup>	1.3192
peak	5526	0.000055	1.3165	peak	4933	0.000092	1.3175
peak	4791	0.000287	1.3130	peak	4407	0.000110	1.3161
peak	4427	0.000183	1.3097	peak	4244	0.000085	1.3155
peak	4399	0.000189	1.3093	peak	3588	0.000247	1.3111
peak	4246	0.000203	1.3071	peak	3340	0.001223	1.3082
peak	4065	0.000246	1.3033	peak	3176	0.001096	1.3056

(Cont'd on next page)

**Table 7.2 (Cont'd)**

CD <sub>3</sub> OH				CD <sub>3</sub> OD			
Spectral feature	$\tilde{\nu}/\text{cm}^{-1}$	$k(\tilde{\nu})$	$n(\tilde{\nu})$	Spectral feature	$\tilde{\nu}/\text{cm}^{-1}$	$k(\tilde{\nu})$	$n(\tilde{\nu})$
$n$ minimum	3487	0.05318	1.237	peak	3124	0.000671	1.3045
$\nu(\text{OH})$ peak	3342	0.1301	1.311	peak	3045	0.000633	1.3020
$n$ maximum	3207	0.06592	1.384	peak	2921	0.000368	1.2967
$n$ minimum	2838	0.01576	1.339	$n$ minimum	2577	0.05923	1.225
$2\delta(\text{COH})$ peak	2776	0.01822	1.342	$\nu(\text{OD})$ peak	2488	0.1430	1.301
$n$ maximum	2716	0.01234	1.347	$n$ maximum	2401	0.07246	1.380
flat	2500	0.01497	1.330	$n$ minimum	2259	0.04136	1.317
$n$ minimum	2256	0.03050	1.289	$\nu(\text{CD})$ peak	2244	0.05777	1.333
$\nu(\text{CD})$ peak	2234	0.05427	1.313	$n$ maximum	2234	0.05293	1.340
$\nu(\text{CD})$ peak	2215	0.05286	1.333	$n$ minimum	2227	0.05307	1.340
$n$ maximum	2197	0.03279	1.351	$\nu(\text{CD})$ peak	2215	0.06007	1.350
$n$ minimum	2143	0.01652	1.325	$n$ maximum	2198	0.04363	1.364
$2\delta(\text{CD}_3)$ peak	2138	0.02066	1.329	$n$ minimum	2143	0.02778	1.347
$n$ maximum	2131	0.01682	1.332	$2\delta(\text{CD}_3)$ peak	2137	0.02965	1.349
$n$ minimum	2076.9	0.075 <sup>b</sup>	1.260	$n$ maximum	2128	0.02505	1.353
$\nu(\text{CD})$ peak	2072.1	0.1474	1.324 <sup>b</sup>	$n$ minimum	2076.9	0.084 <sup>b</sup>	1.271
$n$ maximum	2066.3	0.075 <sup>b</sup>	1.401	$\nu(\text{CD})$ peak	2071.1	0.1630	1.357 <sup>b</sup>
flat	2000	0.00340	1.341	$n$ maximum	2066.3	0.095 <sup>b</sup>	1.425
$n$ minimum	1964	0.00502	1.334	$2\nu(\text{CO})$ peak	1944	0.007949	1.3454
$2\nu(\text{CO})$ peak	1956	0.00578	1.335	$2\gamma(\text{CD}_3)$ peak	1910	0.007269	1.345
$n$ maximum	1948	0.00481	1.335	$2\delta(\text{COD})$ peak	1650	0.002066	1.327
flat	1900	0.00156	1.330	flat	1400	0.001427	1.309
$2\gamma(\text{CD}_3)$ peak	1773	0.00250	1.320	$n$ minimum	1132.0	0.126 <sup>b</sup>	1.136
$n$ minimum	1453	0.03235	1.283	$\delta(\text{CD}_3)$ peak	1124.2	0.2398	1.237 <sup>b</sup>
$\delta(\text{COH})$ peak	1392	0.05534	1.308	$n$ maximum	1117.5	0.164 <sup>b</sup>	1.329
$n$ maximum	1346	0.03896	1.327	$n$ minimum	1105	0.1226	1.307
$n$ minimum	1129.1	0.177 <sup>b</sup>	1.124	$\delta(\text{CD}_3)$ peak	1096	0.1272	1.317
$\delta(\text{CD}_3)$ peak	1121.4	0.3362	1.299 <sup>b</sup>	$n$ maximum	1080	0.1013	1.346
$n$ maximum	1113.6	0.168 <sup>b</sup>	1.473	$\delta(\text{CD}_3)$ peak	1065	0.08523	1.346
$\delta(\text{CD}_3)$ peak	1068	0.03104	1.320	$n$ minimum	983.2	0.237 <sup>b</sup>	1.112
Shoulder	1031	0.02867	1.273	$\nu(\text{CO})$ peak	971.7	0.4550	1.330 <sup>b</sup>
$n$ minimum	990.3	0.268 <sup>b</sup>	1.052	$n$ maximum	969.1	0.229 <sup>b</sup>	1.571
$\nu(\text{CO})$ peak	981.6	0.5038	1.355 <sup>b</sup>	$n$ minimum	904.4	0.03075	1.380
$n$ maximum	973.9	0.273 <sup>b</sup>	1.584	$\gamma(\text{CD}_3)$ peak	901.6	0.03136	1.380
$n$ minimum	897.7	0.04933	1.349	$n$ maximum	896.7	0.02890	1.382
$\gamma(\text{CD}_3)$ peak	885.2	0.05806	1.359	$n$ minimum	843.7	0.03756	1.341
$n$ maximum	872.6	0.04690	1.368	$\delta(\text{COD})$ peak	823.5	0.05518	1.359
$n$ minimum	759.8	0.06370	1.317	$n$ maximum	803.2	0.03599	1.379
$\nu(\text{OH})$ peak	649.9	0.1086	1.362	$n$ minimum	571.8	0.5458	1.296
$n$ maximum	540.9	0.06708	1.409	$\tau(\text{OD})$ peak	483.1	0.1119	1.344
low $\text{cm}^{-1}$	400.2	0.02812	1.386	$n$ maximum	405.0	0.07095	1.397
	350.0	0.02758	1.369	low $\text{cm}^{-1}$	350.0	0.04007	1.384

a Zero means that  $k < 4 \times 10^{-6}$ .

b This value is sensitive to wavenumber.

**Table 7.3** Values of  $k(\nu)$ , the absorption index, between 8000 and 350  $\text{cm}^{-1}$  for methan- $d_3$ -ol,  $\text{CD}_3\text{OH}$ , at 25  $^\circ\text{C}$ .<sup>a,b</sup>

$\text{cm}^{-1}$	$XE$	$YE$	0	1	2	3	4	5	6	7	8	9	10	11	12	13	14	15	16
8000.24	5	-7	0	0	0	0	0	0	0	0	0	0	0	0	0	0	0	0	0
7475.70	5	-7	0	0	0	0	0	0	0	0	41	54	86	141	188	228	268	309	352
6951.15	5	-7	398	443	489	531	579	621	654	690	721	752	775	806	815	822	821	817	819
6426.61	5	-7	808	780	740	695	666	642	619	597	579	558	540	525	508	482	448	416	390
5902.07	5	-7	369	354	344	344	353	372	400	434	467	501	528	542	547	559	511	465	428
5392.95	4	-7	406	383	361	344	328	314	299	285	270	254	244	237	234	224	225	240	253
5130.68	4	-7	253	255	265	277	293	315	350	390	443	505	578	675	781	907	1055	1250	1524
4868.41	4	-7	1852	2176	2447	2674	2812	2872	2834	2734	2592	2427	2247	2065	1884	1721	1570	1438	1321
4606.14	4	-7	1221	1138	1074	1031	1016	1023	1057	1113	1205	1347	1569	1792	1837	1871	1864	1684	1581
4343.87	4	-7	1561	1565	1577	1673	1862	1986	2024	2040	2011	1933	1928	2030	2127	2269	2350	2325	2387
4081.59	4	-7	2449	2463	2429	2294	2151	1985	1804	1630	1493	1381	1297	1241	1209	1200	1221	1274	1347
3819.32	4	-7	1463	1641	1896	2243	2700	3273	3958	4741	5721								
3694.94	0	-7	5793	5881	5952	6030	6117	6204	6289	6380	6487	6591	6703	6837	6943	7062	7206	7293	7418
3678.55	0	-6	760	775	787	806	870	886	908	930	953	977	999	1024	1049	1078	1107	1135	1163
3662.15	0	-6	1194	1231	1261	1293	1330	1367	1406	1443	1483	1525	1567	1610	1657	1705	1752	1800	1852
3645.76	0	-6	1904	1958	2012	2067	2126	2185	2247	2310	2371	2428	2543	2580	2651	2786	2850	2925	3007
3629.37	0	-6	3086	3190	3263	3365	3494	3564	3664	3774	3854	3972	4085	4176	4285	4411	4517	4652	4796
3612.98	0	-6	4879	5008	5144	5254	5401	5539	5669	5809	5953	6091	6246	6399	6548	6705	6835	7006	7189
3589.84	3	-5	866	1029	1221	1435	1682	1958	2269	2607	2969	3360	3771	4205	4657	5135	5629	6140	6653
3458.70	3	-4	716	766	816	865	916	967	1017	1067	1115	1160	1199	1234	1263	1284	1296	1300	1297
3327.56	3	-4	1287	1268	1246	1219	1189	1152	1113	1072	1027	978	929	880	831	783	734	688	643
3196.43	3	-5	5991	5579	5204	4955	4573	4207	3897	3627	3388	3179	2980	2780	2586	2409	2255	2113	1987
3065.29	3	-5	1885	1801	1735	1630	1519	1444	1381	1326	1279	1235	1198	1171	1149	1134	1124	1118	1116
2934.16	3	-5	1121	1130	1148	1170	1195	1228	1267	1310	1356	1404	1452	1501	1551	1602	1647	1690	1730
2803.02	3	-5	1764	1792	1812	1821	1819	1802	1766	1707	1624	1521	1400	1268	1133	1001	877	764	665
2671.89	3	-6	5798	5070	4456	3938	3505	3148	2828	2570	2353	2168	2026	1903	1794	1716	1665	1620	1590
2540.75	3	-6	1561	1553	1540	1521	1515	1499	1478	1462	1437	1409	1391	1393	1404	1441	1480	1527	1597
2409.61	3	-6	1676	1774	1884	2018	2190	2369	2566	2805	3063								
2346.94	0	-6	3098	3132	3170	3209	3246	3287	3326	3363	3405	3450	3488	3526	3564	3611	3665	3706	3748
2330.55	0	-6	3800	3852	3900	3948	4094	4158	4211	4280	4354	4420	4488	4559	4636	4730	4811	4897	4998
2311.26	2	-5	536	579	628	684	750	824	910	1008	1124	1260	1429	1642	1935	2346	2896	3534	4134
2245.69	2	-5	4619	5022	5321	5427	5338	5198	5152	5230	5286	5148	4742	4152	3550	3030	2600	2243	1951
2183.02	0	-5	1888	1828	1732	1679	1629	1582	1538	1496	1456	1420	1385	1352	1323	1295	1268	1243	1221
2165.66	1	-5	1180	1146	1118	1098	1085	1084	1096	1125	1178	1262	1384	1552	1757	1951	2161	2342	1932
2132.88	1	-5	1801	1682	1576	1475	1374	1279	1192	1118	1057	1010	976	956	948	951	964	985	1015
2101.06	0	-5	1034	1056	1079	1105	1134	1167	1203	1243	1288	1339	1397	1464	1541	1629	1735	1862	2014
2084.67	0	-4	220	243	272	313	363	428	512	620	753	912	1089	1262	1402	1474	1459	1358	1201
2068.28	0	-4	1033	879	752	652	572	507	451	401	356	317	282	253	228	207	188	172	157
2051.88	0	-5	1450	1339	1241	1156	1081	1016	960	910	868	831	798	770	744	720	698	675	654
2035.49	0	-6	6333	6127	5924	5721	5531	5356	5173	4999	4845	4701	4576	4469	4378	4147	4085	4031	3981
2018.14	1	-6	3897	3832	3788	3756	3734	3706	3669	3612	3534	3446	3348	3254	3168	3095	3035	2995	2975
1985.35	1	-6	2974	3002	3051	3132	3247	3393	3577	3799	4062	4362	4687	5020	5341	5585	5742	5780	5705
1952.57	1	-6	5527	5274	4970	4642	4313	4000	3705	3435	3194	2981	2789	2622	2472	2337	2219		
1917.85	3	-6	1876	1678	1576	1528	1514	1519	1523	1528	1536	1556	1589	1630	1688	1763	1855	1968	2122
1786.72	3	-6	2309	2443	2516	2545	2555	2575	2613	2667	2744	2850	2969	3097	3237	3387	3552	3720	3888
1659.44	2	-6	3968	4051	4134	4221	4305	4399	4499	4597	4703	4815	4929	5055	5182	5316	5456	5604	5838
1593.87	2	-5	600	617	635	654	673	696	717	741	765	791	819	847	878	910	945	982	1022
1524.45	3	-5	1110	1212	1329	1467	1633	1832	2074	2365	2717	3122	3578	4035	4463	4830	5117	5329	5466
1393.31	3	-5	5532	5510	5375	5124	4757	4346	3943	3588	3293	3055	2858	2699	2560	2425	2293	2180	2067
1262.18	3	-5	1954	1839	1744	1661	1592	1532	1500	1486	1493	1521	1578	1693	1846				
1168.65	0	-5	1870	1896	1922	1949	1977	2005	2037	2073	2110	2149	2190	2235	2287	2344	2408	2474	2545
1152.25	0	-5	2628	2718	2818	2924	3039	3167	3306	3464	3637	3829	4050	4299	4580	4907	5299	5759	6306
1135.86	0	-4	696	776	876	995	1151	1334	1531	1774	2036	2301	2567	2805	3016	3187	3303	3362	3343
1119.47	0	-4	3233	3043	2790	2501	2208	1930	1681	1464	1277	1118	985	875	784	708	646	594	550
1102.11	1	-5	4808	4247	3801	3466	3225	3060	2950	2880	2818	2756	2720	2715	2744	2797	2873	2957	3035
1069.33	1	-5	3087	3106	3091	3045	2975	2895	2810	2733	2666	2612	2572	2544	2529	2525	2538	2559	2603
1036.55	1	-5	2658	2729	2800	2867	2922	2976	3040	3115	3208	3330	3472	3651	3863	4131	4451	4848	5346
1004.73	0	-4	564	598	636	680	731	790	860	944	1044	1165	1313	1495	1718	1989	2310	2679	3077
988.33	0	-4	3482	3883	4257	4571	4787	4933	5033	5038	4945	4762	4497	4154	3779	3414	3061	2732	2440
971.94	0	-4	2181	1951	1747	1568	1409	1269	1147	1039	946	866	796	737	686	641	603	570	540
955.55	0	-5	5139	4905	4700	4516	4350	4201	4069	3951	3841	3740	3647	3554	3472				
936.27	3	-5	3065	2931	2985	3279	3932	4933	5670	5701	4934	4018	3428	3182	3123	3192	3333	3522	3763
805.13	3	-4	405	438	474	513	554	598	643	688	731	772	813	853	894	932	966	998	1025
673.99	3	-4	1051	1069	1082	1086	1083	1075	1061	1041	1019	988	957	920	882	842	802	760	719
542.86	3	-5	6808	6439	6105	5770	5459	5184	4894	4647	4403	4198	3999	3795	3614	3443	3299	3171	3047
411.72	3	-5	2962	2864	2761	2725	2655	2614	2611	2655	2758								

Note: Footnotes a and b follow Table 7.4.

**Table 7.4** Values of  $k(\nu)$ , the absorption index or imaginary refractive index, between 8000 and 350  $\text{cm}^{-1}$  for methanol- $d_4$ ,  $\text{CD}_3\text{OD}$ , at 25  $^\circ\text{C}$ .<sup>a,b</sup>

$\text{cm}^{-1}$	$\text{XE}$	$\text{YE}$	0	1	2	3	4	5	6	7	8	9	10	11	12	13	14	15	16
8000.24	7	-7	0	0	0	0	0	0	0	0	0	0	0	0	0	0	0	0	0
5994.63	5	-7	0	0	0	0	0	0	0	0	0	0	0	0	0	0	0	10	39
5470.09	5	-7	54	47	53	61	82	138	208	250	296	354	431	525	609	689	771	841	891
4945.55	5	-7	921	923	905	879	861	840	827	817	801	768	722	671	625	592	602		
4505.86	3	-7	615	638	673	720	781	846	915	977	1026	1059	1081	1096	1105	1108	1086	1025	937
4374.72	3	-7	848	771	708	656	617	586	562	544	542	566	620	694	747	764	779	813	848
4243.58	3	-7	859	840	794	740	684	628	583	551	537	536	529	520	528	518	459	406	369
4112.45	3	-7	323	283	260	246	243	245	252	252	236	217	201	196	197	200	200	194	188
3987.10	1	-7	185	183	180	178	176	173	172	169	167	165	163	162	160	159	159	157	157
3954.31	1	-7	156	155	156	154	155	154	154	154	153	154	153	152	152	150	150	149	149
3921.53	1	-7	149	147	148	147	146	147	146	147	146	146	147	146	147	147	148	149	149
3888.75	1	-7	151	152	152	154	155	157	158	160	162	162	165	167	168	170	171	173	174
3850.18	3	-7	176	175	176	176	181	186	195	207	221	241	252	288	318	351	391	434	486
3719.04	3	-7	548	621	711	818	940	1073	1212	1359	1508	1657	1803	1947	2086	2215	2324	2406	2455
3587.90	3	-7	2472	2465	2445	2419	2400	2393	2388	2400	2436	2490	2564	2656	2766	2897	3044	3207	3386
3456.77	3	-7	3582	3799	4039	4311	4626	4996	5445	6014	6712	7482							
3383.49	2	-6	836	895	945	980	999	1011	1027	1055			1196	1222	1217	1185	1139	1093	1055
3317.92	2	-6	1025	1006	993	984	977	968	956	94			917	899	872	836	794	752	713
3252.35	2	-7	6792	6510	6296	6146	6071	6066	6130	624			597	6636	6678	6757	6880	7045	7301
3186.78	2	-6	784	900	1056	1085	975	862	785	71			647	633	628	632	644	661	671
3121.22	2	-7	6639	6368	5981	5563	5163	4792	4457	411			3634	3552	3514	3515	3558	3666	3890
3055.65	2	-7	4313	5039	5953	6331	5771	4988	4395	4003			3483	3414	3364	3326	3287	3249	3219
2990.08	2	-7	3202	3201	3223	3267	3338	3408	3448	3443	3401	3347	3301	3275	3290	3339	3420	3514	3599
2924.51	2	-7	3665	3689	3660	3574	3454	3326	3199	3079	2971	2865	2762	2658	2573	2503	2445	2407	2389
2858.94	2	-7	2388	2408	2437	2470	2518	2589	2667	2751	2849	2969	3099	3245	3399	3565	3732	3900	4067
2793.38	2	-7	4225	4366	4492	4592	4674	4731	4765	4788	4806	4821	4857	4921	5023	5176	5397	5700	6114
2729.74	1	-6	636	665	697	734	772	815	869	923	977	1049	1130	1230	1318	1434	1561	1682	1824
2696.95	1	-6	1952	2107	2259	2435	2610	2800	2995	3215	3434	3685	3945	4221	4506	4815	5127	5462	5849
2662.24	2	-5	662	750	849	958	1080	1214	1363	1529	1710	1909	2125	2360	2610	2878	3158	3449	3753
2596.67	2	-4	407	440	476	513	552	592	634	675	717	759	800	841	883	925	968	1013	1058
2527.25	3	-4	1151	1239	1318	1377	1415	1430	1423	1397	1356	1303	1239	1167	1088	1005	920	835	754
2396.11	3	-5	6778	6081	5457	4903	4413	3984	3610	3285	2998	2756	2555	2404	2303	2258	2287	2410	2691
2268.83	2	-5	2942	3317	3835	4459	5061	5524	5763	5723	5504	5293	5234	5255	5612	5896	6007	5829	5422
2203.26	2	-5	4922	4467	4076	3760	3498	3283	3109	2965	2844	2746	2671	2619	2593	2593	2630	2715	2847
2139.62	1	-5	2916	2960	2957	2900	2791	2654	2505	2352	2200	2055	1922	1807	1710	1637	1584	1547	1521
2106.84	1	-4	151	151	152	155	159	165	172	181	193	207	228	257	303	377	501	702	1002
2074.06	1	-4	1362	1608	1565	1266	949	727	576	458	366	297	246	208	179	155	138	124	112
2035.49	3	-6	8166	6692	5981	5590	5056	4563	4331	4335	4670	5377	6461	7570	7944	7648	7383	7306	7287
1904.35	5		7128	6670	5917	4990	4001	3076	2332	1799	1436	1193	1026	911	826	760	717	703	697
1773.27			690	693	708	738	783	835	889	954	1039	1146	1280	1434	1606	1777	1928	2031	2066
1647.27			17	1874	1641	1368	1112	928	797	709	652	617	596	584	578	574	585	594	610
1511.27			29	650	673	701	734	774	815	857	906	962	1028	1105	1192	1291	1391	1485	1570
1375.27			1646	1715	1786	1865	1967	2086	2138	2242	2385	2534	2657	2803	2990	3221	3496	3824	4188
1254.46			784	4385	4507	4617	4734	4828	4952	5040	5230	5335	5448	5609	5760	5925	6083	6278	6477
1221.67	1		668	689	712	732	759	777	808	835	862	890	914	939	970	995	1026	1058	1092
1188.89	1		1126	1160	1202	1245		1335	1383	1432	1486	1547	1613	1687	1769	1860	1964	2079	2206
1156.11	1	-4	235	252	271	294	320	350	386	432	492	573	690	860	1100	1433	1792	2121	2349
1123.32	1	-4	2385	2193	1900	1642	1473	1330	1259	1225	1216	1221	1232	1246	1258	1267	1272	1269	1260
1090.54	1	-4	1241	1213	1176	1132	1083	1036	992	954	924	903	891	881	873	861	842	813	777
1057.75	1	-5	7361	6933	6511	6118	5759	5438	5156	4910	4700	4520	4372	4248	4150	4071	4011	3974	3950
1024.97	1	-5	3947	3957	3989	4034	4098	4175	4274	4395	4545	4732	4963	5251	5612	6068	6666	7459	8545
993.15	0	-4	924	1008	1108	1231	1378	1561	1780	2044	2370	2697	3032	3398	3730	4037	4280	4451	4550
976.76	0	-4	4538	4422	4211	3915	3571	3217	2874	2565	2286	2043	1830	1643	1478	1334	1207	1095	998
960.37	0	-5	9131	8395	7758	7209	6733	6313	5947	5625	5340	5082	4852	4647	4461	4295	4147	4010	3885
943.97	0	-5	3775	3672	3577	3491	3411	3338	3269	3206	3149	3095	3046	3002	2960	2920	2887	2856	2826
924.69	2	-5	2737	2688	2685	2740	2862	3035	3136	2971	2616	2299	2090	1968	1907	1889	1904	1956	2056
859.12	2	-5	2219	2453	2803	3235	3756	4285	4763	5132	5385	5509	5487	5291	4920	4413	3863	3346	2907
793.55	2	-5	2549	2265	2039	1862	1724	1625	1515	1441	1380	1327	1283	1244	1212	1184	1162	1140	1122
727.99	2	-5	1106	1089	1073	1064	1055	1052	1049	1046	1047	1050	1055	1066	1082	1102	1134	1174	1222
662.42	2	-5	1278	1337	1404	1479	1563	1658	1763	1885	2017	2162	2315	2483	2665	2861	3068	3283	3509
596.85	2	-5	3748	3996	4256	4518	4777	5046	5319	5597	5877	6159	6440	6720	7020	7326	7623	7933	8251
531.28	2	-4	856	886	915	944	973	998	1023	1046	1065	1086	1103	1113	1117	1117	1115	1110	1104
465.71	2	-4	1101	1097	1083	1063	1039	1017	992	964	936	907	876	847	817	790	768	737	700
402.07	1	-5	6846	6738	6620	6478	6324	6145	5998	5870	5743	5686	5666	5478	5395	5335	5203	5044	4982
369.29	1	-5	4919	4846	4741	4654	4458	4337	4305	4281	4197	4194	4207						

Note: Footnotes a and b are on next page.

**Table 7.5** The peak positions and peak intensities of the major bands in different representations of the absorption spectra of CD<sub>3</sub>OH and CD<sub>3</sub>OD. <sup>a</sup>

Band	Type of spectrum					
	pATR	<i>k</i> <sup>b</sup>	<i>E</i> <sub>m</sub> <sup>c</sup>		ε'' <sup>c</sup>	α'' <sub>m</sub>
<b>CD<sub>3</sub>OH</b>						
ν(OH)	3318	3342	3345 (96.5)		3334 (0.342)	3350
ν(CD)	2232.5	2234.3	2234.5 (26.9)		2233.8 (0.143)	2234.8
ν(CD)	2213.7	2215.0	2215.2 (26.0)		2214.5 (0.141)	2215.4
ν(CD)	2070.9	2071.8	2071.8 (68.0)		2071.5 (0.395)	2072.1
δ(COH)	1386	1392	1393 (17.1)		1388 (0.145)	1393
δ(CD <sub>3</sub> )	1118.0	1121.2	1121.2 (83.7)		1120.2 (0.896)	1122.2
δ(CD <sub>3</sub> )	1068.0	1067.6	1068.0 (7.36)		1067.8 (0.0820)	1067.4
ν(CO)	976.6	982.0	982.1 (110.0)		980.3 (1.391)	984.1
γ(CD <sub>3</sub> )	884.7	885.5	886.0 (11.4)		885.3 (0.158)	885.8
τ(DCOH)	626	650	662 (15.8)		645 (0.296)	653
<b>CD<sub>3</sub>OD</b>						
ν(OD)	2470	2488	2489 (79.3)		2483 (0.373)	2491
ν(CD)	2243.2	2244.4	2244.5 (28.9)		2244.1 (0.154)	2244.7
ν(CD)	2213.9	2215.0	2215.2 (29.7)		2214.6 (0.162)	2215.4
ν(CD)	2070.2	2071.4	2071.4 (75.4)		2071.1 (0.442)	2071.7
δ(CD <sub>3</sub> )	1122.1	1124.0	1124.0 (60.1)		1123.3 (0.602)	1124.6
δ(CD <sub>3</sub> )	1092.1	1096.1	1096.6 (31.1)		1094.8 (0.335)	1096.8
ν(CO)	972.7	977.4	977.4 (99.3)		976.0 (1.264)	978.8
γ(CD <sub>3</sub> )	901.6	901.8	902.0 (6.30)		901.8 (0.0866)	901.8
δ(COD)	820.9	823.0	823.6 (10.1)		822.5 (0.50)	823.5
τ(DCOD)	459	483	490 (12.1)		477 (0.301)	485

- a The peak positions, in cm<sup>-1</sup> units; obtained from a parabolic fit of the peaks.  
b Some of the peak wavenumbers in this column differ slightly from those in Table 7.2 that were taken at the closest digitized point in the *k* spectrum.  
c The numbers in parentheses are the values of the molar absorption coefficient, *E*<sub>m</sub>, in the unit of 10<sup>3</sup> cm<sup>2</sup> mol<sup>-1</sup>, or the values of imaginary dielectric constant, ε'', at the peak wavenumbers.

**Footnotes to Tables 7.3 and 7.4:**

a) The column headed cm<sup>-1</sup> contains the wavenumber of the first *k*( $\tilde{\nu}$ ) value in the row. The columns headed *XE* and *YE* contain the X-Exponent and the Y-Exponent, respectively, for the row. The columns headed 0, 1, 2, ..., 16, contain the ordinate values, and the headings give the indices of the ordinate values in the row. In a row which starts with  $\tilde{\nu}(0)$ , the wavenumber corresponding to the ordinate indexed *J* is  $\tilde{\nu}(J) = \tilde{\nu}(0) - \frac{15798.002}{16384} \cdot J \cdot 2^{XE}$ .

The *k*( $\tilde{\nu}$ ) values in that row are the ordinate value shown times 10<sup>YE</sup>. Thus the entry indexed 16 in the third row of Table 7.3 shows that  $k = 819 \times 10^{-7} = 8.19 \times 10^{-5}$  at  $\tilde{\nu} = 6951.15 - \frac{15798.002}{16384} \cdot 16 \cdot 2^5 = 6951.15 - 6.6 \approx 6944.55$  cm<sup>-1</sup>.

b) The *k*( $\tilde{\nu}$ ) values in Table 7.3 can be interpolated by the program TRECOVER<sup>17</sup> to the original wavenumber spacing, 0.96423 cm<sup>-1</sup>, and yield the original *k*( $\tilde{\nu}$ ) values accurate to 3% above 7070 cm<sup>-1</sup> and 1% below 7070 cm<sup>-1</sup> except for 2% at a few points between 5210 and 5050 cm<sup>-1</sup>, where *k*( $\tilde{\nu}$ ) values are smaller than 3x10<sup>-5</sup>. For Table 7.4, the interpolation recovers the original *k*( $\tilde{\nu}$ ) values accurate to 5% above 5290 cm<sup>-1</sup> and 1% below 5290 cm<sup>-1</sup>.

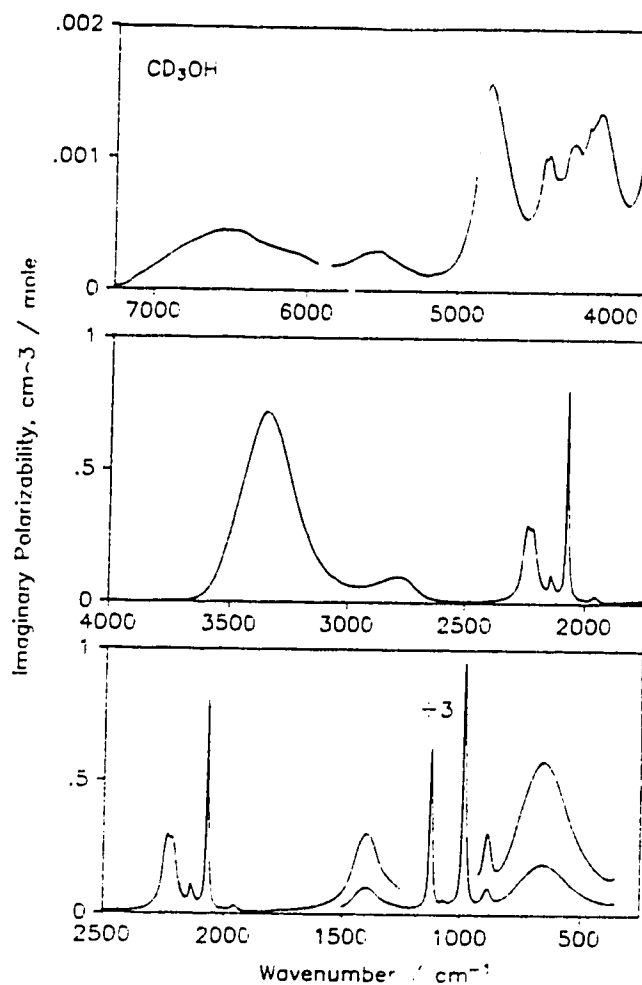


**Figure 7.6A** The imaginary molar polarizability spectra of CD<sub>3</sub>OH at 25°C, calculated from the refractive index spectra in Figures 7.4A and 7.5A under the assumption of the Lorentz local field. The units of  $\alpha''_m$  are cm<sup>3</sup> mol<sup>-1</sup>. In the top box, the ordinate has been expanded 500 times. In the bottom box, the ordinate labels are for the upper curves and must be multiplied by 3 for the lower curve which extends from 1500 to 350 cm<sup>-1</sup>.

The intensity spectrum that is the most directly related to theory, albeit through the approximation of the Lorentz local field, is the imaginary molar polarizability spectrum<sup>5,18,19</sup>,  $\alpha''_m(\tilde{\nu})$ . This was calculated<sup>5</sup> for each compound from the refractive index spectra in Figures 7.4 and 7.5 and the molar volume at 25°C, 40.66 mL mol<sup>-1</sup> for CD<sub>3</sub>OH and 40.83 mL mol<sup>-1</sup> for CD<sub>3</sub>OD. The  $\alpha''_m$  spectra are shown in the units cm<sup>3</sup> mol<sup>-1</sup> in Figure 7.6A for CD<sub>3</sub>OH and Figure 7.6B for CD<sub>3</sub>OD.

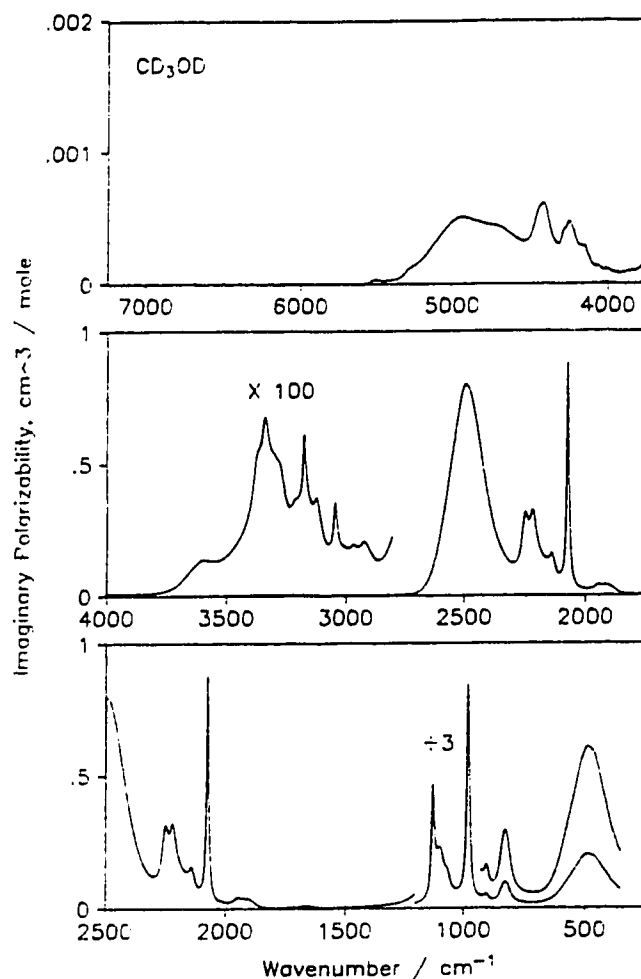


**Figure 7.6B** The imaginary molar polarizability spectra of  $\text{CD}_3\text{OD}$  at  $25^\circ\text{C}$ , calculated from the refractive index spectra in Figures 7.4B and 7.5B under the assumption of the Lorentz local field. The units of  $\alpha_m''$  are  $\text{cm}^3 \text{mol}^{-1}$ . In the top box, the ordinate has been expanded 500 times. In the middle box, the ordinate labels must be divided by 100 for the upper curve. In the bottom box, the ordinate labels are for the upper curves and must be multiplied by 3 for the lower curve which extends from 1200 to  $350 \text{ cm}^{-1}$ .

The densities<sup>14</sup> of  $\text{CD}_3\text{OH}$  and  $\text{CD}_3\text{OD}$  are  $0.867$  and  $0.888 \text{ g mL}^{-1}$  at  $20^\circ\text{C}$  respectively. That of  $\text{CH}_3\text{OH}$  is  $0.79134 \text{ g mL}^{-1}$  at  $20^\circ\text{C}$  and  $0.78660 \text{ g mL}^{-1}$  at  $25^\circ\text{C}$ <sup>20</sup>. The densities of  $\text{CD}_3\text{OH}$  and  $\text{CD}_3\text{OD}$  were taken to be  $0.8623$  and  $0.8833 \text{ g mL}^{-1}$  at  $25^\circ\text{C}$  on the assumption that the temperature dependence is the same for  $\text{CH}_3\text{OH}$ ,  $\text{CD}_3\text{OH}$  and  $\text{CD}_3\text{OD}$ . The molar concentration and volume at  $25^\circ\text{C}$  are, thus,  $24.59 \text{ mol L}^{-1}$  and  $40.66 \text{ cm}^3 \text{mol}^{-1}$  for  $\text{CD}_3\text{OH}$  and  $24.49 \text{ mol L}^{-1}$  and  $40.83 \text{ cm}^3 \text{mol}^{-1}$  for  $\text{CD}_3\text{OD}$ , respectively.



## 7.4 Integrated Intensities

It was noted in Section 7.1 that the separation of the area under the absorption spectrum into integrated intensities of different vibrations could not be carried out with confidence from a single spectrum, but the availability of the spectra of both  $\text{CH}_3\text{OH}$  and  $\text{CH}_3\text{OD}$  enabled the integrated intensities to be determined with an accuracy of about 5%<sup>1,2</sup>. In particular, for all the stretching bands in  $\text{CH}_3\text{OH}$  and  $\text{CH}_3\text{OD}$ , the accuracy of the integrated intensities is believed close to the  $\pm 3\%$  accuracy of the absorption index<sup>2</sup>. In this section, the integrated intensities  $C_j$  under bands in the  $\tilde{\nu}\alpha''_m$  spectrum are obtained for the C–D, O–H, and O–D stretching, the C–O–H in-plane bending, and the torsion, vibrations of  $\text{CD}_3\text{OH}$  and  $\text{CD}_3\text{OD}$ . Except where specified, the areas are measured above zero ordinate.

### 7.4.1 The C–D, O–H and O–D Stretching Bands

The C–D, O–H and O–D stretching regions of the  $\tilde{\nu}\alpha''_m$  spectra of  $\text{CD}_3\text{OH}$  and  $\text{CD}_3\text{OD}$  are shown as curves H and D, respectively, in Figure 7.7 (top). For  $\text{CD}_3\text{OH}$ , the C–D and O–H stretching bands are completely separated by the minimum at  $2455\text{ cm}^{-1}$ , Figure 7.7 (middle). In the C–D stretching region, the total area above zero ordinate is  $0.97\text{ km mole}^{-1}$  between  $2455\text{ cm}^{-1}$  and  $1870\text{ cm}^{-1}$ , where  $1870\text{ cm}^{-1}$  also corresponds to a minimum in  $\tilde{\nu}\alpha''_m$ . This region includes two weak bands, the overtone or combination of the  $\text{CD}_3$  deformations at  $2138\text{ cm}^{-1}$ , and the overtone of the C–O stretch at  $1956\text{ cm}^{-1}$ . The integrated intensity  $C_j$  is  $0.02\text{ km mol}^{-1}$  for the band at  $2138\text{ cm}^{-1}$ , measured above the dashed line between the curve points at  $2156$  and  $2110\text{ cm}^{-1}$  in Figure 7.7 (middle). This intensity is included in the C–D intensity, because it may originate from Fermi resonance of the overtone with the surrounding C–D stretching fundamentals.  $C_j$  of  $2\nu(\text{CO})$  is  $0.01\text{ km mol}^{-1}$ , measured above the line drawn between the curve points at  $1986$  and  $1870\text{ cm}^{-1}$  in Figure 7.7 (middle). This band is more separated from the fundamentals and its intensity is taken to be intrinsic to the overtone, leaving  $C_j = 0.96\text{ km mol}^{-1}$  as the intensity of the C–D stretching vibrations. These values are summarized in Table 7.6 for the C–D stretches and in Table 7.7 for  $2\nu(\text{CO})$ .

The total area between  $3880$  and  $2455\text{ cm}^{-1}$  (Figure 7.7, middle) is  $C_j = 7.65\text{ km mol}^{-1}$ . This is close to the  $7.69\text{ km mol}^{-1}$  found previously<sup>2</sup> for the O–H stretching band of  $\text{CH}_3\text{OH}$ . A broad band at  $2783\text{ cm}^{-1}$ , which is hidden under the C–H stretching bands in the spectrum of  $\text{CH}_3\text{OH}$ <sup>1,2</sup>, is assigned<sup>21</sup> to  $2\delta(\text{COH})$ , the overtone of the C–O–H in-plane bend. The area above the dashed line drawn between the curve points

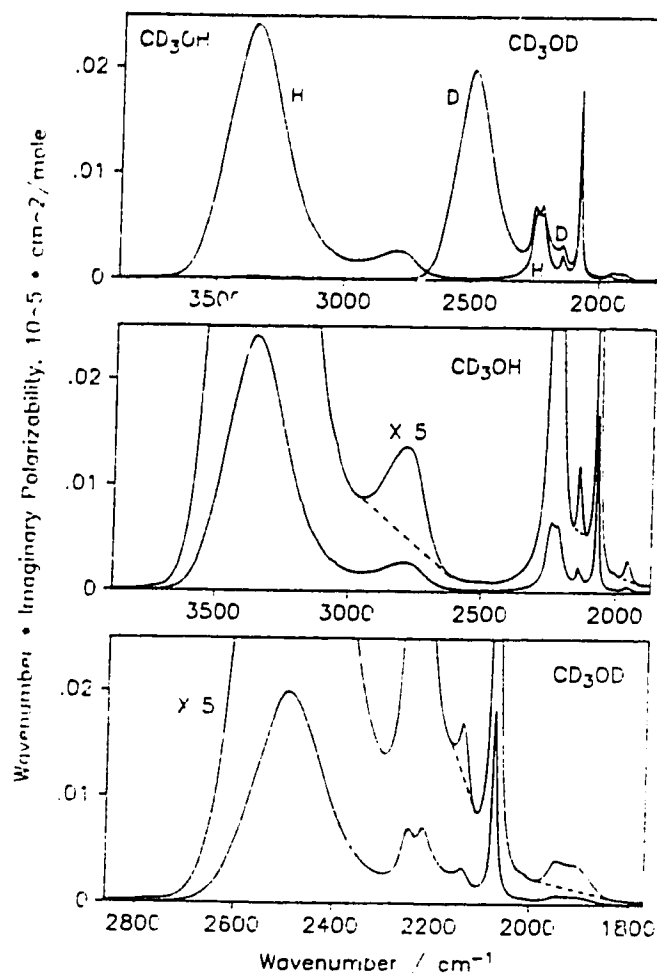


**Figure 7.7** The  $\tilde{\nu}\alpha_m''$  spectra of  $\text{CD}_3\text{OH}$  and  $\text{CD}_3\text{OD}$  in the regions of the O-H, O-D and C-H stretching vibrations. Top box: The  $\tilde{\nu}\alpha_m''$  spectra of  $\text{CD}_3\text{OH}$  (curve H) and  $\text{CD}_3\text{OD}$  (curve D). Middle and bottom boxes: The  $\tilde{\nu}\alpha_m''$  spectra of  $\text{CD}_3\text{OH}$  (middle box) and  $\text{CD}_3\text{OD}$  (bottom box); The dashed lines separate integration regions.

at 2938 and 2620  $\text{cm}^{-1}$  in the upper curve in Figure 7.7 (middle) is  $C_j = 0.25 \text{ km mol}^{-1}$ . The integrated intensity of the O-H stretching mode in  $\text{CD}_3\text{OH}$  is, thus, taken to be  $C_j = 7.40 \text{ km mol}^{-1}$ . If it is assumed that the  $2\delta(\text{COH})$  in  $\text{CH}_3\text{OH}$  has the same intensity as in  $\text{CD}_3\text{OH}$ , the O-H stretching intensity in  $\text{CH}_3\text{OH}$  is  $7.44 \text{ km mol}^{-1}$ , instead of  $7.69 \text{ km mol}^{-1}$  reported previously<sup>2</sup>.

**Table 7.6**  $C_j$  of the C–H, C–D, O–H and O–D stretching bands of liquid methanol.

Molecule	Integrated intensities / km mol <sup>-1</sup>			
	$C_{OH}$	$C_{OD}$	$C_{CH}$	$C_{CD}$
CH <sub>3</sub> OD		4.01 <sup>a</sup>	1.31 <sup>a</sup>	
CD <sub>3</sub> OH	7.40			0.96
CH <sub>3</sub> OH	7.44		1.31 <sup>a,b</sup>	
	7.40 <sup>b</sup>		1.35	
Average	7.42		1.33	
CD <sub>3</sub> OD		3.89		0.96 <sup>b</sup>
		4.01 <sup>b</sup>		0.84
Average		3.95		0.90

a From Ref. 2.

b An assumed value.

The spectrum of CD<sub>3</sub>OD is shown in the bottom box and as curve D in Figure 7.7 (top). The integration limits are again taken at minima in  $\tilde{\nu}\alpha''_m$ , at 2860 and 1770 cm<sup>-1</sup>. If the assumptions are made that the integrated intensity,  $C_j = 0.96$  km mol<sup>-1</sup>, of the C–D stretching vibrations is the same in CD<sub>3</sub>OD as in CD<sub>3</sub>OH, and that all of the  $C_j = 4.89$  km mol<sup>-1</sup> intensity for CD<sub>3</sub>OD between 2860 and 1770 cm<sup>-1</sup> is due to the O–D and C–D stretching vibrations except for a 0.04 km mol<sup>-1</sup> contribution from overtones (see below), the value  $C_j = 3.89$  km mol<sup>-1</sup> is obtained for the O–D stretching vibration. This value is about 3% lower than the 4.01 km mol<sup>-1</sup> found<sup>2</sup> for CH<sub>3</sub>OD.

The intensity assigned above to overtones of CD<sub>3</sub>OD is 0.04 km mol<sup>-1</sup> for the sum of  $2\nu(CO)$  at 1944 cm<sup>-1</sup> and  $2\gamma(CD_3)$  at ~1910 cm<sup>-1</sup>, measured above the dashed line between the curve points at 1984 and 1823 cm<sup>-1</sup> (Figure 7.7, bottom). The small band at 2137 cm<sup>-1</sup> is assigned to the overtone or combination of the CD<sub>3</sub> deformation vibrations. Its area is 0.02 km mol<sup>-1</sup> measured above the dashed line between the curve points at 2155 and 2112 cm<sup>-1</sup> (Figure 7.7, bottom). This area is included in the  $C_j = 0.96$  km mol<sup>-1</sup> value of the surrounding C–D stretching fundamentals, as was done for CD<sub>3</sub>OH. These areas are included in Table 7.6 for the O–D stretch and Table 7.7 for the overtones.

An alternative view of the  $\tilde{\nu}\alpha''_m$  bands of the O–H, O–D, C–H and C–D stretching vibrations is shown in Figure 7.8. It is clear that the O–H stretching vibration has essentially the same intensity in CH<sub>3</sub>OH and CD<sub>3</sub>OH, and the O–D stretching vibration has essentially the same intensity in CH<sub>3</sub>OD and CD<sub>3</sub>OD. The assumption that this is

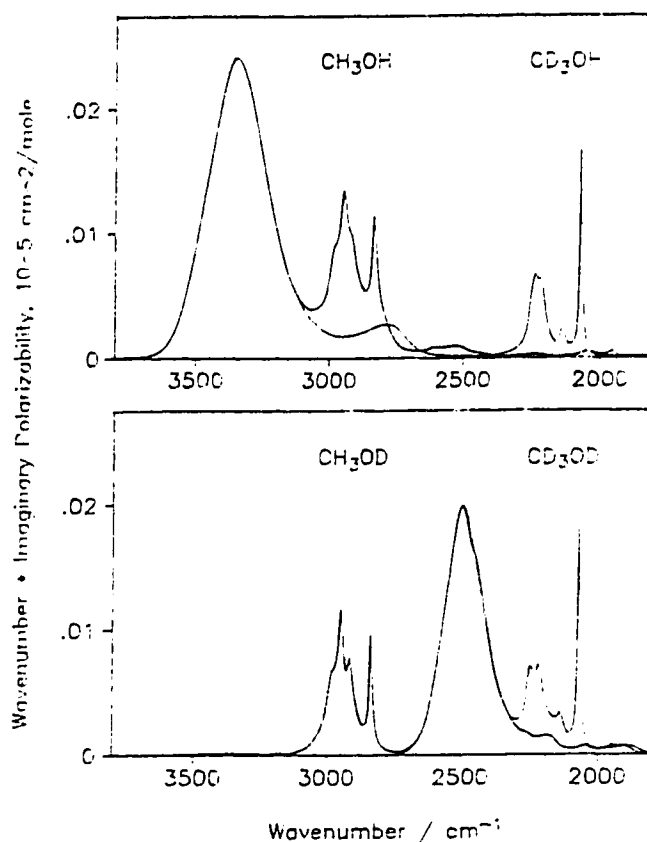


**Figure 7.8** The  $\tilde{\nu}\alpha_m''$  spectra of  $\text{CH}_3\text{OH}$  and  $\text{CD}_3\text{OH}$  (top box) and  $\text{CH}_3\text{OD}$  and  $\text{CD}_3\text{OD}$  (bottom box) in the O–H, O–D, C–H and C–D stretching region.

exactly so, and that the overtone band that is visible for  $\text{CD}_3\text{OH}$  is included under the C–H stretching band of  $\text{CH}_3\text{OH}$  and has the same intensity,  $0.25 \text{ km mol}^{-1}$ , in both liquids, leads to  $C_j = 1.35 \text{ km mol}^{-1}$  for the intensity of the C–H stretching bands in  $\text{CH}_3\text{OH}$ . The analogous assumption that the intensity of the O–D stretching band of  $\text{CD}_3\text{OD}$  equals the  $C_j = 4.01 \text{ km mol}^{-1}$  of the O–D band of  $\text{CH}_3\text{OD}$ <sup>2</sup> yields  $0.84 \text{ km mol}^{-1}$  for the intensity of the C–D stretching band in  $\text{CD}_3\text{OD}$ . These values for the stretching vibrations are summarized in Table 7.6 which includes the averages of the two values found for each band for  $\text{CH}_3\text{OH}$  and  $\text{CD}_3\text{OD}$ . These average values are included in Table 7.7.

**Table 7.7** The integrated intensities, transition moments and dipole moment derivatives of liquids CD<sub>3</sub>OH, CD<sub>3</sub>OD and CH<sub>3</sub>OH. <sup>a</sup>

Band <sup>b</sup>	$\tilde{\nu}_{\max}$ (cm <sup>-1</sup> )	Integration Range <sup>c</sup> (cm <sup>-1</sup> )	$C_j$ (km mol <sup>-1</sup> )	$ R_j^f $ <sup>d</sup> (D)	$\mu_j^2$ <sup>e</sup> (D <sup>2</sup> Å <sup>2</sup> amu <sup>-1</sup> )	Conversion Factor (amu)	$\mu_R$ <sup>f</sup> (D Å <sup>-1</sup> )
<b>CD<sub>3</sub>OH</b>							
$\nu(\text{OH})$	3352	3880–2455	7.40 <sup>g</sup>	0.264	13.8 <sup>3</sup>	0.948	3.62
$2\delta(\text{COH})$	2783	2938–2620	0.25				
$\nu(\text{CD})$	2235/2216/ 2072	2455–1870	0.96 <sup>g</sup>	0.118	1.79	0.532	0.98
$2\nu(\text{CO})$	1957	1986–1870	0.01				
$\delta(\text{COH})$	1393	1846–1159	0.78	0.133	1.46	0.780	1.07
$\tau(\text{DCOH})$	668	930–365	1.01	0.218	1.89	0.661	1.12
<b>CD<sub>3</sub>OD</b>							
$\nu(\text{OD})$	2493	2860–1770	3.95 <sup>g</sup>	0.223	7.38	1.789	3.63
$\nu(\text{CD})$	2245/2216/ 2072		0.90 <sup>g</sup>	0.114	1.68	0.532	0.95
$2\nu(\text{CO})$	1944	} 1984–1823	0.04				
$2\gamma(\text{CD}_3)$	1910						
$\tau(\text{DCOD})$	492	690–325	0.48	0.175	0.90	1.118	1.00
<b>CH<sub>3</sub>OH</b>							
$\nu(\text{OH})$	3354		7.42 <sup>g</sup>	0.264	13.87	0.948	3.63
$\nu(\text{CH})$	2980/2945/ 2833		1.33 <sup>g</sup>	0.120	2.49	0.305	0.87

- a The  $\tilde{\nu}_{\max}$  are peak wavenumbers in the  $\tilde{\nu}\alpha_m''$  spectrum and the areas  $C_j$  are under the  $\tilde{\nu}\alpha_m''$  spectrum<sup>5</sup>.
- b Assignments follow from the literature<sup>6</sup>.  $\gamma$  means rock,  $\delta$  means a valence angle deformation, and  $\tau$  means torsion.
- c When the area is measured above zero ordinate, the integration limits are the minima in the spectrum.
- d  $|R_j^f|^2$  values in D<sup>2</sup> were obtained by multiplying the  $C_j$  values in km mol<sup>-1</sup> by 31.50 and dividing the product by the peak wavenumber of the band<sup>2</sup>. The  $|R_j^f|$  value for the CD<sub>3</sub> stretching vibrations is the square root of the sum of  $|R_j^f|^2$  over all three CD<sub>3</sub> stretching vibrations. The average wavenumber was used in the calculation.
- e  $\mu_j^2$  values, in the units (D Å<sup>-1</sup> amu<sup>-1/2</sup>)<sup>2</sup>, were obtained<sup>5</sup> by multiplying the  $C_j$  values in km mol<sup>-1</sup> by the numerical factor 1.8686. For the CD<sub>3</sub> stretching vibrations, the value is the sum of  $\mu_j^2$  over all three CD<sub>3</sub> stretching vibrations.
- f  $\mu_R$  is the magnitude of the change of dipole moment for unit change in the internal coordinate. The internal coordinate for a bending or torsion vibration is defined as the change in the angle multiplied by 1 Å.
- g From Table 7.6.

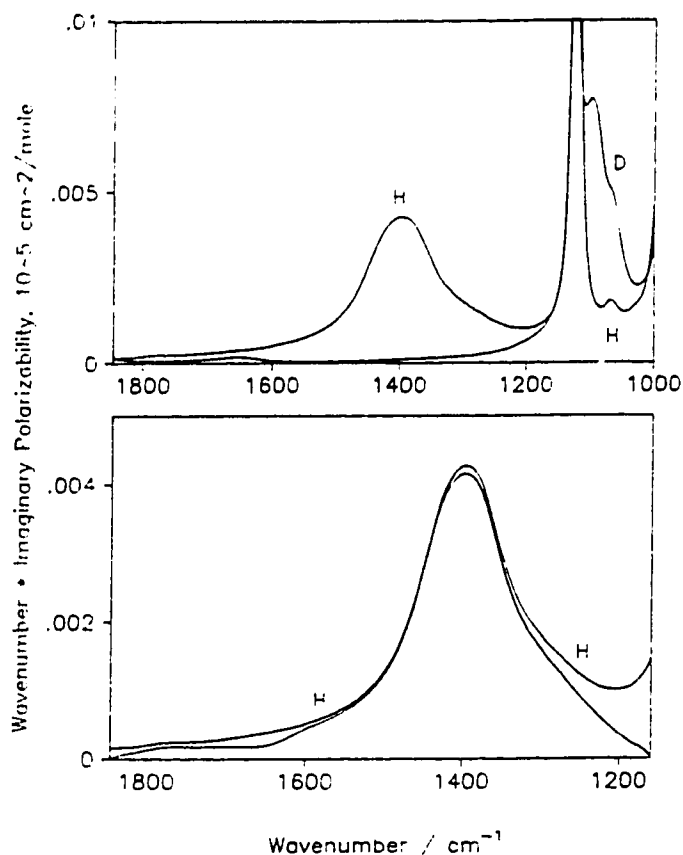


**Figure 7.9** The  $\tilde{\nu}\alpha_m''$  spectra of CD<sub>3</sub>OH (curve H) and CD<sub>3</sub>OD (curve D) in the region of the C–O–H in-plane bending band. The lower curve in the bottom box shows the difference spectrum obtained by subtracting the  $\tilde{\nu}\alpha_m''$  spectrum of CD<sub>3</sub>OH from that of CD<sub>3</sub>OD.

#### 7.4.2 The C–O–H in-Plane Bending Band

The C–O–H in-plane bending band is at 1393 cm<sup>-1</sup> in the  $\tilde{\nu}\alpha_m''$  spectrum of CD<sub>3</sub>OH, curve H in Figure 7.9 (top). Its high-wavenumber side is completely separated from the CD<sub>3</sub> stretching bands, but it overlaps the CD<sub>3</sub> deformation and C–O stretching bands to low-wavenumber. The area above zero ordinate between the minima at 1870 and 1204 cm<sup>-1</sup> is 0.87 km mol<sup>-1</sup>. This area must include contributions from the tails of the CD<sub>3</sub> deformation and C–O stretching bands. The fact that the left side of the CD<sub>3</sub> deformation band of CD<sub>3</sub>OH overlaps that of CD<sub>3</sub>OD shown as curves H and D in Figure 7.9 (top) allows this effect to be minimized by considering the difference

spectrum,  $[\tilde{\nu}\alpha''_m(\text{CD}_3\text{OH}) - \tilde{\nu}\alpha''_m(\text{CD}_3\text{OD})]$ . This difference spectrum is shown as the lower curve in Figure 7.9 (bottom), with the original  $\tilde{\nu}\alpha''_m$  spectrum of  $\text{CD}_3\text{OH}$  as the upper curve marked H. The area under the difference spectrum between the zero ordinate points at 1846 and 1159  $\text{cm}^{-1}$  is  $C_j = 0.78 \text{ km mol}^{-1}$ . This value is assigned to the C–O–H in-plane bending vibration (Table 7.7). Note that the weak bands at 1650  $\text{cm}^{-1}$  for  $\text{CD}_3\text{OD}$  and 1750  $\text{cm}^{-1}$  for  $\text{CD}_3\text{OH}$  have been neglected and this introduces an uncertainty of 0.01  $\text{km mol}^{-1}$  in the value 0.78  $\text{km mol}^{-1}$ .

#### 7.4.3 The Torsion Bands

It was noted previously<sup>2</sup> that the integrated intensities of the H–C–O–H and H–C–O–D torsion vibrations of  $\text{CH}_3\text{OH}$  and  $\text{CH}_3\text{OD}$  are difficult to assess, because they combine at low wavenumber with the absorption by intermolecular motion in the liquid, and they overlap with other fundamental bands at high wavenumber. We know of no reliable way to separate them. The same situation exists for  $\text{CD}_3\text{OH}$  and  $\text{CD}_3\text{OD}$ .

For  $\text{CD}_3\text{OD}$ , the integrated intensity of the D–C–O–D torsion can be estimated in the three ways shown in Figure 7.10 (top), which are the same as were used for  $\text{CH}_3\text{OD}$ <sup>2</sup>. The integration limits are 690  $\text{cm}^{-1}$  and 325  $\text{cm}^{-1}$ , and the  $C_j$  values obtained were 0.58, 0.40 and 0.47  $\text{km mol}^{-1}$ , respectively. The average of the three values,  $0.48 \pm 0.1 \text{ km mol}^{-1}$ , is taken as the integrated intensity  $C_j$  of the D–C–O–D torsion in  $\text{CD}_3\text{OD}$ .

For  $\text{CD}_3\text{OH}$ , Figure 7.10 (bottom), the minimum  $\tilde{\nu}\alpha''_m$  value at 844  $\text{cm}^{-1}$  is too large to allow a vertical line to be drawn to the baseline, so the integrated intensity of the D–C–O–H torsion was assessed in the following two ways. First the high wavenumber side of the torsion band was linearly extended from 830  $\text{cm}^{-1}$  to  $\tilde{\nu}\alpha''_m = 0$  at 930  $\text{cm}^{-1}$ , where 830  $\text{cm}^{-1}$  was chosen somewhat arbitrarily. The area is  $C_j = 1.08 \text{ km mol}^{-1}$  between 930 and 365  $\text{cm}^{-1}$  above zero ordinate and under this extended torsion band. Some of the absorption in this region may be due to the high-wavenumber tail of the absorption by the intermolecular vibrations, so the area was also measured above a straight line drawn between  $\tilde{\nu}\alpha''_m = 0$  at 930  $\text{cm}^{-1}$  and the curve point at 365  $\text{cm}^{-1}$ . This area was  $C_j = 0.94 \text{ km mol}^{-1}$ . The average value of the above two areas,  $C_j = 1.01 \pm 0.07 \text{ km mol}^{-1}$ , is assigned to the D–C–O–H torsion in  $\text{CD}_3\text{OH}$ .

These integrated intensities of the torsion vibrations in  $\text{CD}_3\text{OH}$  and  $\text{CD}_3\text{OD}$  almost equal those obtained previously<sup>2</sup> for  $\text{CH}_3\text{OH}$  and  $\text{CH}_3\text{OD}$ . Figure 7.11 shows clearly that this equality derives from experiment, not from our method of measuring the area. (See the note added in proof at the end of this chapter.)

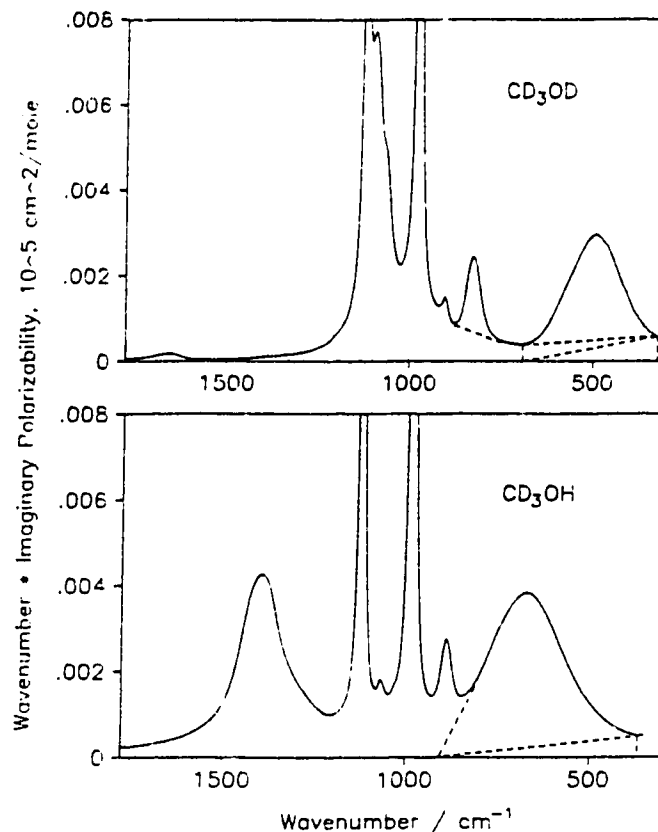


**Figure 7.10** The  $\tilde{\nu}\alpha''$  spectra of  $\text{CD}_3\text{OD}$  (top box) and  $\text{CD}_3\text{OH}$  (bottom box) below  $1770\text{ cm}^{-1}$ . The dashed lines separate integration regions.

#### 7.4.4 The Remaining Bands

The remaining fundamentals are the C–O stretching,  $\text{CD}_3$  deformation and  $\text{CD}_3$  rocking vibrations. They lie between  $1500$  and  $690\text{ cm}^{-1}$  for  $\text{CD}_3\text{OD}$  (Figure 7.10, top), and between  $1204$  and  $844\text{ cm}^{-1}$  for  $\text{CD}_3\text{OH}$  (Figure 7.10, bottom). Their integrated intensities can not be determined with the same confidence as for the other fundamentals, because of strong interaction and heavy overlapping of the bands (Figure 7.10). In fact it is clear that the CO stretching vibration is heavily mixed with the symmetric  $\text{CD}_3$  deformation, because the single strong CO stretching band of  $\text{CH}_3\text{OH}$  and  $\text{CH}_3\text{OD}$  is replaced by two strong bands in the spectra of  $\text{CD}_3\text{OH}$  and  $\text{CD}_3\text{OD}$  (Figure 7.11).

However, some information about the intensities of these bands can be estimated in the following way. The total area from  $1870$  to  $365\text{ cm}^{-1}$  for  $\text{CD}_3\text{OH}$  (Figure 7.10, bottom) is  $3.33\text{ km mol}^{-1}$ .  $1.86\text{ km mol}^{-1}$  of this has been assigned to the C–O–H in-



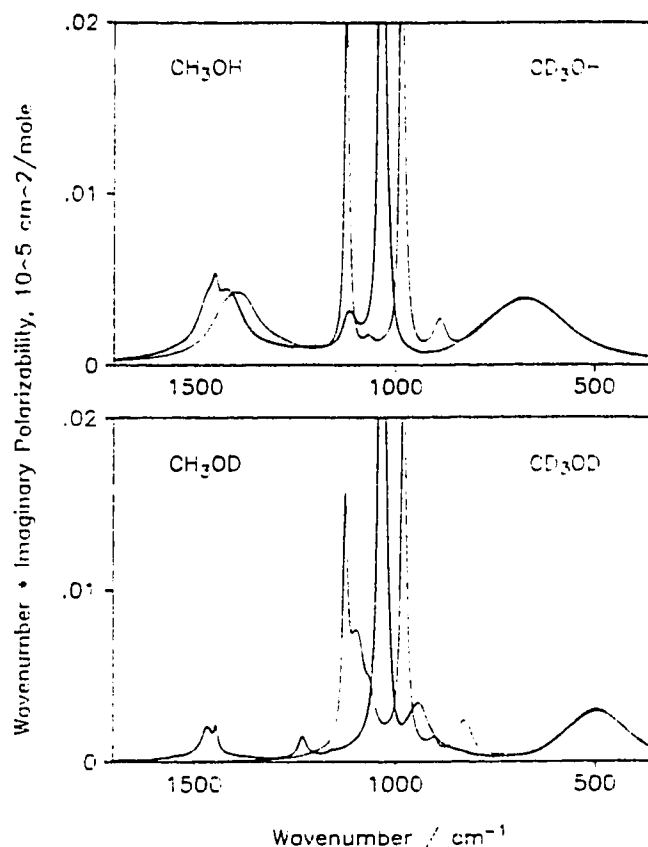


**Figure 7.11** The  $\tilde{\nu}\alpha''_m$  spectra of  $\text{CH}_3\text{OH}$  and  $\text{CD}_3\text{OH}$  (top box) and  $\text{CH}_3\text{OD}$  and  $\text{CD}_3\text{OD}$  (bottom box) between 1700 and 350  $\text{cm}^{-1}$ .

plane bend, the torsion, and the intermolecular vibrations. The remaining  $1.47 \text{ km mol}^{-1}$  is due to the C–O stretching,  $\text{CD}_3$  deformation and  $\text{CD}_3$  rocking vibrations.

For  $\text{CD}_3\text{OD}$  (Figure 7.10, top), the total area from 1530 to 325  $\text{cm}^{-1}$  is  $2.30 \text{ km mol}^{-1}$ . The contribution from the torsion and the intermolecular vibrations is  $0.58 \text{ km mol}^{-1}$ . The remaining  $1.72 \text{ km mol}^{-1}$  is due to the C–O stretching,  $\text{CD}_3$  deformation and  $\text{CD}_3$  rocking vibrations, as for  $\text{CD}_3\text{OH}$  above, plus the C–O–D in-plane bending vibration at  $\sim 824 \text{ cm}^{-1}$ . This bending vibration is to low wavenumber of that in  $\text{CH}_3\text{OD}^2$ , but its  $0.080 \text{ km mol}^{-1}$  area, measured above the straight line between the curve points at 875 and 740  $\text{cm}^{-1}$  in Figure 7.10 (top), is close to the  $0.086 \text{ km mol}^{-1}$  found for  $\text{CH}_3\text{OD}$  when measured in the same way<sup>2</sup>. However, for  $\text{CH}_3\text{OD}$  the intensity of the bending vibration was also estimated to be  $C_j = 0.26 \text{ km mol}^{-1}$ , from the spectrum of  $\text{CH}_3\text{OD}$  from which the C–O stretching band had been subtracted<sup>2</sup>, and it was concluded

that  $0.26 \text{ km mol}^{-1}$  is a more reliable value than  $0.086 \text{ km mol}^{-1}$ . The same value is taken as more reliable for  $\text{CD}_3\text{OD}$ . When this  $0.26 \text{ km mol}^{-1}$  for the bending vibration is removed from the value  $1.72 \text{ km mol}^{-1}$ ,  $C_j = 1.46 \text{ km mol}^{-1}$  is obtained for the sum of the intensities of the C–O stretching,  $\text{CD}_3$  deformation and  $\text{CD}_3$  rocking vibrations in  $\text{CD}_3\text{OD}$ . This value is almost the same as the  $1.47 \text{ km mol}^{-1}$  obtained above for  $\text{CD}_3\text{OH}$ .

In an attempt to check the objectivity of the band separation that led to the above numbers, this region of the spectrum was fitted with classical damped harmonic oscillator bands and, for the motion of hydrogen-bonded OH and OD, Gaussian bands. The fit was excellent, although it is difficult to assign all of the component bands needed to produce the fit. The areas  $1.35$  and  $1.55 \text{ km mol}^{-1}$  were obtained for the sum of the integrated intensities of the C–O stretching,  $\text{CD}_3$  deformation and  $\text{CD}_3$  rocking vibrations of  $\text{CD}_3\text{OH}$  and  $\text{CD}_3\text{OD}$ , respectively, instead of the  $1.47$  and  $1.46 \text{ km mol}^{-1}$  deduced above.

These values for  $\text{CD}_3\text{OH}$  and  $\text{CD}_3\text{OD}$  can be compared with those for  $\text{CH}_3\text{OH}$  and  $\text{CH}_3\text{OD}$ . The C–O stretching,  $\text{CH}_3$  deformation and  $\text{CH}_3$  rocking bands have the intensities  $1.24$ ,  $0.186$  and  $0.15 \text{ km mol}^{-1}$  for  $\text{CH}_3\text{OH}$  and  $1.27$ ,  $0.186$  and  $0.09 \text{ km mol}^{-1}$  for  $\text{CH}_3\text{OD}$ , for totals of  $1.58$  and  $1.55 \text{ km mol}^{-1}$ , respectively. If it is assumed that the  $\text{CD}_3$  deformation and rocking bands have between  $1/2$  and  $1/\sqrt{2}$  of the intensity of the  $\text{CH}_3$  vibrations,  $1.44 \pm 0.04 \text{ km mol}^{-1}$  is obtained from each molecule as the intensity to compare with the  $1.47$  for  $\text{CD}_3\text{OH}$  and  $1.46$  for  $\text{CD}_3\text{OD}$ .

Clearly, the total intensity of the six vibrations (one C–O stretch, three  $\text{CH}_3$  deformations and two  $\text{CH}_3$  rocks) is very similar in  $\text{CH}_3\text{OH(D)}$  and  $\text{CD}_3\text{OH(D)}$ , subject only to the experimental reduction in intensity due to the smaller amplitudes of the deuterium motions.

## 7.5 Transition Moments and Dipole Moment Derivatives

The magnitude of the effective transition moment,  $|R_j^f|$ , of vibration  $j$  can be calculated<sup>2</sup> from the integrated intensity  $C_j$ . If it is assumed that the oscillator is electrically and mechanically harmonic, the change in the molecular dipole moment during the vibration,  $\mu_j$ , can also be calculated<sup>5</sup> from the integrated intensity  $C_j$ . With further assumptions about the coupling between displacements, the changes in dipole moment during bond stretching or angle displacements can be found<sup>1,2</sup>. These calculations for the C–D, O–H and O–D stretching, C–O–H in-plane bending, and D–C–O–H and D–C–O–D torsion vibrations are presented in this section.

The values of the transition moments,  $|R_j^f|$ , and the squares of the dipole moment derivatives with respect to the normal coordinates,  $\mu_j^2 = |\partial\bar{\mu}/\partial Q_j|^2$ , are given in columns 5 and 6 of Table 7.7.

The physical significance of the  $\mu_j^2$  values is not easy to appreciate because they are influenced by the effective mass of the oscillator  $j$  and because they characterize the dipole moment change during the vibration of the molecule as a whole. To remove the influence of the effective mass, the simplest possible treatment was used to calculate values of  $\mu_R = |\partial\bar{\mu}/\partial R|$ , where  $R$  is a valence internal displacement coordinate. The assumptions and treatment have been described<sup>1,2</sup>. The relations were found<sup>2</sup> to be  $\mu_{OH}^2 = 0.948\mu_j^2$ ,  $\mu_{OD}^2 = 1.789\mu_j^2$ , and  $\mu_{COH}^2 = 0.780\mu_j^2$  for the O-H and O-D stretching, and the C-O-H in-plane bending vibrations, respectively, where  $\mu_{OHI} = |\partial\bar{\mu}/\partial r_{OHI}|$ , etc., and the C-O-H bending coordinate is multiplied by 1 Å to yield  $\mu_{COHI}$  in D Å<sup>-1</sup>. The C-D stretching vibrations were treated as the coupled C-D stretching vibrations of an isolated CD<sub>3</sub> group of C<sub>s</sub> symmetry, as were the C-H stretching vibrations of the CH<sub>3</sub> group in CH<sub>3</sub>OH<sup>1</sup> and in CH<sub>3</sub>OD<sup>2</sup>. The symmetric CD<sub>3</sub> stretch (A' under C<sub>s</sub>) was assigned at 2072 cm<sup>-1</sup>, and the antisymmetric CD<sub>3</sub> stretches were assigned at 2235 or 2245 cm<sup>-1</sup> (A') and 2216 cm<sup>-1</sup> (A''), following the work of Günthard and coworkers<sup>6</sup>. The values of the in-plane and out-of-plane diagonal force constants, and of the two  $f_{CD,CD'}$  interaction constants assumed to be equal, were 4.396, 5.055 and 0.2842 m dyn Å<sup>-1</sup> for CD<sub>3</sub>OH and 4.404, 5.076 and 0.3057 m dyn Å<sup>-1</sup> for CD<sub>3</sub>OD. The relation was found to be  $\mu_{CD}^2 = 0.532\mu_j^2$  for both CD<sub>3</sub>OH and CD<sub>3</sub>OD. The D-C-O-H and D-C-O-D torsions were treated as uncoupled oscillators, and the relations were found to be  $\mu_{\tau}^2 = 0.661\mu_j^2$  for CD<sub>3</sub>OH and 1.118 $\mu_j^2$  for CD<sub>3</sub>OD. The factors that convert  $\mu_j^2$  to  $\mu_R^2$  are listed in column 7 of Table 7.7, and the magnitudes of the dipole moment derivatives with respect to the internal coordinates are given in column 8 of Table 7.7.

## 7.6 Discussion

The observed wavenumbers and intensities of the spectral bands of CH<sub>3</sub>OH, CH<sub>3</sub>OD, CD<sub>3</sub>OH and CD<sub>3</sub>OD appear to yield clear information about the coupling between the different internal displacement coordinates, i.e. about whether a normal vibration is purely due to one type of internal coordinate or whether more than one type of internal coordinate take part in the normal vibration. For example, the facts that the O-H stretching bands of CH<sub>3</sub>OH and CD<sub>3</sub>OH overlap in both wavenumber and intensity

(Figure 7.8, top), the O–D stretching bands of CH<sub>3</sub>OD and CD<sub>3</sub>OD overlap in wavenumber and intensity (Figure 7.8, bottom), and that the same integrated intensity is obtained for the C–H and O–H vibrations of CH<sub>3</sub>OH and for the C–D and O–D vibrations of CD<sub>3</sub>OD under two different assumptions (Table 7.6), all indicate that the O–H and O–D stretching displacements do not couple with the C–H or C–D stretching displacements. Thus, the experimental evidence supports the view that the O–H, O–D, C–H and C–D vibrations are pure, with the only coupling being between the motions of the different CH or CD bonds in the methyl group.

Similarly, evidence that the C–O stretching vibrations are pure in CH<sub>3</sub>OH and CH<sub>3</sub>OD is provided by the almost complete overlap in wavenumber and intensity of the C–O stretching bands in CH<sub>3</sub>OH and CH<sub>3</sub>OD (Figure 10 of Ref. 2). This is observed even though neighboring bands shift markedly between the two compounds and the C–O–H in-plane bend is ~390 cm<sup>-1</sup> to high wavenumber in CH<sub>3</sub>OH but the C–O–D bend is ~90 cm<sup>-1</sup> to low wavenumber in CH<sub>3</sub>OD (Figure 11 of Ref. 2). In contrast, evidence that the C–O stretching motion is strongly coupled in CD<sub>3</sub>OH and CD<sub>3</sub>OD, presumably to the symmetric CD<sub>3</sub> deformation, is provided by the replacement of one intense band near 1030 cm<sup>-1</sup> in the spectrum of CH<sub>3</sub>OH and CH<sub>3</sub>OD by two weaker bands of comparable intensity in the CD<sub>3</sub> isotopomers (Figure 7.11).

The calculation of  $\mu_{OH} (= |\partial \bar{\mu} / \partial R_{OH}|)$  and  $\mu_{OD}$  reported above was done under the diatomic molecule approximation. This is equivalent to the assumption that the vibrations are pure, and is justified by the experimental evidence. The values 3.63 and 3.62 D Å<sup>-1</sup> were obtained for  $\mu_{OH}$  of CH<sub>3</sub>OH and CD<sub>3</sub>OH, and 3.66 and 3.63 D Å<sup>-1</sup> for  $\mu_{OD}$  of CH<sub>3</sub>OD<sup>2</sup> and CD<sub>3</sub>OD, respectively.

To the extent that the theory is adequate, the same value of  $\mu_{OH}$  and  $\mu_{OD}$  should be obtained for all isotopomers. The above values are attractively similar, but they can not be directly compared until the rotational correction<sup>22,23</sup> has been applied. The rotational correction arises because the rotation of the permanent dipole moment of the molecule contributes to the dipole moment derivative with respect to the internal (or symmetry) coordinates, and the contribution is different for the different isotopomers<sup>22,23</sup>. We have calculated the absolute corrections<sup>24,25</sup> for some modes, but it is more convenient to use the corrections relative<sup>22,23,26</sup> to CH<sub>3</sub>OH. For the O–H stretch they are 0.0, +0.04 and +0.04 D Å<sup>-1</sup> for CD<sub>3</sub>OH, CH<sub>3</sub>OD and CD<sub>3</sub>OD. These values must be added vectorially to the values of  $\mu_{OH}$  or  $\mu_{OD}$  calculated from experiment before they can be compared with the  $\mu_{OH}$  value of CH<sub>3</sub>OH.

For the vector addition, the direction of  $\partial\bar{\mu}/\partial R_{\text{OH}}$  was taken to be that calculated by Torii and Tasumi<sup>27</sup> in their *ab initio* quantum mechanical treatment of the gas, rather than along the OH bond. This direction is  $19^\circ$  from the OH bond, outside of the C–O–H angle, with the negative end towards the hydrogen atom. This  $19^\circ$  angle agrees with  $18\pm5^\circ$  found<sup>28</sup> by fitting the rotational band contours. The rotational correction is  $42^\circ$  outside the bond with the negative end towards the oxygen. Thus, the values to be compared are 3.63, 3.62, 3.63 and  $3.60 \text{ D}\text{\AA}^{-1}$ , which are in excellent agreement.

The situation is less clear for the C–H and C–D stretching vibrations, because only the sum of their intensities is available and the contributions of the different vibrations can not be separated reliably. The assumptions used to calculate  $\mu_{\text{CH}}$  and  $\mu_{\text{CD}}$  were a) that the vibrations can be treated as the coupled C–H(D) stretching vibrations of an isolated methyl group of  $C_s$  symmetry, b) that the two non-equivalent interaction constants under  $C_s$  are equal, and c) that the three dipole moment derivatives with respect to the C–H(D) stretching internal coordinate have the same magnitude and are aligned with the bond. The values obtained for  $\text{CH}_3\text{OH}$ ,  $\text{CH}_3\text{OD}^2$ ,  $\text{CD}_3\text{OH}$ , and  $\text{CD}_3\text{OD}$  were  $\mu_{\text{CH}} = 0.87$  and  $0.86 \text{ D}\text{\AA}^{-1}$  and  $\mu_{\text{CD}} = 0.98$  and  $0.95 \text{ D}\text{\AA}^{-1}$ , respectively. These values are averaged over the two non-equivalent types of CH(D) bond. The rotational corrections for each bond are less than  $0.02 \text{ D}\text{\AA}^{-1}$  so can not influence the agreement significantly. The  $\sim 12\%$  disagreement between the values of  $\mu_{\text{CH}}$  and  $\mu_{\text{CD}}$  is experimentally significant, and may be due to the simple treatment of the coupling between the three C–H(D) bonds, to the neglect of anharmonicity, or to an incorrect treatment of the intensity contributed by overlapping overtone and combination vibrations.

(See the note added in proof at the end of this chapter.) The rotational correction is particularly important for the torsion vibrations. Experimentally, the integrated intensities are very close for the two OH torsions and also very close for the two OD torsions (Figure 7.11). However, the  $\mu_\tau$  values obtained are 1.07, 1.12, 0.94 and  $1.00 \text{ D}\text{\AA}^{-1}$  for  $\text{CH}_3\text{OH}^2$ ,  $\text{CD}_3\text{OH}$ ,  $\text{CH}_3\text{OD}^2$  and  $\text{CD}_3\text{OD}$ , respectively, perpendicular to the HCOH plane. The rotational corrections relative to  $\text{CH}_3\text{OH}$  are  $-0.12$ ,  $+0.14$  and  $-0.04 \text{ D}\text{\AA}^{-1}$ , also perpendicular to the plane. Accordingly, the values to be compared for the four molecules are 1.07, 1.00, 1.08 and  $0.96 \text{ D}\text{\AA}^{-1}$ , the same to  $\pm 6\%$ . This agreement is consistent with the precision of the integrated intensities, viz.  $\pm 20\%$  for the OD torsions and about  $\pm 8\%$  for the OH torsions.

For the C–O stretching vibration in the  $\text{CH}_3$  compounds<sup>2</sup>,  $\mu_{\text{CO}}$  is 3.99 and  $4.03 \text{ D}\text{\AA}^{-1}$  for  $\text{CH}_3\text{OH}$  and  $\text{CH}_3\text{OD}$ , respectively. The relative rotational correction for

$\text{CH}_3\text{OD}$  is  $-0.03 \text{ D}\text{\AA}^{-1}$  sufficiently aligned with the  $\mu_{\text{CO}}$  direction<sup>27</sup> that the values to be compared are 3.99 and  $4.00 \text{ D}\text{\AA}^{-1}$ . This agreement is consistent with the experimental evidence that the vibrations are pure C–O stretching vibrations. This is in marked contrast to the normal coordinate calculations of Serrallach *et al.*<sup>6</sup> and Mallinson<sup>29</sup> who both found extensive coupling between different types of internal coordinates in these vibrations. They were, however, able to reproduce the relative intensities of the two isotopomers rather well. We plan to explore this further, but it seems possible that the conclusion that the C–O stretching vibrations are pure may in fact be the wrong conclusion to draw from the apparently clear experimental evidence.

In  $\text{CD}_3\text{OH}$  and  $\text{CD}_3\text{OD}$  the obvious coupling between the C–O stretching displacement and the symmetric  $\text{CD}_3$  deformation prevents us from obtaining  $\mu_{\text{CO}}$  by the simple treatment used above. The coupling in this region is even more extensive for  $\text{CD}_3\text{OD}$  than for  $\text{CD}_3\text{OH}$  and involves the  $A'$  asymmetric  $\text{CD}_3$  deformation mode and/or the  $A'$   $\text{CD}_3$  rocking mode. The measured intensities contain information about the coupling that can be extracted by a suitable treatment, and we plan to use *ab initio* calculation of the force constants and intensities (necessarily of the gas) and normal coordinate calculation of the wavenumbers and intensities to try to fit the experimental spectra and, so, extract this information.

The only other vibration for which  $\mu_{\text{R}}$  values were calculated for several isotopomers is the in-plane C–O–H bend. The values of  $\mu_{\text{COH}}$  found for  $\text{CH}_3\text{OH}^2$ ,  $\text{CH}_3\text{OD}^2$  and  $\text{CD}_3\text{OH}$  are 1.03, 0.82 and  $1.07 \text{ D}\text{\AA}^{-1}$ , respectively. The rotational corrections relative to  $\text{CH}_3\text{OH}$  are +0.07,  $-0.01$  and  $+0.04$  for  $\text{CH}_3\text{OD}$ ,  $\text{CD}_3\text{OH}$  and  $\text{CD}_3\text{OD}$ . The  $\partial\bar{\mu}/\partial R_{\text{COH}}$  lies about  $80^\circ$  from the OH bond and outside the COH angle. The correction is about  $40^\circ$  outside the OH bond. Thus, the values to be compared are 1.03, 0.87 and 1.06 for  $\text{CH}_3\text{OH}$ ,  $\text{CH}_3\text{OD}$  and  $\text{CD}_3\text{OH}$ . The difference between the values for the C–O–H and C–O–D vibrations may reflect inaccurate areas or inadequacies in our treatment, and will be explored.

## 7.7 References

1. J. E. Bertie, S. L. Zhang, H. H. Eysel, S. Baluja, and M. K. Ahmed, *Appl. Spectrosc.* **47**, 1100 (1993).
2. J. E. Bertie and S. L. Zhang, *Applied Spectrosc.* **48**, 176 (1994).

3. I. Mills, T. Cvitaš, K. Homann, N. Kallay, and K. Kuchitsu, *Quantities, Units and Symbols in Physical Chemistry*, Blackwell Scientific Publications (Oxford, 1988).
4. N. Sheppard, H. A. Willis, and J. C. Rigg, *Spectrochim. Acta* **43A**, 1 (1987).
5. The appendix in Ref. 1 (Section 5.6 in this thesis).
6. A. Serrallach, R. Meyer, and H. H. Gunthard, *J. Mol. Spectrosc.* **52**, 94 (1974).
7. J. E. Bertie and H. H. Eysel, *Appl. Spectrosc.* **39**, 392 (1985).
8. J. E. Bertie, H. Harke, and M. K. Ahmed, *Croatica Chemica Acta* **61**, 391 (1988).
9. J. E. Bertie, S. L. Zhang, and R. Manji, *Appl. Spectrosc.* **46**, 1660 (1992).
10. J. E. Bertie and S. L. Zhang, *Can. J. Chem.* **70**, 520 (1992).
11. D. G. Cameron, J. P. Hawranek, P. Neelakantan, R. P. Young, and R. N. Jones, in *Computer Programs for Infrared Spectrophotometry XLII to XLVII*, National Research Council of Canada Bulletin **16**, 1977.
12. J. E. Bertie, C. D. Keefe, and R. N. Jones, *Can. J. Chem.* **69**, 1609 (1991).
13. *International Critical Tables of Numerical Data, Physics, Chemistry and Technology*, **7**, 34, McGraw-Hill (New York, 1930).
14. *Catalog, Handbook of Fine Chemicals*, Aldrich Chemical Company, Inc. (Milwaukee, USA, 1992).
15. D. D. Honijk, W. F. Passchier, M. Mandel, and M. N. Afsar, *Infrared Physics* **17**, 9 (1977).
16. J. Alonso, F. J. Bermejo, M. Garcia-Hernandez, J. L. Martinez, W. S. Howells, and A. Criado, *J. Chem. Phys.* **96**, 7696 (1992).
17. J. E. Bertie, R. N. Jones, and Y. Apelblat, *Appl. Spectrosc.* **47**, 1989 (1993).
18. J. E. Bertie, S. L. Zhang, and C. D. Keefe, *J. Mol. Struct.* In press (1994).
19. M. J. Dignam, *Appl. Spectrosc. Rev.* **24**, 99 (1988).
20. *International Critical Tables of Numerical Data, Physics, Chemistry and Technology*, **3**, 27, McGraw-Hill (New York, 1928).
21. M. Falk and E. Whalley, *J. Chem. Phys.* **34**, 1554 (1961).
22. B. L. Crawford, Jr., *J. Chem. Phys.* **20**, 977 (1952).

23. A. D. Dickson, I. M. Mills, and B. L. Crawford, Jr., *J. Chem. Phys.* **27**, 445 (1957).
24. J. H. G. Bode and W. M. A. Smit, *J. Mol. Spectrosc.* **75**, 478 (1979).
25. W. M. A. Smit, J. H. G. Bode, and A. J. van Straten, *J. Mol. Spectrosc.* **75**, 485 (1979).
26. A. J. van Straten and W. M. A. Smit, *J. Mol. Spectrosc.* **56**, 484 (1975).
27. H. Torii and M. Tasumi, *J. Chem. Phys.* **99**, 8459 (1993).
28. B. J. van der Veken, W. A. Herrebout and H. H. Liefvooghe, *J. Mol. Struct.* **268**, 293 (1992).
29. P. D. Mallinson, *J. Mol. Spectrosc.* **58**, 194 (1975).

### 7.8 Note Added in Proof

After this paper was submitted it was realized that the identical wavenumbers, as well as intensities, of the torsion bands of H-C-O-H and D-C-O-H (Sections 7.4.3 and 7.6, and Figure 7.11) mean that the vibrations in question are not torsional vibrations. The torsional G matrix element of CH<sub>3</sub>OH is 1.10 times that of CD<sub>3</sub>OH, indicating that to zeroth order the CD<sub>3</sub>OH torsion would be at 640 cm<sup>-1</sup> when the CH<sub>3</sub>OH torsion is at 673 cm<sup>-1</sup>. Similarly, the ratio of the G matrix element of CH<sub>3</sub>OD to that of CD<sub>3</sub>OD is 1.18, so the CD<sub>3</sub>OD torsion would be at 457 cm<sup>-1</sup> when the CH<sub>3</sub>OD torsion is at 496 cm<sup>-1</sup>.

The bands are best described as due to the out-of-plane motion of the hydrogen (or deuterium) atom in an O-H---O hydrogen bond, in effect a linear O-H---O bending vibration. For this vibration in CH<sub>3</sub>OH, CD<sub>3</sub>OH, CH<sub>3</sub>OD or CD<sub>3</sub>OD, the G matrix elements are independent of the methyl group and the factor F in the relation  $\mu_{\tau}^2 = F \mu_j^2$  is 0.382, 0.382, 0.738 and 0.738, respectively. Thus  $\mu_R$  in Table 7.7 equals 0.85 D Å<sup>-1</sup> for "τ(DCOH)" of CD<sub>3</sub>OH and 0.82 D Å<sup>-1</sup> for "τ(DCOD)" of CD<sub>3</sub>OD. For CH<sub>3</sub>OH and CH<sub>3</sub>OD the corresponding  $\mu_R$  values in Table VII of Ref. 2 (i.e. Table 6.7) are 0.85 D Å<sup>-1</sup> and 0.83 D Å<sup>-1</sup>. The rotational corrections for the isotopomers of the "molecule" CH<sub>3</sub>OH---O can not be calculated because the permanent dipole moment of this "molecule" is not known, but the agreement between the  $\mu_R$  values of the different isotopomers is excellent and reflects the measured agreement between the intensities.



## Chapter 8 Integrated Absorption Intensities, Normal Coordinate Calculation, and Dipole Moment Derivatives of Molecules in Liquid Methanol

### 8.1 Introduction

The real and imaginary refractive index spectra between 8000 and 350  $\text{cm}^{-1}$  have been presented<sup>1-3</sup> in the previous chapters for four isotopomers of liquid methanol,  $\text{CH}_3\text{OH}$ ,  $\text{CH}_3\text{OD}$ ,  $\text{CD}_3\text{OH}$  and  $\text{CD}_3\text{OD}$ . The integrated intensities have been measured as  $C_j$ , the area under the bands in the spectrum of the imaginary polarizability multiplied by wavenumber,  $\tilde{\nu}\alpha''_m(\tilde{\nu})$ . The comparison of the spectra of the different isotopomers has enabled<sup>2,3</sup> some overlapping bands to be separated into contributions from different vibrations. Such separation has been made with confidence for the OH(D) and CH(D) stretching bands<sup>3</sup>, where the intensities obtained for CH(D) stretching vibrations are the combined intensities of all three vibrations. In the low wavenumber region below 1900  $\text{cm}^{-1}$ , the separation was more difficult and could not be reliably done for many bands, especially for the  $\text{CD}_3$  isotopomers in Chapter 7, because of the heavy overlapping of the bands.

The integrated intensities deduced in the previous three chapters were used to calculate the dipole moment derivatives of the molecules with respect to the internal coordinates under the simplest approximation, namely the diatomic harmonic oscillator for the OH, OD and CO stretching vibrations, coupled harmonic oscillators of  $\text{C}_{3v}$  symmetry for the  $\text{CH}_3$  and  $\text{CD}_3$  stretching and deformation vibrations, and the isolated harmonic oscillator for the O—H---O out-of-plane bending vibrations.

In this chapter, the reliability of the integrated intensities obtained in Chapters 5 to 7 is explored by comparing values obtained by curve-fitting the  $\alpha''_m$  spectra and a set “accepted” values of the integrated intensities is obtained.

In order to improve the dipole moment derivatives with respect to the internal coordinates obtained<sup>2,3</sup> in the previous chapters, a complete normal coordinate calculation was made to obtain a set of eigenvectors. Results of this normal coordinate calculation are presented in this chapter. The eigenvectors were used to obtain the dipole moment derivatives with respect to the symmetry coordinates by fitting the calculated intensities to the observed intensities. The derivatives were then converted to those with respect to the internal coordinates.

## 8.2 Integrated Intensities

### 8.2.1 Results from Isotopic Comparison

The absorption intensities of liquid methanol,  $\text{CH}_3\text{OH}$ , and its isotopomers,  $\text{CH}_3\text{OD}$ ,  $\text{CD}_3\text{OH}$  and  $\text{CD}_3\text{OD}$ , have been reported in the previous chapters. The integrated intensities,  $C_j$ , have also been obtained for some normal vibrations. Some overlapping bands were separated by comparing the spectra of different isotopomers and making reasonable assumptions. The results are summarized in columns 4 of Tables 8.1 to 8.4 under the heading "Isotopic comparison" for  $\text{CH}_3\text{OH}$ ,  $\text{CH}_3\text{OD}$ ,  $\text{CD}_3\text{OH}$  and  $\text{CD}_3\text{OD}$ , respectively. The area  $C_j$ , defined<sup>1,4</sup> by eq. (4.11), is the area under the band in the  $\tilde{\nu}\alpha_m''$  spectrum. According to the classical damped harmonic oscillator (CDHO) theory, the wavenumber of the mechanical oscillator is the wavenumber of the peak in  $\tilde{\nu}\alpha_m''$  (Chapter 4). Thus, the peak wavenumbers observed in the  $\tilde{\nu}\alpha_m''$  spectra are given in the third columns of Tables 8.1 to 8.4. Assignments of these peaks are also given in the tables. These peak wavenumbers and assignments of the fundamental vibrations were used as the observed frequencies in the normal coordinate calculation in the next section.

Figure 8.1 shows the high wavenumber regions of the  $\tilde{\nu}\alpha_m''$  spectra of the four isotopomers, with different combinations in each box. The integrated intensities  $C_j$  of the OH(D) and CH(D) stretching vibrations deduced in Chapter 7 are believed to be accurate to a few percent.<sup>3</sup> This accuracy is in little doubt for  $\text{CH}_3\text{OD}$  and  $\text{CD}_3\text{OH}$  because the CH bands are well separated from the OD band for  $\text{CH}_3\text{OD}$  (the dashed spectrum in the top left box) and the OH band is well separated from the CD bands for  $\text{CD}_3\text{OH}$  (the dashed spectrum in the top right box). It is also in little doubt for  $\text{CH}_3\text{OH}$  and  $\text{CD}_3\text{OD}$  because their  $C_j$  values were obtained from those of  $\text{CH}_3\text{OD}$  and  $\text{CD}_3\text{OH}$  in two different ways and the two sets of values are in good agreement as shown in Table 7.6. To obtain the first set, it was assumed that the intensity of the OH stretching vibration in  $\text{CH}_3\text{OH}$  is the same as that in  $\text{CD}_3\text{OH}$  and the intensity of the OD stretching vibration in  $\text{CH}_3\text{OD}$  is the same as that in  $\text{CD}_3\text{OD}$ . This assumption is clearly a direct result from the experimental spectra as shown in the right boxes of Figure 8.1. The top box contains the spectra of  $\text{CH}_3\text{OH}$  and  $\text{CD}_3\text{OH}$ , and the bottom box contains those of  $\text{CH}_3\text{OD}$  and  $\text{CD}_3\text{OD}$ . Therefore, from the separated OD intensity in  $\text{CH}_3\text{OD}$ , the intensity of the CD stretching bands in  $\text{CD}_3\text{OD}$  was obtained from the total intensity of the OD and CD stretching bands in the region. Similarly, from the separated OH intensity in  $\text{CD}_3\text{OH}$ , the intensity of the CH stretching bands in  $\text{CH}_3\text{OH}$  was obtained.

To obtain the second set, it was assumed that the intensity of the CH stretching bands is the same in  $\text{CH}_3\text{OH}$  and in  $\text{CH}_3\text{OD}$  and that of the CD stretching bands is the same in  $\text{CD}_3\text{OH}$  and  $\text{CD}_3\text{OD}$ . This set of comparisons is shown in the left-hand boxes of Figure 8.1. The OH(D) and CH(D) stretching intensities obtained can be compared to those in the first set. Two sets are summarized in Table 7.6 and the average values are collected in Tables 8.1 to 8.4. These averaged values were used in the calculation of the intensity parameters in Section 8.4.

The low wavenumber regions of the spectra are shown in Figure 8.2. In the top box are spectra of  $\text{CH}_3\text{OH}$  and  $\text{CH}_3\text{OD}$ . The single strong band is the CO stretching band. It is almost identical in the two spectra, with the same wavenumber and the same intensity. This fact was used<sup>2</sup> to obtain the area  $C_j$  for the CO stretching band in Chapter 6. The difference spectrum of the two was also used to obtain the  $C_j$  values of other vibrations in Chapter 6. The  $C_j$  values obtained are collected in Tables 8.1 and 8.2 for  $\text{CH}_3\text{OH}$  and  $\text{CH}_3\text{OD}$ , respectively under “Isotopic comparison”. The bottom box of Figure 8.2 shows the spectra of  $\text{CH}_3\text{OH}$  and  $\text{CD}_3\text{OH}$  between 1600 and 350  $\text{cm}^{-1}$ . The out-of-plane bending band of the hydroxyl group at 670  $\text{cm}^{-1}$  has the same intensity and the same wavenumber in the two molecules. This is also true for  $\text{CH}_3\text{OD}$  and  $\text{CD}_3\text{OD}$  as shown in Figure 7.11. From the bottom box of Figure 8.2 it can also be seen that the COH in-plane bending mode, at 1423 and 1393  $\text{cm}^{-1}$  in  $\text{CH}_3\text{OH}$  and  $\text{CD}_3\text{OH}$ , respectively, has similar intensity in both molecules, consistent with expectation. The  $C_j$  values obtained for these vibrations are summarized in Tables 8.1 to 8.4.

As for the deformation and rocking vibrations in these molecules, the separation is more complicated, especially for  $\text{CD}_3\text{OH}$  and  $\text{CD}_3\text{OD}$  where the vibrations are strongly coupled with the CO stretch, and it was found impossible to separate the bands with confidence by comparing the different spectra. Therefore, curve-fitting was used to help separate the overlapping bands. It was also used to separate the combined intensities of the  $\text{CH}_3$  or  $\text{CD}_3$  stretching and deformation vibrations into the contribution from each fundamental.

**Table 8.1** Integrated intensities of CH<sub>3</sub>OH.<sup>a</sup>

CH <sub>3</sub> OH		Observed peak wavenumber	Area $C_j$			Accepted value	
Assignment			Isotopic comparison <sup>b</sup>	Curve-fitting		$C_j$	$\mu_j^2$
$\nu_1$	$\nu(\text{OH})$	3354	7.42	7.34		7.42	13.9
$\nu_2$	$\nu(\text{CH})$ asym	2980	1.33	1.29	0.35	0.39 <sup>c</sup>	0.73
$\nu_9$	$\nu(\text{CH})$	2945			0.55	0.55	1.03
$\nu_3$	$\nu(\text{CH})$ sym	2833			0.39	0.39	0.73
$\nu_6$	$\delta(\text{COH})$	1423	0.73	0.62		0.67±0.06	1.25±0.11
$\nu_4$	$\delta(\text{CH}_3)$ asym	1477	0.19	0.20	0.04	0.04	0.30
$\nu_{10}$	$\delta(\text{CH}_3)$	(1477)				0.00	0.00
$\nu_5$	$\delta(\text{CH}_3)$ sym	1450			0.16	0.16	0.07
$\nu_{11}$	$\gamma(\text{CH}_3)$		0.15	0.18	0.02	0.02	0.04
$\nu_7$	$\gamma(\text{CH}_3)$	1116			0.16	0.16	0.30
$\nu_8$	$\nu(\text{CO})$	1035	1.24	1.16		1.20±0.04	2.24±0.07
$\nu_{12}$	$\delta(\text{O-H}\cdots\text{O})$	673	1.02	1.08		1.05±0.03	1.96±0.06
Overtone and combination bands							
$2\nu_6$			0.25	0.32			
$\nu_4+\nu_{11}$		2596	0.09	0.04			
$\nu_6+\nu_{11}$		2522		0.14			
$\nu_6+\nu_8$		2439					
$2\nu_{11}$		2229		0.02			
$2\nu_8$		2045	0.04	0.03			
$\nu_8+\nu_{12}$ ?				0.18			

a The observed peak wavenumbers are from the  $\tilde{\nu}\alpha_m''$  spectrum. The wavenumber in parentheses was not used in the normal coordinate calculation.  $C_j$  is in km mol<sup>-1</sup> and  $\mu_j^2 = |\partial\bar{\mu}/\partial Q_j|^2$  is in (D Å<sup>-1</sup> amu<sup>-1/2</sup>)<sup>2</sup>.

b The values are from Tables 6.6, 6.7 and 7.7.

c This value contains an extra 0.04 km mol<sup>-1</sup> above that from the curve-fit, to make the total intensity of the CH stretching vibrations equal that from isotopic comparison.

**Table 8.2** Integrated intensities of CH<sub>3</sub>OD.<sup>a</sup>

CH <sub>3</sub> OD		Observed peak wavenumber	Area C <sub>j</sub>			Accepted value	
Assignment			Isotopic comparison <sup>b</sup>	Curve-fitting		C <sub>j</sub>	μ <sub>j</sub> <sup>2</sup>
ν <sub>3</sub>	ν(OD)	2497	4.01	3.76		4.01	7.49
ν <sub>1</sub>	ν(CH) asym	2981	1.31	1.37	0.46	0.43 <sup>c</sup>	0.80
ν <sub>9</sub>	ν(CH)	2947			0.48	0.48	0.90
ν <sub>2</sub>	ν(CH) sym	2836			0.43	0.40 <sup>c</sup>	0.75
ν <sub>8</sub>	δ(COD)	941			0.26	0.34	0.30±0.04
ν <sub>4</sub>	δ(CH <sub>3</sub> ) asym	1467	0.19	0.19	0.12	0.12	0.22
ν <sub>10</sub>	δ(CH <sub>3</sub> )	(1467)			0.00	0.00	0.00
ν <sub>5</sub>	δ(CH <sub>3</sub> ) sym	1447			0.07	0.07	0.13
ν <sub>6</sub>	γ(CH <sub>3</sub> )	1232			0.05	0.05	0.09
ν <sub>11</sub>	γ(CH <sub>3</sub> )	1157			0.01	0.01	0.02
ν <sub>7</sub>	ν(CO)	1034	1.27	1.19		1.23±0.04	2.30±0.07
ν <sub>12</sub>	δ(O-D...O)	496	0.50	0.56		0.53±0.03	0.99±0.06
Overtone and combination bands							
2ν <sub>11</sub>		~2260	0.00	0.01			
ν <sub>7</sub> +ν <sub>11</sub>		2178	0.03	0.14			
2ν <sub>7</sub>		2044	0.07	0.05			
ν <sub>7</sub> +ν <sub>8</sub>		1966		0.04			
2ν <sub>8</sub>		1892		0.05			
2ν <sub>12</sub> ?		1122 1084		0.06			

<sup>a</sup> See footnote a of Table 8.1.

<sup>b</sup> The values are from Tables 6.6 and 6.7.

<sup>c</sup> 0.03 km mol<sup>-1</sup> has been subtracted from the intensity of each of the two A' modes to make the total intensity of the CH stretching vibrations equal to that from isotopic comparison.

**Table 8.3** Integrated intensities of CD<sub>3</sub>OH.<sup>a</sup>

CD <sub>3</sub> OH		Observed peak wavenumber	Area $C_j$			accepted value	
Assignment			Isotopic Comparison <sup>b</sup>	Curve-fitting		$C_j$	$\mu_j^2$
$\nu_1$	$\nu(\text{OH})$	3352	7.40	7.32		7.40	13.8
$\nu_2$	$\nu(\text{CD})$ asym	2235	0.96	0.96	0.31	0.31	0.58
$\nu_9$	$\nu(\text{CD})$	2216			0.28	0.28	0.52
$\nu_3$	$\nu(\text{CD})$ sym	2072			0.37	0.37	0.69
$\nu_4$	$\delta(\text{COH})$	1393	0.78	0.78		0.78	1.46
$\nu_6$	$\delta(\text{CD}_3)$ asym	(1068)		0.58	0.03	0.03	0.06
$\nu_{10}$	$\delta(\text{CD}_3)$	1068			0.07	0.07	0.13
$\nu_5$	$\delta(\text{CD}_3)$ sym	1122			0.48	0.48	0.90
$\nu_8$	$\gamma(\text{CD}_3)$	886		0.15	0.12	0.12	0.22
$\nu_{11}$	$\gamma(\text{CD}_3)$				0.03	0.03	0.06
$\nu_7$	$\nu(\text{CO})$	984		0.66		0.66	1.23
$\nu_{12}$	$\delta(\text{O-H}\cdots\text{O})$	653	1.01	0.93		0.97±0.04	1.81±0.07
Overtone and combination bands							
$2\nu_4$		2783	0.25	0.31			
$2\nu_7$		1957	0.01	0.02			
$\nu_7+\nu_{12}$ ?		(1669)		0.10			

<sup>a</sup> See footnote a of Table 8.1.

<sup>b</sup> The values are from Table 7.7.

**Table 8.4** Integrated intensities of CD<sub>3</sub>OD.<sup>a</sup>

CD <sub>3</sub> OD		Observed peak wavenumber	Area C <sub>j</sub>			Accepted value	
Assignment			Isotopic Comparison <sup>b</sup>	Curve-fitting		C <sub>j</sub>	μ <sub>j</sub> <sup>2</sup>
ν <sub>1</sub>	ν(OD)	2493	3.95	3.93		3.95	7.38
ν <sub>2</sub>	ν(CD) asym	2245	0.90	0.91	0.26	0.25 <sup>c</sup>	0.47
ν <sub>9</sub>	ν(CD)	2216			0.26	0.26	0.49
ν <sub>3</sub>	ν(CD) sym	2072			0.39	0.39	0.73
ν <sub>8</sub>	δ(COD)	824	0.09 or 0.26 <sup>c</sup>	0.08 or 0.19 <sup>d</sup>		0.18±0.08	0.34±0.16
ν <sub>4</sub>	δ(CD <sub>3</sub> ) sym	1125		0.79	0.25	0.25	0.47
ν <sub>10</sub>	δ(CD <sub>3</sub> )	1064			0.04	0.04	0.07
ν <sub>5</sub>	δ(CD <sub>3</sub> ) asym	1097			0.50	0.50	0.93
ν <sub>6</sub>	γ(CD <sub>3</sub> )			0.14	0.12	0.12	0.22
ν <sub>11</sub>	γ(CD <sub>3</sub> )	902			0.02	0.02	0.04
ν <sub>7</sub>	ν(CO)	979		0.58		0.58	1.08
ν <sub>12</sub>	δ(O–D...O)	485	0.48	0.52		0.50±0.02	0.93±0.04
Overtone and combination bands							
2ν <sub>7</sub>		1944	0.04	0.05			
2ν <sub>11</sub>		1910		0.03			
2ν <sub>8</sub>		1651		0.01			
? <sup>d</sup>		(804)		0.11			
2ν <sub>12</sub>		930		0.04			

<sup>a</sup> See footnote a of Table 8.1.

<sup>b</sup> The values are from Table 7.7.

<sup>c</sup> The 0.09 km mol<sup>-1</sup> is the area above the straight line between two curve points to each side of the peak and 0.26 km mol<sup>-1</sup> is an assumed value (see Chapter 7).

<sup>d</sup> A band at 804 cm<sup>-1</sup> necessary for the fit introduces a big uncertainty.

<sup>e</sup> 0.01 km mol<sup>-1</sup> has been subtracted from this value to make the total intensity of the CD stretching vibrations 0.90 km mol<sup>-1</sup>.

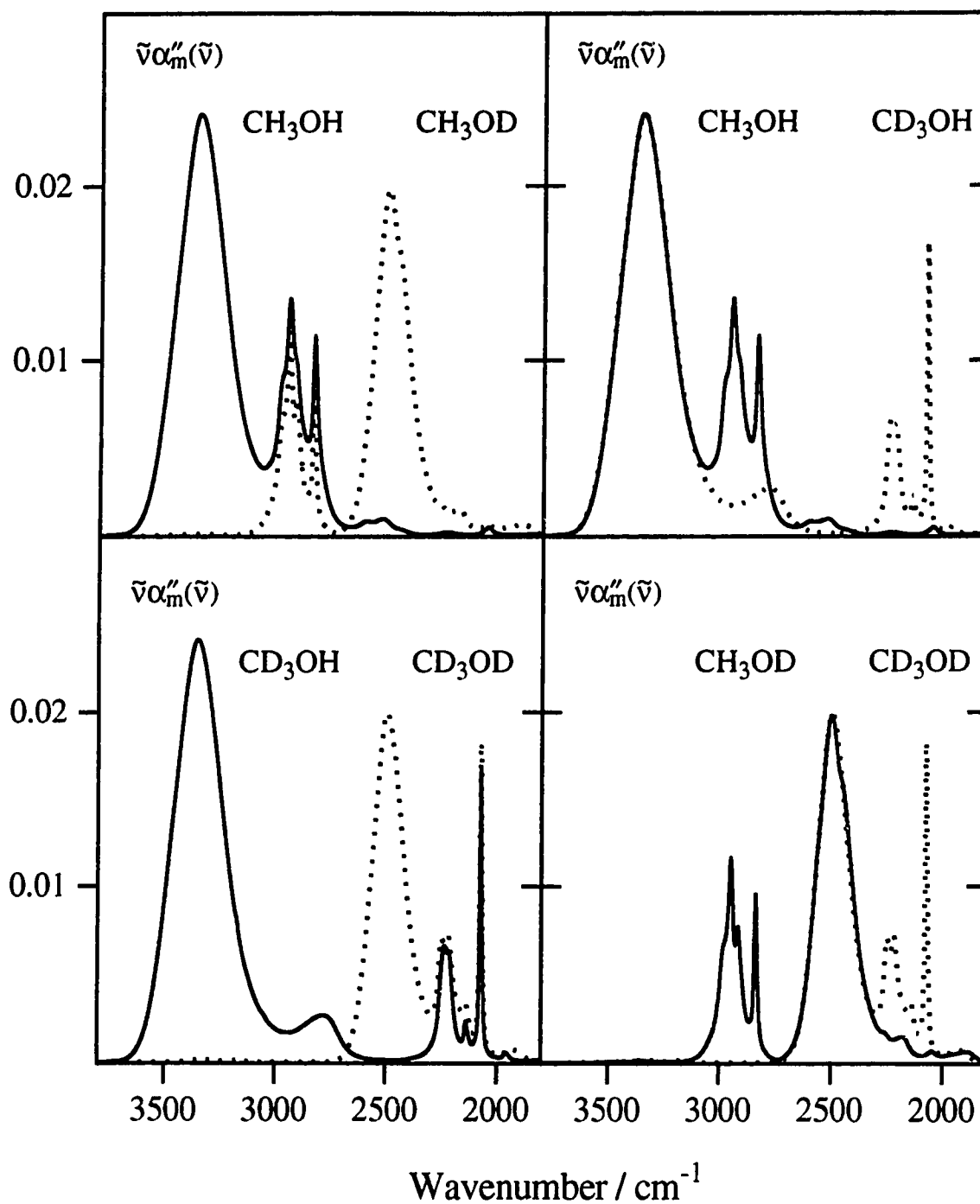


**Figure 8.1** The  $\tilde{\nu}\alpha_m''$  spectra of methanol in the OH(D) and CH(D) stretching regions. The ordinate unit is  $10^5 \text{ cm}^2 \text{ mol}^{-1}$ .



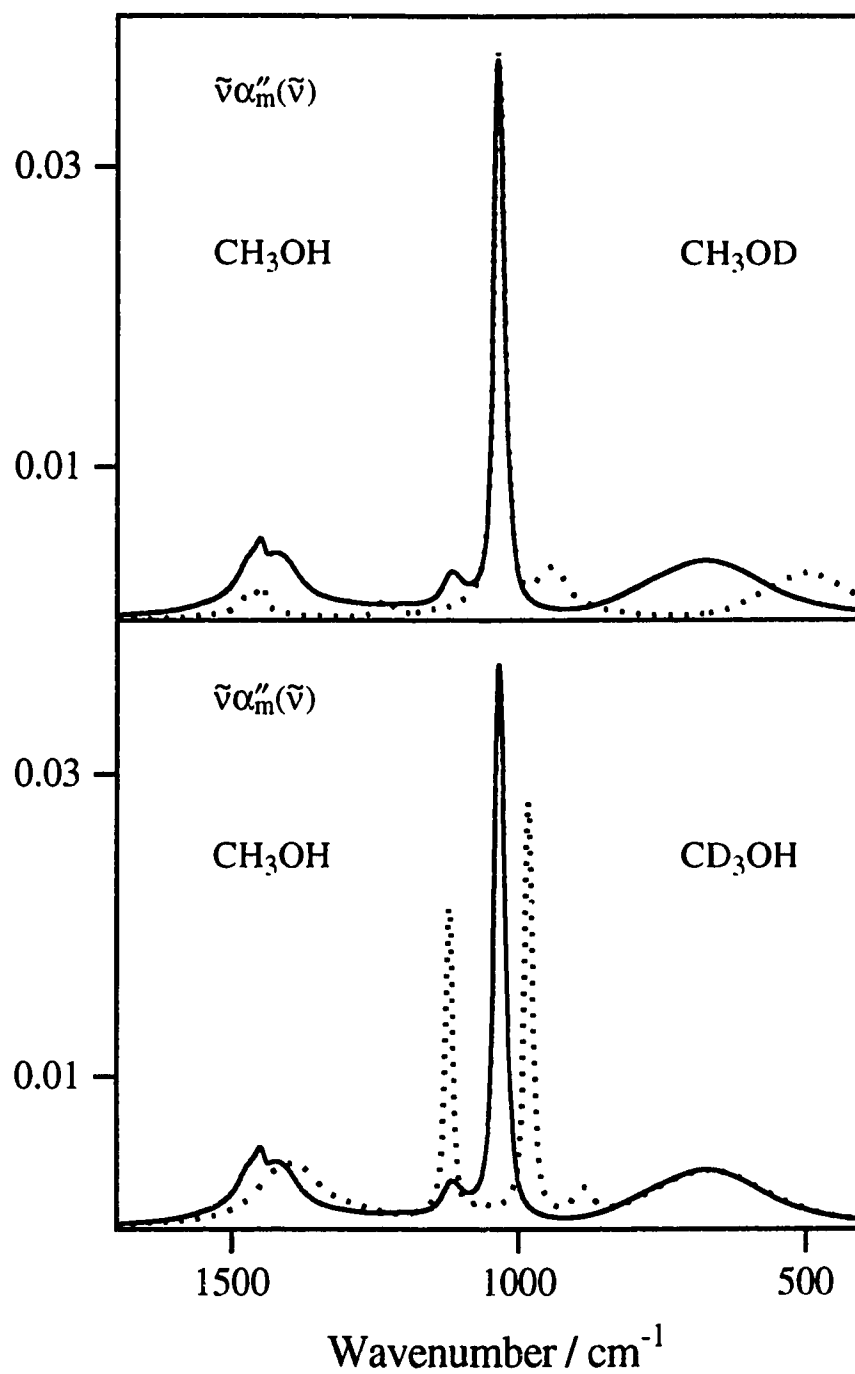


**Figure 8.2** The  $\tilde{\nu}\alpha_m''$  spectra of methanol between 1600 and 400 cm<sup>-1</sup>. The ordinate unit is 10<sup>5</sup> cm<sup>2</sup> mol<sup>-1</sup>.

## 8.2.2 Results from Curve-Fitting

### 8.2.2.1 General

In this section, results of the separation of the imaginary polarizability bands by curve-fitting are presented for all four isotopomers. The bands that could not be separated previously by comparing the isotopic spectra were separated by curve-fitting and the integrated intensity of each normal vibration of the four molecules was determined.

The curve-fitting uses the Array Basic\* routine CURVEFIT supplied in SpectraCalc\*, modified in this laboratory to include the CDHO band shape which was discussed in Chapter 4. A FORTRAN version of this program, also called CURVEFIT, exists for running under OS/2\*\* on personal computers. The FORTRAN program is about 10 times faster and allows access to all of the memory in the computer. Bands due to motion of the hydrogen-bonded H or D atom were fitted with Gaussian bands and all the other bands were fitted with CDHO bands. The  $\alpha''_m$  spectra were fitted, but the areas under the bands fitted to the spectrum were calculated in their  $\tilde{\nu}\alpha''_m$  spectrum through eq. (4.22) for CDHO bands and through

$$C_j = \tilde{\nu}_j \Gamma_j H_j \sqrt{\frac{\pi}{4 \ln 2}} \quad (8.1)$$

for Gaussian bands defined by

$$(\alpha''_m)_j = H_j \exp \left[ (-4 \ln 2 / \Gamma_j^2) (\tilde{\nu} - \tilde{\nu}_j)^2 \right] \quad (8.1a)$$

where  $H_j$  is the height,  $\Gamma_j$  is the FWHH and  $\tilde{\nu}_j$  is the peak wavenumber.

Figures 8.3 to 8.6 show the results of fitting the  $\alpha''_m$  spectra. Part A of each figure shows the high wavenumber part of the spectrum and Part B shows the low wavenumber part. The fits were first done on separate regions. The best fitted parameters from each region were then combined and entered into the FORTRAN version of CURVEFIT to fit the entire spectrum and to obtain the final results shown in these figures. Tables 8.5 to 8.8 list the parameters of all the component bands. The experimental and fitted curves coincide in Figures 8.3 to 8.6 except in a few small regions. The component bands in Figures 8.3 to 8.6 are CDHO bands unless they are labeled G for Gaussian.

\* Array Basic and SpectraCalc are the registered trademarks of the Galactic Industries Corp., Salem, NH.

\*\*OS/2 is a registered trademark of IBM Corp.

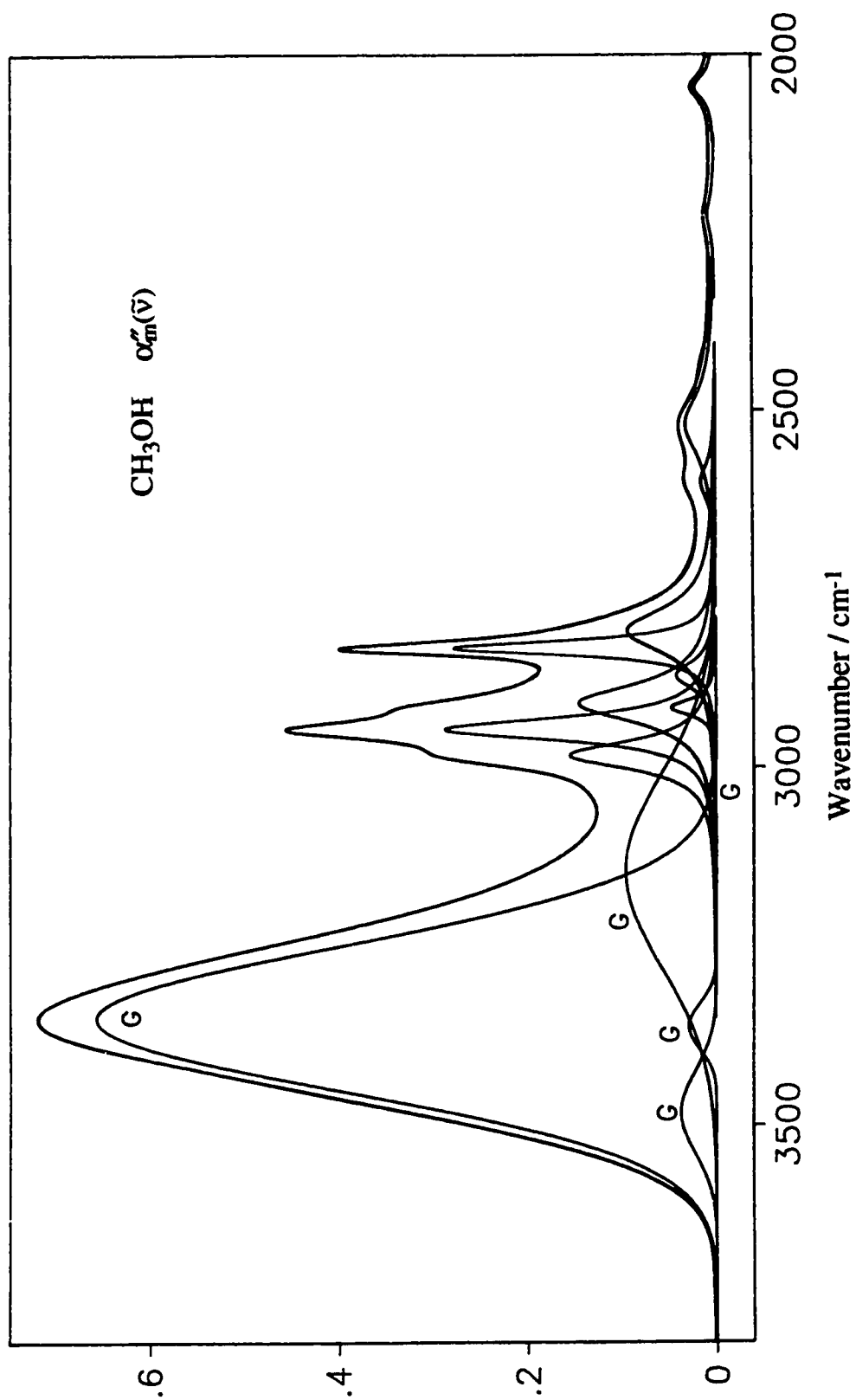


**Figure 8.3A** The  $\alpha_m''(\tilde{\nu})$  spectrum of CH<sub>3</sub>OH from 3800 to 2000 cm<sup>-1</sup>. The top curves: the fitted spectrum, overlapped with the experimental spectrum; The lower curves: the component bands used to obtain the fitted spectrum. Each component spectrum covers the full range, but only the significant part of each band is plotted for clarity. G denotes Gaussian band. The others are CDHO bands.

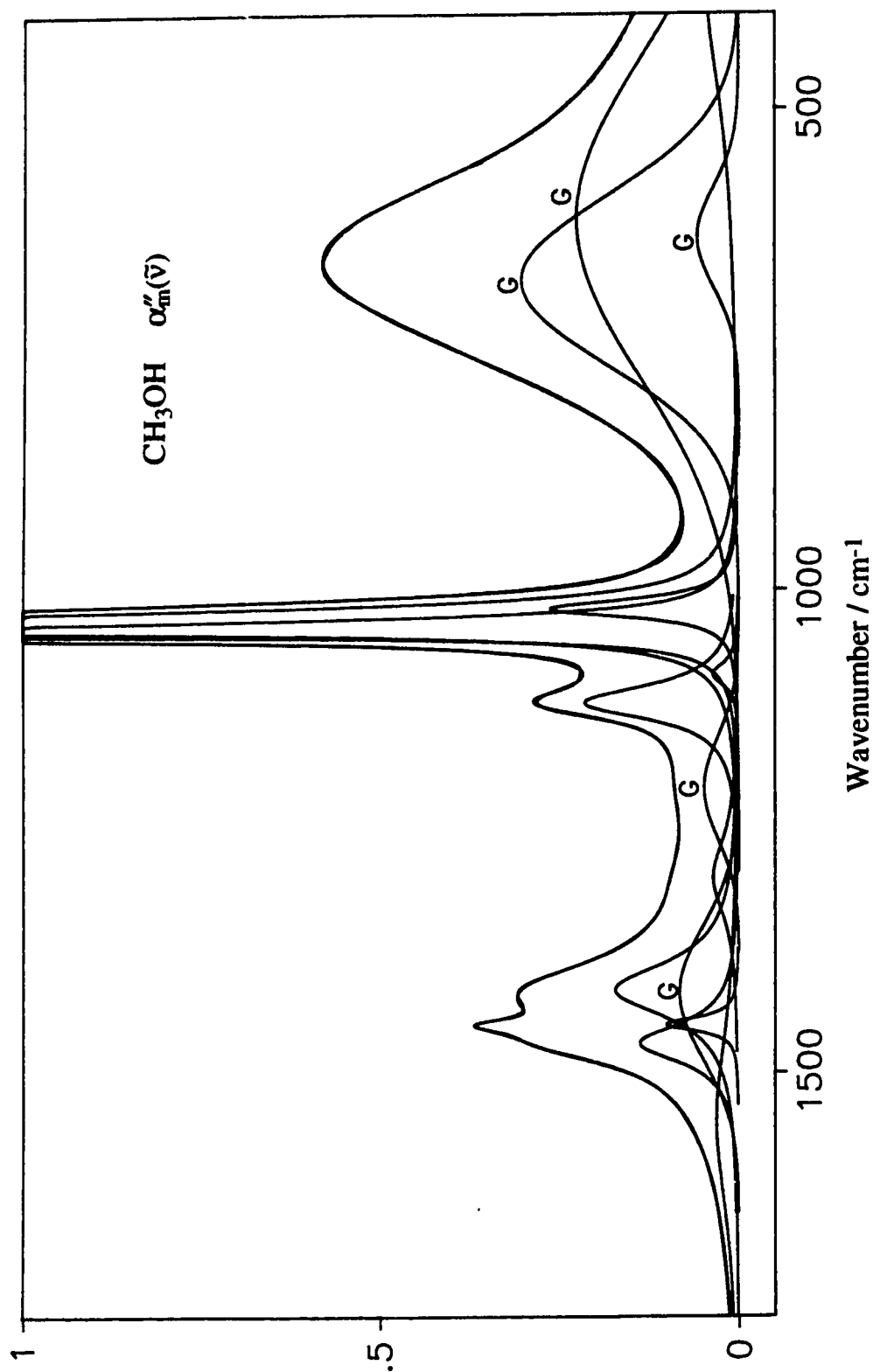


**Figure 8.3B** The  $\alpha_m''(\bar{\nu})$  spectrum of  $\text{CH}_3\text{OH}$  from 1750 to 400  $\text{cm}^{-1}$ . The top curves: the fitted spectrum, overlapped with the experimental spectrum; The lower curves: the component bands used to obtain the fitted spectrum. Each component spectrum covers the full range, but only the significant part of each band is plotted for clarity. G denotes Gaussian band. The others are CDHO bands.

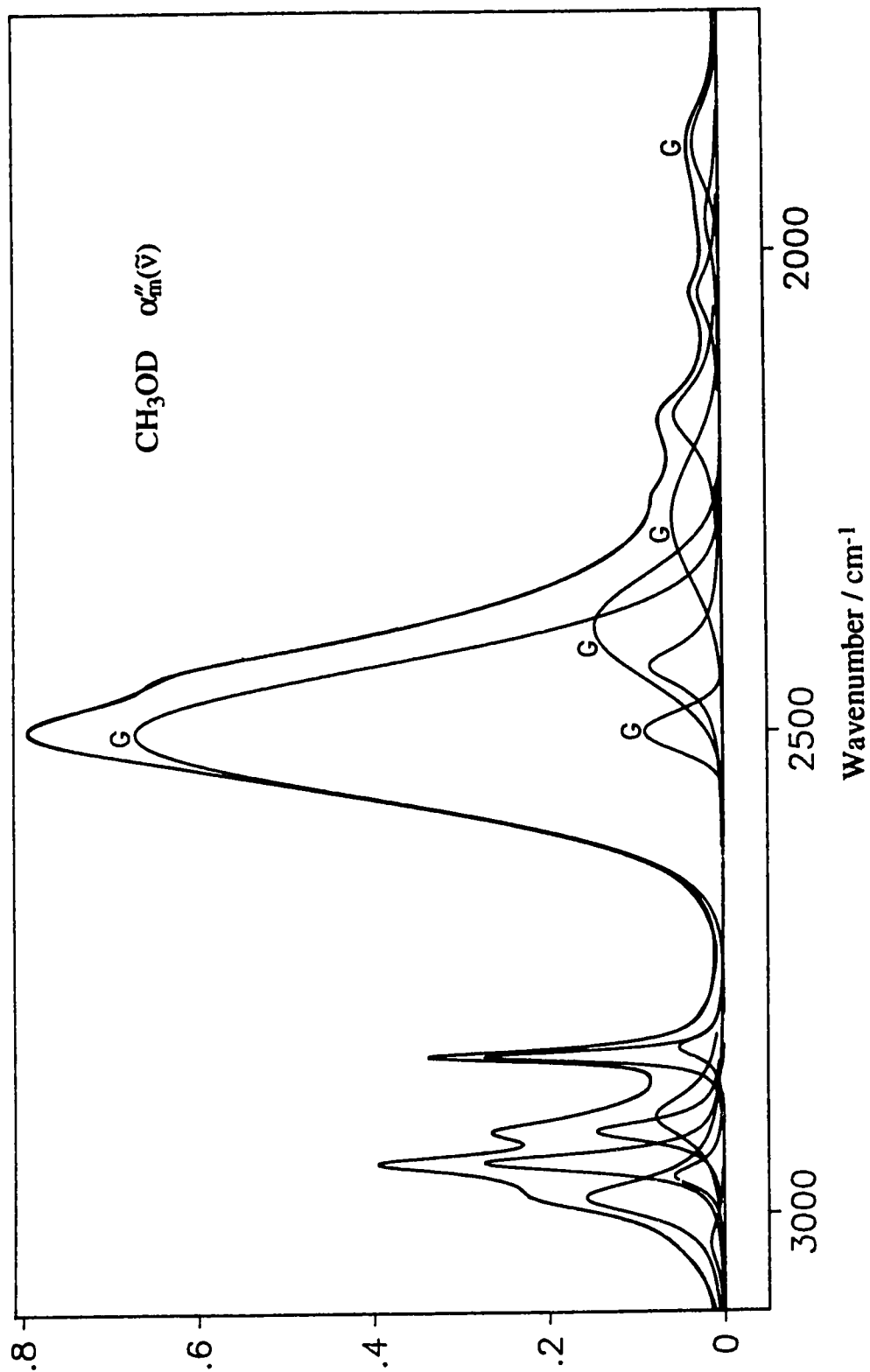


**Figure 8.4A** The  $\alpha_m''(\tilde{\nu})$  spectrum of CH<sub>3</sub>OD from 3100 to 1750 cm<sup>-1</sup>. The top curves: the fitted spectrum, overlapped with the experimental spectrum; The lower curves: the component bands used to obtain the fitted spectrum. Each component spectrum covers the full range, but only the significant part of each band is plotted for clarity. G denotes Gaussian band. The others are CDHO bands.

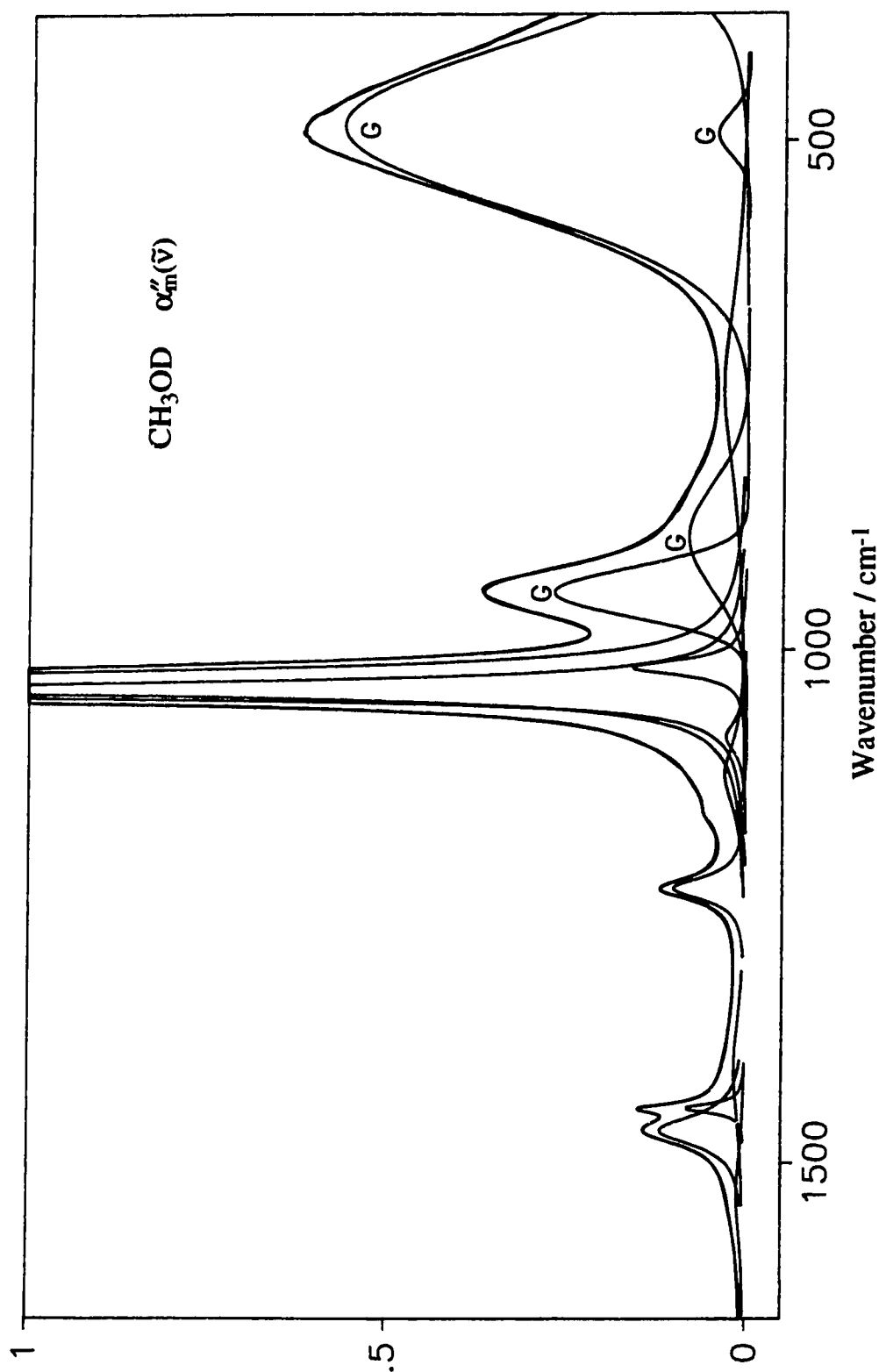


**Figure 8.4B** The  $\alpha_m''(\tilde{\nu})$  spectrum of  $\text{CH}_3\text{OD}$  from 1650 to  $375 \text{ cm}^{-1}$ . The top curves: the fitted spectrum, overlapped with the experimental spectrum; The lower curves: the component bands used to obtain the fitted spectrum. Each component spectrum covers the full range, but only the significant part of each band is plotted for clarity. G denotes Gaussian band. The others are CDHO bands.

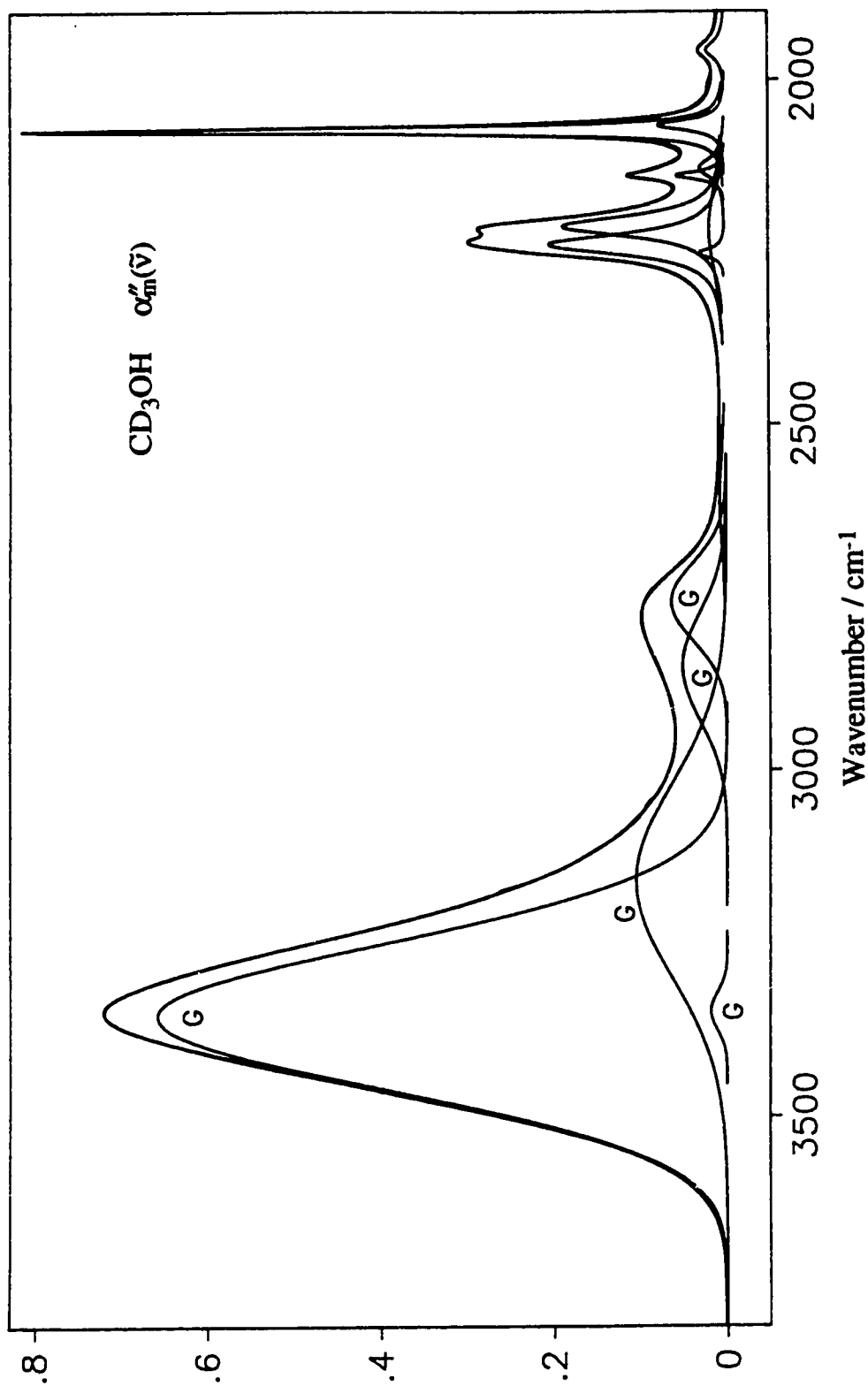


**Figure 8.5A** The  $\alpha_m''(\tilde{\nu})$  spectrum of  $\text{CD}_3\text{OH}$  from 3800 to 1900  $\text{cm}^{-1}$ . The top curves: the fitted spectrum, overlapped with the experimental spectrum; The lower curves: the component bands used to obtain the fitted spectrum. Each component spectrum covers the full range, but only the significant part of each band is plotted for clarity. G denotes Gaussian band. The others are CDHO bands.

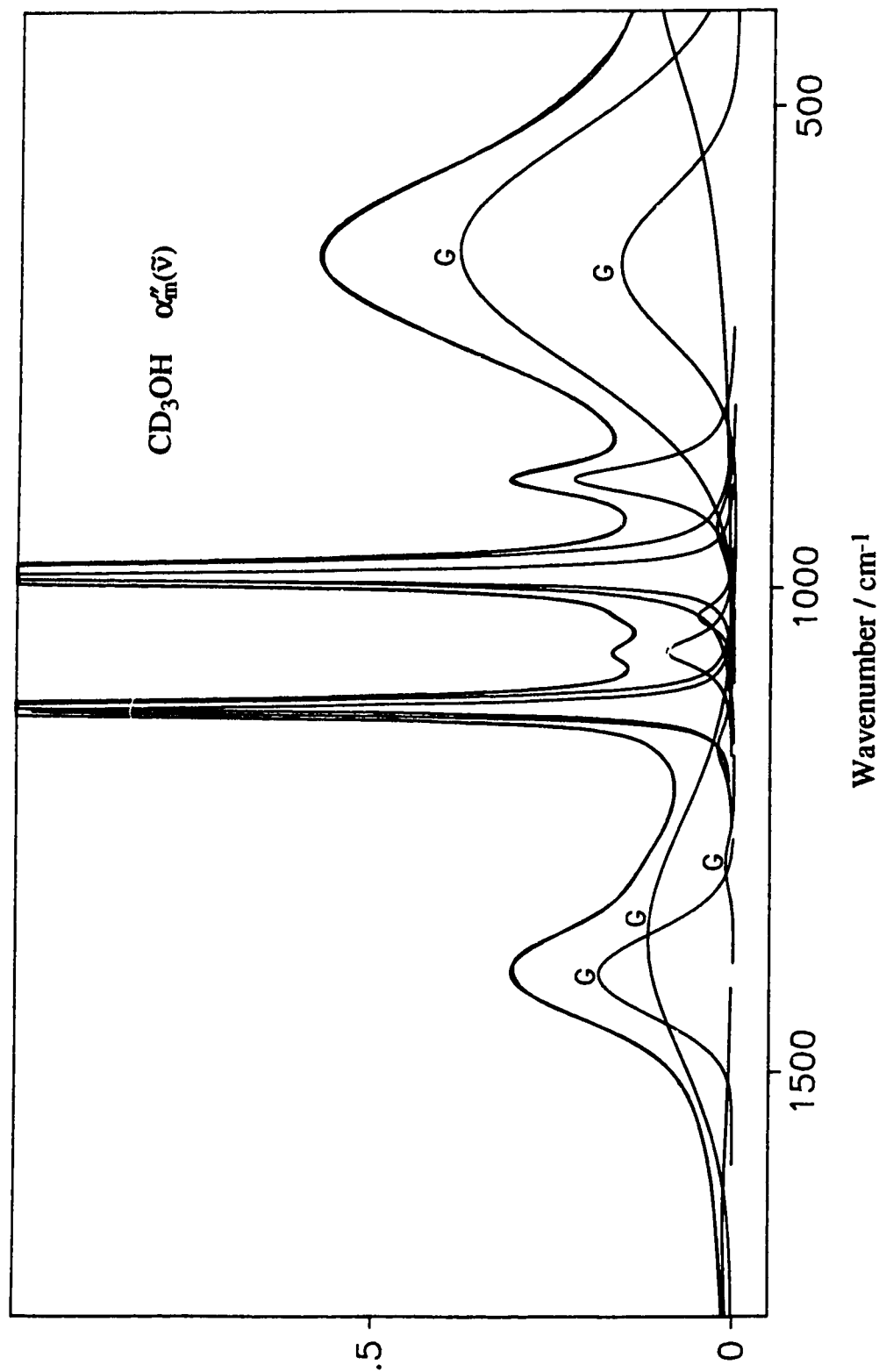


**Figure 8.5B** The  $\alpha_m''(\tilde{\nu})$  spectrum of  $\text{CD}_3\text{OH}$  from 1750 to 400  $\text{cm}^{-1}$ . The top curve: the fitted spectrum, overlapped with the experimental spectrum; The lower curves: the component bands used to obtain the fitted spectrum. Each component spectrum covers the full range, but only the significant part of each band is plotted for clarity. G denotes Gaussian band. The others are CDHO bands.



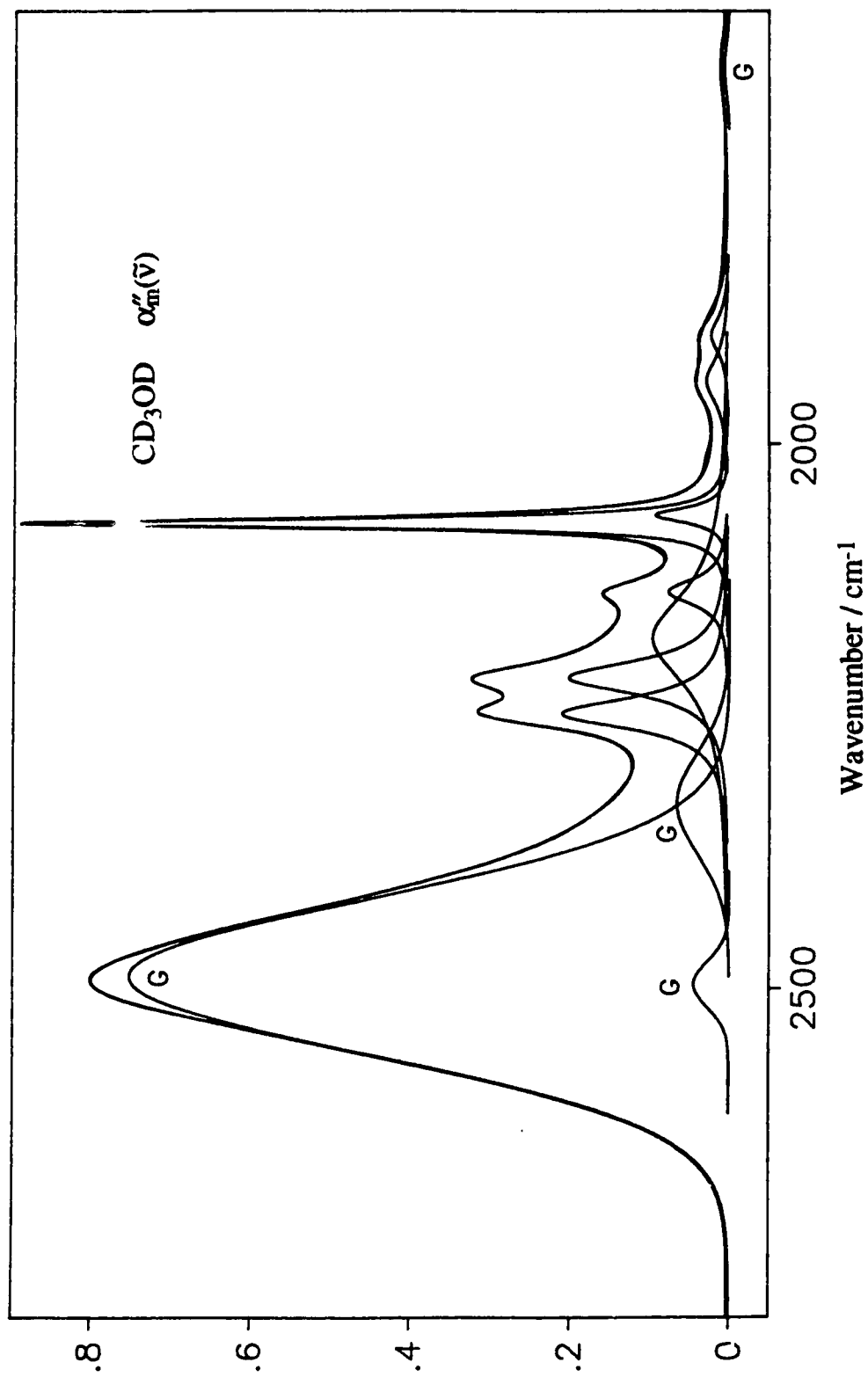


**Figure 8.6A** The  $\alpha_m''(\bar{\nu})$  spectrum of  $\text{CD}_3\text{OD}$  from 2800 to 1600  $\text{cm}^{-1}$ . The top curves: the fitted spectrum, overlapped with the experimental spectrum; The lower curves: the component bands used to obtain the fitted spectrum. Each component spectrum covers the full range, but only the significant part of each band is plotted for clarity. G denotes Gaussian band. The others are CDHO bands.

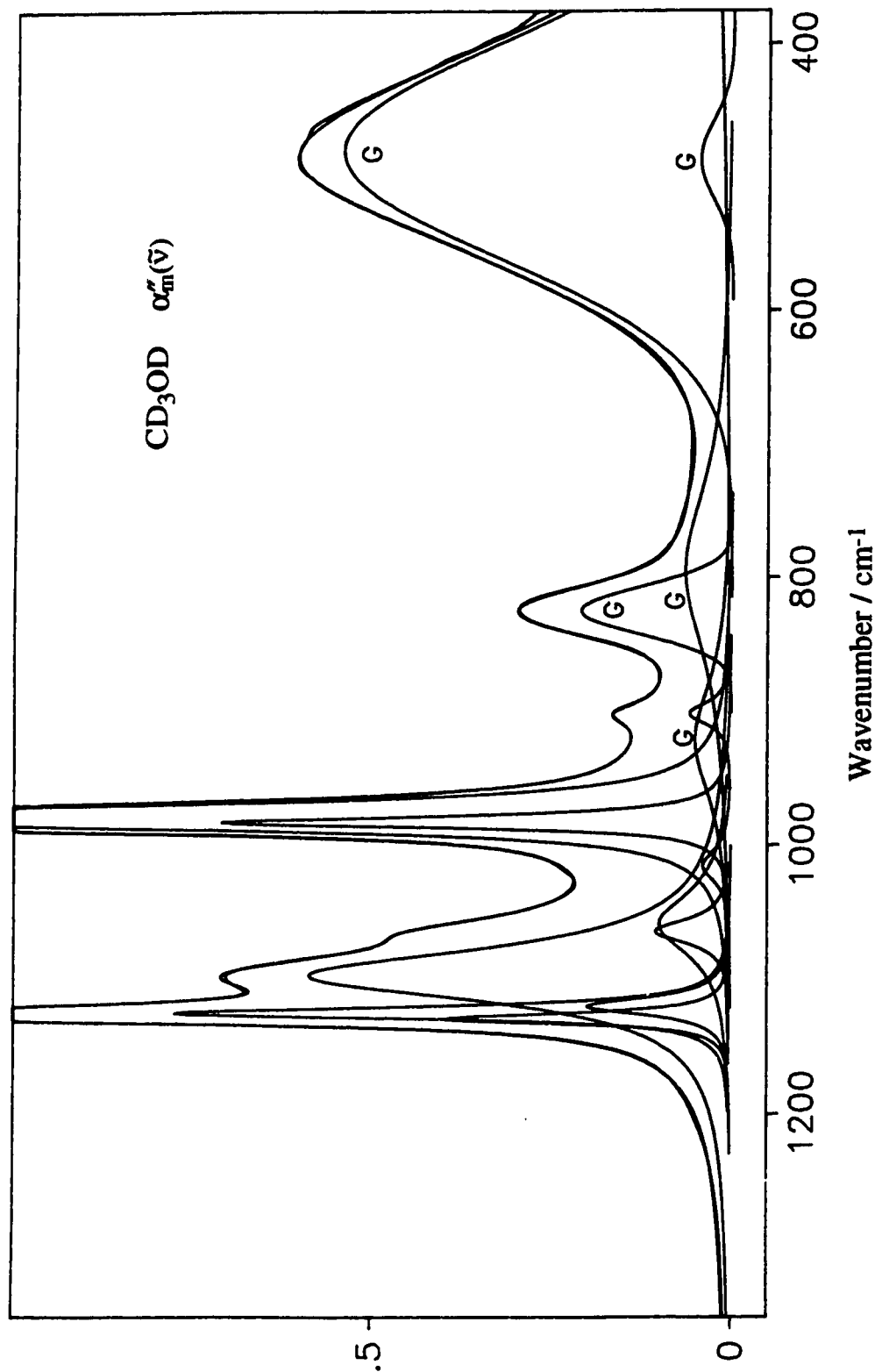


**Figure 8.6B** The  $\alpha_m''(\tilde{\nu})$  spectrum of  $\text{CD}_3\text{OD}$  from 1350 to 375  $\text{cm}^{-1}$ . The top curve: the fitted spectrum, overlapped with the experimental spectrum; The lower curves: the component bands used to obtain the fitted spectrum. Each component spectrum covers the full range, but only the significant part of each band is plotted for clarity. G denotes Gaussian band. The others are CDHO bands.

**Table 8.5** The parameters of the bands fitted to the  $\alpha_m''$  spectrum of CH<sub>3</sub>OH. <sup>a</sup>

CH <sub>3</sub> OH		Observed <sup>b</sup>	Fitted band <sup>c</sup>			Area $C_j$ <sup>d</sup>	
Assignment		$\tilde{\nu}_{\text{obs}}$	$\tilde{\nu}_{\text{max}}$	FWHH	Type	Individual	Total
<b><math>\nu_1</math></b>	<b><math>\nu(\text{OH}), a'</math></b>	3351	3482.6	131	G	0.187	6.91 +0.43 <sup>e</sup> =7.34
			3348.8	239	G	5.604	
			3362.6	75	G	0.079	
			3144.8	317	G	1.024	
			3038.0	47	G	0.012	
<b><math>\nu_2</math></b>	<b><math>\nu(\text{CH}), \text{as}, a'</math></b>	2980	2982.6	47	C	0.346	<b>0.35</b>
<b><math>\nu_9</math></b>	<b><math>\nu(\text{CH}), \text{as}, a''</math></b>	2945	2945.7	37	C	0.496	<b>0.55</b>
<b><math>\nu_4+\nu_{10}</math></b>	<b><math>\nu(\text{CH})+\delta(\text{CH}_3), a''</math></b>	2916	2916.5	26	C	0.057	to $\nu_{\text{OH}}$ <sup>e</sup>
		~2900	2910.6	64	C	0.429	
<b><math>2\nu_5</math></b>	<b><math>2\delta(\text{CH}_3), a'</math></b>	~2880	2871.8	47	C	0.089	<b>0.39</b>
<b><math>\nu_3</math></b>	<b><math>\nu(\text{CH}), \text{s}, a'</math></b>	2833	2832.5	24	C	0.298	
<b><math>2\nu_6</math></b>	<b><math>2\delta(\text{COH}), a'</math></b>	~2805	2809.1	77	C	0.321	0.32
<b><math>\nu_4+\nu_{11}</math></b>	<b><math>\delta(\text{CH}_3)+\gamma(\text{CH}_3), a''</math></b>	2596	2600.6	61	C	0.039	0.04
<b><math>\nu_6+\nu_{11}</math></b>	<b><math>\delta(\text{COH})+\gamma(\text{CH}_3), a''</math></b>	2522	2520.3	108	C	0.136	0.14
<b><math>\nu_6+\nu_8</math></b>	<b><math>\delta(\text{COH})+\nu(\text{CO}), a'</math></b>	2440 <sup>f</sup>					
<b><math>2\nu_{11}</math></b>	<b><math>2\gamma(\text{CH}_3), a'</math></b>	2229	2226.3	60	C	0.016	0.02
<b><math>2\nu_8</math></b>	<b><math>2\nu(\text{CO}), a'</math></b>	2045	2045.9	40	C	0.027	0.03
<b><math>\nu_8+\nu_{12} ?</math></b>		~1560	1554.6	236	C	0.181	0.18
<b><math>\nu_4, \nu_{10}</math></b>	<b><math>\delta(\text{CH}_3), \text{as}, a', a''</math></b>	1477	1469.8	49	C	0.157	<b>0.16</b>
<b><math>\nu_5</math></b>	<b><math>\delta(\text{CH}_3), \text{s}, a'</math></b>	1450	1450.5	17	C	0.039	<b>0.04</b>
<b><math>\nu_6</math></b> <b><math>2\nu_{12} ?</math></b> <b><math>2\nu_{12} ?</math></b>	<b><math>\delta(\text{COH}), a'</math></b>	1422	1418.0	162	G	0.204	<b>0.62</b>
			1414.6	70	C	0.266	
		~1300	1299.0	101	C	0.075	
		~1200	1205.7	123	G	0.077	
<b><math>\nu_7</math></b>	<b><math>\gamma(\text{CH}_3), a'</math></b>	1115	1116.5	42	C	0.159	<b>0.16</b>
<b><math>\nu_{11}</math></b>	<b><math>\gamma(\text{CH}_3), a''</math></b>		1087.9	28	C	0.017	<b>0.02</b>
<b><math>\nu_8</math></b>	<b><math>\nu(\text{CO}), a'</math></b>	~1045	1038.9	13	C	0.397	<b>1.16</b>
		1035	1031.4	17	C	0.669	
		~1015	1018.8	22	C	0.093	
<b><math>\nu_{12}</math></b>	<b><math>\delta(\text{O-H}\cdots\text{O}), a''</math></b>		677.2	207	G	0.455	<b>1.08</b>
		673	633.4	123	G	0.048	
		~610	613.6	390	G	0.580	
		< 400	400 <sup>g</sup>	307	C	0.082	0.08

- a The fundamental vibrations are marked in bold. For the CDHO bands, type C,  $\tilde{\nu}_j$ ,  $\Gamma_j$ , and  $\mu_j^2$  of eq. (4.13) are  $\tilde{\nu}_{\text{max}}$ , FWHH, and  $1.8686C_j$ , respectively. For the Gaussian bands, type G,  $\tilde{\nu}_j$ ,  $\Gamma_j$ , and  $H_j$  of eq. (8.1a) are  $\tilde{\nu}_{\text{max}}$ , FWHH, and  $0.93944 C_j/(\tilde{\nu}_j \Gamma_j)$ , respectively.
- b The observed peak wavenumbers in the  $\alpha_m''$  spectrum. These differ slightly from those in Table 8.1 which are the peak wavenumbers in the  $\tilde{\nu}\alpha_m''$  spectrum.
- c The fitting was done on  $\alpha_m''$  spectrum; The FWHH is the full width of the band at the half height; The Type specifies C for CDHO bands and G for Gaussian bands.
- d The area  $C_j$ , defined by eq. (4.11), was calculated by eqs. (4.22) and (8.1) from the parameters.
- e See text.
- f This shoulder was not fitted because it is very weak.
- g The band is fixed at 400 cm<sup>-1</sup>. See text.

**Table 8.6** The parameters of the bands fitted to the  $\alpha_m''$  spectrum of CH<sub>3</sub>OD. <sup>a</sup>

CH <sub>3</sub> OD		Observed <sup>b</sup>	Fitted band <sup>c</sup>			Area $C_j$ <sup>d</sup>	
Assignment		$\tilde{\nu}_{\text{obs}}$	$\tilde{\nu}_{\text{max}}$	FWHH	Type	Individual	Total
3v <sub>7</sub> ?	3v(CO), a'	~3040	3030.9	54	C	0.041	0.46
v <sub>1</sub>	v(CH), as, a'	2681	2982.8	46	C	0.343	
v <sub>4</sub> +v <sub>7</sub> +v <sub>12</sub> ?			2961.0	29	C	0.077	
v <sub>9</sub>	v(CH), as, a''	2947	2946.1	23	C	0.298	0.48
v <sub>4</sub> +v <sub>10</sub>	$\delta(\text{CH}_3)+\delta(\text{CH}_3)$ , a''	2915	2914.5	27	C	0.181	
v <sub>4</sub> +v <sub>5</sub>	$\delta(\text{CH}_3)+\delta(\text{CH}_3)$ , a'	~2900	2899.3	57	C	0.202	
2v <sub>5</sub>	2 $\delta(\text{CH}_3)$ , a'	~2860	2862.9	18	C	0.008	0.43
v <sub>2</sub>	v(CH), s, a'	2836	2836.5	13	C	0.161	
		~2820	2828.3	26	C	0.060	
v <sub>3</sub>	v(OD), a'		2500.2	46	G	0.110	3.76
		2496	2499.4	157	G	2.811	
		2440	2432.8	51	C	0.163	
		~2380	2392.1	125	G	0.465	
			2279.2	150	G	0.206	
2v <sub>11</sub>	2 $\gamma(\text{CH}_3)$ , a'	2258	2254.1	21	C	0.006	0.01
v <sub>7</sub> +v <sub>11</sub>	v(CO)+ $\gamma(\text{CH}_3)$ , a''	2178	2172.9	75	C	0.136	0.14
2v <sub>7</sub>	2v(CO), a'	2044	2045.5	63	C	0.049	0.05
v <sub>7</sub> +v <sub>8</sub>	v(CO)+ $\delta(\text{COD})$ , a'	1966	1967.0	80	C	0.037	0.04
2v <sub>8</sub>	2 $\delta(\text{COD})$ , a'	1892	1889.4	91	G	0.054	0.05
v <sub>4</sub> , v <sub>10</sub>	$\delta(\text{CH}_3)$ , as, a', a''	~1550	1532.9	101	C	0.027	0.12
		1467	1467.8	35	C	0.097	
v <sub>5</sub>	$\delta(\text{CH}_3)$ , s, a'	1447	1446.0	11	C	0.020	0.07
v <sub>8</sub> +v <sub>12</sub> ?			1410.8	134	C	0.048	
v <sub>6</sub>	$\gamma(\text{CH}_3)$ , a'	1232	1231.7	27	C	0.052	0.05
v <sub>11</sub>	$\gamma(\text{CH}_3)$ , a''	1157	1160.8	32	C	0.008	0.01
2v <sub>12</sub> ?			1122.3	84	C	0.045	0.06
			1084.4	37	C	0.018	
v <sub>7</sub>	v(CO), a'	~1040	1038.2	15	C	0.448	1.19 or 1.19 +0.06
		1034	1030.7	18	C	0.699	
		~1011	1016.4	18	C	0.046	
v <sub>8</sub>	$\delta(\text{COD})$ , a'	940	942.6	57	G	0.153	0.34
		~885	888.8	122	G	0.094	
			751.4	229	C	0.094	
v <sub>12</sub>	$\delta(\text{O-D}\cdots\text{O})$ , a''	491	493.4	50	G	0.012	0.56
		~460	485.1	187	G	0.544	
		< 400	350 <sup>e</sup>	89	C	0.038	0.04

<sup>a</sup> See footnote a of Table 8.5.

<sup>b</sup> The observed peak wavenumbers in the  $\alpha_m''$  spectrum. These differ slightly from those in Table 8.2 which are the peak wavenumbers in the  $\tilde{\nu}\alpha_m''$  spectrum.

<sup>c</sup> See footnote c of Table 8.5.

<sup>d</sup> See footnote d of Table 8.5.

<sup>e</sup> The band is fixed at 350 cm<sup>-1</sup>. See text.

**Table 8.7** The parameters of the bands fitted to the  $\alpha_m''$  spectrum of CD<sub>3</sub>OH. <sup>a</sup>

CD <sub>3</sub> OH		Observed <sup>b</sup>	Fitted band <sup>c</sup>			Area $C_j$ <sup>d</sup>	
Assignment		$\tilde{\nu}_{\text{obs}}$	$\tilde{\nu}_{\text{max}}$	FWHH	Type	Individual	Total
<b>v<sub>1</sub></b>	<b>v(OH), a'</b>	3350	3353.8	247	G	5.807	<b>7.32</b>
			3349.4	64	G	0.044	
		~3160	3160.4	331	G	1.178	
		~2860	2851.6	184	G	0.289	
<b>2v<sub>4</sub></b>	<b>2δ(COH), a'</b>	2783	2757.6	133	G	0.253	<b>0.31</b>
		~2650	2611.1	177	C	0.055	
<b>2v<sub>5</sub></b>	<b>2δ(CD<sub>3</sub>), a'</b>	~2255	2251.4	15	C	0.017	<b>0.31<sup>e</sup></b>
<b>v<sub>2</sub></b>	<b>v(CD), as, a'</b>	2235	2238.1	37	C	0.263	
			2218.2	169	C	0.113	to v <sub>2</sub> , v <sub>3</sub> , v <sub>9</sub> <sup>e</sup>
<b>v<sub>9</sub></b>	<b>v(CD), as, a''</b>	2215	2211.7	36	C	0.239	<b>0.28<sup>e</sup></b>
<b>2v<sub>5</sub></b>	<b>2δ(CD<sub>3</sub>), a'</b>	2138	2138.1	14	C	0.026	<b>0.37<sup>e</sup></b>
<b>2v<sub>10</sub></b>	<b>2δ(CD<sub>3</sub>), a'</b>	2126	2127.6	33	C	0.033	
<b>v<sub>3</sub></b>	<b>v(CD), s, a'</b>	2072	2072.2	10	C	0.234	
		~2060	2065.1	18	C	0.046	
<b>v<sub>6</sub>+v<sub>8</sub> ?</b>		2025 <sup>f</sup>					
		2005 <sup>f</sup>					
<b>2v<sub>7</sub></b>	<b>2v(CO), a'</b>	1957	1956.5	30	C	0.020	<b>0.02</b>
<b>v<sub>7</sub>+v<sub>12</sub> ?</b>		~1660	1669.2	292	C	0.097	<b>0.10</b>
<b>v<sub>4</sub></b>	<b>δ(COH), a'</b>	~1410	1398.7	101	G	0.281	<b>0.78</b>
		1393	1361.9	285	G	0.489	
		~1285	1285.7	59	G	0.009	
<b>v<sub>5</sub></b>	<b>δ(CD<sub>3</sub>), s, a'</b>	~1160	1165.2	59	C	0.025	<b>0.48</b>
		1122	1125.0	12	C	0.204	
			1120.1	12	C	0.251	
<b>v<sub>10</sub></b>	<b>δ(CD<sub>3</sub>), as, a''</b>	~1110	1093.8	40	C	0.006	<b>0.07</b>
		1068	1065.9	38	C	0.060	
<b>v<sub>6</sub></b>	<b>δ(CD<sub>3</sub>), as, a'</b>		1028.6	32	C	0.026	<b>0.03</b>
<b>v<sub>7</sub></b>	<b>v(CO), a'</b>	984	986.3	10	C	0.210	<b>0.66</b>
			981.4	15	C	0.454	
<b>v<sub>11</sub></b>	<b>γ(CD<sub>3</sub>), a''</b>		938.8	70	C	0.027	<b>0.03</b>
<b>v<sub>8</sub></b>	<b>γ(CD<sub>3</sub>), a'</b>	886	887.3	39	C	0.123	<b>0.12</b>
<b>v<sub>12</sub></b>	<b>δ(O–H...O), a''</b>	653	664.6	174	G	0.198	<b>0.93</b>
		~570	649.3	278	G	0.740	
		< 400	400 <sup>g</sup>	353	C	0.238	<b>0.24</b>

<sup>a</sup> See footnote a of Table 8.5.

<sup>b</sup> The observed peak wavenumbers in the  $\alpha_m''$  spectrum. These differ slightly from those in Table 8.3 which are the peak wavenumbers in the  $\tilde{\nu}\alpha_m''$  spectrum.

<sup>c</sup> See footnote c of Table 8.5.

<sup>d</sup> See footnote d of Table 8.5.

<sup>e</sup> The area, 0.11 km mol<sup>-1</sup>, under the broad band at 2218 cm<sup>-1</sup> is arbitrarily distributed to the three fundamental vibrations, 0.03, 0.04, 0.04 km mol<sup>-1</sup> to v<sub>2</sub>, v<sub>3</sub> and v<sub>9</sub>, respectively.

<sup>f</sup> The very weak shoulders can be seen in the experimental spectrum, but were not fitted.

<sup>g</sup> The band is fixed at 400 cm<sup>-1</sup>. See text.

**Table 8.8** The parameters of the bands fitted to the  $\alpha_m''$  spectrum of CD<sub>3</sub>OD. <sup>a</sup>

CD <sub>3</sub> OD		Observed <sup>b</sup>	Fitted band <sup>c</sup>			Area $C_j$ <sup>d</sup>	
Assignment		$\tilde{\nu}_{\text{obs}}$	$\tilde{\nu}_{\text{max}}$	FWHH	Type	Individual	Total
$\nu_1$	$\nu(\text{OD}), a'$	2491 ~2380	2496.0	50	G	0.061	3.57
			2488.1	167	G	3.329	+0.36 <sup>e</sup>
			2330.0	110	G	0.181	=3.93
$\nu_2$	$\nu(\text{CD}), as, a'$	2245	2247.1	35	C	0.256	<b>0.26</b>
$\nu_9$	$\nu(\text{CD}), as, a''$	2215	2214.3	37	C	0.259	<b>0.26</b>
		~2190	2178.8	107	C	0.360	to $\nu_{\text{OD}}$ <sup>e</sup>
$2\nu_5$	$2\delta(\text{CD}_3), a'$	2137	2135.4	28	C	0.072	<b>0.39</b>
$\nu_3$	$\nu(\text{CD}), s, a'$	2072	2071.9	10	C	0.268	
		~2060	2064.9	17	C	0.051	
$\nu_4 + \nu_{11}$	$\delta(\text{CD}_3) + \gamma(\text{CD}_3), a''$	2010 <sup>f</sup>					
$2\nu_7$	$2\nu(\text{CO}), a'$	1944	1941.7	53	C	0.048	0.05
$2\nu_{11}$	$2\gamma(\text{CD}_3), a'$	1910	1899.5	42	C	0.030	0.03
$2\nu_8$	$2\delta(\text{COD}), a'$	1651	1654.1	62	G	0.008	0.01
$\nu_4$	$\delta(\text{CD}_3), s, a'$	~1132	1128.9	9	C	0.063	<b>0.25</b>
		1125	1124.2	10	C	0.139	
$\nu_5$	$\delta(\text{CD}_3), as, a'$	1097	1119.7	14	C	0.053	<b>0.55</b>
			1096.2	49	C	0.497	
$\nu_{10}$	$\delta(\text{CD}_3), as, a''$	1064	1063.1	22	C	0.043	<b>0.04</b>
$\nu_6$	$\gamma(\text{CD}_3), a'$	~1057	1056.6	76	C	0.120	<b>0.12</b>
$\nu_7$	$\nu(\text{CO}), a'$	~985 979	1013.4	26	C	0.016	<b>0.58</b>
			981.7	10	C	0.105	
			977.5	15	C	0.457	
$2\nu_{12} ?$			929.8	86	G	0.036	0.04
$\nu_{11}$	$\gamma(\text{CD}_3), a''$	902	901.5	21	C	0.018	<b>0.02</b>
$\nu_8$	$\delta(\text{COD}), a'$	824	824.1	43	G	0.080	<b>0.19</b>
			804.1	187	G	0.108	
$\nu_{12}$	$\delta(\text{O-H}\cdots\text{O}), a''$	485	484.9	186	G	0.495	<b>0.52</b>
		~465	480.2	78	G	0.023	
		< 400	350 <sup>g</sup>	278	C	0.118	0.12

a See footnote a of Table 8.5.

b The observed peak wavenumbers in the  $\alpha_m''$  spectrum. These differ slightly from those in Table 8.4 which are the peak wavenumbers in the  $\tilde{\nu}\alpha_m''$  spectrum.

c See footnote c of Table 8.5.

d See footnote d of Table 8.5.

e See text.

f This shoulder was not fitted because it is very weak.

g The band is fixed at 350 cm<sup>-1</sup>. See text.

Each fit started with just the peaks that can be seen in the experimental spectra, either by obvious peaks or by anomalous changes in slope. It was found necessary to add a few additional and unsuspected bands to achieve the fit presented. Some of these bands may be real but can not be seen because they hide under other bands. Others may be due to the use of the wrong line shape or to the baseline, so that broad bands had to be used to remedy deficiencies.

The intensities were grouped in the last columns of Tables 8.5 to 8.8 under the following general guidelines. If the band that is assigned to an overtone or combination transition is near a fundamental, it was assumed that the intensity of the overtone or combination band originates from the fundamental and, therefore, was included in the total intensity of the fundamental. If it could not be decided whether the area of a combination or overtone band should be included in a fundamental, it was treated as an uncertainty in the fundamental intensity. The assignment of the individual bands and grouping of the intensities were also guided by comparing the spectra in the similar regions of different species.

In order to minimize the effect of the absorption<sup>1</sup> below  $\sim 400\text{ cm}^{-1}$  on the intensity of the out-of-plane bending mode of the hydroxyl group, a CDHO band with fixed center was used to simulate the tail of the absorption. It was somewhat arbitrarily fixed at  $400\text{ cm}^{-1}$  for  $\text{CH}_3\text{OH}$  and  $\text{CD}_3\text{OH}$ , and at  $350\text{ cm}^{-1}$  for  $\text{CH}_3\text{OD}$  and  $\text{CD}_3\text{OD}$ .

#### 8.2.2.2 The Fit of the $\alpha_m''$ Spectrum of $\text{CH}_3\text{OH}$

Figure 8.3 shows the individual bands required to fit the  $\alpha_m''$  spectrum of  $\text{CH}_3\text{OH}$ . The figure includes the sum of these bands, which is almost indistinguishable from the experimental spectrum. The fit required 31 bands, 24 of which match clear features in the spectrum such as peaks, shoulders and clear anomalies in the slope. Table 8.5 contains the parameters of the fitted bands with the observed wavenumbers of the slope anomalies identified by a tilde.

Seven additional peaks had to be used to fit the spectrum even though no corresponding spectral feature is clear. Four of these seven peaks are Gaussian bands under the OH stretching band (Figure 8.3A). The remaining three extra bands (Figure 8.3B) are one CDHO band superimposed on a Gaussian band to fit the COH in-plane bending band near  $1420\text{ cm}^{-1}$ , one very weak CDHO band at  $1088\text{ cm}^{-1}$  between the  $\text{CH}_3$  rock and the CO stretch, which may well represent the second  $\text{CH}_3$  rock, and one of the

three Gaussian bands required to fit the broad O-H---O out-of-plane bending band near  $600\text{ cm}^{-1}$ .

The areas  $C_j$  corresponding to the bands used to fit the spectrum are listed in Table 8.5. The intensity was assigned to the different transitions as shown in the last column of Table 8.5. Most of the assignments are fairly obvious but the following comments are required. The intensity of the broad, intense CDHO band at  $2911\text{ cm}^{-1}$  was assigned arbitrarily to the OH stretching vibration. This was basically because the fit of the OH and CH stretching region was not as convincing as the result from the comparison of isotopes. The intensity of the broad band at  $1555\text{ cm}^{-1}$  could well originate in the  $\text{CH}_3$  deformations or the COH in-plane bend, and its assignment to the combination transition  $\nu_8 + \nu_{12}$  introduces significant uncertainty in the intensities of these fundamentals. The intensity of four bands between  $1422$  and  $1200\text{ cm}^{-1}$  was assigned to the C-O-H in-plane bend. The lower two could well be due to overtone or combination transitions involving the vibrations that contribute to the out-of-plane O-H---O bend, and this introduces a 25% uncertainty into the intensity of the COH in-plane bend. It is not clear why three bands are required to fit the CO stretching band. The mono  $^{13}\text{C}$  component of the sample may explain the lowest wavenumber band, and the need for two intense bands to fit the strong peak presumably indicates that the peak is not exactly a CDHO peak. Similarly, the need for three Gaussian peaks to fit the band near  $600\text{ cm}^{-1}$  is presumably because the experimental peak is not Gaussian. But the assignment of the intensity is clear in both cases.

The assignment of the intensity to the different transitions is summarized in Table 8.1 with the intensities deduced from the isotopic comparison.

#### 8.2.2.3 The Fit of the $\alpha_m''$ Spectrum of $\text{CH}_3\text{OD}$

Figure 8.4 shows the individual bands required to fit the  $\alpha_m''$  spectrum of  $\text{CH}_3\text{OD}$ . Again, the sum of the bands is almost indistinguishable from the experimental spectrum. The fit required 35 bands, 28 of which match clear features in the spectrum. The parameters of the fitted bands are in Table 8.6 with the observed wavenumbers of the slope anomalies identified by a tilde.

Seven additional peaks had to be used to fit the spectrum even though no corresponding spectral feature is clear. One of these seven peaks is under the CH stretching bands. Two are Gaussian bands under the OH stretching band (Figure 8.4A). The remaining four extra bands (Figure 8.4B) are one broad CDHO band at  $1411\text{ cm}^{-1}$  to



fit the baseline just below the  $\text{CH}_3$  deformation bands, two CDHO bands at 1122 and 1084  $\text{cm}^{-1}$  between the  $\text{CH}_3$  rock and the CO stretch, one Gaussian band required to fit the baseline between the COD bending band at 940  $\text{cm}^{-1}$  and the O–D---O out-of-plane bending band at about 490  $\text{cm}^{-1}$ .

The areas  $C_j$  of the individual bands used to fit the spectrum are listed in Table 8.6. The intensity was assigned to the different transitions as shown in the last column of Table 8.6. Again, most of the assignments are clear but the following three comments are required. First, the area of the broad band at 1533  $\text{cm}^{-1}$  was included in the intensity of the asymmetric deformation band at 1467  $\text{cm}^{-1}$  and the area of another broad band at 1411  $\text{cm}^{-1}$  was included in that of the symmetric deformation band at 1447. In neither case was this assignment clear and they introduce marked uncertainty into the intensities of the  $\text{CH}_3$  deformation vibrations. Second, three bands were, again, needed to fit the CO stretching band, similar to that of  $\text{CH}_3\text{OH}$ . Third, there are two broad bands to low wavenumber of the COD in-plane bending band at 940  $\text{cm}^{-1}$  whose origin is unclear. The areas were included in the intensity of the bending band. One of these bands has an analogue in  $\text{CD}_3\text{OD}$  (Figure 8.6B) and the COH in-plane bands were also fitted by two bands.

The assignment of the intensity to the different transitions is summarized in Table 8.2 with the intensities deduced from the isotopic comparison.

#### 8.2.2.4 The Fit of the $\alpha_m''$ Spectrum of $\text{CD}_3\text{OH}$

Figure 8.5 shows the individual bands required to fit the  $\alpha_m''$  spectrum of  $\text{CD}_3\text{OH}$ . The figure includes the sum of these bands, which is almost indistinguishable from the experimental spectrum. The fit also required 31 bands, 25 of which are clear features in the spectrum such as peaks, shoulders and clear anomalies in the slope. Table 8.7 contains the parameters of the fitted bands with the observed wavenumbers of the slope anomalies identified by a tilde.

Six additional peaks had to be used to fit the spectrum. Two of them are a weak Gaussian band at the center of the OH stretching band and a broad CDHO band in the middle of the CD stretching bands (Figure 8.5A). The remaining four extra bands (Figure 8.5B) are in the low wavenumber region of the spectrum. They are one CDHO band each needed for the strong bands at 1122 and 984  $\text{cm}^{-1}$ , one weak CDHO band to high wavenumber of the CO band, which may represent the third  $\text{CD}_3$  deformation, and one weak CDHO band at 939  $\text{cm}^{-1}$  which may be due to the second  $\text{CD}_3$  rock.

Table 8.7 lists the areas  $C_j$  of the bands used to fit the spectrum. The intensity was assigned to the different transitions as shown in the last column of this table. The following comments are required. A very broad band at  $2218\text{ cm}^{-1}$  (Figure 8.5A) was required to fit the baseline and its intensity was divided between the three stretching fundamentals. The intensities of the bands at  $1399$ ,  $1362$  and  $1286\text{ cm}^{-1}$  were combined to give  $C_j = 0.78\text{ km mol}^{-1}$  for the in-plane bending mode in  $\text{CD}_3\text{OH}$ . The two lower wavenumber bands are analogous to those in  $\text{CH}_3\text{OH}$  and  $\text{CH}_3\text{OD}$ .

The assignment of the intensity to the different transitions is summarized in Table 8.3 with the intensities deduced from the isotopic comparison.

#### 8.2.2.5 The Fit of the $\alpha_m''$ Spectrum of $\text{CD}_3\text{OD}$

Figure 8.6 shows the individual bands required to fit the  $\alpha_m''$  spectrum of  $\text{CD}_3\text{OD}$ . The figure includes the sum of these bands, which is almost indistinguishable from the experimental spectrum. The fit required 27 bands, 22 of which match clear features in the spectrum such as peaks, shoulders and clear anomalies in the slope. Table 8.6 contains the parameters of the fitted bands with the observed wavenumbers of the slope anomalies identified by a tilde.

Five additional peaks had to be used to fit the spectrum even though no corresponding spectral feature is clear. They are a Gaussian band at  $2496\text{ cm}^{-1}$  under the OD stretching band, two CDHO bands near the two strong peak at  $1125$  and  $979\text{ cm}^{-1}$ , a broad Gaussian band at  $930\text{ cm}^{-1}$ , and another broad Gaussian band at  $804\text{ cm}^{-1}$ , to low wavenumber of the COD bending band which is an analogue of that in the other molecules.

The area  $C_j$  of the bands used to fit the spectrum are listed in Table 8.8 along with the intensity assignment in the last column. Most of the intensity assignments are obvious but the following explanation is necessary. The intensity of the broad band at  $2179\text{ cm}^{-1}$  was arbitrarily assigned to the OD stretching vibration for the same reason as in  $\text{CH}_3\text{OH}$ . A weak band at  $930\text{ cm}^{-1}$  whose origin is unclear introduces some uncertainty in the areas of the fundamentals in the region.

The assignment of the intensity to the different transitions is summarized in Table 8.4 with the intensities deduced from the isotopic comparison.

### 8.2.3 *The Accepted Intensities*

The sets of integrated intensities  $C_j$  obtained by the comparison of the  $\tilde{\nu}\alpha_m''$  spectra of isotopomers (Section 8.2.1) and by curve-fitting the  $\alpha_m''$  spectra (Section 8.2.2) are summarized in Tables 8.1 to 8.4.

The agreement between the two sets is very good in most cases. For the OH(D) and CH(D) stretching vibrations, the values from isotopic comparison were preferred because they were so unambiguously obtained from direct measurements of the area for  $\text{CH}_3\text{OD}$  and  $\text{CD}_3\text{OH}$ , and from two different assumptions for  $\text{CH}_3\text{OH}$  and  $\text{CD}_3\text{OD}$  (Section 8.2.1).

However, the intensities of the three CH(D) stretching vibrations must be separated to make them more value in the analysis. The separation used the results of curve-fitting modified to match the total  $\text{CH}_3$  or  $\text{CD}_3$  stretching intensity found by isotopic comparison. For example, the separation from curve-fitting for  $\text{CH}_3\text{OH}$  gives  $C_j = 0.35, 0.55$  and  $0.39$   $\text{km mol}^{-1}$  for  $\nu_2, \nu_9$  and  $\nu_3$ , respectively (Table 8.1). The total intensity of the  $\text{CH}_3$  stretches from isotopic comparison was  $0.04$   $\text{km mol}^{-1}$  higher than the total from curve-fitting, so  $0.04$   $\text{km mol}^{-1}$  was simply added to the intensity of  $\nu_2$ . The separation of the  $\text{CH}_3$  and  $\text{CD}_3$  stretching intensities of the other molecules was made similarly. The intensities of the individual  $\text{CH}_3$  and  $\text{CD}_3$  stretching fundamentals are clearly less certain than their combined intensities.

For the CO stretching vibration and the COH in-plane and out-of-plane bending vibrations of  $\text{CH}_3\text{OH}$  and  $\text{CH}_3\text{OD}$ , the  $C_j$  values from the two methods were averaged. The combined  $C_j$  values of the  $\text{CH}_3$  deformations were very similar by both methods. The values from the fit were taken and, with considerable uncertainty, were divided into contributions from the three vibrations. The values from the fit were also taken for the  $\text{CH}_3$  rocking vibrations, with considerable uncertainty.

The intensity of the COD in-plane bend of  $\text{CD}_3\text{OD}$  was very uncertain by either method and an average value was used. For the  $\text{CD}_3$  compounds, the  $C_j$  values for the out-of-plane H or D bend agreed well and were averaged. Values for the other vibrations below  $2000$   $\text{cm}^{-1}$  were only obtained from the curve-fits.

The  $C_j$  values accepted for use in the calculation of the intensity parameters in Section 8.4 are given in the second last columns of Tables 8.1 to 8.4.

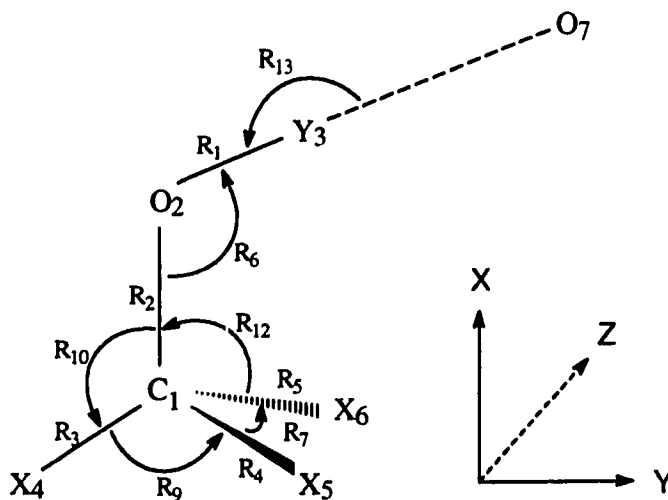


**Figure 8.7** The molecular model for CX<sub>3</sub>OY, where X, Y = H or D, and R<sub>i</sub> defines the internal coordinates (i runs from 1 to 13). The atoms X<sub>4</sub>, C<sub>1</sub>, O<sub>2</sub>, Y<sub>3</sub> and O<sub>7</sub> are in the XY plane. Atomic masses are H=1.008, D=2.014, C=12.011, O=15.999 amu.

The final  $C_j$  values were converted to the values of  $\mu_j^2 = |\partial \bar{\mu} / \partial Q_j|^2$  through the conversion factor given<sup>1</sup> in Section 5.6. These  $\mu_j^2$  values are given in the last columns of Tables 8.1 to 8.4. They are estimated to be accurate to about a few percent for the OH(D) and CH(D) stretching vibrations, close to a few percent for the large values of other vibrations, and above 10% for the small values.

### 8.3 Normal Coordinate Calculation

A normal coordinate calculation of all four isotopic species of methanol was made to obtain a set of force constant parameters and a set of eigenvectors which fit the wavenumbers and reflect the integrated intensities obtained in the previous section.

#### 8.3.1 The Geometry of the Molecules and the Definition of the Coordinates

The molecular model is shown in Figure 8.7 for the six-atom molecules, CX<sub>3</sub>OY, where X, Y = H or D. The molecules were assumed to have C<sub>s</sub> symmetry with the in-plane bond CX<sub>4</sub> trans to the OY bond. An extra oxygen atom, O<sub>7</sub>, hydrogen-bonded to Y was included only for the out-of-plane motion of Y (see below). The geometrical parameters of the molecules were those given by Lees and Baker<sup>5</sup> except for the 3.3° tilt

angle which was assumed to be zero. These parameters are given in Table 5.7. The distance between two oxygen atoms was taken to be 2.80 Å.<sup>6</sup>

Thirteen internal displacement coordinates, one of which is redundant, are defined in Table 8.9. The internal coordinates  $R_1$  through  $R_5$  are the bond stretching coordinates.  $R_6$  is the increase in the in-plane COH angle.  $R_7$  to  $R_9$  are the increases in the XCX angles and  $R_{10}$  to  $R_{12}$  are the increases in the XCO angles. The redundancy is that  $R_7$  to  $R_{10}$  can not all be independent. The coordinates involving angle changes were defined as the changes in the angles multiplied by 1 Å, in order to obtain the force constants in the same unit.

The thirteenth internal coordinate,  $R_{13}$ , was defined as the linear bend of the  $O_2Y_3O_7$  angle out of the plane of the  $C_1$ ,  $O_2$  and  $Y_3$  atoms. The reason that such a bending coordinate was defined rather than a torsion of the OY bond about the CO bond came directly from experiment. This vibration of  $CH_3OH$  or  $CH_3OD$  would have a quite different frequency from that of  $CD_3OH$  and  $CD_3OD$  if it were the torsion. But the experimental spectra show hardly any shift of band position or any change in the intensity from  $CH_3OY$  to  $CD_3OY$  (Figures 7.11 and 8.2). All the other displacements and effects which result from the addition of oxygen  $O_7$  were ignored.

Thirteen normalized symmetry coordinates were constructed, with  $S_9$  ( $A'$  under  $C_s$ ) expressing the exact redundancy. They are also given in Table 8.9. The U matrix relating the internal coordinates to the symmetry coordinates,  $S = UR$ , was obtained from the coefficients in the table.

### 8.3.2 The G Matrices

In Wilson's GF method<sup>7</sup>, one must solve either

$$|GF - \lambda| = 0 \quad (8.2a)$$

where G and F are the inverse kinetic energy and potential energy matrices in terms of the internal coordinates, or

$$|G_s F_s - \lambda| = 0 \quad (8.2b)$$

where  $G_s$  and  $F_s$  are in terms of the symmetry coordinates. In this calculation, the second equation was used.  $G_s$  and  $F_s$  are related to G and F, respectively, by

$$G_s = UGU^t \quad (8.3a)$$

$$F_s = UFU^t \quad (8.3b)$$

where  $U^t$  is the transpose of U and the elements of U are defined by  $S = UR$  and are obtained directly from the equations in Table 8.9. Program GMAT<sup>8</sup> was used to

**Table 8.9** The definition of the internal and symmetry coordinates. <sup>a,b</sup>

Internal coordinates	Symmetry coordinate
$R_1 = \delta r(O_2 - Y_3)$	$S_1 = R_1$
$R_2 = \delta r(C_1 - O_2)$	$S_2 = R_2$
$R_3 = \delta r(C_1 - X_4)$	$S_3 = R_3$
$R_4 = \delta r(C_1 - X_5)$	$S_4 = 0.7071(R_4 + R_5)$
$R_5 = \delta r(C_1 - X_6)$	$S_5 = R_6$
$R_6 = \delta \angle C_1 O_2 Y_3$	$S_6 = 0.4142(R_7 + R_8 + R_9) - 0.4022(R_{10} + R_{11} + R_{12})$
$R_7 = \delta \angle X_5 C_1 X_6$	$S_7 = 0.8165R_7 - 0.4082R_8 - 0.4082R_9$
$R_8 = \delta \angle X_6 C_1 X_4$	$S_8 = 0.8165R_{10} - 0.4082R_{11} - 0.4082R_{12}$
$R_9 = \delta \angle X_4 C_1 X_5$	$S_9 = 0.4022(R_7 + R_8 + R_9) + 0.4142(R_{10} + R_{11} + R_{12})$
$R_{10} = \delta \angle X_4 C_1 O_2$	$S_{10} = 0.7071(R_4 - R_5)$
$R_{11} = \delta \angle X_5 C_1 O_2$	$S_{11} = 0.7071(R_8 - R_9)$
$R_{12} = \delta \angle X_6 C_1 O_2$	$S_{12} = 0.7071(R_{11} - R_{12})$
$R_{13} = \delta \angle O_2 Y_3 O_7$	$S_{13} = R_{13}$

a  $S_1$  to  $S_9$  have A' symmetry under  $C_s$  and  $S_{10}$  to  $S_{13}$  have A'' symmetry.

b It is implied that the angle displacement coordinates,  $R_6$  to  $R_{13}$  are the increases in the angles multiplied by 1 Å.

calculate the  $G_s$  elements. Atomic masses on the  $^{12}\text{C}$  scale were used and are given in the caption to Figure 8.7. The values of the  $G_s$  matrix elements are given in Table 8.10, using the fact that  $G_s$  is a symmetric matrix. The elements in the row and column of  $G_s$  which involve the redundancy  $S_9$  are all zero and were omitted from this table.

### 8.3.3 The Valence Force Constants

In this chapter,  $f_{ij}$  is used for the internal coordinate force constants in the F matrix, and  $F_{ij}$  is used for the symmetry coordinate force constants in the  $F_s$  matrix.

The F matrix contains 61 non-equivalent elements. To reduce this number, the following assumptions were made, based on the experimental facts<sup>1-3</sup> in the previous chapters and the results of a previous calculation of the normal coordinates of methanol<sup>9</sup>.

**Table 8.10** The values of  $(G_s)_{ij}$  for the methanol molecules in the unit  $\text{amu}^{-1}$ .

CH <sub>3</sub> OH A'								
$(G_s)_{ij}$	S <sub>1</sub>	S <sub>2</sub>	S <sub>3</sub>	S <sub>4</sub>	S <sub>5</sub>	S <sub>6</sub>	S <sub>7</sub>	S <sub>8</sub>
S <sub>1</sub>	1.0548	-0.0199	0	0	-0.0416	0	0	-0.0510
S <sub>2</sub>		0.1459	-0.0289	-0.0409	-0.0627	0.1777	0	0
S <sub>3</sub>			1.0756	-0.0376	-0.0549	-0.0617	0.1143	-0.0976
S <sub>4</sub>				1.0489	0.0388	-0.0872	-0.0808	0.0690
S <sub>5</sub>					1.2822	0	-0.0856	0.1288
S <sub>6</sub>						2.0891	0	0
S <sub>7</sub>							2.2270	0.2752
S <sub>8</sub>								1.0057

CH <sub>3</sub> OH A''				
$(G_s)_{ij}$	S <sub>10</sub>	S <sub>11</sub>	S <sub>12</sub>	S <sub>13</sub>
S <sub>10</sub>	1.1022	0.1400	-0.1195	0
S <sub>11</sub>		2.2270	0.2752	0
S <sub>12</sub>			1.0057	-0.0569
S <sub>13</sub>				2.6194

CH <sub>3</sub> OD A'								
$(G_s)_{ij}$	S <sub>1</sub>	S <sub>2</sub>	S <sub>3</sub>	S <sub>4</sub>	S <sub>5</sub>	S <sub>6</sub>	S <sub>7</sub>	S <sub>8</sub>
S <sub>1</sub>	0.5590	-0.0199	0	0	-0.0416	0	0	-0.0510
S <sub>2</sub>		0.1459	-0.0289	-0.0409	-0.0627	0.1777	0	0
S <sub>3</sub>			1.0756	-0.0376	-0.0549	-0.0617	0.1143	-0.0976
S <sub>4</sub>				1.0489	0.0388	-0.0872	-0.0808	0.0690
S <sub>5</sub>					0.7273	0	-0.0856	0.1288
S <sub>6</sub>						2.0891	0	0
S <sub>7</sub>							2.2270	0.2752
S <sub>8</sub>								1.0057

CH <sub>3</sub> OD A''				
$(G_s)_{ij}$	S <sub>10</sub>	S <sub>11</sub>	S <sub>12</sub>	S <sub>13</sub>
S <sub>10</sub>	1.1022	0.1400	-0.1195	0
S <sub>11</sub>		2.2270	0.2752	0
S <sub>12</sub>			1.0057	-0.0569
S <sub>13</sub>				1.3548

(Cont'd on next page)

**Table 8.10** (Cont'd)

CD <sub>3</sub> OH A'								
(G <sub>s</sub> ) <sub>ij</sub>	S <sub>1</sub>	S <sub>2</sub>	S <sub>3</sub>	S <sub>4</sub>	S <sub>5</sub>	S <sub>6</sub>	S <sub>7</sub>	S <sub>8</sub>
S <sub>1</sub>	1.0548	-0.0199	0	0	-0.0416	0	0	-0.0510
S <sub>2</sub>		0.1459	-0.0289	-0.0409	-0.0627	0.1777	0	0
S <sub>3</sub>			0.5799	-0.0376	-0.0549	-0.0617	0.1143	-0.0976
S <sub>4</sub>				0.5532	0.0388	-0.0872	-0.0808	0.0690
S <sub>5</sub>					1.2822	0	-0.0856	0.1288
S <sub>6</sub>						1.2347	0	0
S <sub>7</sub>							1.2035	0.0617
S <sub>8</sub>								0.5912

CD <sub>3</sub> OH A''				
(G <sub>s</sub> ) <sub>ij</sub>	S <sub>10</sub>	S <sub>11</sub>	S <sub>12</sub>	S <sub>13</sub>
S <sub>10</sub>	0.6065	0.1400	-0.1195	0
S <sub>11</sub>		1.2035	0.0617	0
S <sub>12</sub>			0.5912	-0.0569
S <sub>13</sub>				2.6194

CD <sub>3</sub> OD A'								
(G <sub>s</sub> ) <sub>ij</sub>	S <sub>1</sub>	S <sub>2</sub>	S <sub>3</sub>	S <sub>4</sub>	S <sub>5</sub>	S <sub>6</sub>	S <sub>7</sub>	S <sub>8</sub>
S <sub>1</sub>	0.5590	-0.0199	0	0	-0.0416	0	0	-0.0510
S <sub>2</sub>		0.1459	-0.0289	-0.0409	-0.0627	0.1777	0	0
S <sub>3</sub>			0.5799	-0.0376	-0.0549	-0.0617	0.1143	-0.0976
S <sub>4</sub>				0.5532	0.0388	-0.0872	-0.0808	0.0690
S <sub>5</sub>					0.7273	0	-0.0856	0.1288
S <sub>6</sub>						1.2347	0	0
S <sub>7</sub>							1.2035	0.0617
S <sub>8</sub>								0.5912

CD <sub>3</sub> OD A''				
(G <sub>s</sub> ) <sub>ij</sub>	S <sub>10</sub>	S <sub>11</sub>	S <sub>12</sub>	S <sub>13</sub>
S <sub>10</sub>	0.6065	0.1400	-0.1195	0
S <sub>11</sub>		1.2035	0.0617	0
S <sub>12</sub>			0.5912	-0.0569
S <sub>13</sub>				1.3548



**Table 8.11** The 37 initial non-zero force constants in internal coordinate space.<sup>a</sup>

$f_{i,j}$	$R_1$	$R_2$	$R_3$	$R_4$	$R_5$	$R_6$	$R_7$	$R_8$	$R_9$	$R_{10}$	$R_{11}$	$R_{12}$	$R_{13}$
$R_1$	<b><math>f_{1,1}</math></b>	0	0	0	0	0	0	0	0	0	0	0	0
$R_2$		<b><math>f_{2,2}</math></b>	<b><math>f_{2,3}</math></b>	<b><math>f_{2,4}</math></b>	<b><math>f_{2,4}</math></b>	<b><math>f_{2,6}</math></b>	<b><math>f_{2,7}</math></b>	<b><math>f_{2,8}</math></b>	<b><math>f_{2,8}</math></b>	<b><math>f_{2,10}</math></b>	<b><math>f_{2,11}</math></b>	<b><math>f_{2,11}</math></b>	0
$R_3$			<b><math>f_{3,3}</math></b>	<b><math>f_{3,4}</math></b>	<b><math>f_{3,4}</math></b>	0	<b><math>f_{3,7}</math></b>	<b><math>f_{3,8}</math></b>	<b><math>f_{3,8}</math></b>	0	0	0	0
$R_4$				<b><math>f_{4,4}</math></b>	<b><math>f_{4,5}</math></b>	0	<b><math>f_{4,7}</math></b>	<b><math>f_{4,8}</math></b>	<b><math>f_{4,9}</math></b>	0	0	0	0
$R_5$					<b><math>f_{4,4}</math></b>	0	<b><math>f_{4,7}</math></b>	<b><math>f_{4,9}</math></b>	<b><math>f_{4,8}</math></b>	0	0	0	0
$R_6$						<b><math>f_{6,6}</math></b>	<b><math>f_{6,7}</math></b>	<b><math>f_{6,8}</math></b>	<b><math>f_{6,8}</math></b>	<b><math>f_{6,10}</math></b>	<b><math>f_{6,11}</math></b>	<b><math>f_{6,11}</math></b>	0
$R_7$							<b><math>f_{7,7}</math></b>	<b><math>f_{7,8}</math></b>	<b><math>f_{7,8}</math></b>	<b><math>f_{7,10}</math></b>	<b><math>f_{7,11}</math></b>	<b><math>f_{7,11}</math></b>	0
$R_8$								<b><math>f_{8,8}</math></b>	<b><math>f_{8,9}</math></b>	<b><math>f_{8,10}</math></b>	<b><math>f_{8,11}</math></b>	<b><math>f_{8,12}</math></b>	0
$R_9$									<b><math>f_{8,8}</math></b>	<b><math>f_{8,10}</math></b>	<b><math>f_{8,12}</math></b>	<b><math>f_{8,11}</math></b>	0
$R_{10}$										<b><math>f_{10,10}</math></b>	<b><math>f_{10,11}</math></b>	<b><math>f_{10,11}</math></b>	0
$R_{11}$											<b><math>f_{11,11}</math></b>	<b><math>f_{11,12}</math></b>	0
$R_{12}$												<b><math>f_{11,11}</math></b>	0
$R_{13}$													<b><math>f_{13,13}</math></b>

a The internal force constants in bold were determined in this work. It was ultimately necessary to set remainder to zero.

i) There is no potential energy coupling between the OY stretching coordinate ( $R_1$ ) and any other coordinate,  $f_{1,j} = 0$  for all  $j$ . This may be seen from the spectra in the right boxes of Figure 8.1. Further, the normal coordinates calculated for the gaseous molecule, and for the liquid-phase molecule in our preliminary calculations showed the OY stretching vibrations to be almost pure.

ii) There is no potential coupling between the O–Y---O out-of-plane bending coordinate ( $R_{13}$ ) and any other coordinate,  $f_{i,13} = 0$  for all  $i$ .

iii) There is no potential coupling between the CX stretching coordinates ( $R_3$  to  $R_5$ ) and the XCO angle deformation coordinates ( $R_{10}$  to  $R_{12}$ ),  $f_{i,j} = 0$  for  $i = 3$  to  $5$  and  $j = 10$  to  $12$ .

iv) There is no potential coupling between the CX stretching coordinates ( $R_3$  to  $R_5$ ) and the COY in-plane angle deformation coordinate ( $R_6$ ),  $f_{i,6} = 0$  for  $i = 3$  to  $5$ .

The upper half of the (symmetric)  $F$  matrix containing the 37 remaining, non-zero force constants is shown in Table 8.11. The elements of the  $F_s$  matrix were calculated from these 37 elements of  $F$ , yielding the analytical equations in Table 8.12 and the upper

**Table 8.12** The 31 non-zero  $F_{ij}$  expressed in terms of the 37  $f_{ij}$  of Table 8.11. <sup>a</sup>

---

$F_{1,1} = f_{1,1}$
$F_{2,2} = f_{2,2}$
$F_{2,3} = f_{2,3}$
$F_{2,4} = 1.414f_{2,4}$
$F_{2,5} = f_{2,6}$
$F_{2,6} = 0.4142(f_{2,7} + 2f_{2,8}) - 0.4021(f_{2,10} + 2f_{2,11})$
$F_{2,7} = 0.8163(f_{2,7} - f_{2,8})$
$F_{2,8} = 0.8163(f_{2,10} - f_{2,11})$
$F_{3,3} = f_{3,3}$
$F_{3,4} = 1.414f_{3,4}$
$F_{3,6} = 0.4142(f_{3,7} + 2f_{3,8})$
$F_{3,7} = 0.8163(f_{3,7} - f_{3,8})$
$F_{4,4} = f_{4,4} + f_{4,5}$
$F_{4,6} = 0.5857(f_{4,7} + f_{4,8} + f_{4,9})$
$F_{4,7} = 0.5773(2f_{4,7} - f_{4,8} - f_{4,9})$
$F_{5,5} = f_{6,6}$
$F_{5,6} = 0.4142(f_{6,7} + 2f_{6,8}) - 0.4021(f_{6,10} + 2f_{6,11})$
$F_{5,7} = 0.8163(f_{6,7} - f_{6,8})$
$F_{5,8} = 0.8163(f_{6,10} - f_{6,11})$
$F_{6,6} = -0.3333(f_{7,10} + 2f_{7,11} + 2f_{8,10} + 2f_{8,11} + 2f_{8,12}) + 0.1716(f_{7,7} + 4f_{7,8} + 2f_{8,8}$ $+ 2f_{8,9}) + 0.1617(f_{10,10} + 2f_{11,11} + 4f_{10,11} + 2f_{11,12})$
$F_{6,7} = 0.3382(f_{7,7} + f_{7,8} - f_{8,8} - f_{8,9}) + 0.3282(-f_{7,10} - 2f_{7,11} + f_{8,10} + f_{8,11} + f_{8,12})$
$F_{6,8} = 0.3382(f_{7,10} - f_{7,11} + 2f_{8,10} - f_{8,11} - f_{8,12}) + 0.3282(-f_{10,10} - f_{10,11} + f_{11,11} + f_{11,12})$
$F_{7,7} = 0.3333(2f_{7,7} + f_{8,8} - 4f_{7,8} + f_{8,9})$
$F_{7,8} = 0.3333(2f_{7,10} - 2f_{7,11} - 2f_{8,10} + f_{8,11} + f_{8,12})$
$F_{8,8} = 0.3333(2f_{10,10} + f_{11,11} - 4f_{10,11} + f_{11,12})$
$F_{10,10} = f_{4,4} - f_{4,5}$
$F_{10,11} = f_{4,8} - f_{4,9}$
$F_{11,11} = f_{8,8} - f_{8,9}$
$F_{11,12} = f_{8,11} - f_{8,12}$
$F_{12,12} = f_{11,11} - f_{11,12}$
$F_{13,13} = f_{13,13}$

---

<sup>a</sup> The internal force constants in bold were determined in this work.

**Table 8.13** The non-zero  $F_{ij}$  from the  $f_{ij}$  in Table 8.11.<sup>a</sup>

$F_{ij}$	$S_1$	$S_2$	$S_3$	$S_4$	$S_5$	$S_6$	$S_7$	$S_8$	$S_{10}$	$S_{11}$	$S_{12}$	$S_{13}$
$S_1$	<b><math>F_{1,1}</math></b>											
$S_2$		<b><math>F_{2,2}</math></b>	$F_{2,3}^b$	$F_{2,4}^b$	<b><math>F_{2,5}</math></b>	<b><math>F_{2,6}</math></b>	$F_{2,7}^b$	$F_{2,8}^b$				
$S_3$			<b><math>F_{3,3}</math></b>	<b><math>F_{3,4}</math></b>		<b><math>F_{3,6}</math></b>	$F_{3,7}^c$					
$S_4$				<b><math>F_{4,4}</math></b>		<b><math>F_{4,6}</math></b>	<b><math>F_{4,7}</math></b>					
$S_5$					<b><math>F_{5,5}</math></b>	<b><math>F_{5,6}</math></b>	<b><math>F_{5,7}</math></b>	<b><math>F_{5,8}</math></b>				
$S_6$						<b><math>F_{6,6}</math></b>	$F_{6,7}^d$	$F_{6,8}^d$				
$S_7$							<b><math>F_{7,7}</math></b>	<b><math>F_{7,8}</math></b>				
$S_8$								<b><math>F_{8,8}</math></b>				
			A' Block							A'' Block		
$S_{10}$									<b><math>F_{10,10}</math></b>	$F_{10,11}^e$		
$S_{11}$										$F_{11,11}^f$	<b><math>F_{11,12}</math></b>	
$S_{12}$											<b><math>F_{12,12}</math></b>	
$S_{13}$												<b><math>F_{13,13}</math></b>

a The force constants in bold were determined in this work. See the text in Section 8.3.5 for footnotes b to f about the assumptions.

b The constant was set to zero in the calculation.

c  $F_{3,6}$  is related to  $F_{3,7}$  through  $f_{3,8}$  under the assumption that  $f_{3,7} = 0$ .

d The constant was set zero to yield acceptable eigenvectors.

e  $F_{10,11}$ ,  $F_{4,6}$ ,  $F_{4,7}$  are related through two constants  $f_{4,7}$  and  $f_{4,9}$  under the assumption that  $f_{4,8} = 0$ .

f  $F_{11,11} = F_{7,7}$  was used.

half of the (symmetric)  $F_s$  matrix shown in Table 8.13. With the above assumptions, 31 elements of  $F_s$  must be determined. There are 42 observed wavenumbers which suggests that all 31 elements of  $F_s$  should be readily determined. In fact, this is not the case.

There are, for example, 14 known  $CX_3$  deformation and rocking wavenumbers, but there are 19 elements of  $F_s$  that involve these coordinates,  $S_6$  to  $S_8$ ,  $S_{11}$  and  $S_{12}$ . Further, there is only one  $F_s$  element that describes the OH and OD stretching vibrations, but 4 of the known wavenumbers are from this mode. Detailed examination revealed that a further 9 assumptions were required to reduce the number of the  $F_s$  elements. They are detailed in Section 8.3.5.

### 8.3.4 The Observed and Harmonic Wavenumbers

The vibrational wavenumbers and their assignments were used as given in Table 8.14. The assignments were made based on the assignments of the gas molecules suitably modified for the hydrogen-bonding in the liquid. Ideally, the observed wavenumbers

**Table 8.14** Comparison of the experimental and fitted wavenumbers.

<b>CH<sub>3</sub>OH</b>			<b>Wavenumber (cm<sup>-1</sup>)</b>	
<b>Assignment</b>			<b>Observed</b>	<b>Calculated</b>
$\nu_1$	A'	$\nu(\text{OH})$	3625 <sup>a</sup>	3623.8
$\nu_2$		$\nu(\text{CH})$ asym	3141 <sup>a</sup>	3141.1
$\nu_3$		$\nu(\text{CH})$ sym	3003 <sup>a</sup>	3003.0
$\nu_4$		$\delta(\text{CH}_3)$ asym	1477	1475.3
$\nu_5$		$\delta(\text{CH}_3)$ sym	1450	1448.7
$\nu_6$		$\delta(\text{COH})$	1423	1420.2
$\nu_7$		$\gamma(\text{CH}_3)$	1116	1113.2
$\nu_8$		$\nu(\text{CO})$	1035	1034.7
$\nu_9$	A''	$\nu(\text{CH})$	3109 <sup>a</sup>	3109.0
$\nu_{10}$		$\delta(\text{CH}_3)$	–	1488.8
$\nu_{11}$		$\gamma(\text{CH}_3)$	–	1156.4
$\nu_{12}$		$\delta(\text{O-H}\cdots\text{O})$	730 <sup>a</sup>	730.9

<b>CH<sub>3</sub>OD</b>			<b>Wavenumber (cm<sup>-1</sup>)</b>	
<b>Assignment</b>			<b>Observed</b>	<b>Calculated</b>
$\nu_1$	A'	$\nu(\text{CH})$ asym	3141 <sup>a</sup>	3141.0
$\nu_2$		$\nu(\text{CH})$ sym	3003 <sup>a</sup>	3003.0
$\nu_3$		$\nu(\text{OD})$	2639 <sup>a</sup>	2642.4
$\nu_4$		$\delta(\text{CH}_3)$ asym	1467	1468.8
$\nu_5$		$\delta(\text{CH}_3)$ sym	1447	1448.1
$\nu_6$		$\gamma(\text{CH}_3)$	1232	1235.9
$\nu_7$		$\nu(\text{CO})$	1034	1033.3
$\nu_8$		$\delta(\text{COD})$	941	947.1
$\nu_9$	A''	$\nu(\text{CH})$	3109 <sup>a</sup>	3109.0
$\nu_{10}$		$\delta(\text{CH}_3)$	–	1488.8
$\nu_{11}$		$\gamma(\text{CH}_3)$	1157	1156.3
$\nu_{12}$		$\delta(\text{O-D}\cdots\text{O})$	526 <sup>a</sup>	525.4

(Cont'd on next page)

**Table 8.14** (Cont'd)

<b>CD<sub>3</sub>OH</b>			<b>Wavenumber (cm<sup>-1</sup>)</b>	
<b>Assignment</b>			<b>Observed</b>	<b>Calculated</b>
$\nu_1$	A'	$\nu(\text{OH})$	3625 <sup>a</sup>	3623.7
$\nu_2$		$\nu(\text{CD})$ asym	2324 <sup>a</sup>	2326.9
$\nu_3$		$\nu(\text{CD})$ sym	2164 <sup>a</sup>	2164.2
$\nu_4$		$\delta(\text{COH})$	1393	1393.6
$\nu_5$		$\delta(\text{CD}_3)$ sym	1122	1121.8
$\nu_6$		$\delta(\text{CD}_3)$ asym	–	1042.5
$\nu_7$		$\nu(\text{CO})$	984	982.2
$\nu_8$		$\gamma(\text{CD}_3)$	886	881.4
$\nu_9$	A''	$\nu(\text{CD})$	2304 <sup>a</sup>	2301.5
$\nu_{10}$		$\delta(\text{CD}_3)$	1068	1066.1
$\nu_{11}$		$\gamma(\text{CD}_3)$	–	904.0
$\nu_{12}$		$\delta(\text{O–H}\cdots\text{O})$	730 <sup>a</sup>	729.8

<b>CD<sub>3</sub>OD</b>			<b>Wavenumber (cm<sup>-1</sup>)</b>	
<b>Assignment</b>			<b>Observed</b>	<b>Calculated</b>
$\nu_1$	A'	$\nu(\text{OD})$	2639 <sup>a</sup>	2642.2
$\nu_2$		$\nu(\text{CD})$ asym	2329 <sup>a</sup>	2325.9
$\nu_3$		$\nu(\text{CD})$ sym	2164 <sup>a</sup>	2163.8
$\nu_4$		$\delta(\text{CD}_3)$ sym	1125	1126.1
$\nu_5$		$\delta(\text{CD}_3)$ asym	1097	1096.0
$\nu_6$		$\gamma(\text{CD}_3)$	–	1031.8
$\nu_7$		$\nu(\text{CO})$	979	981.7
$\nu_8$		$\delta(\text{COD})$	824	825.7
$\nu_9$	A''	$\nu(\text{CD})$	2299 <sup>a</sup>	2301.5
$\nu_{10}$		$\delta(\text{CD}_3)$	1064	1066.0
$\nu_{11}$		$\gamma(\text{CD}_3)$	902	903.7
$\nu_{12}$		$\delta(\text{O–D}\cdots\text{O})$	526 <sup>a</sup>	524.6

<sup>a</sup> Approximate harmonic wavenumber.

should be corrected for anharmonicity before they are used as data for a normal coordinate calculation, which is intrinsically a harmonic calculation. An approximate correction was possible for the OY and CX stretching modes and the O–Y---O out-of-plane bending mode, as detailed in the following.

For an anharmonic oscillator, the frequency of a fundamental vibration is given to first order by<sup>7</sup>

$$\nu_{0 \rightarrow 1} = \omega_e - 2\omega_e x_e \quad (8.4)$$

where  $\omega_e$  is the harmonic wavenumber and  $\omega_e x_e$  is the anharmonicity constant.

For uncoupled oscillators, the well-known expression for the harmonic wavenumber  $\omega_e$  yields the ratio of the harmonic wavenumbers of a hydrogen oscillator,  $\omega_e^H$ , and its deuterated isotopomer,  $\omega_e^D$ ,

$$\frac{\omega_e^H}{\omega_e^D} = \sqrt{\frac{G^H}{G^D}} \quad (8.5)$$

where  $G^H$  and  $G^D$  are the diagonal G matrix elements for the two molecules. If the oscillator is diatomic, this becomes

$$\frac{\omega_e^H}{\omega_e^D} = \sqrt{\frac{\mu^D}{\mu^H}} \quad (8.5a)$$

where  $\mu$  is the reduced mass of the oscillator.

For the same uncoupled oscillator, a useful relation<sup>10</sup> exists between the anharmonicity constants,  $\omega_e x_e$ , namely

$$\frac{\omega_e x_e^H}{\omega_e x_e^D} = \frac{G^H}{G^D} \quad (8.6)$$

Thus, the known G matrix elements and eqs. (8.4), (8.5) and (8.6) can be used to determine  $\omega_e$  and  $\omega_e x_e$  for the H and D isotopomers from the observed wavenumbers.

This method was used with the diagonal elements of  $G_s$  to approximately correct for anharmonicity the wavenumbers of the OH, OD, CH and CD stretching vibrations and the O–Y---O out-of-plane bending vibration.

For the OH(D) stretching vibrations, the average wavenumber is 3353 cm<sup>-1</sup> for the OH vibrations and 2495 cm<sup>-1</sup> for the OD vibrations. These values with  $G^H = 1.0548$  and  $G^D = 0.5590$  gave

$$\begin{array}{ll} \omega_e^H = 3625 \text{ cm}^{-1}, & \omega_e x_e^H = 136 \text{ cm}^{-1} \\ \text{and } \omega_e^D = 2639 \text{ cm}^{-1}, & \omega_e x_e^D = 72 \text{ cm}^{-1} \end{array}$$

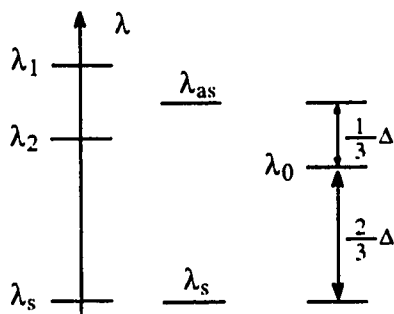


**Figure 8.8** The energy splitting of the stretching vibrations of a  $C_{3v}$   $CX_3$  group.

for the stretching modes. The  $\omega_e x_e^H$  can be compared with the values 115 and 106  $\text{cm}^{-1}$  obtained<sup>11</sup> from the wavenumbers of the fundamental and the first and second overtones.

For the out-of-plane bending vibrations, the average wavenumber is 670  $\text{cm}^{-1}$  for OH and 494  $\text{cm}^{-1}$  for OD. With  $G^H = 2.6194$  and  $G^D = 1.3548$ , these gave

$$\omega_e^H = 735 \text{ cm}^{-1}, \quad \omega_e x_e^H = 30 \text{ cm}^{-1}$$

$$\text{and } \omega_e^D = 526 \text{ cm}^{-1}, \quad \omega_e x_e^D = 16 \text{ cm}^{-1}$$

for the out-of-plane bending modes. The resulting harmonic wavenumbers,  $\omega_e$ , obtained above for the stretching and bending modes are given under the heading "Observed" in Table 8.14.

The correction of the three  $\text{CH}_3$  and three  $\text{CD}_3$  stretching wavenumbers is more complicated. To simplify the problem, an uncoupled CH stretching wavenumber was calculated by noting that for a  $\text{CH}_3$  group of  $C_{3v}$  symmetry with a diagonal force field, the eigenvalue,  $\lambda = 4\pi^2 c^2 \bar{\nu}^2$ , of the (degenerate) asymmetric stretching mode is  $\Delta$  above the uncoupled eigenvalue and that of the symmetric stretching mode is  $2\Delta$  below it. This is illustrated in Figure 8.8. Thus the average of the two asymmetric stretching wavenumbers was calculated and converted to an eigenvalue. The symmetric stretching wavenumber was also converted to an eigenvalue, and the eigenvalue,  $\lambda_0$ , of the uncoupled CH oscillator was calculated as the symmetric eigenvalue plus two thirds of the difference,  $\Delta$ , between the asymmetric and symmetric eigenvalues.

$$\lambda_0 = \lambda_s + \frac{2}{3} \Delta$$

Hence the wavenumber of the uncoupled CH oscillator was found.

The same was done for the CD oscillator. The resulting uncoupled wavenumbers for CH and CD were used with the reduced masses of CH and CD to obtain

$$\begin{aligned} \omega_e^H &= 3085 \text{ cm}^{-1}, & \omega_e x_e^H &= 82 \text{ cm}^{-1} \\ \text{and} \quad \omega_e^D &= 2265 \text{ cm}^{-1}, & \omega_e x_e^D &= 44 \text{ cm}^{-1} \end{aligned}$$

for the uncoupled oscillators. The uncoupled harmonic wavenumbers were converted to eigenvalues and shifted  $\Delta$  up and  $2\Delta$  down and converted back to wavenumbers. The asymmetric stretching modes were then separated by the same amount as the observed wavenumbers to obtain the approximately corrected wavenumbers of the three CH and three CD stretching modes.

The approximate harmonic wavenumbers found in this way are listed in Table 8.14 under the heading "Observed". The remainder of the "observed wavenumber" in Table 8.14 are the peak wavenumbers in the  $\tilde{\nu}\alpha_m$  spectrum.

### 8.3.5 Results and Discussion

After the assumptions made in Section 8.3.3, there remained more  $F_s$  elements,  $F_{ij}$ , than could be determined from the available frequencies. As a result of many trials using the program FPERT<sup>8</sup>, the following additional assumptions were made to further reduce the number of  $F_{ij}$ .

i) There is no potential coupling between the CO and CX stretching coordinates,  $f_{2,3} = f_{2,4} = 0$ .<sup>9</sup> From Table 8.12, this is equivalent to  $F_{2,3} = F_{2,4} = 0$ .

ii) There is no potential coupling between the CO stretching and XCO deformation coordinates,  $f_{2,7} = f_{2,8} = 0$ ; further, the two non equivalent coupling constants between the CO bond stretching and XCO deformation coordinates were set equal,  $f_{2,10} = f_{2,11}$ . These assumptions imply (from Table 8.12) that  $F_{2,6} = -1.206 f_{2,10}$ , and  $F_{2,7} = F_{2,8} = 0$ .

iii) There is no potential coupling between the CX stretching coordinates and the opposite XCO deformation coordinates (Figure 8.7),  $f_{3,7} = f_{4,8} = 0$ .<sup>9</sup> But the coupling constants between the CX stretching and the adjacent XCO deformation ( $f_{3,8}$ ,  $f_{4,7}$  and  $f_{4,9}$ ) exist and are not equal. These constants were found necessary for the error in the calculated CD stretching frequencies to be reduced to about  $3 \text{ cm}^{-1}$  from over  $10 \text{ cm}^{-1}$ . As a result of this assumption,  $F_{3,6}$  and  $F_{3,7}$  are determined by  $f_{3,8}$  only and  $F_{4,6}$ ,  $F_{4,7}$  and  $F_{4,11}$  are determined by  $f_{4,7}$  and  $f_{4,9}$  only.

iv)  $F_{7,7}$  and  $F_{11,11}$  were found to have very similar values and were set equal in the final calculation.



v)  $F_{6,7}$  and  $F_{6,8}$  were set to zero. It was necessary to set  $F_{6,8}$  to zero in order to obtain a set of eigenvectors that gave the nearly equal intensities of the CO stretching vibration in  $\text{CH}_3\text{OH}$  and  $\text{CH}_3\text{OD}$  that is required by the experimental result shown in the top box of Figure 8.2.

In this way, 22 independent symmetrized force constants  $F_{ij}$  were chosen, shown in bold in Table 8.13. They were entered into FPERT<sup>8</sup> and refined to convergence. The converged wavenumbers are given in Table 8.14. The average errors are 1.1, 1.6, 1.6 and 1.9  $\text{cm}^{-1}$  for  $\text{CH}_3\text{OH}$ ,  $\text{CH}_3\text{OD}$ ,  $\text{CD}_3\text{OH}$  and  $\text{CD}_3\text{OD}$ , respectively, which corresponds to 0.1% average error in each case. The values of the 22 independent  $F_{ij}$  are given in Table 8.15. The symmetry coordinate eigenvectors, the elements  $(l_s)_{ij}$  of  $L_s$  in  $S = L_s Q$ , are given in Table 8.16, and were used to calculate the intensities (Section 8.4).

The relations in Table 8.12 and the assumptions given in this section were used to convert the symmetrized force constants  $F_{ij}$  to the internal coordinate force constants  $f_{ij}$ . The resulting  $f_{ij}$  are given in Table 8.15. Most of the transformations from  $F_{ij}$  to  $f_{ij}$  were trivial, but others required assumptions.

Three symmetrized force constants which couple the in-plane COY bending coordinate with the  $\text{CX}_3$  deformation or rock coordinates,  $F_{5,6}$ ,  $F_{5,7}$  and  $F_{5,8}$ , depend on 4 internal force constants,  $f_{6,7}$ ,  $f_{6,8}$ ,  $f_{6,10}$  and  $f_{6,11}$ , which do not influence any other  $F_{ij}$  (Table 8.12). In order to obtain three  $f_{ij}$ , the assumption was made that  $f_{6,7} = 0$  because the coupling between the in-plane COY deformation and the XCO angle deformations is expected to be larger than that between the in-plane COY deformation and the XCX deformations.<sup>9</sup>

The constants involving the deformation and rocking coordinates were more complicated. There were 9 symmetry force constants,  $F_{6,6}$ ,  $F_{6,7} (=0)$ ,  $F_{6,8} (=0)$ ,  $F_{7,7}$ ,  $F_{7,8}$ ,  $F_{8,8}$ ,  $F_{11,11}$ ,  $F_{11,12}$ ,  $F_{12,12}$  to determine 13 internal force constants. The first assumption<sup>9</sup> was that there is no potential coupling between the XCX angle deformation coordinates, i.e.  $f_{7,8} = f_{8,9} = 0$ . This assumption, with the previously used  $F_{7,7} = F_{11,11}$ , leads to  $f_{7,7} = f_{8,8}$ . The second assumption was that there is no potential coupling between the XCO angle coordinates, i.e.  $f_{10,11} = f_{11,12} = 0$ . With these assumptions, the values of  $f_{7,7} (=f_{8,8})$ ,  $f_{10,10}$ ,  $f_{11,11}$ ,  $f_{7,10}$ ,  $f_{7,11}$ ,  $f_{8,10}$ ,  $f_{8,11}$  and  $f_{8,12}$  were obtained. The final force constants are tabulated in Table 8.15.

**Table 8.15** The final force constants  $F_{ij}$  and  $f_{ij}$  in  $\text{mdyn } \text{\AA}^{-1}$ .

$F_{ij}$	value	$f_{ij}$	value
$F_{1,1}$	7.3273	$f_{1,1}$	7.3273
$F_{2,2}$	6.3178	$f_{2,2}$	6.3178
$F_{2,5}$	0.4503	$f_{2,6}$	0.4503
$F_{2,6}$	–1.0602	$f_{2,10}, (f_{2,11}, f_{2,12})^c$	0.8789
$F_{3,3}$	5.0248	$f_{3,3}$	5.0248
$F_{3,4}$	0.0008	$f_{3,4}, f_{3,5}$	0.0006
$F_{3,6}$	0.0208	$f_{3,8}, f_{3,9}$	0.0251
$F_{3,7}^a$	–0.0205	$f_{4,4}, f_{5,5}$	5.3186
$F_{4,4}$	5.4490	$f_{4,5}$	0.1304
$F_{4,6}$	0.3286	$f_{4,7}, f_{5,7}$	0.2718
$F_{4,7}$	0.1469	$f_{4,9}, f_{5,8}$	0.2892
$F_{5,5}$	0.8935	$f_{6,6}$	0.8935
$F_{5,6}$	–0.0565	$f_{6,8}, f_{6,9}$	0.0450
$F_{5,7}$	–0.0367	$f_{6,10}$	0.1049
$F_{5,8}$	0.0332	$f_{6,11}, f_{6,12}$	0.0642
$F_{6,6}$	0.6814	$f_{7,7}, (f_{8,8}, f_{9,9})^e$	0.4756
$F_{6,7}^b$	0	$f_{7,10}$	0.0059
$F_{6,8}^b$	0	$f_{7,11}, f_{7,12}$	0.0227
$F_{7,7}, F_{11,11}$	0.4756	$f_{8,10}, f_{9,10}$	0.0049
$F_{7,8}$	0.0186	$f_{8,11}, f_{9,12}$	0.0541
$F_{8,8}$	1.0237	$f_{8,12}, f_{9,11}$	0.0100
$F_{10,10}$	5.1482	$f_{10,10}$	0.9795
$F_{10,11}^c$	–0.2892	$f_{11,11}, f_{12,12}$	1.0347
$F_{11,12}$	0.0441	$f_{13,13}$	0.1204
$F_{12,12}$	1.0605		
$F_{13,13}$	0.1204		

- a  $F_{3,7}$  is related to  $F_{3,6}$  through  $f_{3,8}$  from the assumption that  $f_{3,7}=0$ . See Table 8.12 and the text in Section 8.3.5.
- b  $F_{6,7} = 0$  and  $F_{6,8} = 0$  used in converting  $F_{ij}$  to  $f_{ij}$  in the table.
- c  $F_{10,11}$  is related to  $F_{4,6}$  and  $F_{4,7}$  through  $f_{4,7}$  and  $f_{4,9}$  from the assumption that  $f_{4,8} = 0$ . See Table 8.12 and the text in Section 8.3.5.
- d  $f_{2,11} = f_{2,12}$  by symmetry are assumed to be the same as the non-equivalent  $f_{2,10}$ .
- e  $f_{8,8} = f_{9,9}$  by symmetry are assumed to be the same as the non-equivalent  $f_{7,7}$ .

**Table 8.16** The symmetrized eigenvectors  $(l_s)_{i,j}$ .<sup>a</sup>

CH <sub>3</sub> OH									
Q <sub>j</sub> (A')	$\tilde{\nu}_j$	S <sub>1</sub>	S <sub>2</sub>	S <sub>3</sub>	S <sub>4</sub>	S <sub>5</sub>	S <sub>6</sub>	S <sub>7</sub>	S <sub>8</sub>
Q <sub>1</sub>	3623.8	-1.0269	0.0213	-0.0053	0.0011	0.0497	-0.0036	0.0012	0.0589
Q <sub>2</sub>	3141.1	-0.0034	0.0160	0.5033	-0.9073	-0.0732	-0.0741	0.0712	-0.1309
Q <sub>3</sub>	3003.0	-0.0046	-0.0440	0.9062	0.4622	-0.0432	-0.0231	0.0978	-0.0582
Q <sub>4</sub>	1475.3	-0.0110	-0.0377	-0.0179	-0.0279	-0.3010	0.7793	-0.7590	-0.6211
Q <sub>5</sub>	1448.7	0.0012	0.0510	0.0025	0.0976	0.0702	-0.9118	-0.8367	-0.4648
Q <sub>6</sub>	1420.2	-0.0070	0.0324	-0.0217	0.0207	-0.9971	-0.3614	0.5678	-0.1997
Q <sub>7</sub>	1113.2	0.0018	-0.0084	0.0118	0.0172	-0.4052	-0.0718	-0.7832	0.5825
Q <sub>8</sub>	1034.7	-0.0045	-0.3716	-0.0081	0.0340	0.1361	-0.7132	0.0209	-0.0266

Q <sub>j</sub> (A'')	$\tilde{\nu}_j$	S <sub>10</sub>	S <sub>11</sub>	S <sub>12</sub>	S <sub>13</sub>
Q <sub>9</sub>	3109.0	1.0455	0.0052	-0.1582	0.0018
Q <sub>10</sub>	1488.8	0.0879	1.1293	0.7759	-0.0501
Q <sub>11</sub>	1156.4	-0.0362	-0.9755	0.6151	-0.0733
Q <sub>12</sub>	730.9	-0.0001	-0.0092	0.0170	1.6160

CH <sub>3</sub> OD									
Q <sub>j</sub> (A')	$\tilde{\nu}_j$	S <sub>1</sub>	S <sub>2</sub>	S <sub>3</sub>	S <sub>4</sub>	S <sub>5</sub>	S <sub>6</sub>	S <sub>7</sub>	S <sub>8</sub>
Q <sub>1</sub>	3141.0	0.0036	0.0158	0.5029	-0.9075	-0.0671	-0.0741	0.0709	-0.1313
Q <sub>2</sub>	3003.0	0.0089	-0.0444	0.9064	0.4617	-0.0367	-0.0231	0.0976	-0.0592
Q <sub>3</sub>	2642.4	0.7471	-0.0314	-0.0142	-0.0016	-0.0675	0.0139	-0.0085	-0.0927
Q <sub>4</sub>	1468.8	-0.0193	-0.0366	-0.0110	-0.0223	-0.0036	0.7490	-0.9538	-0.5990
Q <sub>5</sub>	1448.1	0.0015	0.0577	-0.0001	0.1014	-0.0835	-1.0077	-0.6865	-0.4470
Q <sub>6</sub>	1235.9	-0.0162	0.0240	-0.0246	-0.0125	-0.4741	0.0456	0.8333	-0.5776
Q <sub>7</sub>	1033.3	-0.0092	-0.3703	-0.0084	0.0330	0.1654	-0.7059	0.0509	-0.0520
Q <sub>8</sub>	947.1	-0.0049	-0.0176	-0.0013	0.0122	-0.6766	-0.0769	-0.3667	0.2855

Q <sub>j</sub> (A'')	$\tilde{\nu}_j$	S <sub>10</sub>	S <sub>11</sub>	S <sub>12</sub>	S <sub>13</sub>
Q <sub>9</sub>	3109.0	1.0455	0.0052	-0.1582	0.0017
Q <sub>10</sub>	1488.8	0.0879	1.1293	0.7759	-0.0435
Q <sub>11</sub>	1156.3	-0.0362	-0.9755	0.6153	-0.0555
Q <sub>12</sub>	525.4	0.0000	-0.0044	0.0097	1.1618

(Cont'd on next page)

**Table 8.16** (Cont'd)

CD <sub>3</sub> OH									
Q <sub>j</sub> (A')	$\tilde{\nu}_j$	S <sub>1</sub>	S <sub>2</sub>	S <sub>3</sub>	S <sub>4</sub>	S <sub>5</sub>	S <sub>6</sub>	S <sub>7</sub>	S <sub>8</sub>
Q <sub>1</sub>	3623.7	1.0269	-0.0213	0.0025	-0.0005	-0.0495	0.0004	0.0005	-0.0551
Q <sub>2</sub>	2326.9	-0.0033	0.0072	0.5367	-0.5562	-0.1460	-0.0462	0.1689	-0.1892
Q <sub>3</sub>	2164.2	-0.0026	-0.0741	0.5367	0.4875	-0.0465	-0.0814	0.0789	-0.0386
Q <sub>4</sub>	1393.6	0.0092	-0.0150	0.0516	-0.0161	1.0946	0.0040	-0.1389	0.1922
Q <sub>5</sub>	1121.8	-0.0060	-0.2422	-0.0157	-0.0503	0.1197	0.4649	-0.0679	-0.0354
Q <sub>6</sub>	1042.5	0.0032	-0.0419	0.0044	-0.0293	-0.0327	-0.0597	0.8019	0.5485
Q <sub>7</sub>	982.2	-0.0021	-0.2809	-0.0135	0.0515	0.0671	-1.0028	-0.1128	-0.0241
Q <sub>8</sub>	881.4	0.0024	0.0171	0.0253	0.0024	-0.1955	0.0270	-0.6993	0.4597

Q <sub>j</sub> (A'')	$\tilde{\nu}_j$	S <sub>10</sub>	S <sub>11</sub>	S <sub>12</sub>	S <sub>13</sub>
Q <sub>9</sub>	2301.5	0.7760	0.1046	-0.1949	0.0041
Q <sub>10</sub>	1066.1	0.0635	0.7125	0.6093	-0.1088
Q <sub>11</sub>	904.0	-0.0165	-0.8272	0.4243	-0.1417
Q <sub>12</sub>	729.8	0.0009	-0.0250	0.0437	1.6086

CD <sub>3</sub> OD									
Q <sub>j</sub> (A')	$\tilde{\nu}_j$	S <sub>1</sub>	S <sub>2</sub>	S <sub>3</sub>	S <sub>4</sub>	S <sub>5</sub>	S <sub>6</sub>	S <sub>7</sub>	S <sub>8</sub>
Q <sub>1</sub>	2642.2	-0.7472	0.0323	-0.0157	0.0052	0.0701	-0.0003	-0.0035	0.0856
Q <sub>2</sub>	2325.9	0.0147	-0.0081	-0.5350	0.5584	0.1149	0.0460	-0.1677	0.1862
Q <sub>3</sub>	2163.8	0.0090	0.0737	-0.5394	-0.4850	0.0267	0.0816	-0.0788	0.0373
Q <sub>4</sub>	1126.1	-0.0030	-0.2253	0.0060	-0.0529	0.4567	0.4010	-0.1120	0.1845
Q <sub>5</sub>	1096.0	0.0204	0.0809	0.0426	0.0066	0.5380	-0.2610	-0.0046	0.4775
Q <sub>6</sub>	1031.8	0.0005	-0.0421	-0.0116	-0.0277	-0.2330	-0.0154	0.9292	0.3543
Q <sub>7</sub>	981.7	-0.0049	-0.2832	-0.0153	0.0509	0.0477	-0.9983	-0.0806	-0.0384
Q <sub>8</sub>	825.7	0.0010	0.0075	0.0141	0.0027	-0.3923	0.0155	-0.5354	0.3984

Q <sub>j</sub> (A'')	$\tilde{\nu}_j$	S <sub>10</sub>	S <sub>11</sub>	S <sub>12</sub>	S <sub>13</sub>
Q <sub>9</sub>	2301.5	-0.7760	-0.1046	0.1949	-0.0039
Q <sub>10</sub>	1066.0	-0.0635	-0.7136	-0.6091	0.0761
Q <sub>11</sub>	903.7	-0.0163	-0.8266	0.4264	-0.0744
Q <sub>12</sub>	524.6	0.0005	-0.0066	0.0190	1.1591

a  $\tilde{\nu}_j$  are the calculated wavenumbers.

**Table 8.17** Calculated and observed intensities as  $|\partial\bar{\mu}/\partial Q_j|^2$  in the units (Debye Å<sup>-1</sup> amu<sup>-1/2</sup>)<sup>2</sup>. <sup>a</sup>

$ \partial\bar{\mu}/\partial Q_j ^2$	CH <sub>3</sub> OH		CH <sub>3</sub> OD		CD <sub>3</sub> OH		CD <sub>3</sub> OD	
	expt	calc	expt	calc	expt	calc	expt	calc
<b>A'</b>								
νOH(D)	13.9	13.9	7.49	7.36	13.8	13.8	7.38	7.47
νCH(D) as	0.73	0.85	0.80	0.85	0.58	0.40	0.47	0.36
νCH(D) s	0.73	0.73	0.75	0.81	0.69	0.64	0.73	0.65
δCOH(D)	1.25	1.10	0.56	0.58	1.46	1.54	0.34	0.34
δCH <sub>3</sub> /CD <sub>3</sub> as	0.30	0.23	0.22	0.06	0.06	0.07	0.47	1.01
δCH <sub>3</sub> /CD <sub>3</sub> s	0.07	0.17	0.13	0.11	0.90	0.47	0.93	0.18
γCH <sub>3</sub> /CD <sub>3</sub>	0.30	0.36	0.09	0.35	0.22	0.20	0.22	0.09
νCO	2.24	2.06	2.30	2.11	1.23	1.37	1.08	1.32
<b>A''</b>								
νCH(D)	1.03	0.97	0.90	0.97	0.52	0.49	0.49	0.49
δCH <sub>3</sub> /CD <sub>3</sub>	0.00	0.03	0.00	0.03	0.13	0.01	0.07	0.01
γCH <sub>3</sub> /CD <sub>3</sub>	0.04	0.03	0.02	0.04	0.06	0.01	0.04	0.02
O–H(D)---O	1.96	1.87	0.99	0.97	1.81	1.89	0.93	0.97

a The standard deviations in the fitted  $|\partial\bar{\mu}/\partial Q_j|^2$  from the non-linear least squares fit were 0.25 (D Å<sup>-1</sup> amu<sup>-1/2</sup>)<sup>2</sup> for the A' modes and 0.06 (D Å<sup>-1</sup> amu<sup>-1/2</sup>)<sup>2</sup> for the A'' modes.

## 8.4 Dipole Moment Derivatives

The integrated intensity,  $C_j$ , is directly proportional to  $\mu_j^2$ , the square of the dipole moment derivative with respect to the normal coordinate, eqs. (4.12b) and (A5.21). The  $\mu_j^2$  values are given in Tables 8.1 to 8.4 and are collected in Table 8.17 as the experimental  $\mu_j^2$  values.  $S_i$  is related to  $Q_j$  through the symmetrized eigenvectors  $(l_s)_{i,j}$ , defined by

$$S_i = \sum_j (l_s)_{i,j} Q_j \quad (8.7)$$

Thus,  $(l_s)_{i,j} = \partial S_i / \partial Q_j$  and  $\partial\bar{\mu}/\partial Q_j$  can be related to  $\partial\bar{\mu}/\partial S_i$  through the symmetrized eigenvectors by

$$\frac{\partial \bar{\mu}}{\partial Q_j} = \sum_i \frac{\partial \bar{\mu}}{\partial S_i} (l_s)_{i,j} \quad (8.8)$$

The reverse relation is

$$\frac{\partial \bar{\mu}}{\partial S_i} = \sum_j \frac{\partial \bar{\mu}}{\partial Q_j} (l_s^{-1})_{j,i} \quad (8.9)$$

where  $(l_s^{-1})_{j,i}$  are the inverse symmetrized eigenvectors, the elements of  $(L_s)^{-1}$  in  $Q = (L_s)^{-1} S$ .

In order to calculate  $\partial \bar{\mu} / \partial S_i$  from eq. (8.9), the relative directions of  $\partial \bar{\mu} / \partial Q_j$  must be determined for all normal vibrations in the symmetry block involved. Intensity data from the isotopic molecules can be very useful for this purpose<sup>12</sup>, but low symmetry of the methanol molecule makes this impossible for the A' vibrations, because their  $\partial \bar{\mu} / \partial Q_j$  and  $\partial \bar{\mu} / \partial S_i$  vectors can point in any direction in the X<sub>4</sub>-C-O-Y plane (Figure 8.7). Thus in this work, instead of trying to determine the relative directions of the  $\partial \bar{\mu} / \partial Q_j$  and calculate  $\partial \bar{\mu} / \partial S_i$  through eq. (8.9), eq. (8.8) was used with the directions of the  $\partial \bar{\mu} / \partial S_i$  reported from an ab initio calculation<sup>13</sup>. The  $\partial \bar{\mu} / \partial S_i$  values were fitted to the experimental intensities through eq. (8.8) by non-linear least squares.

The dipole moment derivative can be written in terms of its Cartesian components

$$\frac{\partial \bar{\mu}}{\partial S_i} = \frac{\partial \mu^x}{\partial S_i} \bar{i} + \frac{\partial \mu^y}{\partial S_i} \bar{j} + \frac{\partial \mu^z}{\partial S_i} \bar{k}$$

where  $\bar{i}$ ,  $\bar{j}$  and  $\bar{k}$  are the unit vectors along the x, y and z axes. For molecules of C<sub>s</sub> symmetry,  $\partial \bar{\mu} / \partial S_i$  for the S<sub>i</sub> of A' symmetry lie in the symmetry plane, the xy plane in the coordinate system defined in Figure 8.7. Thus,  $\partial \mu^z / \partial S_i = 0$  for A' coordinates and  $\partial \mu^x / \partial S_i = \partial \mu^y / \partial S_i = 0$  for A'' coordinates.

Thus, for the eight A' normal coordinates,

$$\left| \frac{\partial \bar{\mu}}{\partial Q_j} \right|^2 = \left[ \sum_i \left( \frac{\partial \mu^x}{\partial S_i} \right) (l_s)_{i,j} \right]^2 + \left[ \sum_i \left( \frac{\partial \mu^y}{\partial S_i} \right) (l_s)_{i,j} \right]^2 \quad (8.10)$$

and for the four A'' modes,

$$\left| \frac{\partial \bar{\mu}}{\partial Q_j} \right|^2 = \left[ \sum_i \left( \frac{\partial \mu^z}{\partial S_i} \right) (l_s)_{i,j} \right]^2 \quad (8.11)$$

Torri and Tasumi<sup>13</sup> have calculated the size and direction of the  $\partial \bar{\mu} / \partial S_i$  from ab initio quantum mechanics including correlation. Hence, for the A' modes, they calculated the magnitudes of  $\partial \mu^x / \partial S_i$  and  $\partial \mu^y / \partial S_i$  for all symmetry coordinates. If  $d_i$  is defined by

**Table 8.18** The fitted values of the x,y,z components of  $\partial\bar{\mu}/\partial S_i$ .

$\partial\bar{\mu}/\partial S_i$		$d_i^a$	$x^b$	y	z <sup>b</sup>
S <sub>1</sub>	OY	1.317	2.125 (0.013)	2.913	
S <sub>2</sub>	CO	0.0503	-2.967 (0.233)	-0.149	
S <sub>3</sub>	CX i.p	1.319	0.390 (0.088)	0.514	
S <sub>4</sub>	CX o.p	-0.553	0.818 (0.094)	-0.452	
S <sub>5</sub>	COY	0.1377	1.095 (0.077)	-0.151	
S <sub>6</sub>	CX <sub>3</sub> s. def	0.5564	-0.226 (0.087)	-0.126	
S <sub>7</sub>	CX <sub>3</sub> as. def	4.650	0.074 (0.038)	-0.344	
S <sub>8</sub>	CX <sub>3</sub> rock	0.2374	-0.105 (0.193)	-0.025	
S <sub>10</sub>	CX o.p				0.987 (0.028)
S <sub>11</sub>	CX <sub>3</sub> def				-0.093 (0.078)
S <sub>12</sub>	CX <sub>3</sub> rock				0.295 (0.114)
S <sub>13</sub>	O–Y---O				0.844 (0.009)

a Obtained as ratios from the ab initio calculation<sup>11</sup>.

b The numbers in parentheses are the standard deviations of the parameters from the non-linear least squares fit.

$$d_i = \frac{\partial\mu^y}{\partial S_i} / \frac{\partial\mu^x}{\partial S_i} \quad (8.12)$$

all of the  $d_i$  are known and the relation for the A' modes becomes

$$\left| \frac{\partial\bar{\mu}}{\partial Q_j} \right|^2 = \left[ \sum_i \left( \frac{\partial\mu^x}{\partial S_i} \right) (l_s)_{i,j} \right]^2 + \left[ \sum_i \left( \frac{\partial\mu^y}{\partial S_i} \right) (d_i) (l_s)_{i,j} \right]^2 \quad (8.10a)$$

These equations and Torri and Tasumi's values of  $d_i$  were used to obtain the components of the  $\partial\bar{\mu}/\partial S_i$  from the  $\left| \partial\bar{\mu}/\partial Q_j \right|^2$  values in Table 8.17, the symmetrized eigenvectors in Table 8.16, and the  $d_i$  values in Table 8.18. The non-linear simultaneous equations were solved by a non-linear least squares program MUFIT. For the A' modes, the 32 sets of data were used to calculate the 8  $\partial\mu^x/\partial S_i$  values, from which the  $\partial\mu^y/\partial S_i$  values were calculated through the  $d_i$ . The least squares values are listed in Table 8.18 in the units D Å<sup>-1</sup>, along with the standard deviations. For the A'' modes, the 16 sets of data

**Table 8.19** The calculated values of  $|\partial\bar{\mu}/\partial R|$  in the x,y,z components in units D Å<sup>-1</sup>.

$\partial\bar{\mu}/\partial R$		x	y	z	$ \partial\bar{\mu}/\partial R $
R <sub>1</sub>	OY	2.125	2.913	0	3.61
R <sub>2</sub>	CO	-2.967	-0.149	0	2.97
R <sub>3</sub>	CX i.p.	0.390	0.514	0	0.645
R <sub>4</sub>	CX o.p.	0.578	-0.320	0.698	0.961
R <sub>5</sub>	CX o.p.	0.578	-0.320	-0.698	0.961
R <sub>6</sub>	COY	1.095	-0.151	0	1.11
R <sub>7</sub>	XCX	-0.033	-0.333	0	0.335
R <sub>8</sub>	XCX o.p.	-0.124	0.088	-0.066	0.166
R <sub>9</sub>	XCX o.p.	-0.124	0.088	0.066	0.166
R <sub>10</sub>	XCO i.p.	0.005	0.030	0	0.030
R <sub>11</sub>	XCO o.p.	0.134	0.061	0.209	0.256
R <sub>12</sub>	XCO o.p.	0.134	0.061	-0.209	0.256
R <sub>13</sub>	O–Y---O	0	0	0.844	0.844

were used to calculate the 4  $\partial\mu^2/\partial S_i$  values tabulated in Table 8.18. the quality of the fit is indicated by the calculated values of  $\mu_j^2$  which are tabulated with the accepted values in Table 8.17.

The  $\partial\bar{\mu}/\partial S_i$  values can be used to obtain  $\partial\bar{\mu}/\partial R_j$  through the U matrix,

$$\frac{\partial\bar{\mu}}{\partial R_j} = \sum_i \frac{\partial\bar{\mu}}{\partial S_i} U_{i,j}$$

where  $U_{i,j}$  are the elements of the U matrix given in Table 8.9. The components of  $\partial\bar{\mu}/\partial R_j$  so calculated are given in Table 8.19.

## 8.5 Discussion

The normal coordinate calculations were based on two criteria. First, to obtain a very good fit to all of the experimental wavenumbers with the smallest number of symmetrized force constants,  $F_{i,j}$ . Second, to ensure that the eigenvectors of the CO stretching vibration at 1034 cm<sup>-1</sup> were essentially unchanged between CH<sub>3</sub>OH and



CH<sub>3</sub>OD, so that the experimentally observed equal intensities of this vibration in the two molecules would be satisfactorily explained by the calculation.

Very few force fields were found to satisfy the second criterion. The CO stretching and COH or COD in-plane deformation displacements were heavily mixed in this vibration of CH<sub>3</sub>OH and CH<sub>3</sub>OD, and were differently mixed in the two molecules under most force fields. In spite of extensive exploration it has not been possible to find physically meaningful conditions for the force field to meet the second criterion, because any change in input was likely to cause a result that was not acceptable under this criterion. Thus, at one stage of the refinement it was found that two calculations, which started from the same reasonable force field but used the observed CH and CD stretching wavenumbers in one and the harmonic wavenumbers in the other, converged to different solutions, two of which fitted the wavenumbers equally well, but only one of which met the second criterion. To meet the second criterion, it was found necessary in the final calculations to make three changes. First, to remove the potential interaction between the A' symmetric and asymmetric CH<sub>3</sub> deformation vibrations, by setting  $F_{6,7}$  to zero. Second, to remove the potential interaction between the symmetric CH<sub>3</sub> deformation and the A' CH<sub>3</sub> rock, by setting  $F_{6,8}$  to zero. Third, to include  $F_{5,7}$ , the interaction constant between the asymmetric CH<sub>3</sub> deformation and the in-plane COH (and COD) deformation.

The final force field meets the second criterion, but the failure to understand its origins in spite of extensive study is not satisfying. The sensitivity of the eigenvectors to the force field underlines the potential importance of intensities for deciding between different force fields which reproduce the wavenumbers, thus increasing the probability of obtaining the correct force field. But at the same time it illustrates the frustration that has been experienced by workers in the field, who found that the uncertainties in the eigenvectors caused by uncertainty in the force fields made it very difficult to obtain values of intensity parameters such as  $|\partial\bar{\mu}/\partial R|$  that could be related meaningfully between molecules.

Most of the force constants that were set to zero during the refinement of the  $F_{i,j}$  were included in earlier trials and converged to very small values. Thus, while the final force field is clearly not unique, it is well-based on the available evidence. It should be noted that it is weakest area for the CH<sub>3</sub> and CD<sub>3</sub> deformation and rocking vibrations, because it was not possible to assign reliably all five of these vibrations in any of the isotopomers, and only three were assigned for CH<sub>3</sub>OH and CD<sub>3</sub>OH.

Serrallach, Meyer and Günthard<sup>9</sup> made a very thorough normal coordinate calculation of gaseous and matrix-isolated methanol in 1974. They initially included wavenumbers of the four isotopomers used in this thesis. They also used their revised assignment of the spectra of these molecules, which has been followed in this work. They fitted 44 observed wavenumbers, uncorrected for anharmonicity, to 15 valence force constants, analogous to the  $f_{i,j}$  of this thesis. They used the results of this calculation to assign the spectra of the rotamers of  $\text{CHD}_2\text{OH}$ ,  $\text{CHD}_2\text{OD}$ ,  $\text{CH}_2\text{DOH}$  and  $\text{CH}_2\text{DOD}$ . They then used the 122 wavenumbers of all of these molecules to further refine their 15 force constants. The force constants presented above are consistent with theirs but can not be compared closely for at least three reasons. First, they determined 15 valence force constants but 24 were determined in this work. Second, for the  $\text{CH(D)}$  stretching vibrations they fitted observed wavenumbers to within about  $15\text{ cm}^{-1}$ , and harmonic wavenumbers were fitted to within  $2\text{ cm}^{-1}$  in this work. Third, the hydrogen bonding in the liquid causes the  $\text{OH(D)}$  stretching,  $\text{COH(D)}$  in-plane and out-of-plane deformation vibrations to have quite different wavenumbers from those in the gas. This of course makes the stretching force constants different but, more generally, it also affects most of the vibrations below  $1500\text{ cm}^{-1}$  which prevents meaningful comparison of force constants for these vibrations.

Following an independent careful study of methanol, Mallinson<sup>14-15</sup> determined 28 of the 46 possible symmetrized force constants from wavenumbers of matrix isolated isotopomers of methanol. He used data for  $\text{CH}_3\text{OH}$ ,  $\text{CH}_3\text{OD}$ ,  $\text{CD}_3\text{OH}$ ,  $\text{CD}_3\text{OD}$ ,  $^{13}\text{CH}_3\text{OH}$ ,  $\text{CH}_3^{18}\text{OD}$ , and the two rotamers of both  $\text{CHD}_2\text{OH}$  and  $\text{CH}_2\text{DOH}$ . He approximately corrected all of their wavenumbers for anharmonicity but did not report these corrected wavenumbers. Instead, he reported the observed wavenumbers with the corrected wavenumbers "deharmonized for display"<sup>15</sup>. His symmetry coordinates differed from those in this work, and his treatment of the  $A'$  redundancy differed also. His fit to the observed wavenumbers was generally markedly worse than ours. All of these factors combine to mean that, while Mallinson's force constants are generally consistent with those found in this work, a detailed comparison is not useful.

The calculations yielded a small set of intensity parameters,  $\partial\bar{\mu}/\partial S_i$  and  $\partial\bar{\mu}/\partial R$  vectors that fit the experimental intensities of four isotopomers of methanol to a satisfying degree. Individual cases are discussed below, but it can be noted that the quality of the fit as defined by the standard deviation in  $|\partial\bar{\mu}/\partial Q_j|^2$  (Table 8.17) was  $0.25\text{ (D}\text{\AA}^{-1}\text{amu}^{-1/2})^2$  for the  $A'$  and  $0.06\text{ (D}\text{\AA}^{-1}\text{amu}^{-1/2})^2$  for the  $A''$  vibrations. The standard deviations of the fitted

parameters  $\partial\mu^x/\partial S_i$ , termed here  $\sigma_p$ , range from 0.6% for the OY stretching coordinate and 1% for the O–Y---O out-of-plane coordinate through approximately 10% for the CX stretching, CO stretching, and COY in-plane deformation coordinates to 40 to 80% for the CX<sub>3</sub> deformation and A'' rocking coordinates and 180% for the A' CX<sub>3</sub> rocking motion. A broad generalization that may be useful to state is that the use of curve fits to separate bands has provided  $|\partial\bar{\mu}/\partial S_i|$  values known with roughly 50% uncertainty in cases where no values were available without such fits.

The intensities of the OH and OD stretching vibrations were all determined to  $\leq 2\%$  in this work (Tables 8.1 to 8.4) and were all fitted to better than 2% (Table 8.17).  $|\partial\bar{\mu}/\partial S_i|$  was determined to  $\sigma_p = 0.5\%$  (Table 8.18) and the value obtained for  $|\partial\bar{\mu}/\partial R|$ , 3.61 DÅ<sup>-1</sup> is within 1% of those reported in Table 7.7 from the simple diatomic oscillator model.

To make the dipole moment derivatives with respect to the internal coordinates more meaningful it can be noted that 1 Debye Å<sup>-1</sup> is equivalent to 0.208 electronic charges. Thus a  $|\partial\bar{\mu}/\partial R|$  value of 3.61 DÅ<sup>-1</sup> for the OH stretching displacement is equivalent to 0.75 e<sup>-</sup>. However this should not be interpreted to mean that a fixed charge of 0.75 e<sup>-</sup> is located on the hydrogen and oxygen atoms, although this would give the same value of  $|\partial\bar{\mu}/\partial R|$ , because it is well established that charge flow makes an important contribution to the value of  $|\partial\bar{\mu}/\partial R|$ .

For the CO stretching vibration, the intensities were determined to about 3% for the CH<sub>3</sub>OY and about 7% for CD<sub>3</sub>OY, the latter being heavily coupled with the symmetric CH<sub>3</sub> deformation (Table 8.1 to 8.4). The intensities were fitted 18% low for CH<sub>3</sub>OY and 15 to 20% high for CD<sub>3</sub>OY (Table 8.17), and  $\sigma_p$  for  $|\partial\bar{\mu}/\partial S_i|$  was 8% (Table 8.18). The value of  $|\partial\bar{\mu}/\partial R| = 2.97$  DÅ<sup>-1</sup> (Table 8.19) is 25% below the  $4.01 \pm 0.02$  DÅ<sup>-1</sup> determined from the two CH<sub>3</sub>OY molecules under the harmonic approximation (Table 6.7). It seems probable that the diatomic approximation overestimates this value, but it is clear that the calculation of intensities from the normal coordinates put too much weight on the less reliable intensities of CD<sub>3</sub>OH and CD<sub>3</sub>OD.

The in-plane COY deformation intensity is well fitted. The intensities (Table 8.1 to 8.4) were determined to 10 to 15% for CH<sub>3</sub>OY, 1% for CD<sub>3</sub>OH and about 50% for CD<sub>3</sub>OD, and are fitted to better than 12%, with that of CD<sub>3</sub>OD fitted exactly.  $|\partial\bar{\mu}/\partial S_i|$  was determined with  $\sigma_p = 7\%$  and  $|\partial\bar{\mu}/\partial R| = 1.11$  DÅ<sup>-1</sup> compared with the values 1.03, 0.82 and 1.07 DÅ<sup>-1</sup> determined by the uncoupled approximation (Tables 6.7 and 7.7).

The O–Y---O out-of-plane deformation gives the best result after the OH and OD stretching vibrations, undoubtedly because they were both essentially uncoupled oscillators in the normal coordinate calculation. The intensities were determined to within 6% and fitted to similar accuracy,  $\sigma_p$  for  $|\partial\bar{\mu}/\partial S_i|$  was 1% and the value  $|\partial\bar{\mu}/\partial R| = 0.84 \text{ D}\text{\AA}^{-1}$  agrees with the values 0.82 to 0.85  $\text{D}\text{\AA}^{-1}$  obtained from the isolated oscillator treatment (Section 7.8).

The  $\text{CH}_3$  stretching vibrations yielded  $|\partial\bar{\mu}/\partial S_i|$  values with standard deviations  $\sigma_p$  of 10 to 20% for the  $A'$  symmetry coordinates and 3% for the  $A''$  coordinate. The calculated  $|\partial\bar{\mu}/\partial R|$  values were 0.65  $\text{D}\text{\AA}^{-1}$  for the in-plane CH bond and 0.96  $\text{D}\text{\AA}^{-1}$  for the out-of-plane bonds that are both probably reliable to 10 to 20%. These  $|\partial\bar{\mu}/\partial R|$  values compare with 0.86 to 0.98  $\text{D}\text{\AA}^{-1}$  found from the approximate treatment (Tables 6.7 & 7.7). The reliability of these results is consistent with that of the intensities of the individual fundamentals (Tables 8.1 to 8.8), which was roughly 20% compared with the 1 to 5% probable accuracy of the overall CH and CD stretching intensity.

It is of particular note that the  $|\partial\bar{\mu}/\partial R|$  value for the in-plane CH bond is 0.65  $\text{D}\text{\AA}^{-1}$ , about 30% lower than the 0.96  $\text{D}\text{\AA}^{-1}$  for the out-of-plane bonds. Kindness, McKean and Stewart<sup>16</sup> found a similar result for the CH bond of  $\text{CHD}_2\text{OH}$ , with  $|\partial\bar{\mu}/\partial R|$  equal to 0.89  $\text{D}\text{\AA}^{-1}$  for the in-plane CH, trans to the OH group, and 0.91  $\text{D}\text{\AA}^{-1}$  for the out-of-plane CH bonds, which are trans to the lone pair of electrons on the oxygen atom. The situation is expected to be different for molecules in the liquid, because the electron density around the oxygen atom is changed by hydrogen-bonding, and the present result indicates a greater anisotropy in the electron density in the liquid than in the gas.

The  $\text{CH}_3$  and  $\text{CD}_3$  deformation vibrations are less well known. The total intensity was determined to about 5% for the two  $\text{CH}_3$  isotopomers but only 25% for the  $\text{CD}_3$  molecules. The intensities of the individual vibrations were known to only about  $\pm 20$  to 100%, and two of the twelve were not known. The individual transitions were fitted to at best 15% and at worst a factor of 2, and the total intensity was fitted to between 16% and 50%. The standard deviations of the  $|\partial\bar{\mu}/\partial S_i|$  values were 40 to 80% and yielded  $|\partial\bar{\mu}/\partial R|$  equal to 0.34  $\text{D}\text{\AA}^{-1}$  for the in-plane angle and 0.17 for the two out-of-plane angles. The values reported previously from an approximate treatment were 0.25  $\text{D}\text{\AA}^{-1}$  for both  $\text{CH}_3\text{OH}$  and  $\text{CH}_3\text{OD}$ . The present results suggest that this value is reliable to within a factor of 2.

The  $\text{CH}_3$  and  $\text{CD}_3$  rocking vibrations were the weakest in the spectra and the most poorly determined and this is reflected in the results of the normal coordinate and intensity

**Table 8.20** Comparison of the values of  $|\partial\bar{\mu}/\partial S_i|$  obtained in this work and obtained by the ab initio calculation<sup>13</sup>.

$ \partial\bar{\mu}/\partial S_i $		This work	Ab initio <sup>13</sup>
S <sub>1</sub>	OY	3.61	0.82
S <sub>2</sub>	CO	2.97	3.30
S <sub>3</sub>	CX i.p.	0.65	0.66
S <sub>4</sub>	CX o.p.	0.94	1.02
S <sub>5</sub>	COY	1.10	1.05
S <sub>6</sub>	CX <sub>3</sub> s. def	0.26	0.04
S <sub>7</sub>	CX <sub>3</sub> as. def	0.35	0.19
S <sub>8</sub>	CX <sub>3</sub> rock	0.11	0.38
S <sub>10</sub>	CX o.p.	0.99	0.99
S <sub>11</sub>	CX <sub>3</sub> def	0.09	0.21
S <sub>12</sub>	CX <sub>3</sub> rock	0.29	0.04
S <sub>13</sub>	O–Y---O o.p.	0.94	1.21

calculation. The  $|\partial\bar{\mu}/\partial Q_j|^2$  values of one A' mode of CH<sub>3</sub>OH, CH<sub>3</sub>OD and CD<sub>3</sub>OH were fitted to better than 25%, but the fit for the other vibrations was within a factor of about 2. The  $|\partial\bar{\mu}/\partial S_i|$  values were determined with standard deviations of about 180% for the A' and 40% for the A'' coordinate, and the  $|\partial\bar{\mu}/\partial R|$  values were 0.03 DÅ<sup>-1</sup> for the in-plane coordinate and 0.26 DÅ<sup>-1</sup> for the out-of-plane. These are undoubtedly of the right order of magnitude, but should be used with caution.

The  $|\partial\bar{\mu}/\partial S_i|$  values obtained from the non-linear least-squares fit of the experimental  $|\partial\bar{\mu}/\partial Q_j|^2$  values are compared in Table 8.20 with those calculated by Torii and Tasumi<sup>13</sup> in an ab initio quantum mechanical calculation of an isolated CH<sub>3</sub>OH molecule. An MP2/6-31G ext. basis set<sup>†</sup> was used<sup>13</sup>. The ratio of  $\partial\mu^x/\partial S_i$  to  $\partial\mu^y/\partial S_i$  for the A' modes was the same in both studies because it was used in this work to fix the direction of the  $\partial\bar{\mu}/\partial S_i$  vectors.

<sup>†</sup> The 6-31G ext. basis set is constructed by adding one set of diffuse *sp* (or *s*) functions and one set of diffuse polarization (*d* or *p*) functions to the 6-31G\*\* basis set.

The two sets of values should not agree for the OH stretching and COH in-plane and out-of-plane bending vibrations, because these are directly affected by the hydrogen-bonding in the liquid. It should be noted that Torii and Tasumi's value for the unbonded OH stretching displacement,  $0.82 \text{ D}\text{\AA}^{-1}$ , agrees with that reported<sup>17-19</sup> for  $\text{CH}_3\text{OH}$  in dilute solution in  $\text{CCl}_4$ ,  $1.03 \pm 0.02 \text{ D}\text{\AA}^{-1}$ . This value is enhanced nearly 4 times by the hydrogen-bonding in liquid methanol. It should be noted also that the two sets of values in Table 8.20 suggest that the  $\partial\bar{\mu}/\partial S_i$  values for the in-plane COH deformation motion and the out-of-plane O-H---O motion, which is the torsion for the isolated molecule, are little changed by the hydrogen bonding. Following Zerbi's theory<sup>20</sup>, this allows a distinction to be made between the effects of hydrogen-bonding on the effective charge on the hydrogen atom and on the charge flux when the O-H bond is stretched. The effective charge dominates the intensity of a bending motion, so the effective charge is little changed by the hydrogen-bonding. The charge flux comes into play when a bond is stretched, and it clearly is increased 3 or 4 times by hydrogen-bonding.

For the remainder of the vibrations, Table 8.20 shows excellent agreement between the values determined from experiment through a non-linear least squares fit and those calculated by ab initio quantum mechanics, except for the  $\text{CH}_3$  deformation and rocking vibrations. In particular, the ab initio calculation supports the lower value,  $2.97 \text{ D}\text{\AA}^{-1}$ , of  $|\partial\bar{\mu}/\partial R_{\text{CO}}|$  found from the least squares fit, and supports the result that  $|\partial\bar{\mu}/\partial R_{\text{CH}}|$  of the in-plane CH bond is 30 to 40% smaller than that for the other two CH bonds.

The two sets of values do not agree for the  $\text{CH}_3$  deformation and rocking bands, in fact the values for the rock and deformation are almost interchanged. The result of the present work that the  $|\partial\bar{\mu}/\partial S_i|$  value for the A" deformation is smaller than that for the rock suggests that these vibrations, which were not well determined experimentally, have not been satisfactorily fitted by the normal coordinate calculation.

## 8.6 References

1. J. E. Bertie, S. L. Zhang, H. H. Eysel, S. Baluja, and M. K. Ahmed, *Appl. Spectrosc.* **47**, 1100 (1993).
2. J. E. Bertie and S. L. Zhang, *Appl. Spectrosc.* **48**, 176 (1994).
3. J. E. Bertie and S. L. Zhang, *J. Chem. Phys.* In press (November, 1994).
4. J. E. Bertie, S. L. Zhang, and C. D. Keefe, *J. Mol. Struct.* **324**, 157 (1994).

5. R. M. Lees and J. G. Baker, *J. Chem. Phys.* **48**, 5299 (1968).
6. A. H. Narten and A. Habenschuss, *J. Chem. Phys.* **80**, 3387 (1984).
7. E. B. Wilson, J. C. Decius, and P. C. Cross, *Molecular Vibrations*, McGraw-Hill (New York, 1955).
8. J. H. Schachtschneider, *Technical Report, 57-65*, Shell Development Company (Emeryville).
9. A. Serrallach, R. Meyer, and H. H. Günthard, *J. Mol. Spectrosc.* **52**, 94 (1974).
10. G. Herzberg, *Molecular Spectra and Molecular Structure. I. Spectra of Diatomic Molecules*, D. Van Nostrand, Princeton, 1950. P142.
11. C. Bourderon and C. Sandorfy, *J. Chem. Phys.* **59**, 2527 (1973).
12. *Vibrational Intensities in Infrared and Raman Spectroscopy*, Ed. W. B. Person and G. Zerbi, Elsevier, Amsterdam, 1982.
13. H. Torii and M. Tasumi, *J. Chem. Phys.* **99**, 8459 (1993).
14. P. D. Mallinson and D. C. McKean, *Spectrochim. Acta* **30A**, 1133 (1973).
15. P. D. Mallinson, *J. Mol. Spectrosc.* **58**, 194 (1975).
16. A. Kindness, D. C. McKean and D. Stewart, *J. Mol. Struct.* **224**, 363 (1990).
17. S. Singh, D. Schiöberg and W. A. P. Luck, *Spectrosc. Lett.* **14**, 141 (1981).
18. H. H. Eysel and J. E. Bertie, *J. Mol. Struct.* **142**, 227(1986).
19. J. E. Bertie, H. Harke, M. K. Ahmed, and H. H. Eysel, *Croat. Chem. Acta* **61**, 391 (1988).
20. C. Castiglioni, M. Gussoni and G. Zerbi, *J. Mol. Struct.* **198**, 475 (1989).

## Chapter 9 Conclusion

This thesis has presented the most complete experimental study of the vibrational intensities of a small but not too simple molecule to date, and one of the most complete analyses of the intensities of all vibrations that has been attempted for any molecule. It is very rare for such a careful attempt to be made to separate the intensities of overlapping bands, and rare for attention to be paid to the complex region below  $1500\text{ cm}^{-1}$ . Usually attention is focused on the stretching vibrations at high wavenumber, undoubtedly to avoid the significant complication caused by coupling of different molecular displacements in the normal vibrations.

The achievements of the work for this thesis may be summarized as follows.

The original computation procedures of converting pATR spectra to the real and imaginary refractive index spectra were found to give only about 4% accuracy before this work was started. Significant improvements of the method have been made in this work and the accuracy of the improved method was explored in two aspects. First, the KK transform used in the method to transform the imaginary refractive index spectrum to the real refractive index was explored in terms of its substitute, the FFT-based Hilbert transform, to increase the speed of the calculation without loss of accuracy. The algorithm for such a Hilbert transform has been presented and it gives 0.05% accuracy. Second, the overall accuracy of the procedures was explored using synthesized spectra. The current overall accuracy was found to be to about 0.2%, except for 0.5% for the strongest bands that can be measured in the CIRCLE cell.

Different integrated intensities,  $A_j$ ,  $B_j$  and  $C_j$ , can be obtained from different absorption spectra. Consequently, the accuracy was explored to determine the best method for obtaining the dipole moment derivatives from these different integrated intensities. It was found that the method through  $C_j$ , the area under the  $\tilde{\nu}\alpha''_m$  spectrum, gives the best accuracy.

The infrared spectra of  $\text{CH}_3\text{OH}$ ,  $\text{CH}_3\text{OD}$ ,  $\text{CD}_3\text{OH}$  and  $\text{CD}_3\text{OD}$  have been measured with the ordinates accurate to about 3% and, as usual, the wavenumbers accurate to  $0.1\text{ cm}^{-1}$ , i.e. to 0.025% at  $400\text{ cm}^{-1}$  and 0.002% at  $6000\text{ cm}^{-1}$ . The real and imaginary refractive index spectra were calculated from the spectra, the former accurate to about 0.2% and the latter to about 3%. These are themselves fundamental optical properties, because the result of any well defined infrared experiment can be calculated from them.



The refractive index spectra were transformed without loss of accuracy into the real and imaginary dielectric constant spectra, which were included for the record but not used and, under the assumption of the Lorentz local field, into the imaginary molar polarizability spectra of the four isotopomers. To obtain integrated intensities of all of the transitions, the spectra had to be dissociated into their component bands. This was done by two methods, namely by comparing of the spectra of the different isotopomers and by fitting the spectra by the near-Lorentzian classical damped harmonic oscillator bands and, for the motions of the hydrogen bonded hydrogen or deuterium atom, Gaussian bands. The sets of the integrated intensities generally agreed well. An accepted set of intensities was obtained from the results of these two methods. The estimated accuracies of these integrated intensities ranged from  $\pm 1\%$  to  $\pm 25\%$  for the different vibrations, except for the individual methyl deformation vibrations and the methyl rocking vibrations where integrated intensities could only be determined to within a factor of 1.5 to 2.

A normal coordinate calculation was made to fit the wavenumbers of the fundamentals in the  $\tilde{\nu}\alpha_m''$  spectra, with the OH, OD, CH and CD stretching and O-H---O out-of-plane deformation wavenumbers corrected for anharmonicity. This calculation was constrained to match the experimental result that the intensity and wavenumber of the CO stretching vibration are the same in  $\text{CH}_3\text{OH}$  and  $\text{CH}_3\text{OD}$ . The eigenvectors from this calculation were used, with the directions of the  $\partial\bar{\mu}/\partial S_i$  vectors calculated by Torii and Tasumi from ab initio quantum mechanics, to calculate 8 values of  $\partial\mu^x/\partial S_i$  ( $A'$ ) by a non-linear least squares fit of the 32 observed integrated intensities for the  $A'$  modes. By the same method, the 4 values of  $\partial\mu^z/\partial S_i$  ( $A''$ ) were calculated from 16 integrated intensities for the  $A''$  modes. The changes in dipole moment of the molecule during displacement of the different valence coordinates were then calculated from these quantities. In favourable cases the latter provide a single parameter that explains the intensities in all four molecules very well to a percent or two, and in the worst case they indicate the order of magnitude of the change in dipole moment. Other theoretical treatments of the experimental data are possible, and the data are presented in full to make this possible.

The difficulty of transforming intensity data into properties of specific displacements in the molecule through normal coordinate transformations has troubled earlier workers and were clearly a significant limitation in this work. The increased use of help from ab initio calculations will undoubtedly help this problem, but ab initio calculations are intrinsically for isolated molecules, and must be used with caution for molecules in the liquid. Nevertheless it is always the case that better results are obtained from better data,

and in the present case the data has independent value as the fundamental optical properties of the liquid samples. It is clear that our knowledge and use of the intensity axis of infrared spectra will be markedly advanced by the continued measurement of vibrational spectra of liquids to the few percent ordinate accuracy of this work, and by the continued use of isotopic comparison, curve-fitting, and critical recognition of the difficulties of separating the integrated intensities of the different vibrations.